STUDIES ON NON-LITHOGRAPHIC TECHNIQUES FOR NANOSTRUCTURING OF THIN FILMS AND SURFACES

A thesis
Submitted for the degree of

Doctor of Philosophy
in
Physics

By

Prashant Kumar

School of Physics, University of Hyderabad, Hyderabad-500046, India.

December 2008.

DECLARATION

I hereby declare that the content embodied in this thesis entitled **"*Studies on non-lithographic techniques for nanostructuring of thin films and surfaces*"** is the result of investigations carried out by me under the supervision of **Dr. M. Ghanashyam Krishna**, for the degree of ***Doctor of Philosophy (PhD)*** in Physics at the School of Physics, University of Hyderabad, Hyderabad, India.

Place: Hyderabad
Date: **(Prashant Kumar)**

CERTIFICATE

This is to certify that the work described in this thesis has been carried out by **Mr. Prashant Kumar** under my supervision at **School of Physics, University of Hyderabad**, Hyderabad, India and this has not been submitted for any degree or diploma at this or any other university.

Place: Hyderabad
Date: **(Dr. M. Ghanashyam Krishna)**

Dean,
School of Physics,
University of Hyderabad.

ACKNOWLEDGEMENTS

I would like to acknowledge the encouragement and support by my thesis supervisor and mentor Dr. M. Ghanashyam Krishna. He is a unique amalgam who has in him a nice chemist and brilliant physicist simultaneously. The research training imparted by him is of immense help for the way forward in research career. His mode of training has been simply superb. I would be happy to continue with him, the sweet relationship which, has shaped up over the years; for my research life ahead.

Money is not everything but is very important and crucial in shaping up of human life. My acknowledgements for University of Warwick, UK and in particular for Prof. A. K. Bhattacharya now at University of Oxford are due to financial support to my research when it counted, I mean in early years. Moreover, I thank University grants commission and for that matter Prof. A. P. Pathak for fellowship to me under CAS-Physics scheme for the last part of Ph.d.

It would be unfair on my part if I do not acknowledge countless efforts and leadership by my supervisor Dr. M. Ghanashyam Krishna who established the thin film laboratory of its kind in India at school of Physics. My thanks are also for them who have been part of the group who have attracted the huge funding from department of science and technology (DST) and in turn bringing most advanced scientific instruments to the university. I would be happy to be associated with and working under the theme of "DST Centre of Nanotechnology" in future.

I would thank Prof A. K. Bhatnagar and Dr. K. C. James Raju for their continued support throughout my research. I would thank Prof. S. N. Kaul, Prof. C. S. Sunandana and Prof. Chatterjee; both from School of Physics for occasional physics discussions we had. I would like to thank Prof. Vipin Srivastava and Prof. V. S. S. Sastry; the current and previous dean, school of physics, for their leadership activities in School of Physics.

Facilities provided by University grants commission (UGC) under SAP and UPE program and Department of science and technology (DST) under ITPAR programme are gratefully acknowledged.

My acknowledgements are for Dr. A. K. Singh who answered patiently my curiosities in Bachelor's at BHU Varanasi. I would like to personally thank my Master's supervisor Prof. Prasenjit Sen at JNU, New Delhi; who helped me immensely in Master's experimental project. He imparted experimental curiosity to me and introduced me to the beautiful Nanoworld.

I would like to thank few materials scientists in India with whom I shared my views and discussed a few things. The list includes Prof. R. C. Budhani from IIT Kanpur, Prof. Ganeshan from IUC Indore, Prof. O. N. Srivastava at BHU Varanasi, Prof. C. N. R. Rao at JNC Bangalore and Dr. Indranil Das from SINP.

My sincere thanks are for CIL staffs who helped me during last 5 years research. The list includes the name of Mr. Murthy, Dr. Manjunath, Mr. Suresh, Ms. Rama Devi and Mr. Nageshwara Rao for their continuous help in time. Again I would like to acknowledge the help from Mr. Ravi Shankar at School of Physics for doing XRD for my thin films. I would like to thank all staffs at School of Physics office including Mr. T. Abraham who takes lot of responsibility without a complaint. I would like to thank all the staffs from science workshop with special mention of Mr. Vincent.

I would like to thank all my well wishers from physics department including Dr. Shuhojit Sarkar, Dr. Phani Murli Krishna, Dr. Bharthi Mohan, Mr. Trivikram Rao, Mr. Sanjeev kumar, Mr. Ashutosh Abhayankar, Dr. Basheed, Mrs. Thejal Abraham, Miss. Juby George, Mr. Joji Kurian, Mr. Sultan Mohammad, Mr. T. Abhilash, Mr. Ch. Ravi Kumar, Mr. Sathish Ayala, Mr. N. Sathish, Mr.Swaroop and Dr. Vekatram Nalla.

I would like to thank all my labmates who made the stay pleasant. The list includes Dr. Uma Mahendra Kumar, Mr. Venkat Sarvanan, Dr. D. Pamu, Mr. G. Lakshmi Narayana, Mr. Sudhindran, Mr. Vasu, Mr. Rambabu and Mr. Lakshun. I would like to mention the alumni who were very co-operative. Those are Mr. Polysetty Sriniwas, Mr. Ayan Bhattacharya, Mr. Ragam Srinawasa Rao, and Dr. Madhurima. Special thanks to Mr. Rajeeb Brahma and Mr. Venkat Sarvanan for their help in optical characterizations time to time.

I would like to thank whole heartedly the friendship and support extended by Mr. M. S. R. N. Kiran with whom I have shared a lot more apart from my experimental work. Apart from being an encouraging labmate, he has been very nice as a person to me. I would like to continue co-operation in research with him.

I would like to thank my parents, elder sister Bhavna, younger brother Jayant and younger sister Rashmi for supporting me to become materials scientist.

Acknowledgements will be half if I do not mention the support of my better half Mrs. Shipu, who apart from taking care of family matters have been supporting for my research from last two years.

List of Publications:

1. "Dynamic force microscopy of ultrathin Ni and Ag thin films deposited by pulsed laser deposition", **Prashant Kumar**, M. Ghanashyam Krishna, A. K. Bhatnagar, A. K. Bhattacharya, Journal of material research, Vol. 23, 1826 **(2008).**
2. "Excimer laser nanostructuring of silicon surfaces", **Prashant Kumar**, M. Ghanashyam Krishna, A. K. Bhattacharya, Jour. of Nanoscience and Nanotechnology Vol.9, No. 2, 1–9 (**2009**)
3. "DC Electric field induced surface nanostructuring of Ni and In thin films", **Prashant Kumar**, M. Ghanashyam Krishna, A. K. Bhattacharya, International Journal of Nanoscience, Vol. 7, Nos. 4 & 5 (**2008**) 1–7
4. "Template assisted growth of nanowires", **Prashant Kumar**, M. Ghanashyam Krishna, A. K. Bhatnagar, A. K. Bhattacharya, International Journal of Nanomanufacturing (IJNM) (**In Press**)
5. "The effect of micro structural growth at nanoscale for nickel thin films on the magnetization reversal behaviour". **Prashant Kumar**, M. Ghanashyam Krishna, A. K. Bhattacharya (communicated to Bulletin of Materials Science)
6. "Photoluminescence study of laser nanostructured silicon surface", **Prashant Kumar**, M. Ghanashyam Krishna, A. K. Bhattacharya (communicated).
7. "Comparison of nanostructuring of gold thin films with DC Electric field and excimer laser as high energy trigger", **Prashant Kumar**, M. Ghanashyam Krishna, A. K. Bhattacharya. (communicated)
8. "Surface plasmonic peak shift for field and laser nanostructured Indium thiin films", **Prashant Kumar**, M. Ghanashyam Krishna, A. K. Bhattacharya. (communicated)
9. "Excimer laser nanostructuring of α-alumina surface", **Prashant Kumar**, M. Ghanashyam Krishna, A. K. Bhattacharya (communicated).

AUTHORSHIP TO THE CHAPTER OF BOOK

10. Book chapter (chapter no. 4 "Non lithographic approaches to surface nanostructuring") in a book titled "Emerging nanotechnologies for manufacturing" edited by Waqar Ahmed and Mark Jackson, to be published by Micro and Nanotechnologies, William Andrew Inc.), M. Ghanashyam Krishna and **Prashant Kumar**, (**In press**; to be published in **Jan 2009**).

Contents

Page No.

Chapter-1

Introduction

Abstract:

This chapter introduces the topic and motivation of the thesis. It has three major sections. The first section deals with the introduction of nanostructured surfaces and materials in general and its variety of applications. Major technological applications of nanostructures / nanostructured surfaces are described and their impacts on the functionality of the material surface are discussed. The second part deals with lithographic nanostructuring techniques. Varieties of nanostructures fabricated via lithographic techniques are reviewed. At the end of second section, the limitations and shortcomings of lithographic techniques and the need for non-lithographic techniques are pointed out. Developments in non-lithographic techniques are reviewed in the third section. Among non-lithographic techniques, self-assembled early stages of thin film growth, template assisted growth, field assisted nanostructuring, laser assisted nanostructuring technique and VLS growth techniques are reviewed. Relevant theoretical treatment based on thermodynamic approaches is also presented.

1.1 Introduction to Nanotechnology and nanostructured materials

Nanotechnology

Nanotechnology, loosely defined as the fabrication of functional structures with dimensions in the 1-100 nanometer range has emerged as a promising field of research. During the last decade, developments in the areas of materials, surface microscopy, fabrication and computational engineering have converged to provide remarkable capabilities for understanding, fabricating and manipulating structures at the atomic level.

Research in nanoscience is exploding, both because of the ability to construct matter and molecules one atom at a time and significant societal impact of the new technical capabilities that permit creation of materials and devices. The rapid evolution of this new science and the opportunities for its application promise that nanotechnology will become one of the dominant technologies of the 21st century. Nanotechnology is becoming increasingly interdisciplinary due to its broad range applications.

Nanostructured materials

Nanostructured surfaces/material in general are highly functional and the ultimate goal of the nanostructuring process is to tailor the desired properties by designing and building at the nanoscale. One important effect of the nanostructuring process is to change the overall material behaviour that can itself be used to manipulate the material behaviour at nanoscale. Varieties of nanostructuring techniques have developed and are still developing to cater to the need of the technology. Among these, lithographic approaches (which are primarily top-down approaches) have been adopted by the industry. However, there are some drawbacks in using those approaches. That is the reason non-lithographic approaches have to be developed. Non-lithographic techniques in general depend mainly on material growth under some constraints which help them to be grown in a pre-determined fashion. These constitute predominantly bottom-up approaches. Non-lithographic techniques are not well developed yet and a number of studies are still required to establish unambiguous ways to fabricate nanodevices at the level to be employed in nanomanufacturing.

1.2 Device applications of nanostructures

Features like nanowires, nanodots, nanopillars, nanopins, nanopores are extremely useful for nanodevice applications used in optical, optoelectronic, magnetic data storage, field emission devices, and flat panel displays and various other industries. Few selected applications are mentioned in the following sub-sections.

Nanowires can be utilized to fabricate electronic devices like FET. For example, Jin et. al. [1] have fabricated array of nanodevices based on nanowires as shown in Figure-1.1.

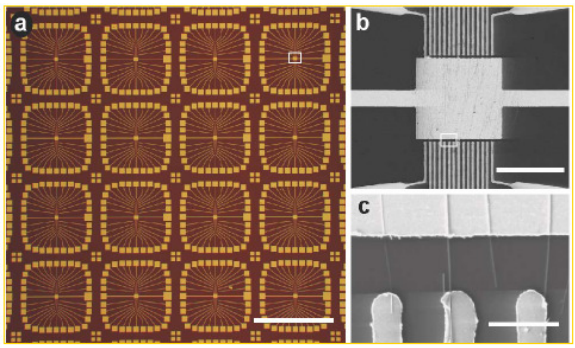

Figure-1.1 Device made up of nanowire arrays (a) Optical micrograph of integrated metal electrode arrays deposited on top of patterned parallel NW arrays defined by photolithography. (Scale bar 1 mm.) (b) Scanning electron micrograph of central active region of a repeat unit of the electrode. (Scale bar 40 μm.) (c) Scanning electron micrograph of three NW devices connected between common and finger electrodes. (Scale bar 3 μm.) (Ref. Jin et. al.)

The schematic of silicon nanowire-based solar cells p-n junction on metal foil is described in Figure-1.2. A promising current density of 1.6 mA/cm^2 for 1.8 cm^2 cells was obtained, and broad external quantum efficiency was measured [2] with a maximum value of 12 % at 690 nm. The optical reflectance of the silicon nanowire solar cells is reduced by one to two orders of magnitude compared to planar cells. A typical design of InP nanowire based solar cell [3] is as shown in Figure-1.3.

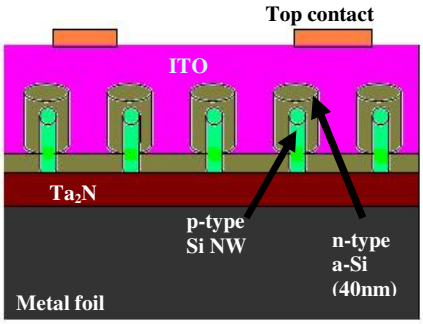

Figure-1.2 Schematic of silicon nanowire solar cells. (Ref. Tsakalakos et. al.)

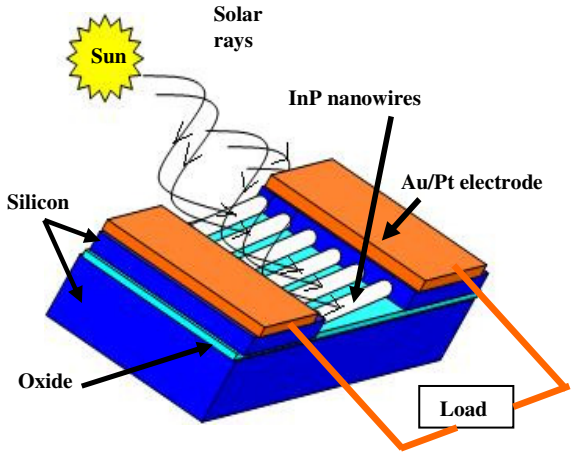

Figure-1.3 InP nanowire based solar cell. This type of solar cell will have high quantum efficiency resulting in high photon to electrical conversion efficiency (presumably higher than 50%). (Ref. Sarkar's webpage)

In lithium ion battery science, recent research has focused on nanoscale electrode materials to improve electrochemical performance. The high surface to volume ratio and excellent surface activities of 1D nanostructured materials have stimulated great interest in their development for the next generation of power sources.[4]

Si nanowires have been used for memory devices [5] with oxide/nitride/oxide stacked layers as the gate dielectrics and charge storage media as shown in Figure-1.4. A large memory window with high on/off-state current ratio due to the small radius and intrinsic doping of the Si nanowire is obtained. In addition, the simple reversible write/read/erase operations have been implemented with these memory devices. The

dynamics of the nanowire / nitride charge exchange and its effect on the threshold voltage and memory retention have been investigated.

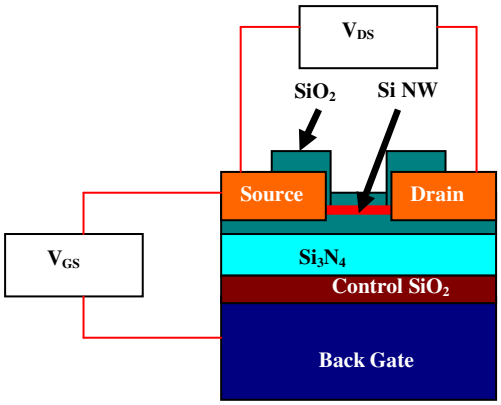

Figure-1.4 Schematic of nanowire memory device. (Ref. Li et. al.)

Synthesis of hierarchically branched semiconducting SnO_2 nanowire has been reported [6] on metallic Sb-doped SnO_2 nanowires by the sequential seeding of multiple nanowire generations with Au nanoparticles as catalysts. Such semiconducting nanowire/metallic backbone complex structures increase the potential functionality of SnO_2 nanowires. Branched SnO_2 nanowire films are used as sensing materials for high-performance ethanol sensor fabrication as shown in Figure 1.5. The nanowire sensors show sub-ppm sensitivity and fast response and recovery times at 300 °C. A linear relationship between sensitivity and the ethanol vapour concentration was observed.

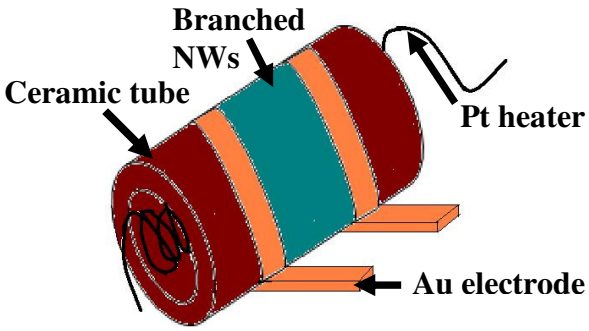

Figure-1.5 Schematic of its application for ethanol sensor. (Ref. Wan et. al.)

Recent work [7] has shown that ZnO nanostructures have good field-emission performance. A comparison of the emission characteristics of ZnO nanopins such as *I-V* curve, thermal stability, and aging process with those of carbon nanotubes showed that the emission characteristic of ZnO nanopins is close to that of carbon nanotubes. However, the emission performance of ZnO nanopins is much better than that of carbon nanotubes after baking at high temperature. Therefore, ZnO nanopins can be considered as field emitters in a field-emission-display device.

Although the electrical integration of chemically synthesized nanowires has been achieved with lithography, optical integration, which promises high speeds and greater device versatility, remains unexplored. Individual crystalline oxide nanoribbons can act as subwavelength optical waveguides [8] and nanoscale photonic elements. The length, flexibility, and strength of these structures enable their manipulation on surfaces, including the optical linking of nanoribbon waveguides and other nanowire elements to form networks and device components.

A technique to grow a single tungsten nanowire at a predetermined location has been reported [9] by using field emission in a low-pressure tungsten carbonyl atmosphere. A sharp tip is first made to contact the intended location of growth. Electrical current is then passed through the contact. When the contact is broken, the resulting localized plasma discharge at the point of breakage causes the initiation of formation of a nanowire. Continued growth at low currents results in a single nanowire a few nanometres in diameter and up to tens of micrometres in length. The nanowire is over coated by a thin carbon layer which protects the metal core from oxidation and corrosion. Electrical measurements of nanowires grown between two pads show resistivity one to two orders of magnitude higher than that of bulk tungsten. The technique can be applied to the interconnection of nanostructures to electrodes on a die.

Nanowire LEDs that emit ultraviolet light (a key wavelength range required for many light-based nanotechnologies including data storage) is well-suited for scaling to commercial production have been fabricated [10]. Nanowires made of semiconductor materials [11] are being used to make prototype lasers and light-emitting diodes with emission apertures roughly 100 nm in diameter. Nano-sources of light may have

many applications, including "lab on a chip" devices for identifying chemicals and biological agents, scanning-probe microscope tips for imaging objects smaller than is currently possible, or ultra-precise tools for laser surgery and electronics manufacturing. Uses of various material nanowires as variety of sensors are summarised in the following table 1.1.

Nanowire materials	**Applications**	**Advantages**	**Ref.**
Pd	H_2 gas sensor	Quick response time operating at room temperature	[12]
Semiconducting oxides: ZnO, SnO_2, and In_2O_3	CH_4, NH_3, CO, NO_x, O_2 gas sensors	High sensitivity Works at room temperature (low power)	[13]
Single crystalline silicon	Biological and chemical sensors for life sciences, health care, pharmacy	Electrical detection Online (real time) detection Fast response time Ultrasensitivity High selectivity	[14,15]
Ag	Plasmon polariton transport	Ease of fabrication	[16]
Au	Detection of Hg in H_2O, Biosensors	Online detection, fast response time, high sensitivity	[17]
Bi	Magnetic field sensor, Bio magnetic sensors	GMR	[18]
TiO_2	Humidity sensors	Sensitive and broad range of measurement, from 2 to 92%.	[19]

Table-1.1 Sensor applications of nanowires

Applications of nanowires for chemical sensors [20] and biosensors [21] have been reviewed recently.

A field emission triode device has been fabricated [22] using self-organized nanodot arrays as the electron emission source. Uniform nanodot arrays of titanium oxide were prepared from an Al / Ti film stack on silicon substrates by electrochemical anodization. The field emission triodes with titanium oxide nanodot emitters exhibited a low gate turn-on voltage of 45 V and high emission current density of 25 mA/cm^2 at 120 V. The excellent electric properties and easily controllable fabrication process of the nanodot triodes show potential applications [23] for field emission displays and vacuum microelectronics.

Fabrication of self-assembled Au nanodots has been reported by high temperature annealing of Au thin films on SiO_2, $Pb(Zr,Ti)O_3$ (PZT) thin films and $PbTiO_3$ nanodots and on their application to ferroelectric nanocapacitors [24] as top electrodes. When Au films 5-20 nm thick were annealed at 500-900 °C, aggregation of Au thin films occurred, and isolated Au nanodots were formed. By annealing Au films 10 nm-thick at 500 °C for 10 min in air, Au nanodots with average lateral sizes of 82 and 122 nm were obtained on SiO_2 and PZT, respectively. Au nanodots were also fabricated on $PbTiO_3$ nanodots, demonstrating the possibility of fabricating ferroelectric nanocapacitors with self-assembled top electrodes and ferroelectrics.

In concept, nanopores can be used for DNA analysis. For this purpose, an electrochemical system is used, where an applied voltage drives a flow of ions through a nanopore. The DNA molecule to be analysed is then driven through the pore, also by the applied voltage, blocking the flow of ions as it does so. This ion flow can be measured as a current flowing in the electrical circuit, and because the pore is chosen to have a diameter sufficiently small that DNA is forced to pass through as a linear strand, the molecule's properties—length, and ultimately sequence—can be determined based on the duration of current blockage, and variations in its magnitude.

Novel optical elements with already demonstrated capabilities are: Photonic Crystals [25], optical short pass filters [26, 27], Bragg and Rugate mirrors obtained by modulating porosity with depth [28]. Emerging applications only partially demonstrated include: Non-linear elements (e.g. strong frequency doubling in porous GaP [29] and Si [30]) including phase matching, integrated waveguides [31], and novel anisotropic (e.g. birefringent) materials [32]. Porous layers are generally useful

for MEMS applications, most simply as sacrificial layers, but also as a kind of dielectric layer or as thermal insulation. A large scale effort intends to use porous Si as electrodes for micro fuel cells [33]. The extremely low thermal conductivity has been employed for ultrasonic generation [34]. In one of the so far very few large scale application, Canon uses porous layers as a kind of "zipper" during the fabrication of silicon on insulator (SOI) wafers [35]. Porous layers are as buffer layers for demanding epitaxial processes, e.g. GaN on SiC [36]. Porous layers serve as templates for nanorods or nanotubes of many different kinds [37].

One of the recent interests [38] of the scientific community is to experimentally investigate vortex states of superconductors. Magnetic dots fabricated on superconducting layer can be one of the ways (as is depicted in Figure-1.6) to control vortex states due to it becoming most possible pinning sites. Further such a structure can be of great importance for understanding novel phenomena like field-induced superconductivity and domain wall superconductivity.

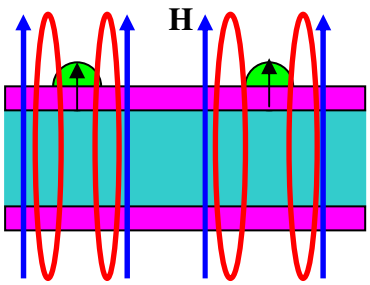

Figure-1.6 Magnetic dots mediated superconducting vortex state pinning.

1.3 Size-Dependent Properties of materials

Apart from direct applications for device applications in modern industries, nanostructuring has developed as an individual discipline because it changes the material behaviour and nanomaterial is no more behaving as its bulk counterpart. Nanomaterial is a new novel material of the present time where much scope is there to explore. Surface atoms possess more energy than bulk atoms. Consequently, surface atoms are more chemically reactive. Nanoparticles possess enhanced chemical reactivity. Examples: NASA is exploring aluminum nanoparticles for rocket

propulsion due to their explosiveness. Macroscopic gold is chemically inert. Gold nanoparticles are used to catalyze chemical reactions.

As nanocrystal size decreases; surface energy increases and melting point decreases e.g., 3 nm CdSe nanocrystal melts at 700 K compared to bulk CdSe at 1678 K.

Colour of thin film materials is also size dependent. For example, gold in bulk form is golden yellow colour; while the colour for diminished thicknesses are as follows, 30-500nm- metallic, turbid, crimson to blue, 3-30nm- red metallic transparent, < 1nm-gold clusters-orange, non metallic and 1 angstrom-atom-colourless.

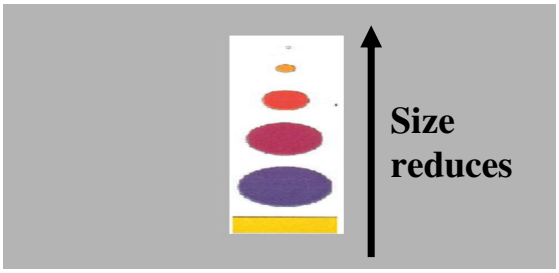

Figure-1.7 Change of colour of nanoparticle with reduction in size.

At the nanometer scale, electrical insulators begin to fail to block current flow. A quantum mechanical effect known as tunnelling occurs at nanoscale. Tunneling current increases exponentially as the thickness of the insulator is decreased. Tunneling is the basis of the scanning tunneling microscope and covalent chemical bonding. Many nanoelectronic and molecular electronic devices use tunneling to their advantage (e.g., single electron devices, resonant tunneling diodes, etc.).

Disk capacity is doubling every 9 months. As the volume of a magnetic bit is decreased, its stability decreases [39]. (superparamagnetic effect). Nanometer thick films of magnetic and electrically conductive materials experience large variations in electrical resistance in the presence of a magnetic field. The phenomenon of Giant magnetoresistance is used to read bits in hard disks. Quantum spin tunnelling between nanometer thin layers is expected to revolutionalize the data storage industry and the quest for non volatile memories with extremely high memory packing density will be

fulfilled. Very recently application of nanostructured materials in data storage has been in news [40, 41].

The metastability of nanocrystalline materials is a major challenge which can be addressed by controlling the chemistry of interfaces [42]. The hardness increases with decreasing grain size in accordance with Hall-Petch model. However, below a critical grain size a decrease in hardness or softening is observed with a further decrease in grain size. These observations are modeled in view of intragrain deformation (Hall-Petch regime) and intergrain deformation (grain boundary shear/sliding) in the softening regime. To understand such effects, underlying surface and interface chemistry has to be understood which can be done via self-assembled nanostructure growth techniques.

1.4 Nanostructuring techniques

Nanostructured surfaces can broadly be classified into two major categories according to their applications. The first category of nanostructures are those which can be patterned using extensive post processing lithographic steps and are applicable mainly for nanoelectronic devices. The second category of nanostructures can be realized via in-situ or ex-situ methods. To realize such nanostructuring via in-situ method, grain growth is controlled by providing favourable and optimized preparation conditions. Examples of in-situ nanostructuring are assembled thin film growth at early stages, template assisted growth and VLS growth etc. For the case of ex-situ nanostructuring however, external high energy density triggers have to be utilized. Examples of ex-situ nanostructuring techniques are use of laser, electric field, magnetic field, ion beam or electron beam induced nanostructuring.

1.5 Lithographic techniques for nanostructuring

1. Photolithography [43] (a) Deep UV lithography [44, 45] (b) X-ray lithography [46]
2. Interference Lithography [47-49]
3. Nanoimprint lithography [50-53]
4. Nanosphere lithography [54]
5. Electron beam lithography [55]

6. Scanning Probe Lithography

(a) Voltage pulse[56] (b) STM CVD[57](c) Local Electrodeposition [58](d) Dip-Pen Nanolithography [59-64](e) Field induced oxidation (f) Feedback controlled Lithography (g) STM manipulation[65]

1.6 Limitations and challenges for lithographic approaches

As the feature size reduces, so does the intensity of the nanoline as illustrated in Figure- 1.8. This limits the minimum feature size. For electron beam and ion beam lower energy has to be used for lower feature sizes but the precision of dimensions of devices becomes worse. At higher energy, however, due to larger damage, resolution of lines gets disturbed.

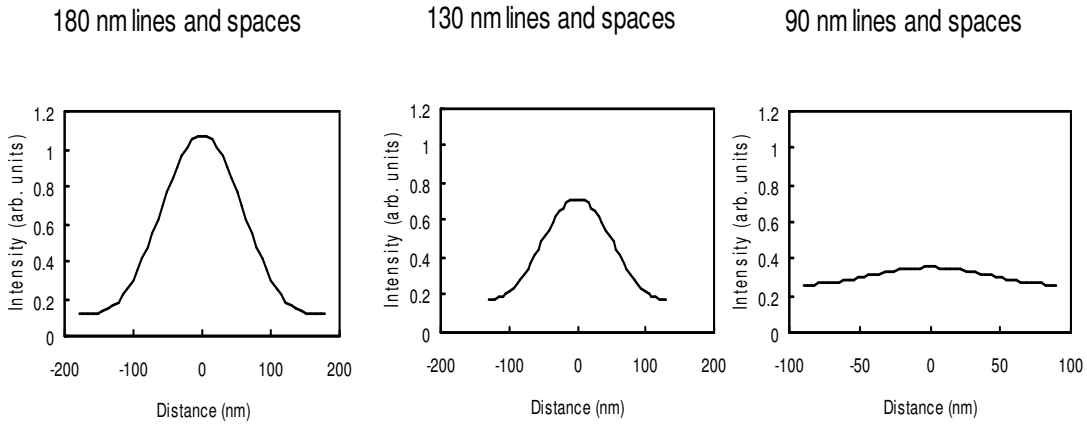

Figure-1.8 Intensity of nanolines fabricated via optical lithography for a width of (a) 180nm, (b) 130nm and (c) 90nm.

The time taken to perform the fabrication of nanodevices is extremely long. It takes 14-16 hours to execute few arrays of patterns to be realized. Fabrication of nanodevice structures with high level of accuracy involves a large number of post-processing steps; therefore fabrication cost is extremely high, which ultimately makes such devices infeasible. Huge financial investments, time, skilled personnel and lot of efforts are required to achieve nanostructures via lithographic approaches.

1.7 Need of development of non-lithographic techniques

Nanostructured materials which exhibit superior properties to their microcrystalline counterparts are prospective materials for large number of applications. As a consequence, there is a great interest in the development of fabrication methods that do not require post processing. In this context, the possibility of forming nanostructures and nanostructured material via non-lithographic routes have a significant role in paving the way for their widespread applications, especially those which affect humanity e.g. in power generation, environmental protection etc. Parallel to the development of nano-lithographic techniques, non lithographic techniques which solve the challenges posed by lithographic approaches have to be developed.

1.8 Introduction to Non-lithographic techniques

There has been recent interest in an intermediate approach that falls between the top down and bottom-up approach. Such techniques rely on providing favourable thermodynamic conditions during or after growth to realize nanostructures. Such techniques fall under the category of **non-lithographic techniques** for nanostructuring and are cost effective solutions to achieve nanoparticle arrays, nanowires, nanopillars and other "nano-forms" that will result in functionality and can be integrated in to existing processing technologies without adding many steps. In many cases these techniques can produce very local effects in the nanometer range, thus obviating the need for very tedious process steps as in the case of lithography based technologies. Among non lithographic approaches there are several other techniques of fabrication e. g. ion beam irradiation [66], electron beam irradiation, microwave assisted nanostructuring [67], anodic oxidation assisted nanostructuring [68] and strain relief driven nanostructuring [69-70], sol-gel method [71-84], arc discharge [85-88] and chemical processing [89-90]. In this thesis however, among non-lithographic techniques, we will concentrate primarily on first four major techniques out of following five techniques namely,

(a). Controlled early stage of thin film growth technique

(b). Template assisted technique for fabrication of nanowires,

(c). Laser assisted nanostructuring techniques

(d). Electric field induced nanostructuring technique and

(e). Vapour-Liquid-Solid technique

as far as experimental investigations are concerned.

(a) <u>Controlled early stage of thin film growth technique</u>

Self assembly is the simplest method to attain nanostructured surfaces. Varying the preparation parameters, or in other words providing the favourable growth conditions, one can control the wettability of the condensate material and the contact angles which are responsible for shape and size of the condensed material nanoparticles and thereby physical properties of nanomaterials can be altered for various possible applications. Usually thin film thickness, substrate temperature, substrate material, and rate of deposition are the parameters which affect the grain size heavily.

<u>Thin film growth modes:</u>

When a vapour molecule condenses onto a substrate, it forms a solid in the absence of any external forces, there are primarily three interaction terms which decide the free energy of this system of vapour + solid + substrate as is illustrated in Figure-1.9. Therefore change in free energy in adding atoms of vapour to the system will be given by:

$$\Delta G = k [\gamma_{AS} + \gamma_{VS} - \gamma_{AV.}]$$

where γ terms subscripted by AS, VS and AV correspond to interaction terms for substrate-solid, vapour-solid and substrate-vapour respectively. For vapour to condense, free energy minimization has to take place.

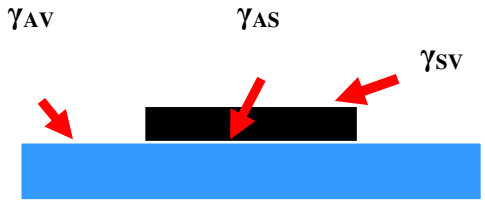

Figure- 1.9 Interaction terms responsible for thin film growth

There are three thin film growth modes (as shown in Figure- 1.10) depending upon the relative magnitude of these three interaction terms. If γ_{AV} exceeds the addition of other two interaction terms then the growing layer reduces surface energy and "wets" the surface completely. Usually, this leads to a smooth, layer-by-layer growth. Such a growth mode is termed as **"Frank- Van der Merwe Growth (FV)"**. However, if γ_{AV} is supressed by the other two terms together then the growing layer; in that case, growing layer will minimize interface energy and its own surface energy. As a result, the additive layer "balls up" on the surface. Such a growth mode is termed as "**Vollmer-Weber Growth (VW)**". In some cases; the balance of forces changes during growth. Typically the first layer wets surface but subsequent layers do not. This change in balance of forces is often due to strain in the growing layer, typically due to a mismatch in lattice constants between substrate and solid to be formed. Such a thin film growth mode is known as **"Stranski-Krastanov Growth (SK)".** As size of the cluster increases, number of atoms in the cluster per unit volume decreases and therefore, one can selectively stop the thin film growth process at a particular moment to realize the particular size and shape.

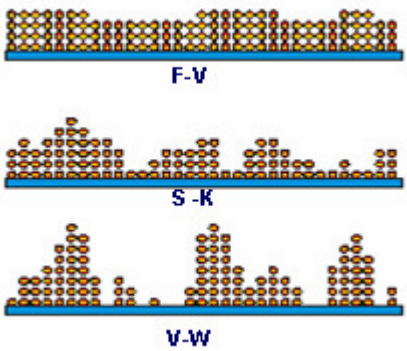

Figure- 1.10 Three modes of thin film growth.

As the size of cluster increases, number of atoms in cluster per unit volume reduces (as shown in Figure- 1.11).

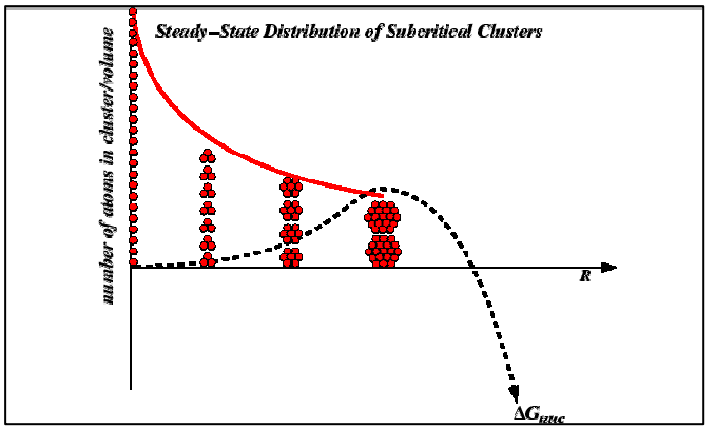

Figure-1.11 Variation of number of cluster / Vol. with the size of cluster.

Effect of substrate temperature:

Apart from the thin film thickness (Figure- 1.12 (a)) and substrate temperature (Figure 1.12 (b)) Rate of deposition is another dominant parameter affecting the grain size (Figure-1.12 (c)); that determines the microstructural growth of ultrathin films [91].

The thermal accommodation coefficient is given by

$$\alpha_T = (E_v - E_r) / (E_v - E) = (T_v - T_r) / (T_v - T) .$$

where E_V, E_r, and E are energy of the incident vapor, the material before reaching equilibrium, and the material after reaching equilibrium. T's are corresponding temperature values.

Higher substrate temperature ensures higher mobility of adatoms on the substrate surface. With heating of the substrate, densification occurs, and the grain wall boundary width is thinned. At ambient temperature deposition conditions, because

sufficient energy is not available for mobility of adatoms on the substrate surface, the size is not enhanced much due to coalescence.

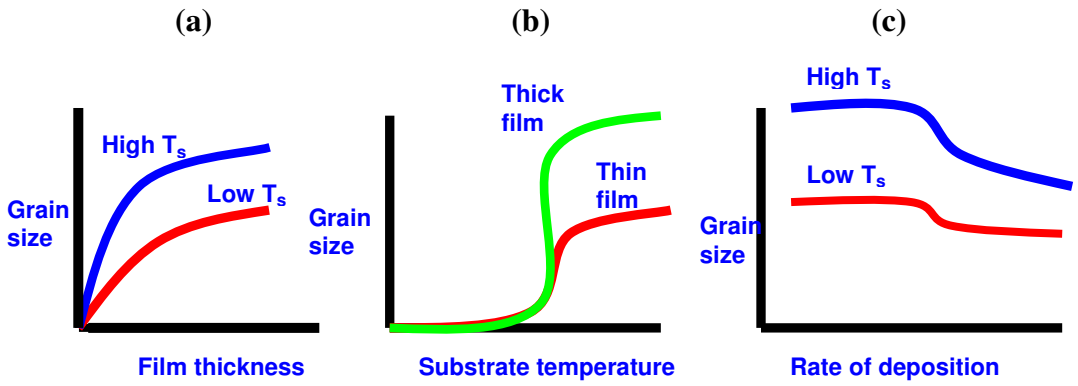

Figure- 1.12 **T**rends of grain size with (a) film thickness, (b) substrate temperature and (c) rate of deposition. [Ref. Thun et. al.]

Zhongliang et. al.[92] showed that Pd nanowires can be self assembled via electroless deposition. In the absence of templates, the growth of nanowires through self assembly route suffers mainly from three problems, one is the periodicity of nanostructures, second is the isolation of nanocomponents, and third is the ability to make electrical connections. The use of templates has been reported extensively in the past decade to fabricate site specific nanostructures. In brief, the role of the template is to guide the growth of nanofeatures. Porous templates and linear templates are usually used for fabricating vertical and planar assembly of nanowires and nanodots, single layer as well as multilayers of the concerned material. Pd nanowires have been grown via self assembled technique [93]. Similarly cobalt nanocrystal superlattice has been achieved via self-assembled technique [94].

Sun et. al [95] achieved FePt nanopatterns using solution phase metal salt reduction. Pt-acetylacetonate reduces to Pt and $Fe(CO)_5$ decomposes to Fe. Baker et. al. [96] performed UV exposure followed by sonication of Diblock copolymer/Fe/FeF_2 followed by Ion milling gives and obtained nanoporous structures. Barth et. al. [97] were successful in achieving self-assembled growth of cobalt atoms on Pt [997] surface. The separations between the self-organized chains were observed to be 2nm.

In brief:

1. The substrate determines the free energy term which in turn determines the contact angle and shape of the particle formed, apart from the critical size of the particles.
2. The substrate temperature determines the flatness of the grains and the areal coverage density of the film.
3. The rate of deposition determines the extent of clustering, which for thermal evaporation is controlled by the evaporation source temperature value and for laser deposition is controlled by the laser energy density.
4. Film thickness is very crucial for early stages of growth and determining the particle size.

(b) Template assisted technique for fabrication of nanowires

Directional growth of nanowires is very essential for device level applications for using them as interconnects between electrodes or even from one layer to another in a layered fabrication process.

Template assisted growth [98-105] ensures the fine placement of condensate to eventually yield periodic structures. Porous alumina templates are favoured due to the ease of preparation, ease in release of fabricated nanocomponents and high pore density (10^{11} pores / cm^2), and the. Under certain conditions, very good periodicity of the pore arrangement can be achieved, which is required in many technological applications. Apart from these qualities, porous alumina can withstand very high temperature without change in its pore periodicity and spacing (up to 800^0 C) as desired for the processing of the fabricated nanostructures.

When exposed to air or water, aluminium oxide forms on the surface of aluminium, but the oxide thickness is in the nm range. However, anodization of aluminium can result in the formation of flat nanoporous aluminium oxide film, commonly called aluminium barrier type films. The electropolished aluminium is anodized in a strong acid (pH<4). The acid typically used is 15% sulphuric acid, 3% oxalic acid and 5% phosphoric acid.

The chemical reactions involved in the porous oxide growth are:

(At the anode) $\mathbf{2\ Al+3H_2O = Al_2O_3+6H^+ +6e^-.}$

(At the cathode) $\mathbf{6H^+ +6e^- = 3H_2.}$

(Dissolution of alumina) $\mathbf{Al_2O_3+6H^+ = 2\ Al^{3+} + 3H_2O.}$

Al Mawlawi et. al.[106] showed that the dependence of pore density **ρ,** **(** expressed in terms of pores / $\mathring{A}^2$) as a function of anodizing voltage is given by

$$\rho = \alpha / (d + \beta V)^2$$

where α is a constant (= 1.15), d is the pore diameter, β is a constant also dependent on the acid and temperature. Pore diameter is in the range 8-100nm. Increasing the soaking time of porous alumina in phosphoric acid, is found to increase pore diameter [107].

A detailed two step procedure was adopted by Choi et. al. [108] for achieving well aligned array of nanopores in alumina. In this, a pure aluminium sheet (99.999 % purity) was degreased in acetone and electropolished at a voltage of 20 V for 2 min. The electropolished aluminum sheet was anodized by immersing it in 0.3 M oxalic acid for 12 h under a constant voltage of 40 V. Then, it is etched in an aqueous mixture solution of phosphoric acid (6 wt %) and chromic acid (1.8 wt %) in order to remove the irregular porous oxide layer formed during the first anodization. The subsequent second anodization, with the same condition as the first anodization, but a different period of time, depending on the desired thickness of the oxide layer, yielded a highly ordered hexagonal nanopore array of anodic aluminium oxide (AAO) template. To separate an AAO membrane from the AAO template, a saturated $HgCl_2$ solution was applied. The separated AAO membrane was rinsed with de-ionized water several times. An additional pore widening process was conducted in 5-wt% phosphoric acid at 30 ^{0}C in order to obtain the desired pore diameter. The obtained AAO membrane was cleaned and annealed at 200 ^{0}C in vacuum for 1 h.

Crouse et. al.[109] devised a technique (as shown in Figure-1.13) to achieve gold nanopillars using anodized porous alumina as the template on titanium coated silicon substrate. It was then subjected to reactive ion etching to etch out titanium inside alumina pores that were refilled with gold by evaporation. A final reactive ion etching step gives free standing gold nanopillars.

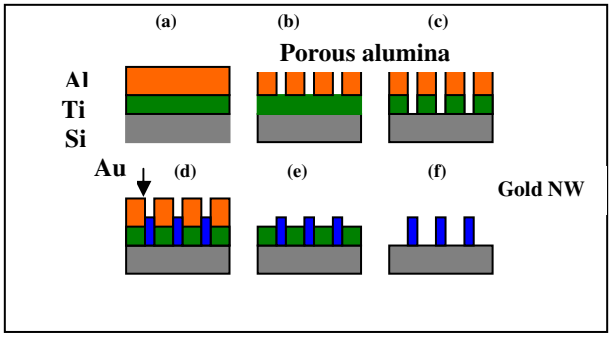

Figure-1.13 Technique to grow metallic nanopillars

Masuda et. al. [110-114] developed a replication technique (as shown in Figure-1.15) by which a nanohole array on alumina can be transferred on other metals. This way it is possible to overcome some of the disadvantages presented by porous alumina (namely chemical and thermal instability and low mechanical strength). The schematic is as shown in the Figure 1.14 below. In this method, porous alumina is first detached from the bottom Al by soaking in mercuric chloride solution followed by the removal of the barrier layer by soaking in 5 % phosphoric acid. A thin layer of gold is then evaporated at the bottom. Methyl methacrylate monomer containing 5 % benzoyl peroxide, which acts as an initiator for the polymeryzation, is injected into the holes under vacuum conditions and is polymerized by UV irradiation. After removal of alumina layer with 10 % NaOH, a replicated negative type of PMMA with cyllinderical structutre is obtained. At the bottom of array of PMMA, a thin layer of metal is present. For the preparation of Pt nanohole array, electroless deposition of metal was carried out. PMMA may be removed by soaking in acetone. A variety of nanostructures can be prepared using the above replication technique.

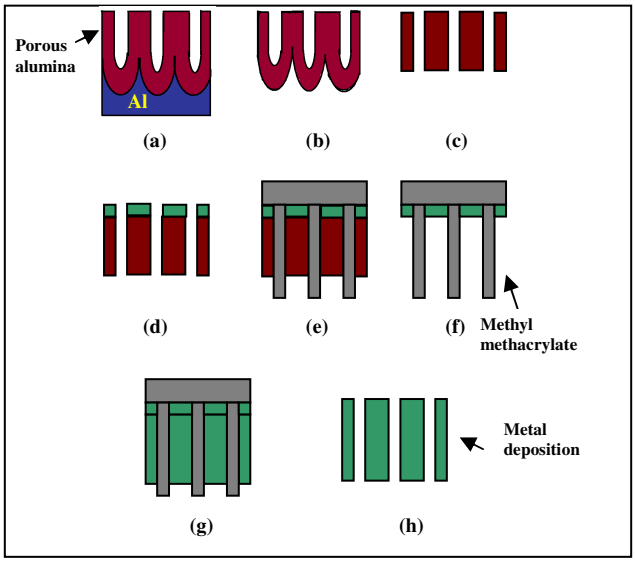

Figure-1.14 Technique to replicate nanoporous pattern from alumina to metal

Fan et. al. [115] used gold mask as achieved by replication technique (Figure- 1.15) from AAO template and used it to realize gold dots on GaN/Si substrate to obtain patterned ZnO nanowire array. The detailed scheme is as shown.

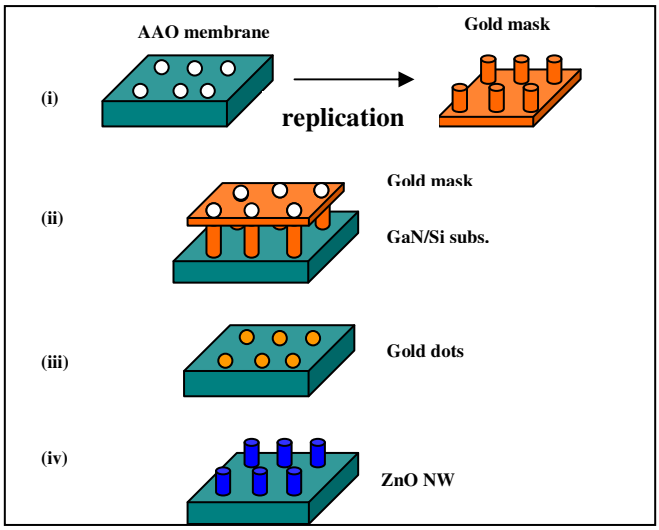

Figure-1.15 Gold mask technique to fabricate metallic nanopillars (schematic).

Using a similar method, Deki et. al. [116] fabricated nanopillars of oxide and ceramics using solution route.

Magnetic nanostructures are useful for technological applications, because information can be stored as magnetic bits. Magnetization reversal can be conveniently used as magnetic switch. Apart from the magnetoresistive random access memory (MRAM) application of multilayer Ferromagnet (FM) / Non magnet (NM) / Ferromagnet (FM) tunnel junction, Ferromagnet (FM) / Antiferromagnet (AFM) superlattices are applicable as Giant magnetoresistive (GMR) sensors. Vertical magnetic nanowires have applications in Current perpendicular to plane giant magnetoresistance (CPP GMR). Small isolated magnetic islands themselves are magnetic domains. For such a system of magnetic dots, the condition $\Delta E = kT$ can be extended up to the superparamagnetic limit. An ordered perpendicular/longitudinal medium should exhibit much lower noise, as compared to the disordered medium. Thus, the signal to noise ratio for possible magnetic media for data storage applications is increased. Materials like Fe, Co and Ni electrodeposited into nanopores serve as a model system for the study of magnetic properties, interactions, and thermal stability of nm sized magnetic dots. The magnetic wires thus formed are cylindrical in shape and are hcp, fcc and bcc for Co, Ni and Fe nanowires. Coercive field in perpendicular directions usually is 5-7 times higher than that for the parallel orientation. The nanowires possess uniaxial anisotropy with easy axis perpendicular to the film plane. The large anisotropy arises mainly due to the shape anisotropy. The large perpendicular squareness and high remanence together with high coercive field can make these materials useful for magnetic recording media.

Coercive field is usually independent of the length but is dependent on the diameter of nanowire (coercive field decreases with increase in diameter). Such increase in coercive field [117-119] can be attributed to the multidomain structures at higher diameter. Li et. al.[120] found for 11nm diameter Fe nanowires that activation volume is 1×10^{-18} cm^3 and it is smaller than the actual particle volume suggesting that magnetization reversal is non-uniform. Peng et. al. [121] used TEM and electron diffraction and suggested that actually each nanowire consists of chain of dots, each dot being single crystalline. Zeng. et. al. [122] and Metzger et. al. [123] worked on Co nanowire while Nielsch et. al. [124] worked on nickel nanowires.

Electrodeposited magnetic nanowires in alumina nanopores as prospective candidates for data storage, suffer due to non uniform length. However, according to Yin et. al.[125], by fine tuning electrodeposition parameters, one can obtain uniform magnetic nanowires. Pulse reverse electrochemical deposition with a waveform consisting of square cathodic pulse and longer anodic one can give good uniformity [126-127] in size of magnetic nanowires. Magnetic bimetallic alloy nanowires [128-130] containing a percentage of Fe/Co/Ni have been successfully synthesized in nanoporous alumina. CPP GMR for FM/NM multilayer films usually are higher than the CIP GMR, and therefore, fabrication of FM/NM is of scientific interest to the industry. Alumina membrane template assisted technique was extended to fabricate such multilayers [131] and study GMR.

Semiconducting nanowires, nanorods, nanodots, nanocones, nanopins etc. are interesting due to their broad range of application. Electrochemically, the most easily fabricated semiconductors are II-VI semiconductors e.g. CdS, CdSe. There are three approaches to elctrodeposition of semiconductors. The first method [132] is deposition of metal in alumina nanopores followed by etching of alumina surface by phosphoric/ chromic acid to access metallic surface for sulphur or arsenic vapour to attain metal sulphide or arsenide nanostructures. The second method deals with electrolysis of sulphuric acid, causing the sulphide atoms to be deposited in pores. This is followed by ac electrodeposition of Cd in pores, allowing S to react with Cd. In the third method [133], a solution of dimethylsulfoxide containing salt of M (50mM) (M = Cd, Pb, Zn etc.) and X (X = S, Se, Te etc.) is used. CdS, CdSe, PbSe, ZnSe nanowires have been synthsized by this method and this method is found useful for the application of such nanowires for diode, transistor, photodetectors, and light emitting diodes. An interesting effect namely electronic bistability [134] of CdS nanowires can be used for inexpensive ultradense non volatile static random access memory. For the preparation of $Cd_{1-x}Mn_xSe$ nanowire [135], an electrolyte consisting of cadmium perchlorate and manganese perchlorate and selenium powder dissolved in dimethyl sulphoxide can be used. M/SC/M heterostrucres e.g. Fe/ CdSe/Fe heterostructures can be synthesized. These fabrication techniques can have advantage [136-137] to study spin transistor, spin quantum computers. Lead [138], Bismuth [139], and gold [140-143] nanowires also have been electrodeposited in alumina nanopores.

Template-synthesized polymers [144-145] are expected to have applications in microelectronics, drug delivery, bioencapsulation, ultratrace chemical analysis, and second order templates for the growth of other nanoarrays. Carbon nanotube electronics are expected to provide a viable alternative to silicon. Recently IBM reported [146] the development of an array of transistors using carbon nanotubes and the development of a computer circuits using single walled carbon nanotube. Carbon nanotubes also find use as cold cathode flat panel display [147]. Carbon nanotubes can also be used to encapsulate [148] other materials like Fe, Co. Well ordered carbon nanotubes have been synthesized [149-150] in nanoporous alumina membrane template.

Nanowires can work like template in some cases as was shown by Goldberger et. al. [151] that ZnO nanowire can work like template for GaN nanowire growth. Self assembled nanospheres (3D polystyrene spheres) can be conveniently used as template to fabricate metallic nanobowl arrays [152].

Physical vapour deposition (PVD) of metals on inert substrates such as highly oriented pyrolytic graphite (HOPG) can be used [153-155] to generate a large number of interesting and potentially useful structures with dimensions in the nanometer range as demonstrated in schematic diagram shown in Figure-1.16. Control of the experimental parameters of substrate temperature and metal atom flux can be used to tailor the resulting nanostructure arrays. Penner's group [158-163] have grown sub-monolayer quantities of gold via PVD on an HOPG substrate to achieve dendritic islands of gold (at RT deposition condition) and large arrays of gold "beaded wires" (at 400 °C substrate temperature).

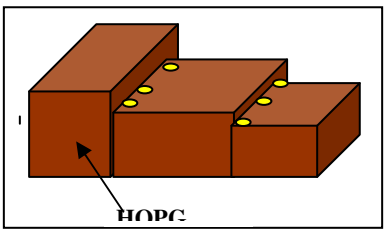

Figure-1.16 Schematic of bead assembly on HOPG staircases.

Alumina is an interesting material and by heating at very high temperature e.g. 1600^0C-1800^0C for few hours, ripple kind of structures develops as a result of heating. [10$\underline{11}$] and [10$\underline{12}$] planes are tilted usually at 32.4^0 and 17.6^0 with respect to the horizontal with a crest and trough pattern. Alumina being a good dielectric, at crests, the electric field value is very high due to singularity present.

Near the crests,

$$\mathbf{E = K\ \rho^{-\beta}},$$ where ρ is the distance from the tip and

$$\mathbf{\beta = (\pi - \alpha) / (2\pi - \alpha) = 0.22}$$ (Singularity in Electric Field).

Ravi Shankar et. al. [164] have used such faceted alumina slanted surface to conveniently control the growth of nanoparticle on such crests. They have done a number of experiments to achieve good control over the dewetting process with the variation of substrate temperature and pressure. They propose two basic models (as shown in Figure- 1.17), that the condensate can follow to assemble on the crests, one is assembly of nanoparticles and other is the formation of nanowires. For evaporation, 1800^0C temperature and 10^{-4} Torr was used.

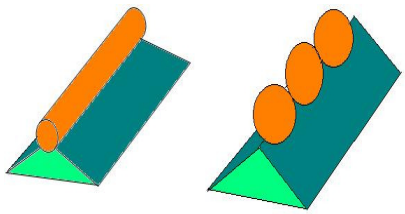

Figure-1.17 Two basic models of condensate assembly.

Carbon nanotube itself has been used [165] in longitudinal as well as vertical position to work as a template to grow metallic and semiconductor nanowires, nanotubes.

Partridge et. al. [166] designed V-Grooves on Si/SiO_2 by the selective etching process. Then into the v-groove, metal vapour was condensed using nanocluster deposition. Thereafter using argon ion etching the rest of the material was cleaned, leaving only

continuous nanowires (as shown in Figure- 1.18). Such a growth of nanowires does not require any extra effort to give interconnections for electrical measurements, since it is already organized in a line.

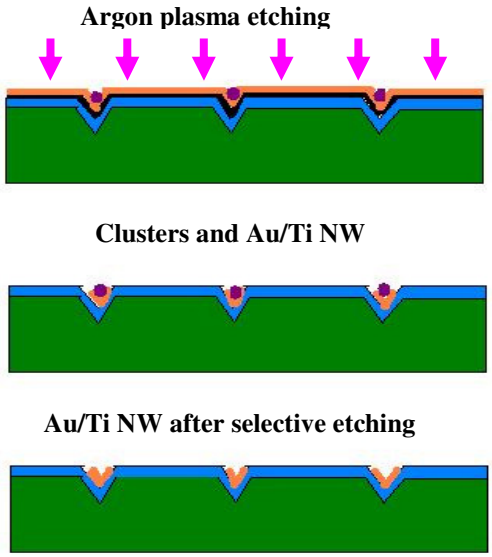

Figure-1.18 Sequence of formation of clustered metallic nanowire.

Obliquely incident deposition fluxes cause geometric capture anisotropy at a grain edge through the process of self-shadowing as illustrated in Figure 1.19. [167] The more oblique the incident flux angle and the more anisotropic the grain shape, the faster the rate of texturing. Nuclei distributed across the surface will lead to ballistic shadowing of the surrounding regions. This restricts further growth to the tops of the nuclei which develop into columnar structures. Columns will grow oriented toward the source, forming an angle with the substrate normal. [168]. Differences in surface free energies and in rates of mass transport along different crystallographic surfaces lead to anisotropic grain growth rates and to the development of anisotropic, faceted, grain shapes.

$$\tan\alpha = 2\tan\beta \,.$$

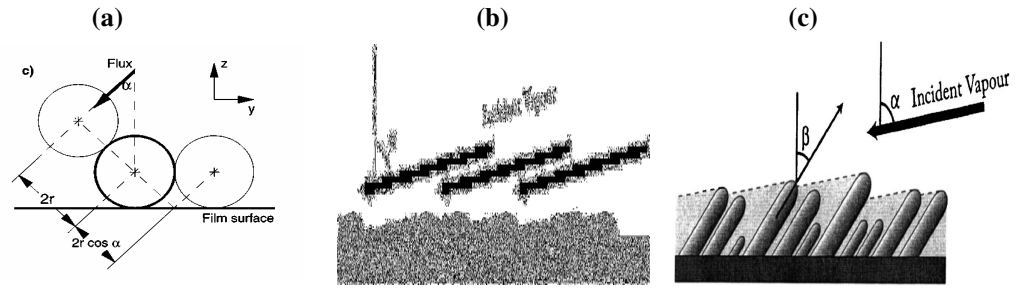

Figure-1.19 Shadowing phenomena (a) atomic self-shadowing, (b) shadowing at early stage of nanowire growth, (c) shadowing at mature growth of nanowire.

Surface diffusion can be considered to be a thermally activated Arrhenius-type process where the diffusion coefficient *D* is proportional to

$$D \ \alpha \ \exp(-E_a) / k_B T s$$

Surface diffusion counteracts to the shadowing effect. Therefore at lower temperature of growth, diffusion is minimal, and shadowing effect is prominent.

Deposition on wedge shaped textured surfaces

When the incident vapour faces a wedge shaped texture, the accessibility of vapour is reduced (as shown in Figure- 1.20) and effective angle of incidence is determined by the wedge angle.[168]

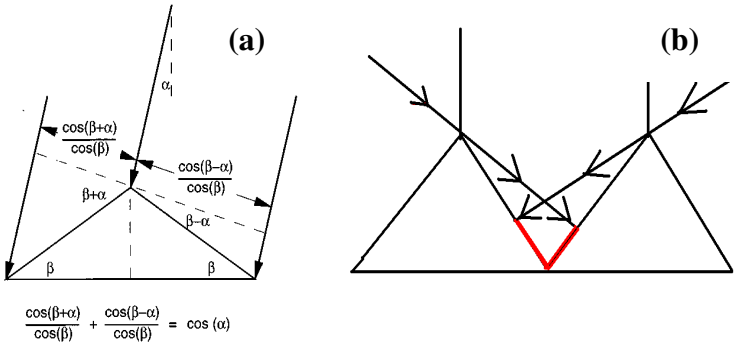

Figure- 1.20 Shadowing near a (a) single wedge, (b) pair of wedges placed close to each other making a v-trench.

The V-groove can be assumed to be two wedges in contact with each other in such a way that the supply of the vapour in the valley region is restricted and therefore coverage of material is minimal. The shadowing due to the external faces of the wedges results in a restricted condensation leading to the formation of nanowires or nanoparticle arrays within the trench.

Depending on the coverage, You et. al. [169] have recently been successful in achieving nanodot arrays or nanowire array of Pt / $ErSi_2$ heterostructures as shown in Figure-1.21.. Reactive ion etching was used to clean the surface except in regions where well patterned heterostructures were formed.

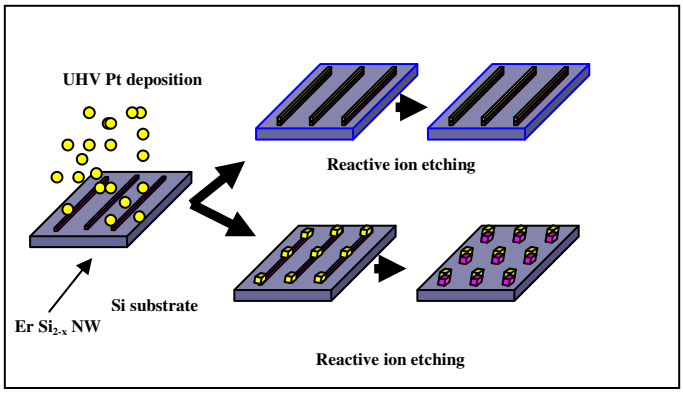

Figure-1.21 Schematic of patterning of Pt/$ErSi_2$ nanowire and nanodot array on silicon substrate.

(c) <u>Electric field induced nanostructuring technique</u>

A technique that has been considered recently for nanostructuring of thin films is the electric field induced approach as shown in Figure-1.22. The thermodynamics of grain growth in the presence of electric fields is quite well understood. It is known that due to a free energy minimization process the grain growth is both accelerated and enhanced. Similarly the nucleation rates for crystallization are expected to increase due to local Joule heating effects. It is also well known that the polarizibility of metal nanoparticles is different from their bulk counterparts. However, there are very few reports, as will be discussed in detail in results and discussion chapter.

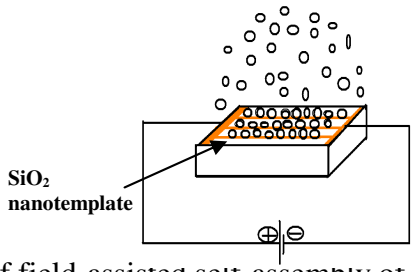

Figure-1.22 Schematic of field-assisted self-assembly of nanoparticles.

Metal-induced lateral crystallization of amorphous Si has been investigated [170] under a wide range of electric fields. Wang et. al. [171] investigated field aided lateral crystallization of silicon at 2.5 kV/cm. They found that branches add at 90 degrees. They concluded that three effects are responsible for regrowth process namely, electromigration, chemical potential and electric potential gradient. Jang et. al. demonstrated [172] that electric field enhances the rate of MIC. They showed that crystallization time at 500 ^{0}C decreases from 25 hours to 10 minutes on application of a modest electric field value 80Vcm^{-1}. Electric field alignment of vertical In_2O_3 nanowires has been reported at 2.3 kV/cm [173]. Under electric field, lateral growth of aligned mutilwalled carbon nanotubes was achieved at 20 kV/cm by Jang et. al. [174]. Zhang et. al. [175] have reported field alignment effects on single walled carbon nanotubes. According to them, large induced dipole moments lead to large aligning torques and forces on the nanotube, and prevent randomization of nanotube orientation by thermal fluctuations and gas flows.

Ichinokawa et. al. [176] investigated the influence of electromigration and thermomigration. They found that with electron beam traversal, movement of metallic nanoislands can be controlled by the reversal of field direction. Saka et. al. [177] applied electric field on material inside the trench in the presence of a thermal input, yielding metallic nanowires. They have explained the formation based on electromigration phenomena.

(d) **Laser induced nanostructuring technique**

The unique combination of high pulse energy, high average power and deep ultraviolet (UV) wavelength make excimer laser capable of ablating a wide range of materials leading to several effects.

•Surface drilling.
•“non-thermal” energy delivery by a short wavelength radiation of the surface leading to modification
•high-temperature ablative plasma leading to catastrophic damage
•bulk heating and melting of these materials, accompanied by the following subsurface boiling in the melt pool and resulting melt expulsion off the target.
•Nanopore and nanoparticle formation on the target surface due to ejection of neutral atoms or ion out of the target and backscattering of those ejected entities respectively.
•Material ejection from an illuminated surface.
•The deposition of a thin film on the surface of the specimen used as a target.

Apart from optical properties change, laser induced surface features can also be used for further growth of nanostructures [178]. It has recently been shown that silicon becomes luminescent [179] in the visible range when they undergo size reduction to the nanometer dimensions. Creation of a thin layer on silicon surfaces using the intense conditions at the focus of a high-intensity, excimer laser pulse can make silicon highly absorbing (bulk silicon has low absorption due to its indirect band gap) and an excellent choice for photovoltaic applications [180]. Further, desired band gap of silicon can be accomplished in nanostructured form due to which it will find applications in antireflection coatings for micro lens application [181]. Anisotropic growth features will give rise to gradient in refractive index and therefore can be used for polarization sensitive Si based optical devices [182]. Nanostructured porous silicon can be used as sensitive sensor to chemical species Si nanowires [183-190] as special forms of crystalline Si are expected to exhibit unusual quantum confinement effects as well as potentially useful applications. Recently research is on for its high performance Lithium battery anode application [191] and memory applications [192] apart from its unusual electrical, optical, mechanical, and chemical properties, because of their small dimensions, unique shapes, and high surface-to-volume ratio. Apart from silicon, noble metal, Al_2O_3, GaAs, graphite etc. surface have been nanostructured for various applications. Thin film surfaces have been laser irradiated mainly for laser crystallization and partly for various assembled structures.

Kabashin et. al. [193] used excimer laser for 200 pulses to nanostructure Si and reported on the consequent PL spectra. They observed significant changes in the PL

spectra due to laser irradiation. Pedraza et. al. [194] used various media and laser energy density (0.6-0.8 J/cm^2) for 400-500 pulses in vacuum and helium to nanostructure silicon surface. Henly et. al. [195] nanostructured silicon thin film surface using KrF excimer laser in vacuum upto at 10J/ cm^2 fluence at 50 shots and at 10Hz rep rate. They have shown that such nanostructured surfaces can be used for catalytic growth of vertical carbon nanotubes. They have nanostructured nickel and silver films too. Loreti et. al. [196] used excimer laser to anneal amorphous silicon seed layers deposited on a metallic Ti/Pd/Ag multilayer.

Cone formation by laser irradiation of silicon surface has been an interest in recent years. Resolidification starts at the edge of the molten zone and proceeds towards its centre. In contrast to the usual behaviour of materials with melting, the density of liquid Si, ρ_l (l-Si)= 2.52 g / cm^3, is larger than the density of solid Si, ρ_s (c-Si) = 2.32 g /cm^3. Thus, the volume of silicon increases during solidification. As a consequence, during cooling the liquid silicon is squeezed radially to the centre and forms a protrusion. As a result, a solid cone surrounded by a ring-shaped trench is formed.

(e) <u>Vapour-Liquid-Solid technique</u>

In the Vapour-Liquid-Solid process, as described in figures, 1.23(a) and 1.23(b), a liquid alloy droplet composed of metal catalyst component(such as Au, Fe etc.) and nanowire component (such as Si, III-V component, II-VI compound, oxide etc.) is first formed under the reaction conditions. The metal catalyst can be rationally chosen from the phase diagram by identifying metals in which the nanowire component element is soluble in the liquid phase but do not form solid compound more stable than the desired nanowire phase. As described in table-1.2, there exists a eutectic temperature for the combination of the nanowire component and the catalyst component. The essence is that ideal metal catalyst should be physically active but chemically stable. The best catalysts for various nanowires are Au (for ZnO NW), Fe (for SiO_2 NW), Co (for SiO_2 NW), Ni (for Ga_2O_3 NW).

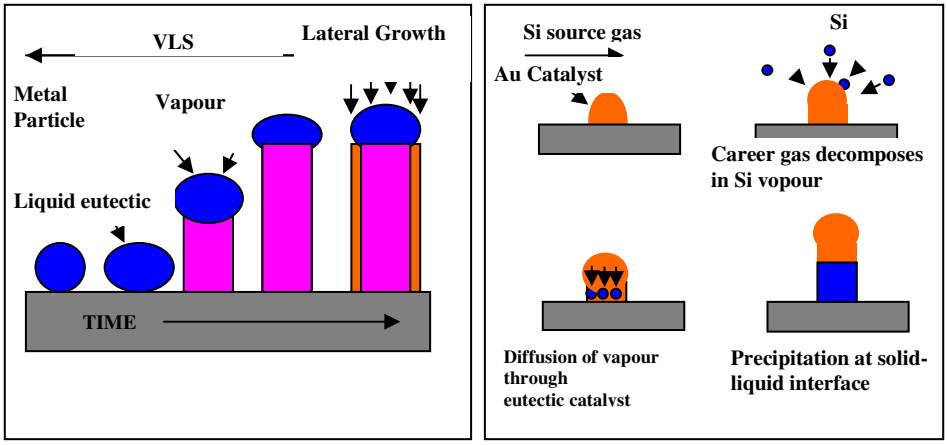

Figure-1.23 (a) VLS growth mechanism, (b) Detailed VLS phenomena

The liquid droplet serves as a preferential site for adsorption of gas phase reactant and when supersaturated, the nucleation site for crystallization. Nanowire growth begins after the liquid becomes supersaturated in the reactant materials and continues as long as the catalyst alloy remains in a liquid state and the reactant is available. During the growth, the catalyst droplet directs the nanowires's growth direction and defines the diameter of the nanowire. Ultimately the growth terminates when the temperature is below the eutectic temperature of the catalyst alloy or the reactant is no more available. Therefore nanowires as obtained from VLS process have diameters as that of the catalyst nanoparticle at the other end and if the catalyst nanoparticle is still present, then it is inferred that nanowire growth was governed by VLS mechanism. The eutectic temperatures for the alloy formation of the nanowire component and the catalyst component are tabulated in Table 1.2.

Alloys	Eutectic temperature
Au-Si	360 ºC
Au-GaAs	630 ºC
Au-Ge	360 ºC
Ag-Si	837 ºC
Fe-Si	>1200 ºC
Al-Si	577 ºC
Al-Ge	419 ºC

Table 1.2 Table for eutectic temperatures for the alloy formation of the nanowire component and the catalyst component. (Ref. Givargizov et.al.[197])

Except for SiO_2, all other nanowires are well crystalline, mostly oriented along [111] direction. The VLS crystal growth mechanism was first proposed by Wagner et. al. [198] for silicon whisker growth. Essentially they reduced $SiCl_4$ using hydrogen in the presence of Au, Pt, Ag, Pd, Cu, Ni etc. as catalyst. Westwater et. al. [199] used pyrolysis of SiH_4 with Au as a catalyst to obtain silicon nanowires. To date, ZnO [200], SiO_2 [201], Ga_2O_3 [202], In_2O_3 [203] nanowires have been grown successfully using VLS technique. Sharma et. al. [204] successfully have grown germanium nanowire on silicon [111] substrates using the VLS technique. Because nanowires of binary and more complex stoichiometries can be created using the VLS mechanism, it is possible for one of these elements to serve as the VLS catalyst. The major advantage of a self-catalytic process is that it avoids undesired contamination from foreign metal atoms typically used as VLS catalysts. Self catalytic behavior has been reported when the direct reaction of Ga with NH3 or direct evaporation of GaN was used to produce GaN nanowires [205-206]. The precise control of nanowire lengths and diameters using a self-catalytic VLS technique, as well as the universality of this approach, has yet to be demonstrated. Lee et. al. [207] successfully showed that gold can be used as a catalyst for ZnO nanowire growth by VLS route. E. I. Givargizov

[197] studied in detail the VLS crystal growth technique in 1975. His study shows the equilibrium state is given by the equation in the case of silicon nanowire growth:

$$\Delta\mu_{NW} = \Delta\mu_{bulk} - 4\,(\alpha\Omega)\,/d.$$

$$\Delta\mu_{bulk} = \mu_{bulk} - \mu_{vap}.$$

$$\Delta\mu_{NW} = \mu_{NW} - \mu_{vap}.$$

where, nanowire, bulk, and vapour are the effective chemical potentials of silicon in the nanowire, in the bulk material and in the vapour phase respectively, d is the diameter of the nanowire, **Ω** is the atomic volume of silicon, and the specific surface free energy of the wire. This relation shows that there is a critical diameter, d_c, at which the growth stops completely and given by the following expression:

$$\Delta\mu_{bulk}/\,kT = 4\,(\alpha\Omega)\,/kTd_C.$$

where, *k* is Boltzmann's constant and *T* the temperature, d_c the critical diameter. This can be explained by the fact that for very small nanodroplets the effective chemical potential of silicon in the wire becomes higher than for the vapour phase.

1.9 Primary objective of the thesis and materials selection

(i) Objective

Based on the preceding literature review, the objectives of the current thesis were formulated as follows.

1. To study the nature of process of vapour condensation on a substrate to achieve control over early stages of thin film growth and therefore realize nanostructured thin films.
2. To realize nanostructured thin films by using simple templates resulting in the formation of nanoparticle arrays and nanowires.
3. To control the thermodynamics of grain growth, crystallization and organization under the influence of external triggers such as electric field and laser irradiation leading to nanostructuring of thin films and bulk surfaces.

4. To study in each case, the microstructure, structure and optical, magnetic and electronic properties of the nanostructured materials.

(ii) Material selection

The material selection was driven by their relevance to applications and these are nickel, indium, gold and silicon.

(a) Nickel

Properties

Nickel is silvery-white magnetic metal which is inert to oxidation and naturally magnetostrictive (negative magnetostriction). Most common oxidation state of nickel is +2, though 0, +1, +3 and +4 Ni complexes are observed. The unit cell of nickel is a face centered cube with a lattice parameter of 0.352 nm giving a radius of the atom of 0.125 nm. Nickel is used in many industrial and consumer products, including stainless steel, magnets, coinage, and special alloys. It is also used as a catalyst for hydrogenation, for plating and as a green tint in glass.

Applications of nickel thin films

1. Nickel nanodots for magnetic recording [208]
2. Temperature-driven spin reorientation transition in nickel thin film [209]
3. Nickel metal induced crystallization of silicon [210]
4. Thin film magnetic heads with thin nickel under layers [211]
5. Thin film nickel temperature sensor [212]
6. Structural transition at few monolayer thicknesses [213]

(b) Indium

Properties

It is a rare shiny white, soft, malleable and easily fusible element.

Applications of indium thin film

1. Surface plasmonic devices-[214-216]
2. It is widely used in thin-films to form lubricated layers [217]

3. Used to coat bearings in high-performance aircraft

4. When evaporated onto glass, forms a mirror which is as good as those made with silver but has higher corrosion resistance. [218]

(c) Gold

Properties

Gold is a bright yellow noble metal which is a good conductor of heat and electricity, dense, soft, malleable, ductile, inert to most chemicals and resistant to oxidative corrosion.

Application of gold thin films

1. Surface plasmonic devices –[219-222]
2. Electronics, (used as conducting layer, interconnects; concentration of free electrons 5.90×10^{22} cm^{-3}.)
3. Produces a deep, intense red color when used as a coloring agent in cranberry glass.
4. As gold is a good reflector of electromagnetic radiation such as infrared and visible light as well as radio waves, it is used for the protective coatings on many artificial satellites, in infrared protective faceplates in thermal protection suits and astronauts' helmets and in electronic warfare planes.

(d) Silicon

Properties

Silicon is a gray semiconductor with negative temperature coefficient of resistance which is inert to most of the acids piezoresistive, strong, very brittle, and prone to chipping.

Applications of silicon thin films

1. Principal component of most semiconductor devices, e. g. in transistors [223-224], integrated circuits

2. Its native oxide is easily grown in a furnace and forms a better semiconductor/dielectric interface than any other material.

3. Nanocrystalline and nanostructured silicon is a good candidate for solar cells [225] and in displays.

4. Nanostructured silicon is used for chemical imaging [226], biomedical applications e. g. culturing of mammalian cells [227] and anisotropically nanostructured silicon can be used for optical devices e.g. silicon-based optical devices: retarders, dichroic Bragg Reflectors, dichroic microcavities and Si based polarizers [228]

(iii) Summary of the material selection

In summary, Nickel has been selected for nanostructuring, because of its magnetic nature and possible size and shape dependent effects on magnetic reversal behaviour. Indium and gold thin film nanostructuring has been performed mainly due to size and shape dependent surface plasmonic applications. Nanostructured silicon surfaces and thin films have strong candidature for applications in solar cells, and displays.

References

[1]. S. Jin, D. Whang, M.C. McAlpine, R. S. Friedman, Y. Wu and C. M. Lieber, Nano Lett. 4, 915 (2004)

[2]. L. Tsakalakos, J. Balch, J. Fronheiser, and B. A. Korevaar, O. Sulima and J. Rand, Appl. Phys. Lett. 91, 233117 (2007)

[3] http://www.ece.ucdavis.edu/~mrsarkar/research.htm

[4] C. R. Sides, C. R. Martin, Adv. Mater. 17, 125 (2005)

[5] Q. Li, X. Zhu, H. D. Xiong, S. M. Koo, D. E. Ioannou, J. J. Kopanski, J. S. Suehle and C. A. Richter, Nanotechnology 18, 235204 (2007)

[6] Q. Wan, J. Huang,Z. Xie,T. Wang, E. N. Dattoli, and W. Lu
Appl. Phys. Lett. 92, 102101 (2008)

[7] L. Wei, X. Zhang, Z. Zuoya J. Vac. Sci. Technol. B 25, 608 (2007).

[8] M. Law, D. J. Sirbuly, J. C. Johnson, J. Goldberger, R. J. Saykally, P. Yang, Science, 305, 1269 (2004)

[9] C. H. Oon and J. T. L. Thong, Nanotechnology 15, 687 (2004)

[10] A. Motayed, A. Davydov, M. He, S. N. Mohammed and J. Melngailis. Appl. Phys. Lett. 90, 183120 (2007)

[11] K. A. Bertness, N. A. Sanford, J. M. Barker, J. B. Schlager, A. Roshko, A. V. Davydov and I. Levin. Jour. Electr. Mater. 35, 576, (2006)

[12] K. T. Kim, S. J. Sim, S. M. Cho, IEEE Sensors, 6, 509 (2006)

[13] E. Comini, C. Baratto, G. Faglia, M. Ferroni, A. Vomiero, G. Sberveglieri, IEEE Conference series COMMAD 2006, 1-4244-0578-5, 315 (2006)

[14] X.T. Zhou, J.Q. Hu, C.P. Li, D.D.D. Ma, C.S. Lee, S.T. Lee, Chemical Physics Letters 369, 220 (2003)

[15] A. Agarwal, K. Buddharaju, I. K. Lao, N. Singh, N. Balasubramanian, D. L. Kwong, Sensors and Actuators A 145, 207 (2008)

[16] A. Graff, D. Wagner, H. Ditlbacher, and U. Kreibig, Eur. Phys. J. D 34, 263 (2005)

[17] Y. Lu, M. Yang, F. Qu, G. Shen, R.Yu, Bioelectrochemistry 71, 211, (2007)

[18] F. Y. Yang, Kai Liu, C. L. Chien, and P. C. Searson, Phys. Rev. Lett. 82, 3328 (1999)
[19] J. J. Steele, IEEE Sensors, 8, 1422 (2008)
[20] X. J. Huang, Y. K. Choi, Sensors and Actuators B: Chemical , 122, 659 (2007)
[21] U. Yogeswaran, S. M. Chen, Sensors, 8, 290 (2008)
[22] T. Matsuyama, Y. Kawata, Jpn. J. Appl. Phys., 45, 1438 (2006)
[23] P. L. Chen, W. J. Huang, J. K. Chang, C. T. Kuo, and F. M. Pan, Electrochem. Sol. Stat. Lett., 8, H83 (2005)
[24] H. Fujisawa, Y. Morimoto, M. Shimizu, Jap. Jour. Appl. Phys. 45, 7262 (2006).
[25] K. Busch, S. Lölkes, R.B. Wehrspohn, and H. Föll, in "Photonic Crystals: Advances in Design, Fabrication, and Characterization", Wiley-VCH Verlag GmbH & Co. KGaA, Weinheim (2004).
[26] V. Lehmann in "Electrochemistry of silicon", Wiley-VCH, Weinheim (2002).
[27] V. Kochergin, "Omnidirectional Optical Filters", Kluwer Academic Publisher, Boston (2003).
[28] C. Mazzoleni and L. Pavesi, Appl. Phys. Lett. 67, 1983 (1995)
[29] I. M. Tiginyanu, I. V. Kravetsky, S. Langa, G. Marowsky, H. L. Hartnagel, and H. Föll, phys. stat. sol. (a) 197(1/2) (2003)
[30] T.V. Dolgova, A.I. Maidykovski, M.G. Martemyanov, A.A. Fedyanin, O.A. Aktsipetrov, G. Marowsky, V.A. Yakovlev, G. Mattei, N. Ohta, and S. Nakabayashi, J. Opt. Soc. Am. B 19, 2129 (2002).
[31] S. Langa, S. Frey, J. Carstensen, H. Föll, I.M. Tiginyanu, M. Hermann, and G. Böttger, Electrochem. Sol. State Lett. 8, C30 (2005).
[32] V. Kochergin, M. Christophersen, and H. Föll, Appl. Phys. Lett. 86(1), 042108 (2004).
[33] H. Föll, J. Carstensen, and S. Frey, Mater. Res. Soc. Symp. Proc. 876E, R12.1.1 (2005)
[34] H. Shinoda, T. Nakajima, K. Ueno, and N. Koshida, Nature 400, 853 (1999).
[35] T. Yonehara, "BESOI with porous silicon: ELTRAN", in "Properties of porous silicon", ed. L.T. Canham, IEE-Books, London (1997).
[36] C. K. Inoki, T. S. Kuan, C. D. Lee, A. Sagar, R. M. Feenstra, D. D. Koleske, D. J. Diaz, P. W. Bohn, and I. Adesida, J. Electron. Mater. 32, 855 (2003).
[37] M. Steinhart, Z. Jia, A. K. Schaper, R. B. Wehrspohn, U. Gösele, and J. H. Wendorff, Adv. Mat. 15, 706 (2003).

[38] Institute for Nanoscale Physics and Chemistry webpage www.kuleuven.be/inpac
[39] J. W. Toigo, Scientific American, 282, 58 (2000).
[40] Z. Z. Bandic, D. Litvinov, M. Rooks, MRS Bulletin, 33, 831 (2008)
[41] C. A. Ross and J. Y. Cheng, MRS Bulletin, 33, 838 (2008)
[42] J. Narayan, Mat. Res. Soc. Symp. Proc., 750, Y2.6.1 (2003)
[43] K. N. Lee, S. W. Jung, W. H. Kim, M. H. Lee, K. S. Shin, W. K. Seong, Nanotechnology 18, 445302 (2007)
[44] R. Waser (ed.), "Nanoelectronics and Information Technology", Chapter 9. New York: John Wiley and Sons (2003)
[45] G. Timp (ed.) "Nanotechnology", Chapter 4 Springer-Verlag New York, Inc., NY (1999)
[46] R. Waser (ed.), "Nanoelectronics and Information Technology", Chapter 9. New York: John Wiley and Sons (2003)
[47] M. Farhoud, M. Hwang, H.I. Smith, M. L. Schattenburg, J. M. Bae, K. Youcef-Toumi, C.A. Ross, IEEE Trans. Magn. 34, 1087 (1998).
[48] T. A. Savas, M. Farhoud, H. I. Smith, M. Hwang, C. A. Ross, J. Appl. Phys. 85 6160 (1999)
[49] L. J. Heyderman, H. H. Solak, C. David, D. Atkinson, R. P. Cowburn, and F. Nolting Appl. Phys. Lett. 85, 4989 (2004)
[50] J. H. Lee, K. Y. Yang, S. H. Hong, H. Lee, K. W. Choi, Microelectronic Engineering 85, 710 (2008)
[51] S. Y. Chou, P. R. Krauss, W. Zhang, L. J. Guo and L. Zhuang J. Vac. Sci. Technol. B 15, 2897 (1997)
[52] P. R. Krauss and S. Y. Chou, Appl. Phys. Lett., 71, 3174 (1997).
[53] M.C. Hart, R. Best, C. Terris, Appl. Phys. Lett., 81, 1483 (2002).
[54] H. J. Fan, B. Fuhrmann, R. Scholz, F. Syrowatka, A. Dadgar, A. Kros, M. Zacharias, Jour. Crys. Growth 287, 34 (2006)
[55] R. Juhasz, N. Elfström, J. Linnros, Nano Lett., 5, 275 (2005)
[56] C. H. Park, S. Bae, H. Lee, Colloids and surfaces A, 284, 552 (2006)
[57] F. Wirth, V. M. Awschalom, Phys. Rev. B, 57, 14028 (1998).
[58] D. Hofmann, W. Schindler, J. Kirschner, Appl. Phys. Lett. 73, 3279 (1998)
[59] J. H. Lim, D. S. Ginger, k. B. Lee, J. Heo, J. M. Nam, C. A. Mirkin, Angew. Chem. Int. 20, 2411 (2003)
[60] R. D. Piner, J. Zhu, F. Xu, S. Hong, C. A. Mirkin Science, 283, 661 (1999)

[61] S. Hong, J. Zhu, C. A. Mirkin, Science 286, 523 (1999)

[62] I. V. Kourkine, C. S.Slone, E. T. Singewald, C. A. Mirkin, Science 288, 1808 (2000)

[63] A. Noy, A.E. Miller, J.E. Klare, B.L. Weeks, B.W. Woods, and J.J. De Yoreo, Nano Lett. 2, 109 (2002).

[64] B. L. Weeks, A. Miller, A. Noy, J. J. D. Yoreo, Phys. Rev. Lett. 88, 255505 (2002).

[65] P. A. Hasegawa, Science 258, 1763 (1992)

[66] A. Cuenat, M. J. Aziz, Mat. Res. Soc. Symp. Proc., 707, A3.8.1/N2.8.1 (2002)

[67] Q. Lu, F. Gao, D. Li, S. Komarneni , AZOJOMO, 1, 1 (2005)

[68] S. Inoue, S. Z. Chu, K. Wada, D. Li, H. Haneda, Sci. Technol. Adv.Mat. 4, 269, (2003)

[69] H. Brune, M. Giovannini, K. Bromann, K. Kern, Nature, 394, 451 (1998)

[70] F. S. Flack, B. Yang, M. Huang, M. Marcus, J. Simmons, O. M. Castellini, M. A. Eriksson, F. Liu, M. G. Lagally, Mater. Res. Soc. Symp. Proc., 849, KK1.3.1 (2005)

[71] H. Nakamura, Y. Matsui, J. Amer. Chem. Soc., 117, 2651 (1995)

[72] M. Zhang, Y. Bando, K. Wada, J. Mater. Res., 16, 1408 (2001)

[73] L. H. Wang, S. Tomura, F. Ohashi, M. Maeda, M. Suzuki, K. Inukai, J. Mater. Chem., 11, 1465 (2001)

[74]. H. P. Lin, C. Y. Mou, Science, 273, 765 (1996)

[75]. M. Adachi, T. Harada, M. Harada, Langmuir, 16, 2376 (2000)

[76]. M. Harada, M. Adachi, Adv. Mater. 12, 839 (2000)

[77]. Z. Y. Yuan, W. Z. Zhou, Chem. Phys. Lett., 333, 427 (2001)

[78]. H. P. Lin, C. Y. Mou, S. B. Liu, Adv. Mater., 12, 103 (2000)

[79]. M. E. Spahr, P. Bitterli, R. Nesper, M. Muller, F. Krumeich, H. U. Nissen, Angew. Chem. Int. Ed. Engl., 37, 1263 (1998)

[80]. K. S. Pillai, F. Krumeich, H. J. Muller, M. Niederberger, R. Nesper, Sol. Stat. Ion. 141, 185 (2001)

[81]. H. J. Muhr, F. Krumeich, U. P. Schonholzer, F. Bieri, M. Niederberger, L. J. Gauckler, R. Nesper, Adv. Mater. 12, 231 (2000)

[82]. M. Niederberger, H. J. Muhr, F. Krumeich, F. Bieri, D. Gunther, R. Nesper, Chem. Mater., 12, 1995 (2000)

[83]. S. Kobayasi, K. Hanabusa, N. Hamasaki, M. Kimura, H. Shirai, Chem. Mater., 12, 1523 (2000)

[84]. C. Hippe, M. Wark, E. Lork, G. S. Ekloff, Microporous Mesoporous Mater., 31, 235 (1999)
[85]. G. S. Park, W. B. Choi, J. M. Kim, Y. C. Choi, Y. H. Lee, C. B. Lim, J. Crys. Growth, 220, 494 (2000)
[86] W. Q. Han, P. K. Redlich, F. Ernst, M. Ruhle, Solid. State Comm., 115, 527 (2000)
[87]. T. W. Ebessen, P. M. Ajayan, Nature, 358, 220 (1992)
[88]. S. Iijima, T. Ichihashi, Nature, 363, 603 (1993)
[89]. T. Kasuga, M. Hiramatsu, A. Hoson, T. Sekino, K. Nihara, Langmuir, 14, 3160 (1998)
[90]. T. Kasuga, M. Hiramatsu, A. Hoson, T. Sekino, K. Niihara, Adv. Mater. 11, 1307 (1999)
[91]. R.E. Thun, in chapter "Physics of thin films", G. Hass (Ed.), "Advances in Research and Development", Academic Press Inc., New York, 1, 187 (1963)
[92]. Z. Shi, J. A Szpunar, S. Wu, Microsc. Microanal. 11, 1528 (2005)
[93]. C. T. Black, C. B. Murray, R. L. Sandstrom, S. Sun, Science 290, 1131 (2000)
[94]. S. Sun, C. B. Murray, D. Weller, L. Folks, A. Moser Science 287, 1989 (2000)
[95]. B. Liu, R. T. Schuller, Phys. Rev. B 63, 060403 (2001).
[96]. J. V. Barth, G. Costantini, K. Kern, Nature, 437, 671 (2005)
[97]. J. S. Yin, Z. L. Wang, Adv. Mater. 11, 469 (1999)
[98]. M. Li, R. B. Bhiladvala, T. J. Morrow, J. A. Sioss, K. K. Lew, J. M. Redwing, C. D. Keating, T. S. Mayer, Nature nanotechnology, 3, 88 (2008)
[99]. P. B. Amama, B. A. Cola, T. D. Sands, X. Xu, T. S. Fisher, Nanotechnology, 18, 385303 (2007)
[100]. V. D. R. Caffarena, J. L. Capitaneo, R. A. Simao, A. P.Guimaraes, Materials Research 9, 205 (2006)
[101]. W. Lee, M. K. Jin, W. C. Yoo, E. S. Jang, J. H. Choy, J. H. Kim, K. Char, J. K. Lee, Langmuir 20, 287 (2004)
[102]. L. Zhaoa, M. Steinhart, M. Yosef , S. K. Lee, S. Schlecht, Sensors and Actuators B 109, 86 (2005)
[103]. K. Yamamoto, H. Kohno, S. Takeda, S. Ichikawa, Appl. Phys. Lett. 89, 083107 (2006)
[104]. J. Goldberger, R. He, Y. Zhang, S. Lee, H.Yan, H. J. Choi, P. Yang, Nature 422, 599 (2003)

[105] D. AlMawlawi, N. Coombs, M. Moskovits, J. Appl. Phys. 70, 4421 (1991)
[106]. L. Menon, M. Zheng, H. Zeng, S. Bandopadhyay, D. J. Sellmyer, J. Electron. Mater. 29, 510 (2000)
[107]. Y. C. Choi, J. Kim, J. K. Han and S. D. Bu, J. B. Park, H. Lee, B. K. Ahn, Jour. Kor. Phys. Soc. 49, S523 (2006)
[108]. D. Crouse, Y. H. Lo, A. E. Miller, M. Crouse, Appl. Phys. Lett. 76, 49 (2000)
[109]. H. Masuda, T. Mizuno, N. Baba, T. Ohmori, J. Electroanal. Chem. 368, 333 (1994)
[110]. P. Hoyer, N. Baba, H. Masuda, Appl. Phys. Lett. 66, 2700 (1995)
[111]. P. Hoyer, H. Masuda, J. Mater. Sci. Lett. 15, 1228 (1996)
[112]. H. Masuda, H. Tanaka, N. Baba, Chem. Lett. 1990, 621 (1990)
[113]. H. Masuda, K. Nishio, N. Baba, Jap. J. Appl. Phys. 31, L1775 (1992)
[114]. H. J. Fan, W. Lee, R. Scholz, A. Dadgar, A. Krost, K. Nielsch, M. Zacharias, Nanotechnology 16, 913 (2005)
[115]. S. Deki, S. Iizuka, A. Horie, M. Mizuhata, A. Kajinami, J . Mater . Chem. 14 , 3127 (2004)
[116]. D. AlMawlawi, N. Coombs, M. Moskovits, J. Appl. Phys. 70, 4421 (1991)
[117]. L. Menon, M. Zheng, H. Zeng, S. Bandyopadhyay, D. J. Sellmyer, J. Electron. Mater. 29, 510 (2000)
[118]. L. S. Jacobs, C. P. Bean, Phys. Rev. 100, 1060 (1955)
[119]. F. Li, R. M. Metzger, J. Appl. Phys. 81, 3806 (1997)
[120]. Y. Peng, H. L. Zhang, S. L. Pan, H. U. Li, J. Appl. Phys. 87, 7405 (2000)
[121]. H. Zeng, M. Zhang, R. Skomski, D. L. Sellmyer, Y. Liu, L. Menon, , J. Appl. Phys. 87, 4718 (2000)
[122]. R. M. Metzger, V. V. Konovalov, M. Sun, T. Xu, G. Zangari, B. Xu, M. Benakli, W. D. Doyle, IEEE Trans. Magn. 36, 30 (2000)
[123]. K. Nielsch, R. B. Wehrdpohn, J. Kirschner, U. Gosele, S .F. Fischer, H. Kronmuller, Appl. Phys. Lett. 79, 1360 (2001)
[124]. A. J. Yin, J. Li, A. J. Bennet and J. M. Xu, Appl. Phys. Lett. 79, 1039 (2001)
[125] R. M. Metzger, M. Sun, G. Zangari, M. Shamsuzzoha , Mater. Res. Soc. Symp. Proc. 636, D9.33.1 (2001)
[126] M. Sun, G. Zangari, M. Shamsuzzoha , R. M. Metzger, Appl. Phys. Lett., 78, 2964, 2001.

[127]. L. Menon, S. Bandopadhyay, Y. Liu, H. Zeng, D. J. Sellmyer, J. Nanosci. Nanotechnol. 1, 149 (2001)
[128]. S. Kawai, R. Ueda, J. Electrochem. Soc. 122, 32 (1975)
[129]. H. Daimon, O. Kitakami, O. Inagoya, A. Sakemoto, Japan. J. Appl. Phys. 30, 282 (1991)
[130] P. R. Evans, G. Yi, W. Schwarzacher, Appl. Phys. Lett. 76, 481 (2000)
[131]. M. Moskovits, International patent, 5202290 (1993)
[132]. D. Xu, X. Shi, G. Guo, L. Gui, Y. Tang, J. Phys. Chem. B 104, 5061 (2000)
[133]. N. Kouklin, S. Bandopadhyay, S. Tereshin, A. Varfolomeev, D. Zaretsky, Appl. Phys. Lett. 76, 460 (2000)
[134]. D. Routkevich, A. A. Tager, J. Haruyama, D. Almawlawi, M. Moskovits, J. M. Xu, IEEE Trans. Electron. Devices 43, 1646 (1996)
[135]. D. J. Pena, B. Razavi, P. A. Smith, J. K. Mbindyo, M. J. Natan, T. S. Mayer, T. E. Mallouk, C. D. Keating, Mater. Res. Soc. Symp. Proc. 636, D4.6.1 (2001)
[136]. N. A. Gershenfeld, L. A. Chuang, Science 275, 350 (1997)
[137]. G. Yi, W. Schwarzacher, Appl. Phys. Lett. 74, 1746 (1999)
[138]. X. F. Wang, L. D. Zhang, J. Zhang, H. Z. Shi, X. S. Peng, M. J. Zhang, J. Fang, J. L. Chen, B. J. Gao, J. Phys. D 34, 418 (2001)
[139] G. L. Hornyak, C. J. Patrissi, C. R. Martin, J. Phys. Chem. B 101, 1548 (1997)
[140]. C. A. Foss, Jr., G. L. Hornyak, J. A. Stockert, C. R. Martin, J. Phys. Chem. 98, 2963 (1994)
[141]. P. Forrer, F. Schlottig, H. Siegenthaler, J. Appl. Electrochem. 30, 533 (2000)
[142]. S. L. Pan, D. D. Zeng, H. L. Zhang, H. L. Li, Appl. Phys. A 70, 637 (2000)
[143]. H. Cao, C. Tie, Z. Xu, J. Hong, H. Sang, Appl. Phys. Lett. 78, 1592 (2001)
[144]. M. A. Rouhi, Chem. Eng. News 79, 29 (2001)
[145]. A. Hellemans, IEEE Spectrum 38, 6 (2001)
[146]. A. G. Rinzler, J. H. Hafner, P. Nikolaev, L. Luo, S. G. Kim, D. Tomanek, P. Nordlander, D. T. Colebert, R. E. Smalley, Science 269, 1550 (1995)
[147]. S. Liu, J. Xhu, Appl. Phys. A 70, 673 (2000)
[148]. J. S. Suh, J. S. Lee, Appl. Phys. Lett. 75, 2047 (1999)
[149]. Z. H. Yuan, H. Huang, H. Y. Dang, J. E. Cao, B. H. Hu, S. S. Fan, Appl. Phys. Lett. 78, 3127 (2001)
[150]. T. Iwasaki, T. Motoi, T. Den, Appl. Phys. Lett. 75, 2044 (1999)

[151]. J. Goldberger, R. He, Y. Zhang, S. Lee, H. Yan, H. J. Choi, P. Yang, Nature 42, 599 (2003)
[152] A. K. Srivastava, S. Madhavi, T. J. White and R. V. Ramanujan, J. Mater. Chem. 15, 4424 (2005)
[153]. L. Vazquez, A. H. Creus, P. Carro, P. Ocon, P. Herrasti, C. Palacio, J. M. Vara, R. C. Salvarezza, A. J. Arvia, Jour.Phys. Chem. 96, 10454 (1992)
[154]. R. T. Pötzschke, C. A. Gervasi, S. Vinzelberg, G. Staikov, W.J. Lorenz, Electrochimica Acta 40, 1469 (1995)
[155]. J.V. Zoval, Jour. Phys. Chem. 100, 837 (1996)
[156]. H. Martin, A. H. Creus, P. Carro, R.C. Salvarezza, A. J. Arvia, Langmuir 13, 100 (1997)
[157]. M. P. Zach, K. H. Ng, and R. M. Penner, Science 290, 2120 (2000)
[158]. Y. Gimeno, A. H. Creus, S. González, R. C. Salvarezza, A. J. Arvia, Chem.of Materials 13, 1857 (2001)
[159]. Y. Gimeno, A. H. Creus, P. Carro, S. González, R. C. Salvarezza, A. J. Arvia, Jour. Phys.Chem. B, 106, 4232 (2002)
[160]. F. Favier, E. C. Walter, M. P. Zach, T. Benter, R. M. Penner., Science 293, 2227 (2001)
[161] J. V. Zoval, J. Lee, S. Gorer, R. M. Penner, Jour. Phys. Chem. B 102, 1166 (1998)
[162]. M. P. Zach, J. T. Newberg, L. Sierra, J. C. Hemminger, R. M. Penner, J. Phys. Chem. B 10, 1021/jp034452k (2003)
[163]. M. P. Zach, K. Inazu, K. H. Ng, J. C. Hemminger, and R. M. Penner, Chem. Mater. 14, 3206 (2002)
[164]. N. Ravishankar, V. B. Shenoy, C. B. Carter, Adv. Mater. 16, 76 (2004)
[165] X. Xiong, P. Makaram, K. Bakhtari, S. Somu, A. Busnaina, J. Small, N. McGruer, J. Park, Mater. Res. Soc. Symp. Proc. 901E, Ra04-01.1 (2006)
[166]. J.G. Partridge, S.A. Brown, C. Siegert, A.D.F. Dunbar, R. Nielson, M. Kaufmann, R.J. Blaikie, Microelectronic Engineering 73, 583 (2004)
[167]. O. P. Karpenko, J. C. Bilello, S. M. Yalisove, J. Appl. Phys. 82, 1397 (1997)
[168]. M. M. Hawkeye, J. Vac. Sci. Technol. A 25, 1317 (2007)
[169]. J. P. You, J. H.. Choi, S. Kim, X. Li, R. Williams, R. Ragan, Nano Lett. 6, 1858 (2006)

[170]. H. Kanno, A. Kenjo, T. Sadoh, M. Miyao, Mater. Res. Soc. Symp. Proc. 891, EE06-08.1 (2006)
[171]. Y. Wang, L. Wang, B. Tang, D. K. Choi, Thin Solid Films 515, 2507 (2006)
[172] J. Jang, J. Y. Oh, S. K. Kim, Y. J. Choi, S. Y. Yoon, C. O. Kim, Nature 395, 481 (1998)
[173]. S. Q. Li, Y. X. Liang, T. L. Guo, Z. X. Lin, T. H. Wang, Materials Letters 60, 1492 (2006)
[174]. Y. T. Jang, J. H. Ahn, B. K. Ju, Y. H. Lee, Sol. Stat. Comm. 126, 305 (2003)
[175]. Y. Zhang, A. Chang, J. Cao, Q. Wang, W. Kim, Y. Li, N. Morris, E. Yenilmez, J. Kong, H. Dai, Appl. Phys. Lett. 79, 3155 (2001)
[176]. T. Ichinokawa, H. Itoh, Y. Sakai, J. Anal. At. Spectrom. 14, 405 (1999)
[177]. M. Saka, R. Ueda, J. Mater. Res. 20, 2712 (2005)
[178] Y. F. Guan, A. V. Melechko, A. J. Pedraza, M. L. Simpson and P. D. Rack, Nanotechnology 18, 335306 (2007)
[179]. D. Riabinina, C. Durand, F. Rosei, M. Chaker, Physica Status Solidi, (a) 204, 1623 (2007)
[180]. G. Conibear, M. Green, R. Corkish, Y. Cho, E. C. Cho, C. W. Jang, T. Fangsuwannarak, E. Pink, Y. Huang, T. Puzzer, T. Trupke, B. Richards, A. Shalav, K. L. Lin, Thin Solid Films 511, 654 (2006)
[181] T. D. James, J. S. Milne, A. J. Keting, G. Parish, C. A. Musca, J. M. Dell, L. Faraone, IEEE Transactions 431, 1-4244-453-3 (2006)
[182]. J. Diener, N. Kunzner, E. Gross, D. Kovalev, M. Fujii, Phys. Stat. Sol. 202, 1432 (2005)
[183]. A. M. Morales, C. M. Lieber, Science 279, 208 (1998)
[184]. T. Ono, H. Saitoh, and M. Esashi, Appl. Phys. Lett. 70, 1852 (1997)
[185] Y. F. Zhang, Y. H. Tang, N. Wang, D.P. Yu, C. S. Lee, I. Bello, S. T. Lee, Appl. Phys. Lett. 72, 1835 (1998)
[186] N. Wang, Y. H. Tang, Y. F. Zhang, C. S. Lee, S. T. Lee, Chem. Phys. Lett. 283, 368 (1998)
[187]. Y. F. Zhang, Y. H. Tang, N. Wang, C. S. Lee, I. Bello, S. T. Lee, J. Cryst. Growth 197, 136 (1999)
[188]. N. Wang, Y. F. Zhang, Y. H. Tang, C. S. Lee, S. T. Lee, Appl. Phys. Lett. 73, 3902 (1998)
[189]. Y. H. Tang, Y. F. Zhang, C. S. Lee, N. Wang, D. P. Yu, I. Bello, and S.

T. Lee, Mater. Res. Soc. Symp. Proc. 526, 73 (1998)
[190]. N. Wang, Y. H. Tang, Y. F. Zhang, C. S. Lee, S. T. Lee, Phys. Rev. B 58, R16024 (1998)
[191]. C. K. Chan, H. Peng, G. Liu, K. McIlwrath, X. F. Zhang, R. A. Huggins, Y. Cui, Nature Nanotechnology 3, 31 (2008)
[192]. Q. Li, X. Zhu, H. Xiang, S. M. Koo, D. E. Ionnou, J. Kopanski, J. S. Suehlee, C. A. Richter, Nanotechnology 18, 235204 (2007)
[193]. A.V. Kabashin , M. Meunier, Materials Science and Engineering B 101, 60 (2003)
[194]. A. J. Pedraza, J. D. Fowlkes, Y. F. Guan, Appl. Phys. A 77, 277 (2003)
[195]. S. J. Henley, J. D. Carey, S. R. P. Silva, Applied Surface Science 253, 8080 (2007)
[196]. S. Loreti, A. Santoni, J. Lancok, I. Menicucci, C. Minarinic, D. D. Sala, Thin Solid Films 458, 1 (2004)
[197]. E. I. Givargizov, Journal of Crystal Growth 31, 20 (1975)
[198]. R. S. Wagner, W. C. Ellis, Appl. Phys. Lett. 4, 89 (1964)
[199]. J. Westwater, D. P. Gosain, S. Tomiya, S. Usui, H. Ruda, J. Vac. Sci. Technol. B 15, 554 (1997)
[200]. H. Huang, S. Mao, H. Feick, H. Q. Yan, Y. Y. Wu, H. Kind, E. Weber, R. Russo, P. D. Yang, Science 292, 1897 (2001)
[201]. Q. Liu, S. S. Xie, L. F. Sun, D. S. Tang, W. Y. Zhou, C. Y. Wang, W. Liu, Y. B. Li, X. P. Zhou, G. Wang, J. Mater. Res. 16, 683 (2001)
[202]. C. Choi, W. S. Kim, Y. S. Park, S. M. Lee, D. J. Bae, Y. H. Lee, G. S. Park, W. B. Choi, N. S. Lee, J. M. Kim, Adv. Mater. 12, 746 (2000)
[203]. J. Zhang, F. Jiang, Z. Dai, J. Phys. D: Appl. Phys. 36, 2046 (2003)
[204]. V. Sharma, B. V. Kamenev, L. Tsybeskov, Mater. Res. Soc. Symp. Proc. 832, F7.20.1 (2005)
[205]. M He, P. Zhou, S. N. Mohammad , G. L. Harris, J. B. Halpern , J. Cryst. Growth 231, 357 (2001)
[206]. S. M. Zhou, Y. S. Feng, L. D. Zhang, Chem. Phys. Lett. 369, 610 (2003)
[207]. C. Y. Lee, T. Y. Tseng, S. Y. Li, P. Lin, Tamkang Jour. Sci. Engg. 6, 127 (2003)
[208] B. D. Terris, M. Albrecht, G. Hu, T. Thomson, and C. T. Rettner, IEEE Trans. Mag. 41, 2822 (2005)

[209]. B. Cheng, K. Yang, B. L. Justus, W. J. Yeh, Mat. Res. Soc. Symp. Proc. 721, E5.6.1 (2002)
[210] S. X. Hui, Z. D. Lin, Chinese Physics B 17, 3495 (2008)
[211]. H. Sing, K. Man, W. Zhiguo, M. Shuyun, Z. C. Wu, US Patent 0212855 (2007)
[212]. K. P. Ash; M. S. Miller; F. E. Stageberg, US Patent 5666250 (1997)
[213]. A. C. M. Chen, J. M. Lommel, US Patent 3660158 (1972)
[214]. P. Le Fevre1; H. Magnan and D. Chandesris, Eur. Phys. J. B 10, 555 (1999)
[215]. J. R. Sambles, A.P.Hibbins, M.J.Jory, H. Azizbekyan, Jour. Mod. Optics 47, 1227 (2000)
[216]. O. Stenzel, A. Stendal, M. Roder, C.V. Borczyskowski, Pure Appl. Opt. 6, 577 (1997)
[217]. J. C. Lemonnier, G. Jezequel, J. Thomas, J. Phys. C 8, 2812 (1975)
[218]. G. W. Stachowiak, A. W. Batchelor in "Engineering tribology", second edition, Elsevier ISBN 0750673044, 9780750673044, 422 (2000)
[219]. P. Mulvancy, J. P. Juste, M. Giersig, L. M. L. Marzan, C. Pecharroman, Plasmonics 1, 61 (2006)
[220]. R. Gupta, M. J. Dyer, W. A. Weimer, Jour. Appl. Phys. 92, 5264 (2002)
[221]. H. G. Craighead, G. A. Niklasson, Appl. Phys. Lett. 44, 1134 (1984)
[222] Y. Yang, S. Matsubara, M. Noganmi, J. Shi, W. Huang, Nanotechnology 17, 2821 (2006)
[223]. L. Dong, R. L. Yue, Intl. Jour. Infrared and Millimeter Waves 24, 1351 (2003)
[224]. S. Tanaka, Y. Watanabe, K. Shirai, Y. Ogiwara, United States Patent 4979006 (1990)
[225]. L. Q. Song, W. Z. Meng, G. X. Hua, Z. Ying, S. Jian, X. J. Ping, Chinese Phys. 15, 3033 (2006)
[226]. T. Yoshinobu, W. Moritz, F. Finger, M. J. Schoening, Mater. Res. Soc. Symp. Proc. 910, 0910-A20-01 (2006)
[227]. S. C. Bayliss, R. Heald, D. I. Fletcher , L. D. Buckberry, Adv. Mater. 11, 318 (1999)
[228]. J. Diener, N. Künzner, E. Gross and D. Kovalev, M. Fujii, Mat. Res. Soc. Symp. Proc. 797, W1.8.1 (2004)

Chapter-2

Experimental

Abstract:

This chapter describes experiments carried out as part of the present thesis, which are essentially four non-lithographic techniques employed for nanostructuring thin films and bulk wafer surfaces. Instruments used, data analysis and corresponding experimental conditions under which experiments were executed are presented. Characterization techniques for physical properties viz structural, microstructural, optical, magnetic, magnetic transport and photoluminescence have been described.

2.1 Brief introduction of experimental design

To employ non-lithographic techniques to surface nanostructuring, in-situ as well as ex-situ nanostructuring techniques were employed. In-situ nanostructuring was achieved by two methods, first by self-assembled early stage of thin film growth and second by template assisted growth. Ex-situ nanostructuring was achieved by employing external triggers such as DC electric field and Excimer laser; to nanostructure bulk wafer surfaces and also already formed thin films. The effects of nanostructuring on various physical properties of thin films and bulk surfaces have also been studied. In the following sections, these four non-lithographic techniques have been described in detail. These non-lithographic techniques have been described in different sections as follows:

- Controlled early stage of thin film growth technique
- Template assisted technique for fabrication of nanowires
- Electric field induced nanostructuring technique
- Laser assisted nanostructuring technique

At the end of the chapter, all instruments used for characterization have been introduced in brief and methods for data extraction are described. Among these instruments x-ray diffractometer, scanning electron microscope, atomic force microscope, vibrating sample microscope, ferromagnetic resonance, UV-VIS-NIR spectrophotometer, laser scanning confocal microscope are the major ones.

2.2 Controlled early stage of thin film growth technique

To achieve self-assembled early stage of thin film growth, physical vapour deposition techniques namely resistive thermal evaporation and pulsed laser deposition were employed. These two techniques have been chosen for current study because these techniques provide the possibility of thin film deposition at low rate of deposition and hence better control to observe the effect of other preparation parameters on thin film growth. For both the cases, the effect of thickness, substrate temperature and substrate material were studied on thin film growth at early stage. Nickel was used as the

material in the thermal evaporation case and nickel and silver materials were used as the materials in the pulsed laser deposition case.

Substrate preparation

Substrate cleaning is of prime importance in thin film coating at early stages because the presence of any foreign material dust can affect growth. Therefore in thin film processing, utmost care has to be taken to ensure that substrate surface is dust free, stain free and smooth.

Most of the thin film coatings were done on commercially available borosilicate glass (BSG), amorphous quartz, single crystal silicon (311) and single crystal MgO (001) substrates. The silicon and MgO substrates were one side polished. For cutting the substrates, commercially available diamond scribers was employed. Care was taken not to stain the substrates while handling them. To achieve smooth and dust free substrates, thorough cleaning steps were followed, which are described in below. For borosilicate glass, all 6 steps were followed, whereas for quartz, silicon and MgO cases; cleaning was started from the third step onwards. Ultrasonic cleaner (as shown in Figure- 2.1(a)) was used for cleaning purpose and an oven (as shown in Figure-2.1(b)) which can go upto 300^0C was used for drying purpose.

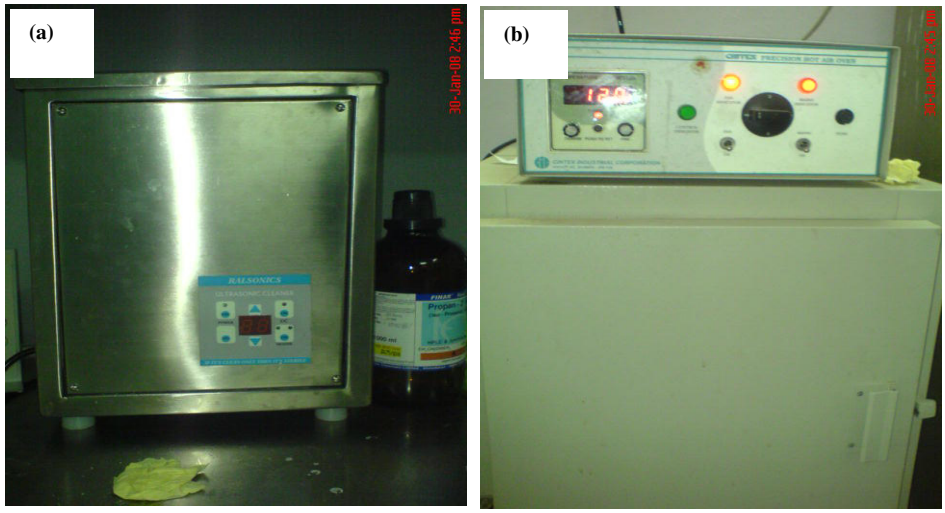

Figure-2.1 (a) Ultrasonic cleaner (Ralsonics, Mumbai, India), (b) Hot air Oven (up to 300^0C) (Cintex Ind. Corp., Mumbai, India)

Substrate cleaning steps:

1. First of all cleaning the substrate with soap solution and flushing it properly in flowing tap water to remove stains.
2. Drying at 80^0C for 10 minutes.
3. Ultrasonic cleaning in acetone medium for 15 minutes at 50^0C.
4. Ultrasonic cleaning in iso-propyl alcohol for 15 minutes at 50^0C.
5. Ultrasonic cleaning in doubly distilled water for 15 minutes at 50^0C.
6. Drying of substrates at 150^0C for 20 minutes.

(a) Resistive thermal evaporation

A resistive thermal evaporation unit (Cooke's vacuum products, CV 600 M) was used for coating which is equipped with an oil diffusion pump working in series with the mechanical pump. Maximum vacuum achieved has been found to be 1 x 10^{-6} mbar for the system on which experiments have been carried out (as shown in Figure- 2.2). Rough vacuum was measured by pirani gauge (Hind Hivac digital pirani gauge DPG-001 which can measure vacuum upto 10^{-3} mbar) and high vacuum was measured by ionization gauge (Cooke's ionization gauge which can measure pressures between 1 x 10^{-4} to 1 x 10^{-9} mbar). Thickness of films was monitored by quartz crystal thickness monitor (QCTM) (Hind Hivac thickness monitor model DTM-101) and confirmed in a profilometer after deposition (Ambios technology, Model XP-1) with a resolution of +/- 1 nm. From the fractional frequency change of the quartz crystal, which is given externally by an electronic oscillator, rate of deposition and the thickness can be measured. Three parameters have to be fed into the thickness monitor and those are density of material, acoustic impendence and tooling factor. For nickel, density (DNT) and acoustic impendence (ACI) are 8.910 g/cc and 26.680 ($\times 10^5$ gm/cm^2 sec) respectively. Tooling factor (TFC) is a correction term for the thickness because of difference in the distances of substrate and the quartz crystal with respect to the evaporation source. To make it simple, quartz crystal was placed at the same distance as that of the substrate. In such a condition, TFC value will be 100. After every 20 coatings, quartz crystal was either cleaned or replaced, because several coatings usually diminish the sensitivity of the QCTM.

Figure- 2.2 Photographic image of thermal evaporation system.

Thermal evaporation should be carried out in high vacuum due to two reasons. First is to avoid oxidation and second to enable evaporated atoms to reach onto the substrate surface due to enhanced mean free path. Rate of deposition can be controlled by varying filament current and thereby the source temperature. Nickel wire of diameter 0.25 mm and purity 99.998 % (from Sigma Aldrich) was used for thermal evaporation. Tungsten filament boats were utilized as source material. Several experiments were carried out with the same set of preparation conditions to establish the reproducibility of the results therein. For example, for each thickness at room temperature deposition conditions and for each substrate temperature for 50nm thin film of nickel onto BSG substrates, films were made ten times to verify the reproducibility. For thickness variation, substrate material and substrate temperature variation experiments, only the particular variables were changed; keeping rest all other experimental conditions same. For such control, rate of deposition was kept constant in a controlled manner.

Preparation parameters which were fixed

(a) **Rate of deposition**- 0.1-0.4 Å/s. This low value of rate of deposition has been chosen to observe the effect of other preparation parameters more explicitly.

(b) **Base pressure**- 1 x 10^{-6} mbar. This is the limit with the vacuum system which consists of a mechanical pump in combination with oil diffusion pump. Working pressure for the deposition of thin films was 3 x 10^{-6} mbar (high vacuum).

(c) **Source-substrate distance**- 10cm. This distance is optimal to yield very low rate of deposition and hence good control.

Preparation parameters varied to observe the effect on surface nanostructures

(a) **Variation of substrate materials**

Three substrates were used for nickel coating to study the substrate material effects. Those were, BSG, Si and MgO. The choice of amorphous glass and single crystal substrate has been made intentionally to investigate the effect of substrate crystalline order on the growth and crystalline order of the thin film materials. Silicon substrate had [311] preferred orientation and MgO had [200] and [220] preferred orientations. Both were one side polished and silicon was an n-type wafer. Prior to coating, MgO Substrates were heated for 5 minutes at 100^0 C, to remove moisture, if any.

(b)**Variation of substrate temperature**

An electrical filament heater housed in a stainless steel box with Eurotherm temperature controller was used for the purpose. Thin films of thickness 50nm were coated onto borosilicate glass (BSG) substrates at temperatures varying from ambient to 593K. Experiments were carried out for higher substrate temperature too, but beyond 600K, no change has been observed in the microstructure. Maximum limit was, however, 723K above which BSG substrate starts softening and at 743K it melts.

(c) **Variation of thickness**

For the thickness variation experiments, borosilicate glass substrates were coated with nickel thin films in the thickness range of 20-500nm. The choice of this thickness range has been made to observe the effect of the transition from island like growth to the continuous layer growth on long range crystalline order and magnetic properties

Characterizations of thermally evaporated nickel thin films

X-ray diffractometry was done with powder X-ray diffractometer, (INEL, XRG 3000) with Cobalt K_α line**.** Debye-Scherrer's formula was used to calculate the average crystallite size. $a = (k \lambda) / (\beta \cos \theta)$ where k = 0.94, λ = 1.78Å, β is the full width

at half maximum in radian and θ is the angle of incidence. A silicon standard was used for calibration to take into account instrumental broadening. The residual strain was calculated, from $\epsilon = (\Delta d)/d = (d - d_{bulk}) / d_{bulk}$ where d is the observed interplanar spacing for the thin film and d_{bulk} is that for the bulk material.

Quantitative information about magnetization was achieved from Vibrating Sample Magnetometer (Lakeshore Cryotronics, Model no.7400) having sensitivity in the range of μemu. Air-gap between magnets is fixed at 3 cm and for low magnetic moment samples (μemu), high time constants that permit lower field sweeping rate were used. The changes in flux caused by the vibrations are translated into a change in current in pick-up coils of the instruments, which registers a particular magnetization. To achieve large signal to noise ratio, a large area of the sample covering total area of sample holder was taken. A field limit of +/- 0.5 T in the steps of 0.005 or 0.01 T was adopted to achieve better accuracy. Hysteresis plots were taken in parallel orientation of films. Volume of the thin film has been calculated as the product of the area of the film coated on the substrate and the thickness measured in surface profilometer. The saturation magnetization is the saturation magnetic moment per unit volume of the film. We have plotted M_S / M_S (Bulk), where M_S (Bulk) refers to the saturation magnetization for bulk nickel having a value 470 emu / cc.

Atomic force microscopy (Seiko, Japan Model SPA 400) was used to characterize the morphology of the films made on different substrates. The images were acquired in the non-contact dynamic force mode and phase imaging is a popular technique coupled to this mode of operation. When the tip is in momentary contact it is affected by the dynamic properties of the material underneath. The detected signal from the cantilever by the photodiode has a slight phase lag from the driving signal sent to the piezo actuator. As a consequence, the variations in microstructure due to the presence of different elements, partial oxidation, granularity as well as evolution of the grain structure can be analyzed much better using these phase contrast images in contrast to the topographical images. We demonstrate that this technique is particularly useful in the case of magnetic thin films where the properties are critically dependent on the surface roughness and the distribution of grain size and the ratio of grain-to-grain boundary area.

(b) Pulsed laser deposition

Thin films of nickel and silver were deposited by pulsed laser deposition. Targets of nickel and silver (from Sigma Aldrich) were irradiated at an angle of 45° by a pulsed and focused KrF laser beam of wavelength 248 nm and pulse full width at half maximum (FWHM) of 30 ns (Lambda Physik, COMPEX Pro201F, Gottingen, Germany). Figure-2.3 (a) shows the assembled PLD system used for the present work (Advanced process technology, Pune) which, essentially consists of a laser source and a high vacuum chamber connected with a mechanical pump-turbo pump combine. Laser parameters include wavelength 248 nm, maximum pulse Energy 700 mJ, maximum average power 7 W, and maximum repetition rate 10 Hz. The major components (as shown in Figure- 2.3) of the pulsed laser deposition system are four target assembly, target rotation motors, turbo pump and the interfacing circuit which interfaces between computer and the PLC.

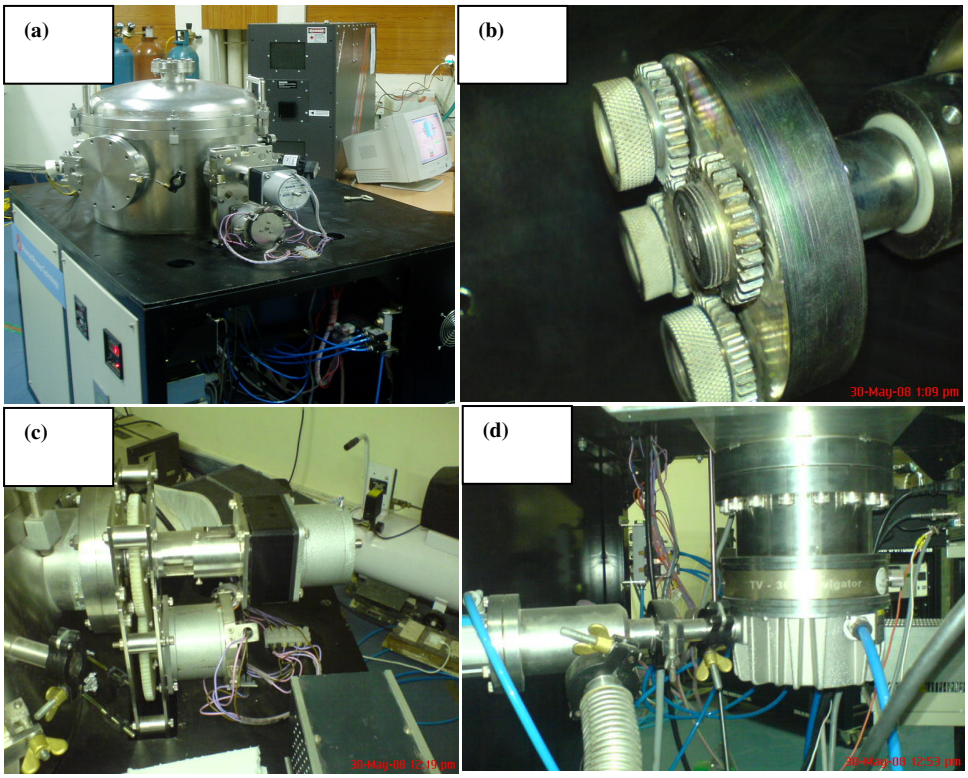

Figure- 2.3 Photographic image of (a) the PLD system, (b) target assembly, (c) target rotation mechanism and (d) turbo molecular pump.

When laser beam is incident on the metallic target, due to laser material interaction several phenomena take place simultaneously. Surface material evaporation, ionization and sputtering; all these happens at a time; as a result, plasma plume (as shown in Figure-2.4) is generated in the vicinity of the target surface.

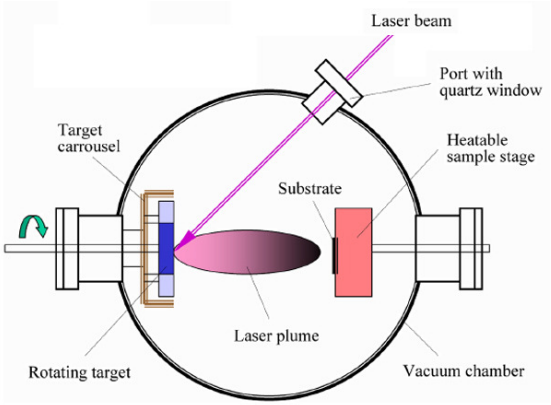

Figure- 2.4 Schematic of laser ablation

The plasma plume achieved was as shown in Figure 2.5. All laser ablation experiments were carried out in high vacuum (1 x 10^{-6} mbar). To measure thickness of ultrathin films, steps were achieved in ultrathin films using a mask, and then surface profiles were recorded in a surface profilometer (XP-1 of Ambios Technology, Santa Cruz, CA) having an accuracy of ±1 nm. The thickness of all the films was between 4 and 10 nm.

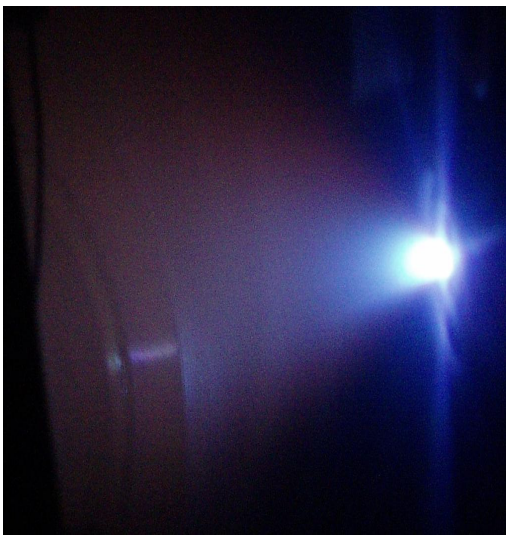

Figure 2.5 Photographic image of the laser induced plume.

Preparation parameters

(a) **Rate of deposition**- 0.1-0.3 Å/s. To investigate substrate and substrate temperature effects, the laser energy was kept constant and low enough to provide a low rate of deposition. The rate of deposition was varied by varying the incident laser energy.

(b) **Base pressure**- 1 x 10^{-6} mbar. This is the limit with the vacuum system which consists of a mechanical pump in combination with a turbo molecular pump. Working pressure for the deposition of thin films was 3 x 10^{-6} mbar (high vacuum).

(c) **Reprate –** The laser source can give laser pulses at reprates between 1 and 10 Hz.

Variable preparation parameters to observe the effect on surface nanostructures

(a) Variation of thickness

For the thickness variation experiments, borosilicate glass substrates were coated with nickel and silver thin films in the thickness range of 4-10nm. The choice of this thickness range has been made to observe the effect of the transition from island like growth to the continuous layer growth onto the ultrathin film nanostructural growth. This range of thickness is different from that of thermally evaporated thin films which remain island like even at higher thickness.

(b)**Variation of substrate temperature**

An electrical filament heater housed in a stainless steel box equipped with digital temperature controller was used for the purpose. Thin films of nickel and silver were coated onto borosilicate glass (BSG) substrates at temperatures varying from ambient to 573K. Experiments were carried out for higher substrate temperature too, but beyond 600K, not much observable change has been observed onto the microstructure. Maximum limit feasible was however 723K above which BSG substrate starts softening and at 743K it melts.

(c) **Variation of substrate materials**

Four substrates were used for nickel coating to investigate substrate material effects. These were, BSG, quartz, Si and MgO. These substrates, apart from providing different wettability, are different in terms of crystalline order facilitating the study of crystalline order in thin films.

(d) **Variation in laser energy**

Energy used for ablation was varied between 50 and 500 mJ. This is the energy range where apparent changes were registered and have been reported in this thesis.

(e) **Target-to-substrate distance**

Target to substrate distance was varied from 6 to 10 cm. This experiment was planned to study the effect of distance on the size distribution of particles in thin films.

Characterization of PLD thin films of nickel and silver

Atomic force microscope (model SPA 400 of Seiko Instruments, Chiba, Japan) in dynamic force mode was used to observe the microstructural growth of ultrathin films. The dynamic force mode is the intermittent contact mode that provides topography as well as phase contrast information. Phase changes in the signal are particularly sensitive, as shown, to minor changes in microstructure and hence useful for imaging grain boundaries. Phase imaging has also served as an additional tool to image deep features that are difficult using topographical images. Grain size was measured from the phase contrast images for 100 individual grains and histograms representing the distribution of grain diameter were plotted. Subsequently, statistical mean grain diameter, standard deviation from the mean grain diameter, skewness estimate from the Gaussian fit, and aspect ratio (mean grain diameter/average height of all grains with respect to the reference) were calculated. All these statistical values were then plotted against the variation in laser energy, substrate temperature and substrates.

2.3 Template assisted technique for fabrication of nanowires

To achieve organized growth / guided growth of nanofetaures in situ, v-trench template (of various diameters by using different forces normal to the substrate surfaces) were achieved by making use of a commercial diamond scriber (manual hand held diamond scriber with various tip diameter 5-50μm and also a precision diamond scriber instrument). Ultrasonic cleaning for 30 min was carried out before and after trench formation to wipe out all the dust from the substrate including the silica dust due to scribing. Then the substrates were dried for an hour at 473K. In another experiment; to achieve trench-to-trench isolation of the nanowires, use was made of a sacrificial layer of Maleic acid, which is water-soluble at ambient temperature. Borosilicate glass (BSG) has been used as substrates in general.

Such trench templated BSG surfaces have been employed (as shown in Figure 2.6) as substrates in the path of physical vapours by various coating techniques namely, resistive thermal evaporation, DC sputtering and pulsed laser deposition techniques. Usual thickness of thin film coating has been kept in the range of 10-100nm. All the thin films deposition on v-trench templates have been carried out at ambient temperature conditions, so that lateral diffusion onto the surface is minimal and the organized growth of nanofeatures can be realized. Nickel, indium and silicon have been thermally evaporated at high vacuum 1 x 10^{-6} mbar in a vacuum chamber (Cooke's vacuum products, CV 600 M pumping system) onto v-groove templated BSG substrates.

Nickel thin films were also deposited by PLD [KrF excimer laser (wavelength = 248 nm) (Lambda Physik, Compex Pro. Model 201F) at a power density of 0.05–0.2 J/cm^2] onto v-trench templated BSG substrate. All the deposition by PLD was carried out at a rep rate of 5 Hz, in high vacuum of 1 × 10^{-6} mbar (mechanical pump in combination with turbo pump) without using any processing gas in the vacuum chamber (Advance Processing Technology Pvt. Ltd.). The laser beam is incident on the nickel (99.998% pure, Alpha Aeser) sheet target in an oblique direction and the substrate was held in front of the target parallel to the target sheet at a distance of 10 cms.

Gold deposition was carried out using DC sputtering [at the pressure in 0.1 mbar region and at DC power of 600 W] onto v-groove templated BSG substrates.

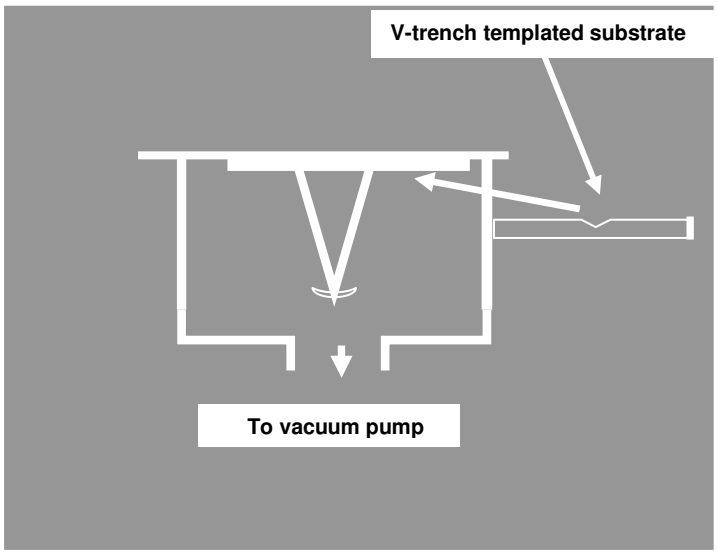

Figure- 2.6 Schematic of template assisted growth of nanowire.

Characterization

The profile of the trenches, that is, depth, width and roughness were measured in a surface profilometer (Model XP-1 of Ambios Technology, USA). Film thicknesses and roughness were also measured using the same profilometer. The morphology of the nanowires was determined using images obtained in a Philips XL 30 ESEM Scanning Electron Microscope (SEM) as well as an atomic force microscope (SPA 400 of SII Inc., Japan) operating in the non-contact Dynamic Force Microscopy (DFM) mode. The non-contact images give both topography and the phase contrast images, both of which were used to analyze the overall morphology of the nanowires. Magnetic anisotropy of nickel nanowires was studied from FMR spectra and the transport studies were carried out using usual MR setup. MR was calculated from the relation: MR (%) = $(R_H - R_0)/R_0$ where, R_H and R_0 are resistance in the presence of field and zero field, respectively. Optical reflectance studies of gold and indium nanowires were carried out in a UV-VIS-NIR spectrophotometer (JASCO, Model V570) in the wavelength range of 190–2500 nm. The specular reflectance of the wires was measured at near-normal incidence (6^o) using an Aluminium mirror as the standard.

2.4 Electric field induced nanostructuring technique

DC electric field has been used as high energy density trigger to achieve nanostructures in bulk silicon wafer surface and the surface of as deposited thin films of nickel, indium, gold and silicon.

(a) Bulk silicon wafer surface

To achieve nanocrystallization of semiconducting silicon wafer, field treatments were carried out on commercially available silicon wafer (after cleaning steps) by the DC voltage source. Semiconductor surfaces of silicon [400] (0.5mm thick, n-type, one side polished) were thoroughly cleaned ultrasonically For nanostructuring silicon surfaces; use was made of DC electric field in the range of 0.1-1.5 kV/cm and sharp electrode pins of tip area, 0.1 mm^2. Electrode pins were kept exactly normal to the semiconductor surface plane. Experimentation with electrode pin separation and time of application of DC electric field were done and clear effects were observed at an optimized distance of 3mm distance of electrode pins and for 20 seconds of application of DC electric field.

(b) Thin films

To achieve nanocrystallization and hence functionalization of PVD thin films (<100 nm) coated on BSG substrates, post deposition nanostructuring has been carried out for thermally evaporated (at ambient temperature in a high vacuum at the base pressure of 1×10^{-6} mbar and a rate of deposition of 0.1–0.4 nm/s) nickel, indium and silicon thin films and DC sputtered (in Argon atmosphere) gold thin films by applying DC electric field in the range 0.1-3.5 kV/cm using APLABS high voltage supply (as shown in Figure 2.7(a)) and commercially available pins. The schematic of the experimental design was as shown in the Figure 2.7 (b).

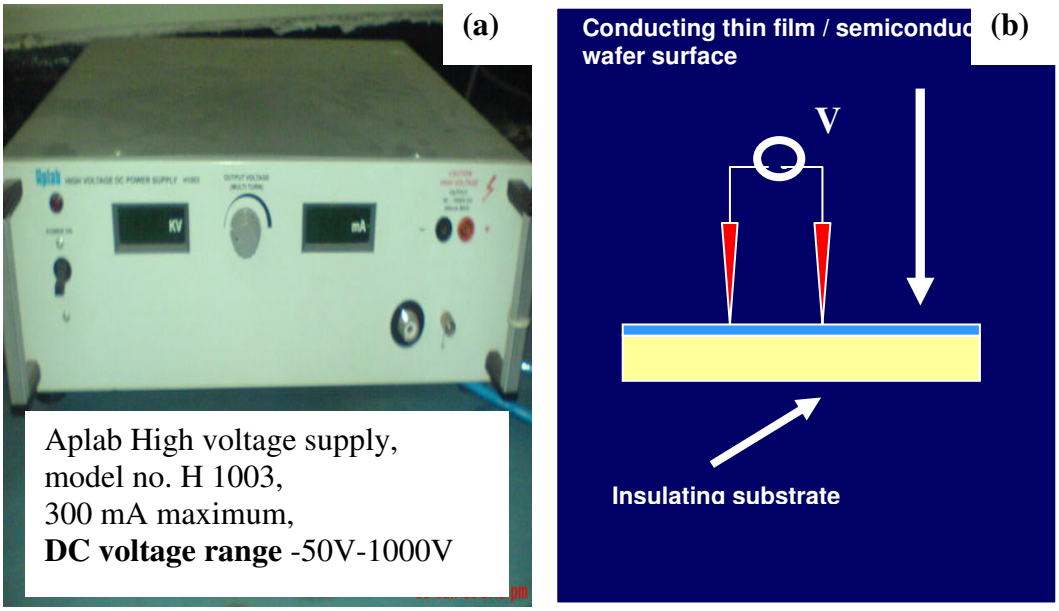

Figure- 2.7 (a) Camera picture of DC electric field source, (b) schematic of electric field induced nanostructuring experiment.

Pure (99.998%, 0.5mm diameter, Sigma Aldrich) nickel and indium wires were placed in tungsten spiral source that was located at a distance of 8–10 cm from the substrates. Si thin film was however coated using silicon granules in a molybdenum boat. Film thicknesses were measured *in situ* using a quartz crystal thickness monitor and confirmed *ex situ* by a surface profilometer (XP-1 of Ambios Technology, USA). After the thin film deposition, pieces were cut from the thin film already coated onto the substrates and cut pieces having all of the same area were then subjected to DC electric field treatments. Various thin films were placed in an electric field (1–3.3 kV/cm) using a DC power supply (APLABS India, model H 10003) between electrode pins having a tip area of 0.1mm^2 and a separation of 2–5mm. The pins are those that are normally employed in two probe measurements using multimeters. Commercially available pins of different tip sizes were used, but only results with tips of area 0.1mm^2 are reported. The effect of the tip area on the nanostructuring is the subject of a separate study. To investigate the effect of the field applied normal to the substrate plane on growth features; the nickel thin film was sandwiched between two silver electrodes as shown in Figure 2.8. A layer of silver paint was applied to the

substrate prior to the deposition of the Ni film. It was partially masked during the deposition of the metal layer. A dot of silver paint of a known area was then applied on top of the Ni film. The Ni layer was thus sandwiched between two silver layers.

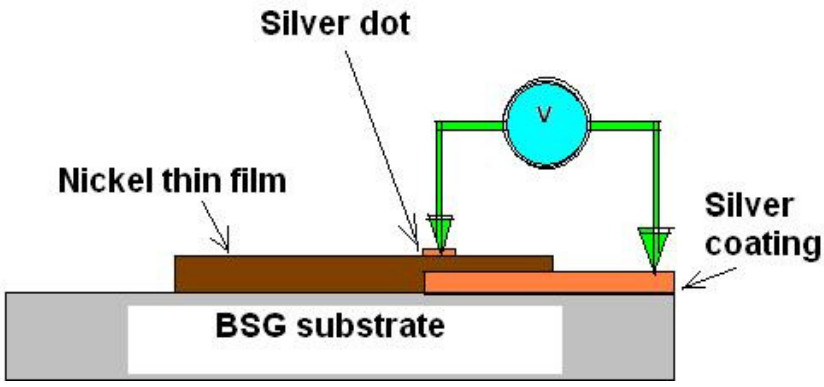

Figure 2.8 Schematic for normal field application

Characterization

The morphology of the field nanostructured silicon surfaces, as-deposited thin films and field nanostructured thin films was determined by using a scanning electron microscope (PHILIPS XL-30 ESEM) as well as an atomic force microscope (SPA 400 of SII Inc., Japan) operating in the intermittent contact dynamic force microscopy (DFM) mode. The crystallographic texture of the films was investigated using an INEL powder x-ray diffractometer equipped with a cobalt target (wavelength = 0.178 nm) and Philips X-ray diffractometer with Cu target (wavelength = 0.154nm). Specular reflection was measured in a UV-VIS-NIR spectrophotometer. Photoluminescence spectra for field nanostructured silicon surfaces were obtained in a Leica laser scanning confocal microscope.

2.5 Laser induced nanostructuring technique

Excimer laser was used as high energy density trigger to nanostructure bulk silicon wafer surface as well as thin films of various materials viz. nickel, indium, gold and silicon.

Bulk silicon wafer

The surface of [311] oriented Silicon wafers were irradiated by a KrF excimer laser (Compex pro 201F of Lambda Physik, Germany with λ = 248 nm, τ = 30 ns and maximum energy of 700 mJ). The silicon surfaces were cleaned ultrasonically in acetone, isopropyl alcohol and distilled water and dried in an oven at 80^0 C for 20 minutes. The incident laser fluence was varied from 0.1 to 5 J/cm^2 by varying the area of the laser spot on the surface and the surface was exposed to a maximum of 1000 shots at each angle of incidence (10^0, 20^0, 30^0, 45^0 and 90^0). The laser beam area was controlled by using a concavo-convex lens as shown in Figure 2.9.

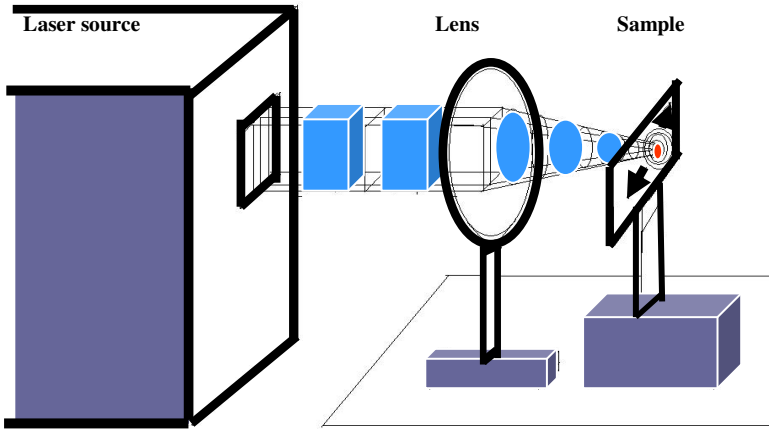

Figure 2.9 Schematic of laser induced nanostructuring experiment

Laser irradiation was carried out below and above ablation threshold of the silicon wafer. A stainless steel blade edge and 30 μm diameter copper wire were employed to mask the irradiation, at 0.15 J/cm^2, to investigate the proximity effect on the morphological reconstruction.

Thin films

Nanoparticulate(10-100nm) thin films of nickel, indium, gold and silicon were coated by PVD routes (In, Si and Ni by thermal evaporation and gold by DC sputtering). Excimer laser was used as high energy density trigger for surface nanostruturing. Pieces were cut from the same thin film after deposition and cut pieces were subjected to various excimer laser fluences and number of shots. To look into excimer laser nanostruturing, KrF Excimer laser (248nm) in unfocussed condition (at laser fluence

0.01-0.05 J/cm^2) was used to irradiate thin indium, gold, silicon and nickel films at normal incidence for upto few tens of shots.

Characterization

To study the spatial spread of the beam, after irradiation, the area of the laser spot was determined using an optical microscope (Olympus Model MX51). The morphology of the laser nanostructured silicon wafer, as deposited thin films and nanostructured thin films was determined by using an Atomic Force Microscope (SPA 400 of SII Inc., Japan) operating in the intermittent contact Dynamic Force Microscopy (DFM) Mode. X-ray diffractometry was carried out in Philips powder X-ray diffractometer equipped with copper target (λ = 1.54Å) and an Inel X-ray diffractometer (CPS 120 of Inel, France, with Cobalt target, λ = 1.78 Å). Specular reflectance spectra were acquired in UV-VIS-NIR spectrophotometer, Jasco International, model-V-570. Leica laser scanning confocal microscope was used for photoluminescence measurements on laser nanostructured silicon surface.

2.6 Characterization Instruments

(a). **X-ray diffractometer**

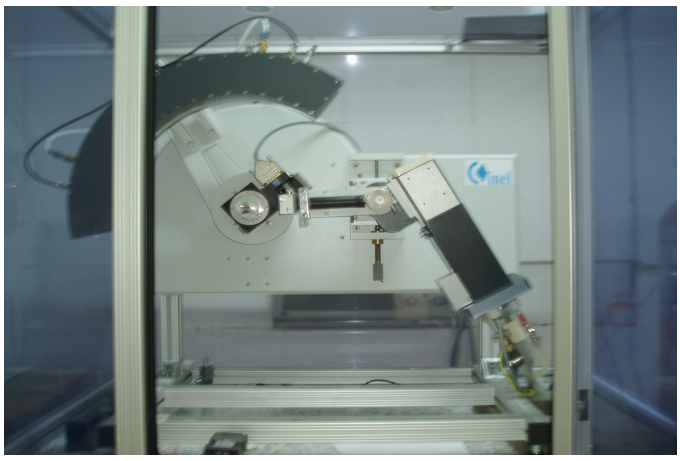

Figure - 2.10 Photographic image of X-ray diffractometer

X-ray diffractometry was done with Inel powder X-ray diffractometer with Cobalt K_α line and also with Philips powder X-ray diffractometer with Copper K_α line**.** In the first instrument, detector is available at each position and therefore detection occurs

always and this instrument is quite useful for thin films where counts are usually very less and are comparable to the noise level. A silicon standard was used for calibration to take into account instrumental broadening.

Average crystallite size

Scherrer's formula was used to calculate the average crystallite size. $a = (k \lambda) / (\beta \text{ Cos } \theta)$ where k = 0.94, λ = 1.78Å, β is the full width at half maximum in radian and θ is the angle of incidence. β is calculated from the given x-ray diffraction data. For the XRD peak, first position of the peak is determined accurately and then full width at half maximum as illustrated in Figure 2.11.

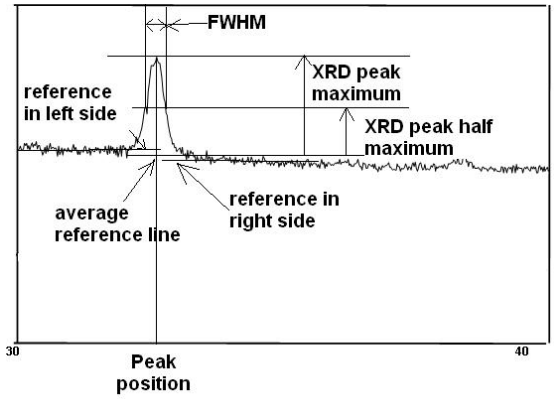

Figure 2.11 determination of crystallite size from XRD data.

Residual strain

The reasons of strain in the sample usually are the preparation conditions which do not allow the system to relax. For getting unstrained thin films, lattice matching between the thin films and substrates, matching of coefficient of thermal expansion of both the thin film and substrate material and of course high substrate temperature conditions. If all the conditions are fulfilled, films grow layer by layer epitaxially on the substrate and films are quite strain free. When any of the above condition is not fulfilled, films grown show some strain which might have various origins. In such cases, instrumental broadening has to be taken care of. Due to strain in thin film or bulk, inter-planar spacing changes effectively and therefore the peak position shifts

and peak becomes more and more asymmetric as compared to the unstrained sample. The residual strain was calculated, from formula

$\epsilon = (\Delta d)/d = (d - d_{bulk}) / d_{bulk}$,

d has been obtained from XRD peak position by using the formula

$d = n\lambda / 2 \sin\theta$

where d is the interplanar spacing.

(b) <u>Scanning Electron microscope</u>

Scanning electron microscope (Figure 2.12) uses secondary electrons for imaging purposes. By applying a current through the filament, thermionic emission of electrons can be achieved. The generated electrons are focussed in front of an anode and to move the electrons down the column, a voltage difference between the tungsten filament and the anode is applied. This voltage difference is called the accelerating voltage and can be varied between 0.2 and 40 kV determining the energy and wavelength of the electrons within the beam. The beam of electrons is condensed and focussed as a fine spot on the specimen by 2 to 3 electromagnetic lenses located in the microscope column. Upon interaction of the electron beam with the sample, various signals (secondary electrons, back scattered electrons and x-rays) are produced and can be detected. The secondary electron detector detects low energy electrons produced near the surface of the specimen providing a predominantly topographical image.

Figure- 2.12 Photographic image of scanning electron microscope

(c). Atomic force microscope

Atomic force microscope (AFM), whose parts are as shown in Figure-2.13, can measure the vertical deflection of the cantilever with pico meter resolution by using an optical lever. The optical lever operates by reflecting a laser beam off the cantilever. Angular deflection of the cantilever causes a twofold larger angular deflection of the laser beam.

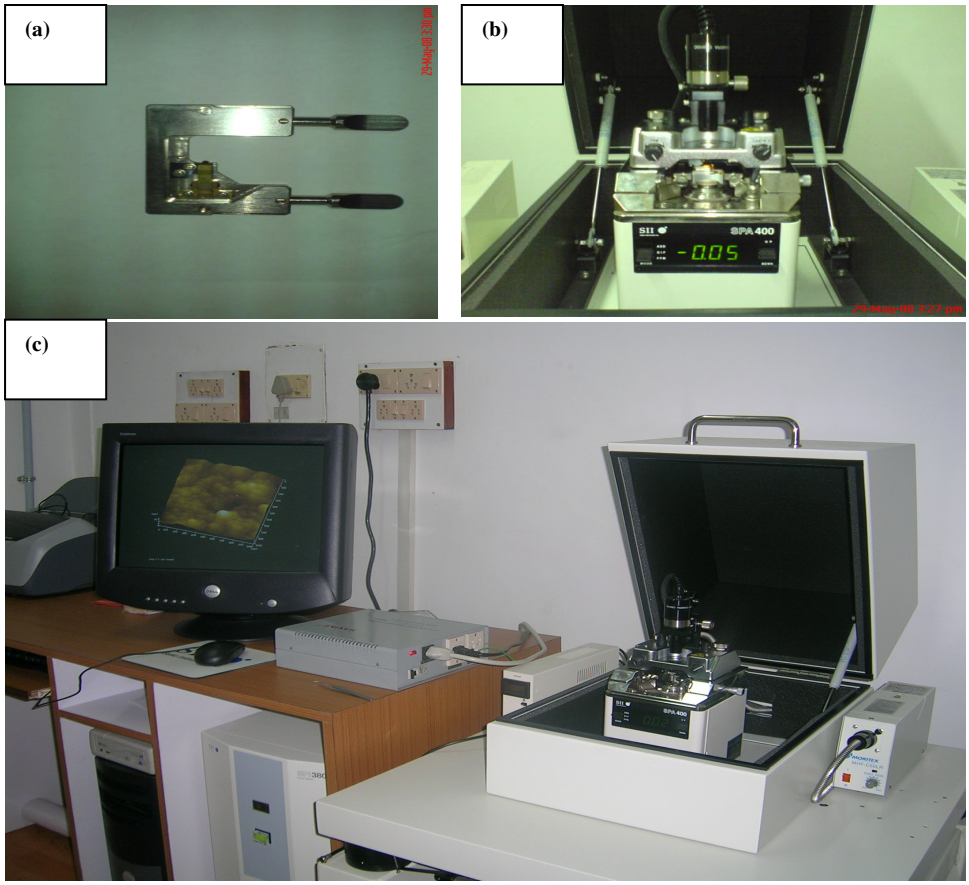

Figure-2.13 Scanning probe microscope (a) tip holder, (b) sample stage and chamber, (c) SPM with display.

The reflected laser beam (as shown in Figure- 2.14) strikes a position-sensitive photodetector consisting of two side-by-side photodiodes. The difference between the two photodiode signals indicates the position of the laser spot on the detector and thus the angular deflection of the cantilever. Since the cantilever-to-detector distance generally measures thousands of times the length of the cantilever, the optical lever greatly magnifies motions of the tip. The flexible cantilever exerts lower force to sample thus less distortion and less damage. AFM cantilevers have generally spring

constant less than 0.1 N/m. Higher the resonance frequency of cantilever, faster and better the imaging. To obtain both low spring constant and high frequency (>2 KHz), the mass of cantilever should be very small ~ 10^{-10} Kg.

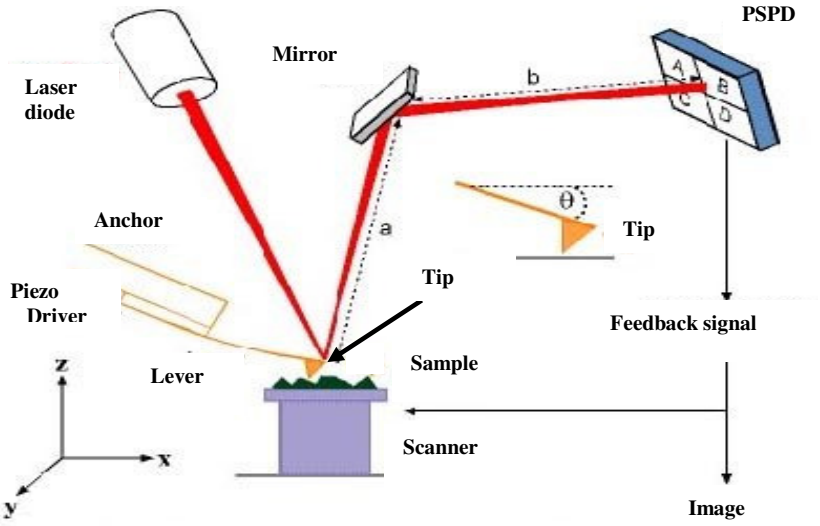

Figure- 2.14 Schematic of scanning probe microscope

AFM is very much vulnerable to noise. The power line (50 Hz) and higher harmonics of it are predominant noise sources. The AFM can not image true surface in such a case. Reduction of vibration of any kind is the most important factor in determining the image quality. Even though one can remove noise from image by using Fourier Transform (FT), there will be significant loss of information. In addition the tip will be blurred out and so called "end radius" will increase and the resolution becomes poor. Sometimes the noise can be tackled by using oblique angle of scan. Faster scan (20 scan per second) picks less noise in Contact Mode but also gets less information of surface. Scan Rate 5 or 10 Hz is preferable. For very rough surfaces, Z-height mode of imaging is preferable.

Comparison between AFM and DFM mode

Scanning probe microscope can be used in contact as well as non-contact mode (as shown in Figure- 2.15), accordingly it is termed as AFM or DFM. AFM can give good images for very small nanostructures as compared to DFM, but DFM is a better

tool for slightly rough samples. In DFM mode SPM tip remains safe for long time due to non-contact.

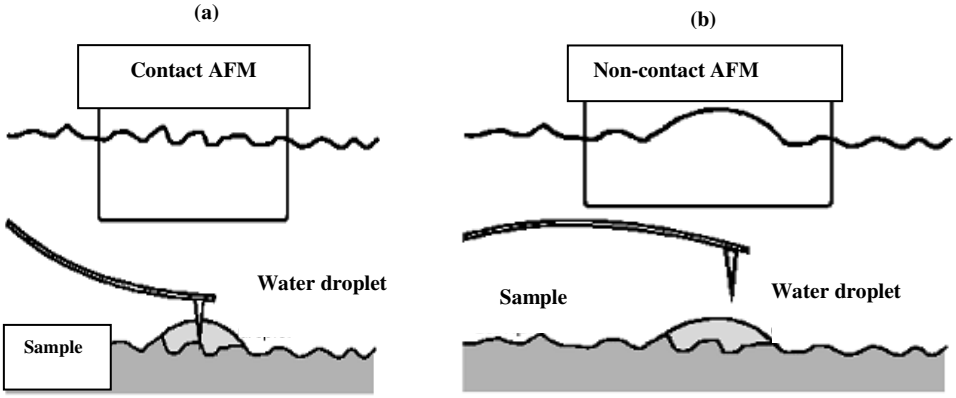

Figure 2.15 Modes of operation of scanning probe microscopy, (a) contact mode, (b) non-contact mode.

Phase imaging

When running in Wave Mode using amplitude feedback with a fixed resonant frequency, a phase-shift signal is generated (as illustrated in Figure- 2.16) and this can produce image contrast - and we call this scan mode as Phase Contact Mode (PCM). The exact nature of the interaction mechanism that creates the phase shift signal is uncertain; however, one mechanism almost certainly involves sticking of the probe to the surface, causing a delay time in the cantilever resonance pattern, relative to before the instant that the tip makes its brief contact. There is a lot of current interest in Phase Mode. Much of the work has been done with heterogeneous mixtures of polymers, which tend to respond well to PCM because; the modulus properties of the polymer are readily resolved. Phase Mode can yield results that are similar in appearance to Lateral force microscopic mode (LFM); however, PCM is generally more sensitive in producing meaningful image contrast. Furthermore, PCM seems to produce image contrast on a greater variety of sample types than does LFM.

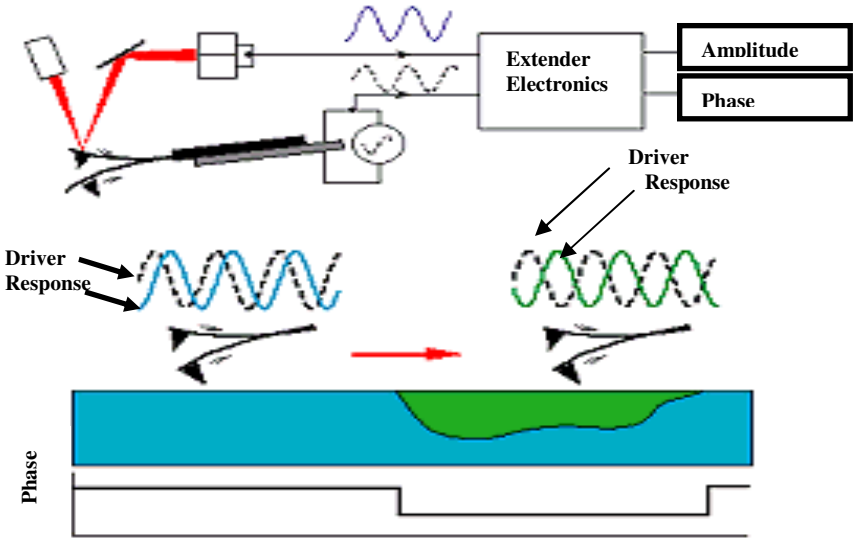

Figure 2.16 Phase imaging principle

Average grain size, standard deviation in grain size, Root mean square roughness, aspect ratios of grains etc. are statistically determined from the line profiles [as shown in schematic in figure 2.17 (b)] taken on the atomic force images (Figure 2.17(a)). Very large numbers of grains are considered (usually 100 or more) to achieve better values of statistical averages.

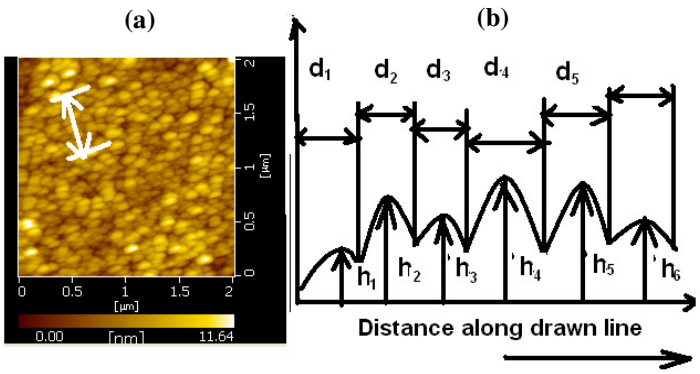

Figure 2.17 (a) A typical AFM image, (b) schematic of line profile.

(d). UV-VIS-NIR spectrophotometer

The optical study of a thin film is mainly concerned with the physical phenomena like transmission, absorption, reflection and also the interaction of photon energy with matter and consequent changes in electronic states. The reflectance (at 6^0 angle of incidence) of the films were measured using a UV-VIS-NIR double beam spectrophotometer (as shown in Figure 2.18(a)) with an accuracy of ±0.2 nm. Before recording the spectra, a 100% base line was established by performing the back correction. The wavelength range of the instrument was 190 to 2500 nm. The specular reflectance curves were taken using an aluminum mirror (provided by the supplier) as the reference. UV-VIS-NIR spectrophotometer (as shown in Figure- 2.18(a)). A three dimensional view of spectrophotometer is shown in Figure 2.18(b). A reference beam is usually required for quantification of reflectance/absorbance (as shown in Figure 2.18(c)). A simple spectrophotometer consists of a source of radiation (hydrogen lamp), a double beam monochromator of grating-to-grating type, which disperses the light so that only a limited band of wavelengths is allowed to irradiate the sample and a photo multiplier tube serves as a detector. Spectrophotometer (JASCO Model V-570 whose schematic line diagram is shown in Figure 2.19) was used for measuring reflectance spectra predominantly. Reflection minima for an opaque surface correspond to absorption maxima. Therefore, for metallic thin films at particular wavelengths where no ripples/humps are expected otherwise; if reflectance spectra show minima, it usually symbolizes plasmonic peaks. Plasmonic peak in metallic thin films are signature of the material concerned. For thin films in particular, plasmonic peak usually shifts with preparation parameters like thickness (due to change in dimensionality), substrate temperature and rate of deposition (due to the change in packing density) etc. In the context of present thesis, with the application of external trigger like electric field and Excimer laser, grain size and grain shape has change and therefore it is expected that these surface feature changes will have effect on plasmonic peak.

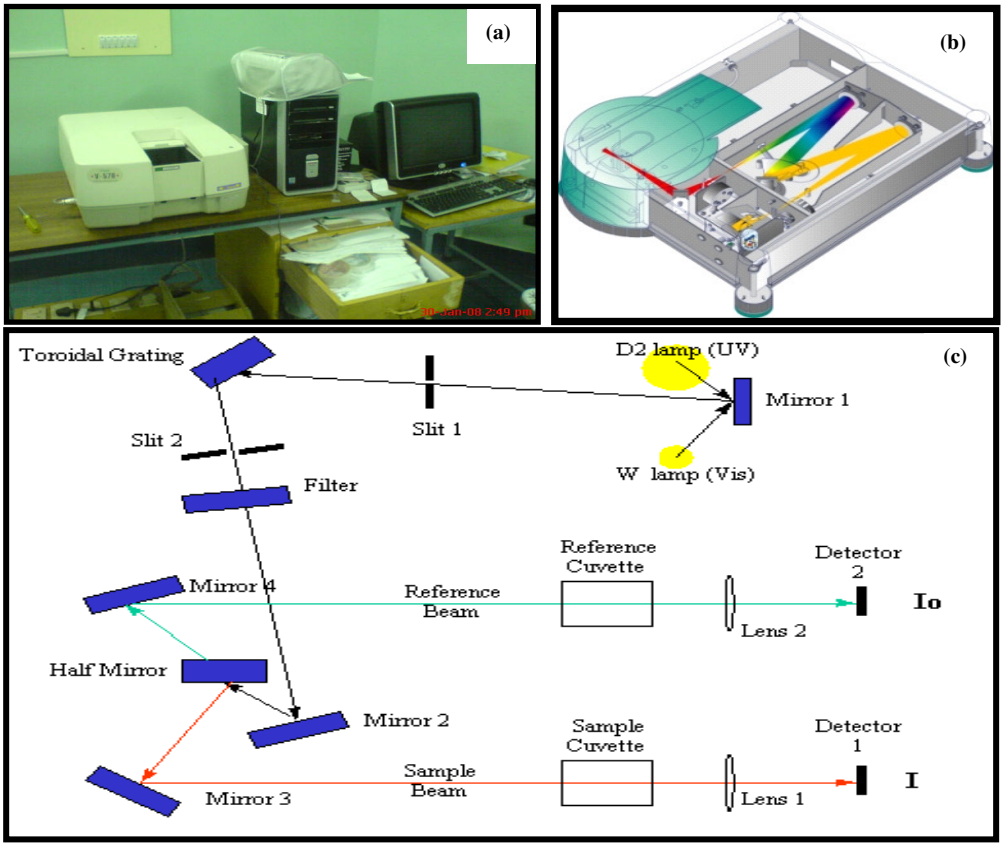

Figure 2.18 UV-VIS-NIR spectrophotometer, (a) Photographic image, (b) 3D image showing cross section, (c) usual schematic of reference and sample beam.

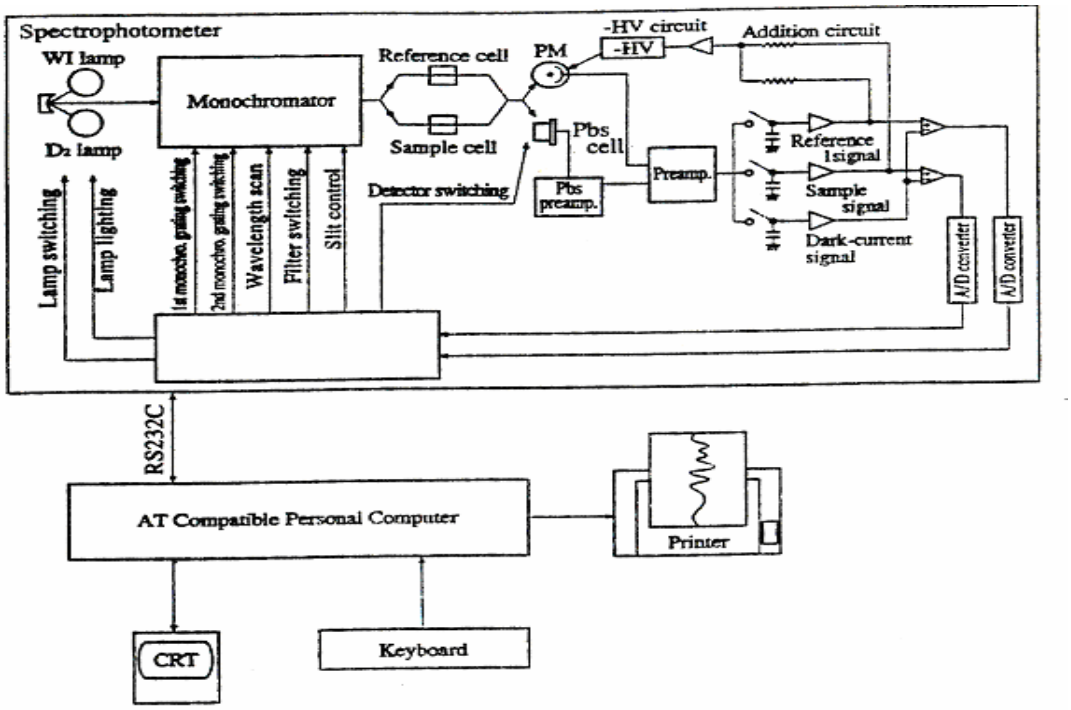

Figure- 2.19 Line diagram of UV-VIS-NIR spectrophotometer (Jasco model V-570).

(e). **Laser scanning confocal microscope**

In a confocal laser scanning microscope (Figure 2.20), a laser beam passes through a light source aperture and then is focused by an objective lens into a small (ideally diffraction limited) focal volume within a fluorescent specimen. A mixture of emitted fluorescent light as well as reflected laser light from the illuminated spot is then recollected by the objective lens. A beam splitter separates the light mixture by allowing only the laser light to pass through and reflecting the fluorescent light into the detection apparatus. After passing a *pinhole*, the fluorescent light is detected by a photodetection device (a photomultiplier tube (PMT) or avalanche photodiode), transforming the light signal into an electrical one that is recorded by a computer.

Figure- 2.20 Photographic image of laser scanning confocal microscope

The detector aperture obstructs the light that is not coming from the focal point, as shown by the dotted gray line in the image. The out-of-focus light is suppressed: most of the returning light is blocked by the pinhole, resulting in sharper images than those from conventional fluorescence microscopy techniques, and permits one to obtain images of various z axis planes (also known as *z stacks*) of the sample. Confocal microscopy provides the capacity for direct, noninvasive, serial optical sectioning of specimens with a minimum of sample preparation as well as a marginal improvement in lateral resolution.

(f). <u>Vibrating sample magnetometer</u>

Quantitative information about magnetization was achieved from Vibrating Sample Magnetometer (Lakeshore Cryotronics, Model no.7400) (as shown in Figure 2.21 (a)) having sensitivity in the range of μemu. Air-gap between magnets is fixed at 3 cm and for low magnetic moment samples (μemu), high time constants that permit lower field sweeping rate were used. The changes in flux caused by the vibrations are translated into a change in current in pick-up coils of the instruments, which registers a particular magnetization.

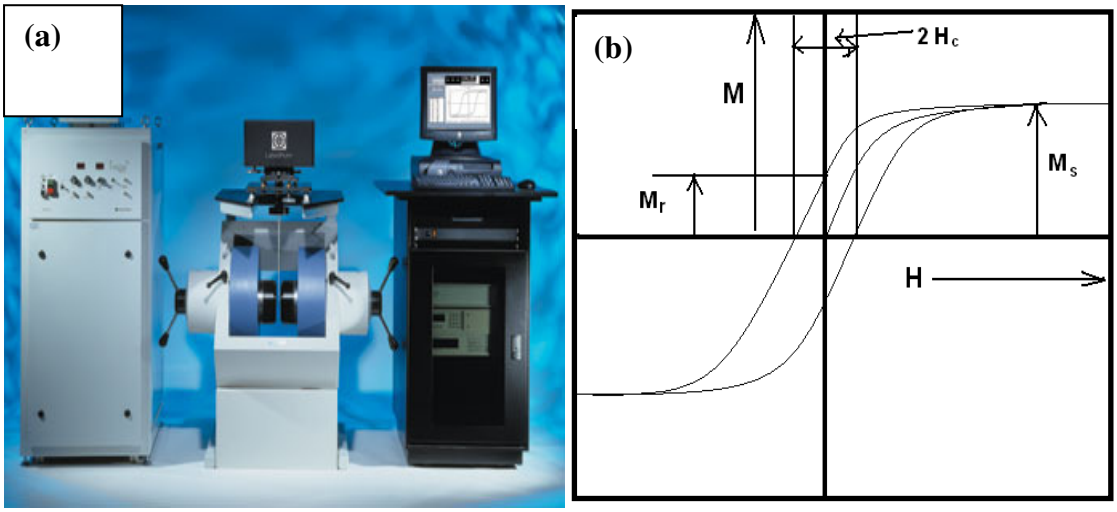

Figure- 2.21 (a) Camera picture of Vibrating sample magnetometer, (b) introduction of various parameters derived from hysteresis loop.

To achieve large signal to noise ratio, we have taken large area of the sample covering total area of sample holder. A field limit of +/- 0.5 T in the steps of 0.005 or 0.01 T was adopted to achieve better accuracy. Volume of the thin film has been calculated as the product of the area of the film coated on the substrate and the thickness measured in surface profilometer.Magnetic moment per unit volume is magnetization. Hysteresis plots (M vs. H) were taken in parallel orientation of films. Saturation magnetization (M_S), coercive field (H_c) and Remainence (M_r) are defined as illustrated in Figure 2.21 (b) for a given magnetization hysteresis loop. We have plotted M_S / M_S (Bulk), where M_S (Bulk) refers to the saturation magnetization for the bulk nickel having value 470 emu / cc.

(g). Ferromagnetic Resonance spectrometer

Ferromagnetic resonance spectroscopy (FMR) (as shown in Figure 2.22), a form of electron spin resonance spectroscopy, can serve as a rapid technique for assessing the magnetic anisotropy of and magnetostatic interactions between individual particles in a polycrystalline sample. It is based upon the Zeeman effect, which is the splitting between electron spin energy levels that occurs in the presence of a magnetic field. The Zeeman effect allows a ground-state electron to absorb a photon with energy equal to the splitting between the energy states.

Figure- 2.22 Ferromagnetic resonance spectrometer

In a magnetic material, magnetic anisotropy (whether magnetocrystalline, shape, or stress-induced) and interparticle interactions contribute to the energy of the particles within a sample and thereby alter the resonance energy. As a result, FMR can be used to probe these parameters. Resonance field is very sensitive to magnetic anisotropy of the material and therefore resonance field values are the first indicators of magnetic anisotropies.

(h). Magneto resistance measurement

At higher magnetic field resistance of a material usually drops down and the percentage reduction as compared to the original one is called magnetoresistance. Usually electromagnet (as shown in Figure 2.23(a)) is used as a source of magnetic field and a four point probe (as shown in Figure 2.23(b)) kit is utilized for resistance measurements.

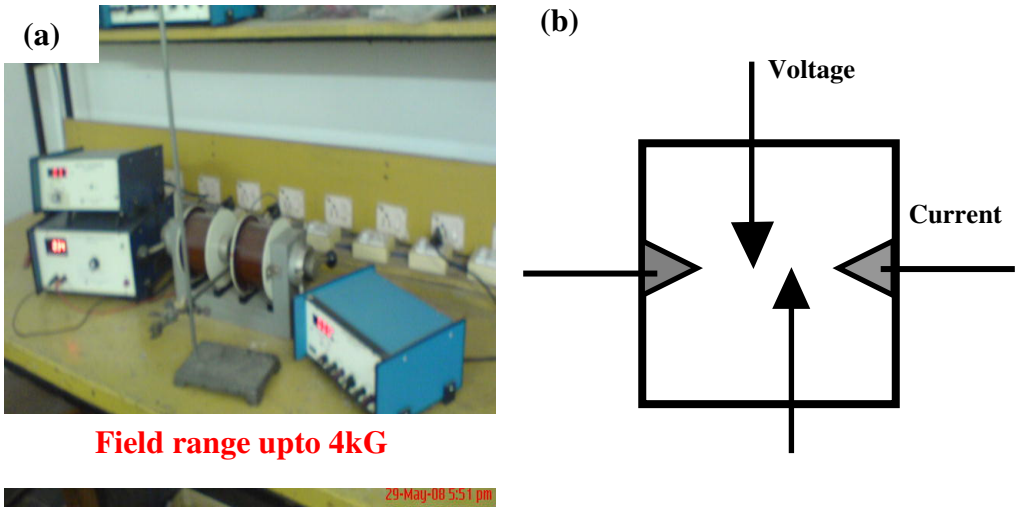

Figure- 2.23 Magnetoresistance measurement kit, (a) Experimental set up and (b) schematic of measurements.

Magnetoresistance is usually represented in terms of percentage and is the fractional change in the resistance value when the sample is inserted in a magnetic field. The value of magneto resistance, its sign and its slope with the magnetic field can reveal a lot about magnetization reversal property, which is dependent on preparation parameters and other factors.

R = dV/dI

MR (%) = [(R_F – R_0) /R_0] x 100.

Chapter-3

Results and discussions

Abstract:

This chapter deals with the results of the investigations on surface nanostructuring by various non-lithographic techniques carried out as part of this thesis. Judicious selection of preparation parameters (thickness, substrate material, substrate temperature and rate of deposition) has yielded assembled growth in the form of isolated nanodots, organized nanodots, nanoparticle clusters and various other useful nanostructures. Physical properties are found to be strongly dependent on nanostructure shape and size. V-trench templated growth of condensate has given growth in the form of organized nanodots and nanowires. Surface plasmonic behaviour for gold and indium case and magnetic behaviour for nickel case has been found to be quite strongly affected by the lower dimensionality. Excimer laser irradiation of amorphous thin films has made them nanocrystalline accompanied by surface plasmonic peak shifts. In the case of single crystal silicon, a transition to nanocrystalline phase is observed with the appearance of photoluminescence. DC electric field as a high energy density trigger has been used to nanostructure thin films and bulk silicon and it was observed that application of field also yields effects similar to that of the laser as far as nanocrystallization of amorphous thin films and nanocrystallization of single crystal silicon surface is concerned. However, one major significant effect with DC electric field has been observed is that, it can give rise to anisotropic growth in field direction.

Section 3.1

Controlled early stage of thin film growth

3.1.1 Resistive thermal evaporation

Abstract

Nanostructuring by controlling growth at early stages of thin film deposition is demonstrated in this section. It is shown that the film-substrate interfacial energy and the wettability of the condensate molecules on different substrate surfaces can be exploited to realize different nanostructures. Thin films of Ni were grown on to Borosilicate Glass (BSG), silicon (311), MgO (001) substrates by thermal evaporation. The effect of process parameters on the resulting nanostructures is investigated. The deposited films were in the thickness range of 10-500 nm. The effect of thickness, substrate and substrate temperature has been studied. Phase contrast microscopy revealed that the grain sizes increase from a value of 30 –50 nm at ambient temperature to 120-150 nm at 503 K and remain approximately constant in this range up to 593K. The existence of grain boundary walls of width 30-50 nm is demonstrated using phase contrast images. The grain boundary area also stagnates at higher substrate temperature. There is pronounced shape anisotropy as evidenced by the increased aspect ratio of the grains as a function of substrate temperature. Nickel thin films of 50nm show the absence of long-range crystalline order at ambient temperature and a preferred [111] orientation at higher substrate temperatures. The crystallite size, coercive field and magnetization energy density first increase and achieve a maximum at a critical value of thickness and decrease thereafter. There is a transition from nanocrystalline to crystalline order that causes a peak in the coercive field in the region of transition as a function of thickness and substrate temperature. The saturation magnetization on the other hand increases with increase in substrate temperature.

[A] Introduction

Elemental nickel and nickel based thin films are extremely important for a variety of magnetic applications [1-11]. The scaling down of thin film based devices requires the deposition of these films to lower and lower thicknesses, thereby throwing up new challenges in terms of the evolution of microstructure and structure and the properties of interest, both electrical and magnetic. It is known that the early stages of thin film formation, i.e. in the thickness range of 5 to 50 nm, is very sensitive to the processing techniques and parameters used [12-19]. The microstructural and structural parameters that influence the performance of magnetic devices involving thin (5-50 nm) films include surface roughness, crystallographic texture, morphology, shape anisotropy, grain size and shapes. The influence of substrate temperature on the growth and magnetic properties of thin films has been studied intensively and it has also been established that properties such as coercivity, remanence, and saturation magnetization are strongly dependent on the microstructure, crystallographic texture and the processing parameters under which the films are deposited [20-31]. There are, however, some issues for which experimental evidence is still lacking. For example, there is very little evidence for the grain and grain boundary evolution in the early stages of Ni film formation. The critical thickness for crystallization of Ni is also not very clear. The role of the film-substrate interface in determining the magnetic properties of the films is also not well understood.

The objective of the present work therefore is to establish the nature of grain growth at thickness of the order of 50 nm, the existence (or the lack) of a critical thickness for crystallization and the strain and roughness profile for Ni films grown by evaporation on to BoroSilicate Glass (BSG), Si (111) and MgO (001) substrates at ambient and elevated temperatures. A correlation with magnetic behaviour of the films is also made. Phase contrast microscopy is demonstrated as a viable technique for monitoring the grain boundary evolution in very thin films.

[B] **Results and discussion**

(a) **Microstructure**

(i) Effect of thickness

As the thickness of nickel thin films is increased, the surface morphology changes as shown in Figure 3.1. At 50nm thickness the surface consists of features that were isolated nanodots (60-120 nm dia) which became nanoclustered (nanoparticle dia 100-120nm, cluster dia 400-700 nm) at 100nm and transformed to island-like overlayer on a continuous layer at the bottom (with semi major and semi minor axes in the ranges 600-800nm and 300-400nm respectively) at 150nm finally becoming a continuous thin film thereafter. Such a change can be seen only at minimal rate of deposition.

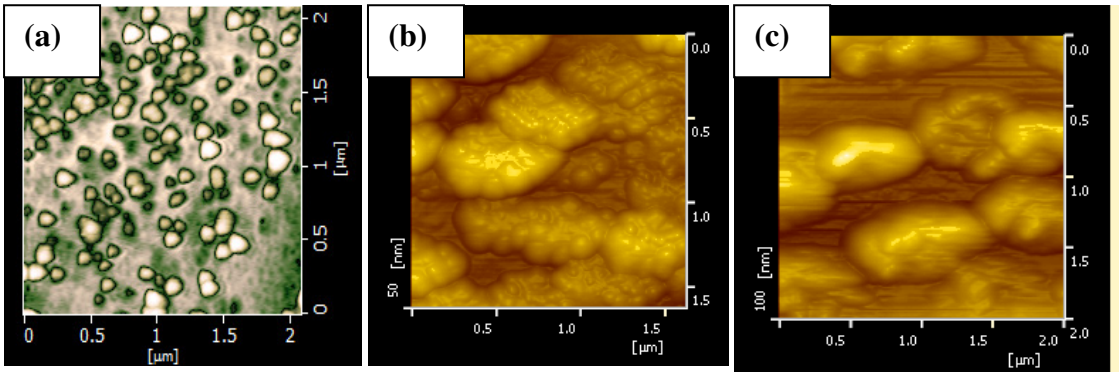

Figure-3.1 Atomic force microscopic images in DFM mode for thicknesses (a) 50nm, (b) 100nm and (c) 150nm

According to Gafner et. al. **[32]**, formation of a cluster structure depends on the cooling conditions usually after the onset of crystallization. It was demonstrated that for slow cooling condition, the FCC lattice of nickel evolves and for the rapid cooling condition icosohedral structure evolves. In the current work, cluster of nanoparticles have been observed for ambient temperature deposition conditions indicating quenching of the vapour molecules on impact with the substrate surfaces. As a consequence, when an island forms, strain will be larger at the rim of the particles due to surface tension effect because of quenching. Therefore, the next particle landing on the substrate will preferentially occupy the rim position and so on, resulting eventually in self-organized growth.

(ii) Effect of substrate material

The role of the substrates in determining the morphological features is shown in figure 3.2 (a), (b) and (c) respectively, for 50nm nickel thin films coated on BSG, MgO and silicon respectively. Figure 3.2(d) shows the microstructural features for 70nm nickel thin film on silicon. Borosilicate glass gives rise to nanoparticulate nickel thin films having a large distribution in particle size while MgO gives rise to columnar kind of growth and silicon substrate interestingly gives rise to self-organization of nanoparticles. Nickel nanoparticles of diameters 80-120 nm have self-organized up to 3-4μm of length on silicon substrate. Further increasing the thickness to 70nm on the silicon substrate, gives rise to the growth of linear chains of average diameter 150-200 nm.

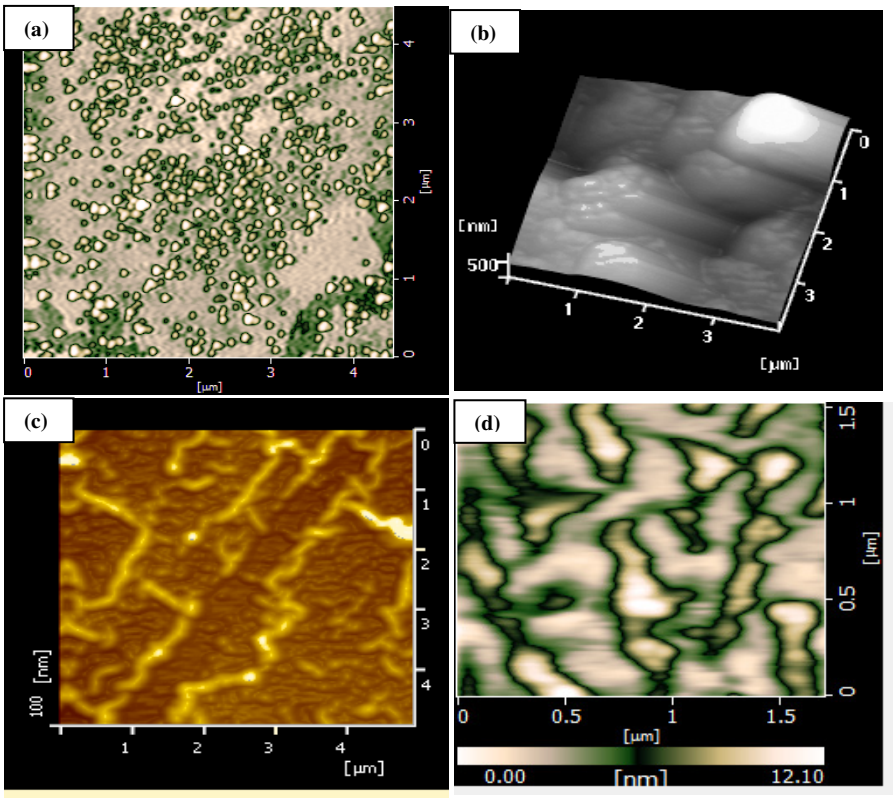

Figure-3.2 Atomic force microscopic images in DFM mode for nickel thin films (a) for 50nm nickel thickness on BSG substrate, (b) 50nm thickness on MgO substrate, (c) 50nm thickness on Silicon substrate and (d) 70nm thickness film on Silicon substrate.

Fujikawa et. al. [**33**] have proposed that the interaction of nickel clusters and the support surface regulates the nickel thin film feature size. Hence, as observed here,

the selection of the support surface plays a dominant role in determination of the organization shape.

Although the precise mechanism of the long particle chain formation is difficult to be clarified, it is most likely related to the heteroepitaxial processes in the Ni / $NiSi_2$ system. The grains comprising the Ni epilayer have a cubic lattice with a lattice constant equal to that of $NiSi_2$, i.e., the Ni film grows mechanically strained. It follows from the classical theory of heteroepitaxy that the strain energy increases linearly with the film thickness until the latter reaches some critical value, which is a function of the lattice mismatch between a film and a substrate. Above this critical thickness, the strain energy exceeds the sum of substrate surface energy and the interface energy and is released via rapid and spontaneous structural changes. The way in which the relaxation process occurs also depends greatly on the details of lattice mismatch. At 70nm thickness of nickel on the silicon substrate, fragmentation of organized assembly as compared to that for 50nm deposition on silicon substrate indicates that the organization process is strain mediated. Moreover, apart from apparent fragmentation, flattening of the features also reveal the same.

(iii) Effect of substrate temperature

The microstructural evolution of the Ni films coated onto glass substrates at elevated substrate temperatures was investigated by means of Dynamic force microscopy both in the topography (figure 3.3(a) to (d)) and phase contrast (figure 3.4(a) to (d)) image modes. For ambient temperature (RT) deposited thin films, spherical particles of average diameter of 30-50nm are visible (Figure-3.3(a)) with a clear island like microstructure. At 503K substrate temperature, spherical particles of diameter 100-120nm form (Figure-3.3(b)). At 543K-substrate temperature, the grain size is in the range of 120-150nm (Figure-3.3(c)) that further increases to result in elongated grains with average diameter of approximately 150nm (Figure-3.3(d)) at 593K substrate temperature. The effect of increasing substrate temperature is therefore to increase the grain size of the films and cause densification resulting in a completely continuous film.

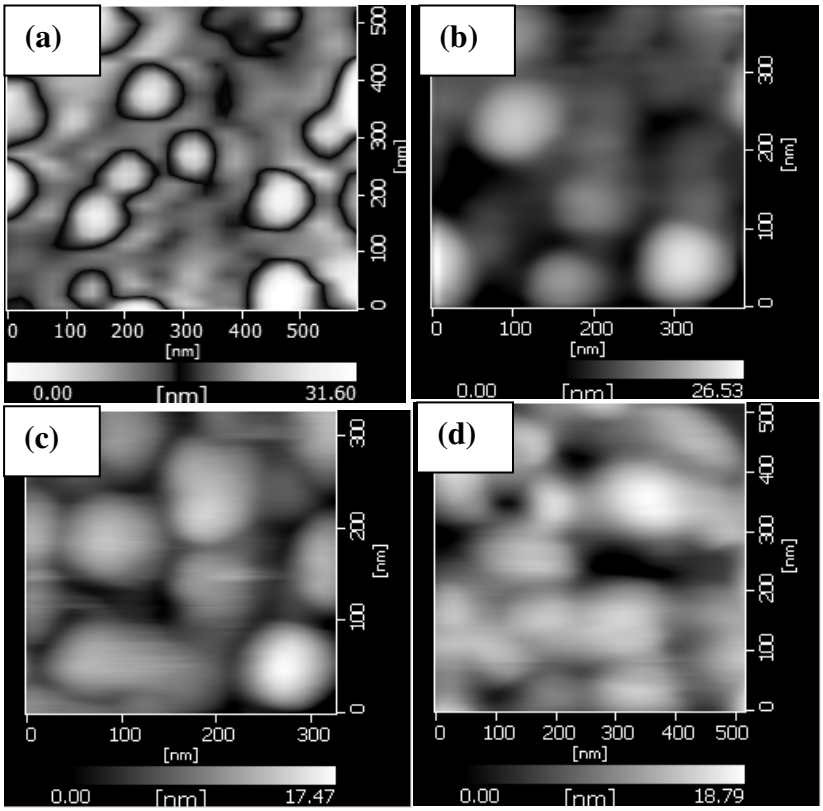

Figure-3.3 Atomic force microscopic topographical images for 50nm thin film coated at different substrate temperatures for substrate temperatures (a) RT, (b) 503, (c) 543 and (d) 593 K respectively.

The phase contrast images for these films reveal the microstructural evolution much more explicitly. Figures 3.4(a) to (d) correspond to the phase contrast images of the films deposited at temperatures from RT to 593K and are for the same samples shown in figures 3.3(a) to (d). It is evident that at ambient temperature the island like structure also has discontinuities that are of the order of the size of the grains. As the substrate temperature is increased, the increase in grain size is evident, but another interesting feature that is also revealed is that the width of the grain boundary walls decreases as a function of the increase in substrate temperature. The grain boundary walls have been indicated on the images. It thus follows that, as the substrate temperature is increased not only is there an increase in the grain size but there is also an increase in the ratio of the grain to grain boundary area that is the primary reason

for densification of the films. At room temperature, the grain boundaries are 20-40nm thick with a corresponding grain size of 30 to 50 nm. At 593 K substrate temperature while the grain size is 150nm or greater, the grain boundaries are between 20 to 50nm (Figure-3.4(d)).

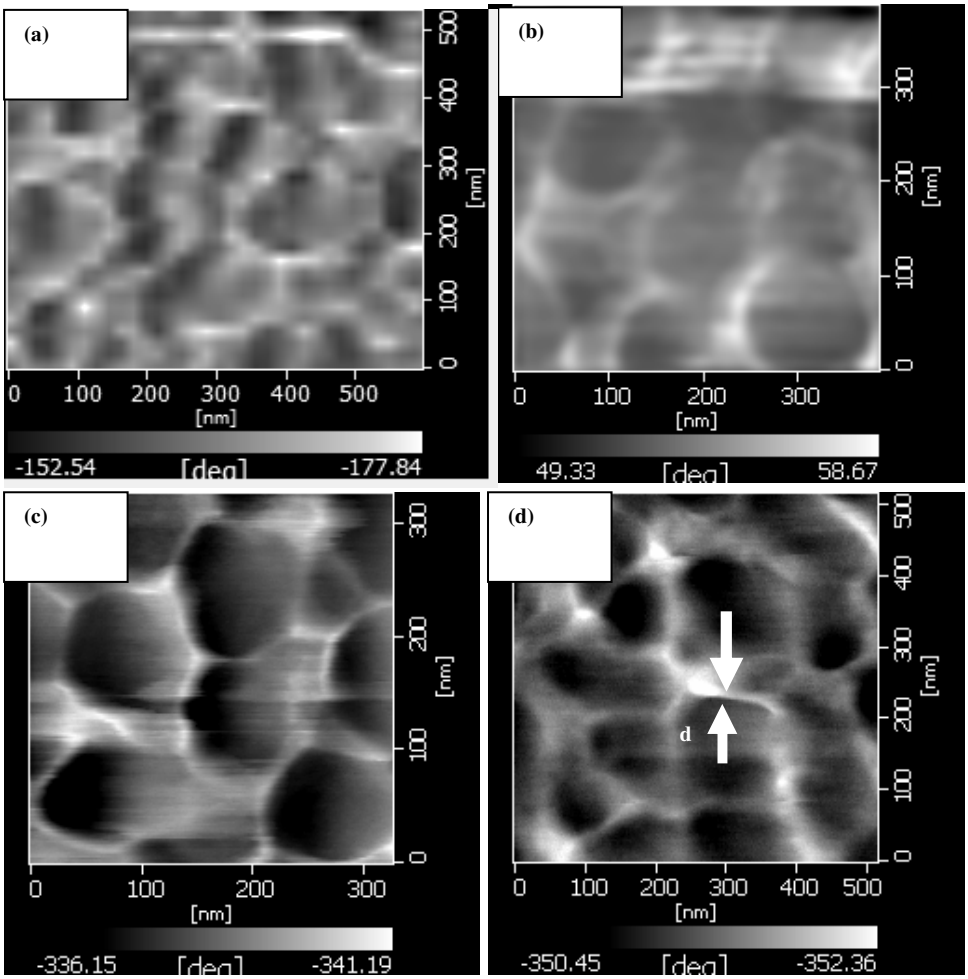

Figure-3.4 Atomic force microscopic topographical images for 50nm thin film coated at different substrate temperatures for substrate temperatures (a) RT, (b) 503, (c) 543 and (d) 593 K respectively.

The observations of thin film growth at elevated substrate temperature are in qualitative agreement with models proposed for grain growth and preferred texture in thin films as well as their experimentally observed impact on magnetic properties [**34-35**]. For example it has been proposed [**34**] that when the nuclei grow as spherical-cap-shaped islands, they will be surrounded by a zone of width d, in which any atom deposited on the substrate surface within a distance d, of a pre-existing island will

diffuse to that island and become part of it instead of becoming part of a new nucleus. The width, d, is a function of substrate temperature and the rate of deposition. The observed microstructure in the present case clearly provides evidence for the existence of this diffusion width in the form of grain boundary walls as shown in figure 3.4. Other models **[35]** predict the stagnation or retardation of grain growth observed in the present case. The stagnation is due to the competition between and minimization of the driving forces for grain growth, which include grain boundary, surface and elastic- strain energies. As observed in the present case it has been proposed that the intrinsic stress will be very large in the initial stages of growth and relaxation will be observed as substrate temperature increases for a given thickness. Interestingly, it has been shown that the predominantly [111] texture for FCC metal thin films is possible due to surface energy minimization at high substrate temperatures whereas the [100] texture dominates at lower substrate temperatures. This is also in qualitative agreement with the results of the present study.

(b) <u>Long range crystalline order</u>

(i) Effect of thickness

The XRD patterns of Ni films of thickness ranging from 90 nm to 500 nm on BSG substrates are shown in figure 3.5(a). The 500 nm nickel film exhibits peaks representing four planes namely, [111], [200], [220], [311] that are observed at thicknesses down to 130 nm. However, for the 90nm film only one peak representing the plane [111] is visible, which is no longer observed at 50 nm.

(ii) **Effect of substrate material**

The XRD patterns of nickel films of thickness 50nm, on different substrates have been shown in figure 3.5(b). On all the substrates viz. silicon, MgO and glass substrates, films are amorphous at 50nm thickness.

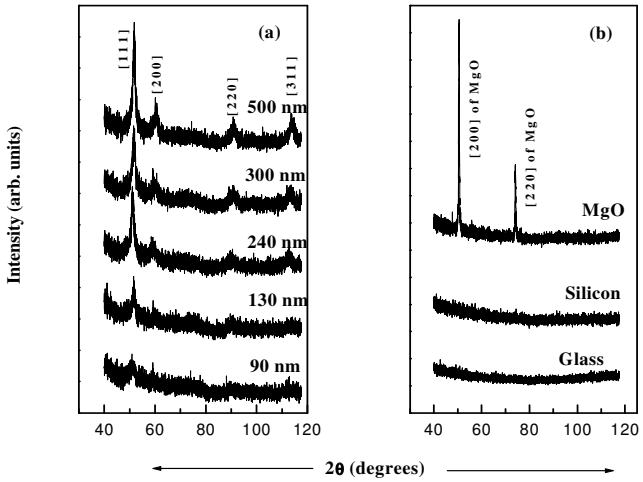

Figure-3.5 XRD of nickel thin film coated on glass substrate for the thickness of coating (a) different thicknesses, (b) 50nm film on different substrates.

The transition from crystallinity to nanocrystallinity is exhibited over a window of thickness where there is large variation in crystallite size and some volume of the material is amorphous.

(iii) Effect of substrate temperature

XRD patterns of the films deposited at ambient, 503, 543 and 593K substrate temperatures respectively are shown in Fig. 3.6. The figure clearly shows the evolution of long-range order at relatively higher substrate temperature. For example, at the substrate temperature of 503K, one peak corresponding to [111] appears (Figure-3.6 (b)) and at 543K, the two peaks namely [111], [200] appear (Figure-3.6(c)) with the [200] peak being relatively lower in intensity. The predominantly [111] texture is retained even at 593 K substrate temperature. The absence of long-range orders even at substrate temperature as high as 723K for 50 nm thick Fe-Ni films has been reported earlier. On crystallization, the films in that study also exhibited a predominant [111] texture [**36**]. In the present study, long-range order is

established only for substrate temperatures $\geq$ 503K as evidenced from the x-ray diffraction patterns. Grain size too increases as the substrate temperature is increased to 503K. From 503K to 593K substrate temperature, grain size as well as crystallite size both increase and residual strain reduces, and as a consequence coercive field is reduced, as discussed later.

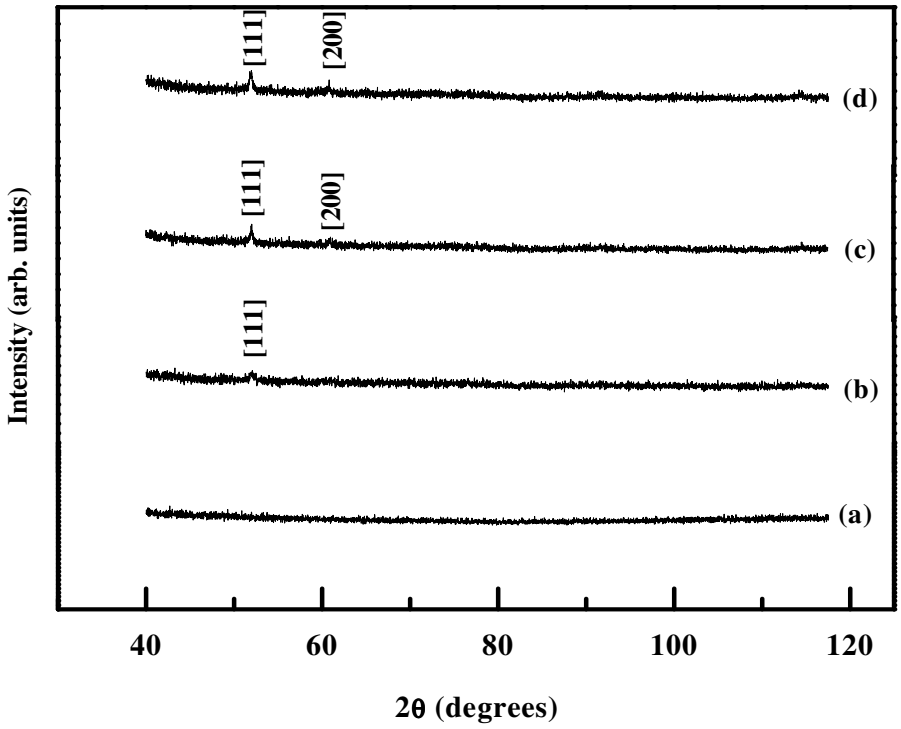

Figure-3.6 XRD of nickel thin film coated on glass substrate at substrate temperatures (a) RT, (b) 503K, (c) 543K and (d) 593K.

(c) Magnetic properties

(i) Effect of thickness The VSM hysteresis loops for nickel for different thickness are shown in figure 3.7(a). It is observed that the coercive field reduces to zero, as the thickness of nickel film is decreased.

(ii) Effect of substrate material Figure-3.7(b) represents hysteresis loops of 50 nm nickel films on different substrates. The coercive field for the films on the glass is lower than those for the films on silicon and MgO substrates. This may be due to the better short-range order of the films deposited on the crystalline substrates.

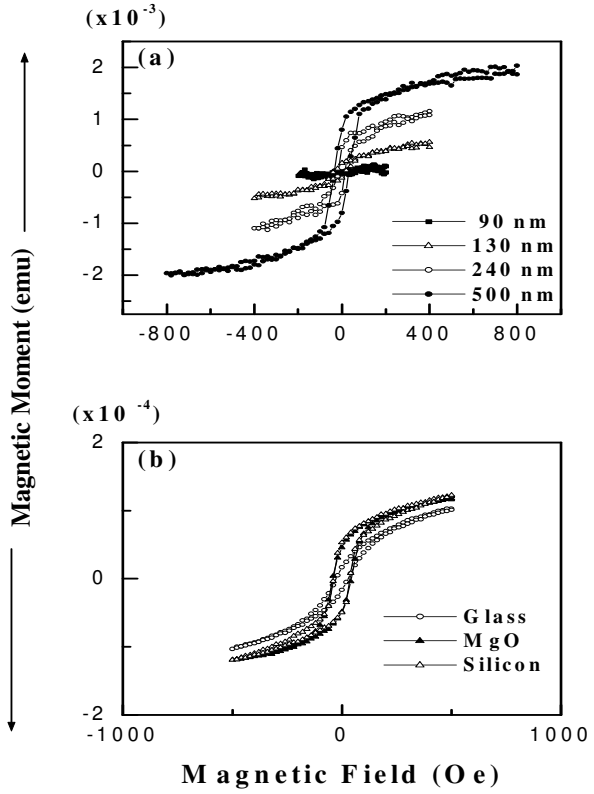

Figure-3.7 Hysteresis loops for nickel thin films (a) of different thicknesses and (b) of thickness 50nm deposited onto different substrates.

(iii) Effect of substrate temperature

From the VSM hysteresis loops (figure 3.8) recorded for films deposited at various substrate temperatures it can be observed that coercive field first increases with increase in substrate temperature from RT to 503K (fig. 3.8 (a) to (c)) and then decreases with the rise of substrate temperature up to 593K (Figure-3.8(d)). The normalized saturation magnetization is enhanced and saturation field is reduced at elevated substrate temperature. Clearly at RT and up to 503 K substrate temperature,

the thin film is completely in the nanocrystalline region, but on further increase in substrate temperature it makes a transition to the crystalline region (long range order evolves), causing a decrease in the coercive field beyond 503 K substrate temperature, symbolizing crystalline magnetic behaviour.

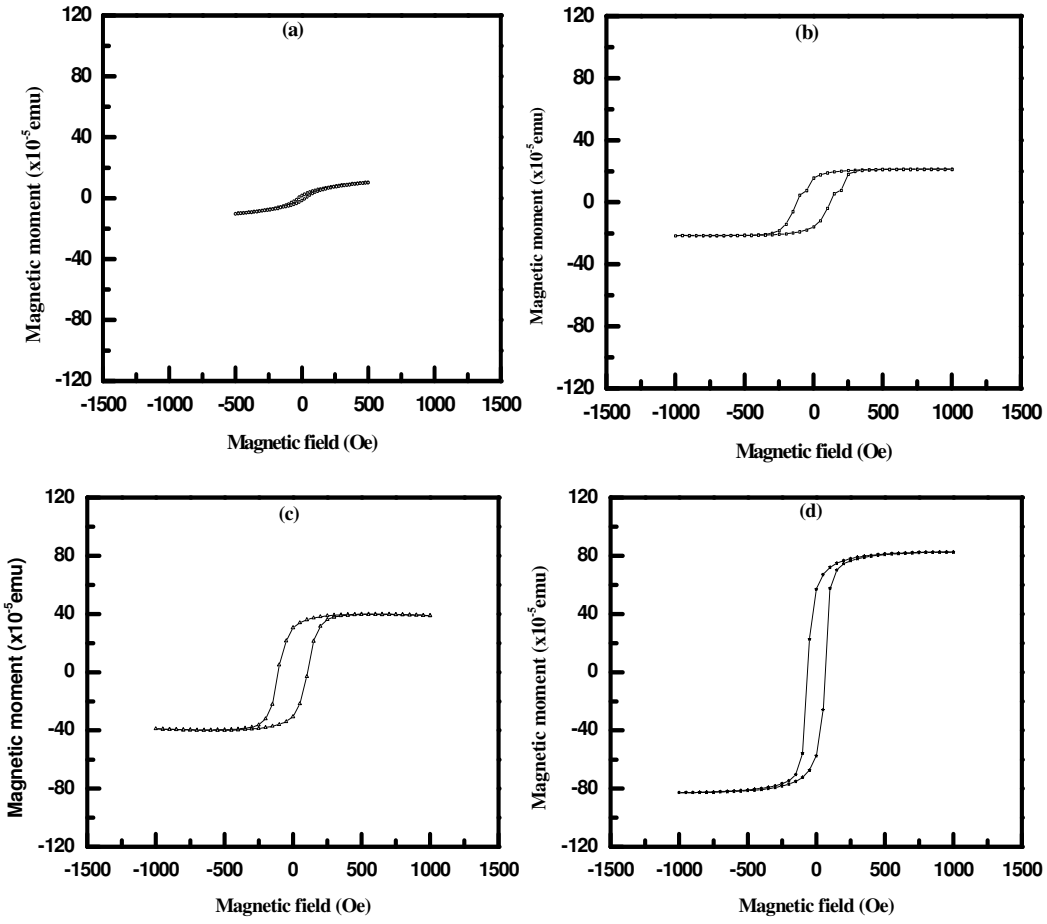

Figure-3.8 VSM hysteresis loops for nickel thin film on glass substrate of same thickness 50 nm at different substrate temperatures (a) RT, (b) 503, (c) 543 and (d) 593K.

(d) Discussion

(i) Variation of thickness

The variation of coercive field, crystallite size and magnetization energy density for nickel films (of thickness range 500 nm to 90 nm) with thickness is shown in figures

3.9 (a), (b) and (c) respectively. Crystallite size is found in the range 5-9 nm. The crystallite size gradually increases with the increases of thickness of the film. However, both coercive field and magnetization energy density first increase and then at large thickness start reducing.

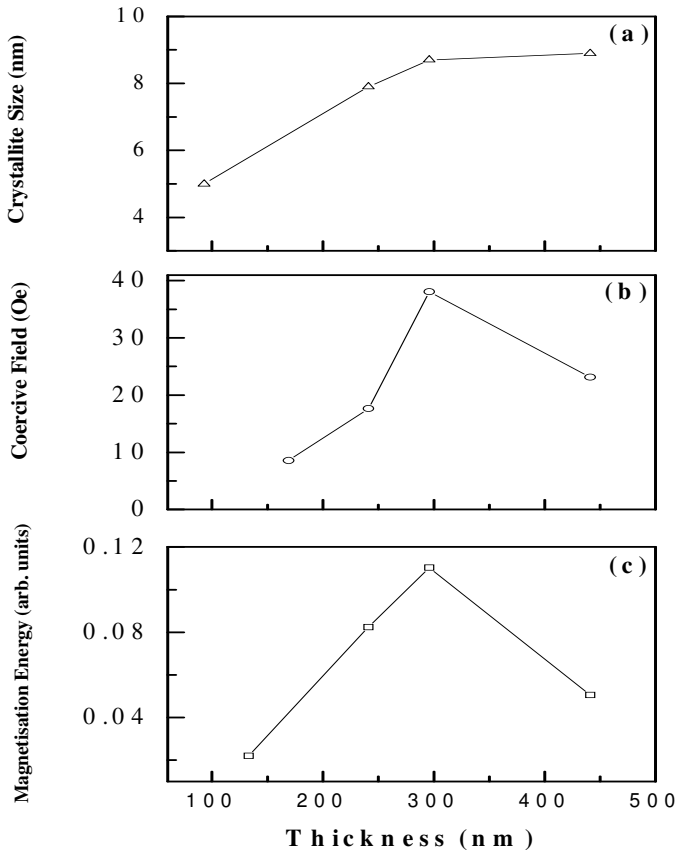

Figure-3.9 **V**ariation with the thickness of nickel thin films, of (a) crystallite size, (b) coercive field and (c) magnetization energy density.

Finite size effects have been examined earlier theoretically **[37]** and experimentally **[38-40]**. Coercive field for thin film varies as $H_{ci}/H_{ci0} = 1 - [D_p/D]^{3/2}$ when its thickness is cut **[41]**, where H_{ci0} is $2K_uV / \mu$ [when T = 0] , K_u is the uniaxial anisotropy constant and V is the volume of the ferromagnet, and D is the diameter of the magnetic particles. Below a critical diameter D_p, coercivity is zero, because of thermal effects that are strong enough to spontaneously demagnetize the previously saturated assembly of particles. However, geometry, finite size effects and structure can all have significant effect on the magnetization response of nanoparticles. The trend in coercive field with cluster size of the films as modeled atomistically by

Zheng [**42]** using Monte Carlo Simulation supports the present results. The crystalline to nanocrystalline transition in magnetic behaviour due to size effect has been illustrated and explained earlier [**31, 43]**. Nanocrystalline magnetic behaviour is expected in Island Metallic Films (IMF) while crystalline magnetic behavior is expected in Continuous Metallic Films (CMF). There is, however, no sharp division of these two regimes viz. IMFs and CMFs.

(ii) Variation of substrate temperature

The trends of crystallite size, grain size, and surface roughness, coercive field and normalized saturation magnetization as a function of the substrate temperature is shown in Figure 3.10. Crystallite size increases with the increase of substrate temperature while coercive field too increases up to 503K and then decreases. Saturation magnetization increases with the substrate temperature very slowly up to 503K and rapidly thereafter. Surface roughness (RMS) increases from 0.73 nm to 3.42 nm while substrate temperature rises from RT to 593K. This result is in agreement with the report [**44]** on microstructural growth of Cu thin films with the substrate temperature.

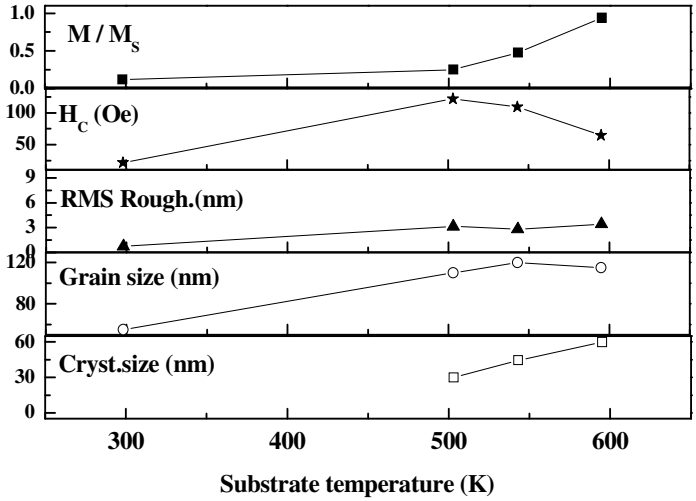

Figure-3.10 Variation of crystallite size (nm), grain size (nm), RMS roughness, coercive field and normalized saturation magnetization vs. substrate temperature for 50 nm thin films

Residual strain increases with the decrease in thickness (Figure 3.11). Similar large strain has been reported earlier [**45]** at this thickness range for RT deposition conditions. As the substrate temperature increases to 593K, the residual strain is negligibly small indicating that the system is more relaxed at higher substrate temperature.

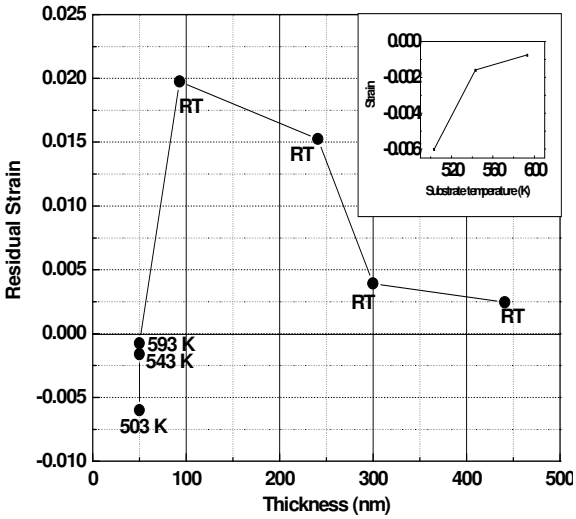

Figure-3.11 Residual strain vs. thickness and substrate temperature for 50 nm thin film, inset is residual strain vs. substrate temperature.

3.1.2 Pulsed laser deposition

Abstract

Ultrathin films (6-10nm) of Silver and nickel were deposited by pulsed laser deposition (PLD) in high vacuum (1 x 10^{-6}mbar). Microstructural evolution of these films as function of incident laser energy, substrate temperature, substrate material (borosilicate glass, fused silica, MgO (100) and Si (311)) and target-substrate distance was studied in detail using Dynamic force microscopy. It is shown that with increase in laser energy incident on the target there is a substantial increase in particle size in the film. The effect of increased laser energy on microstructure is much more drastic than that for the increase of substrate temperature. In general, denser packing of nanoparticles and increased extent of clustering has been observed at elevated substrate temperature. Higher laser energy gives rise to higher average grain size, higher packing density and higher extent of clustering. It is observed that the aspect ratio is dependent on incident laser fluence, substrate temperature but more drastically on the substrate material. Substrate coverage and aspect ratio of the grains are particularly dependent on the nature of crystallinity of the substrates.

[A] **Introduction**

Pulsed laser deposition (PLD) was first conceived as a technique to aid in the synthesis of multicomponent and complex materials in thin film form.[**46-50]**. The basic process involves the ablation of the target material by a focused pulsed-laser beam. PLD is, for many reasons, a versatile technique. Since, in this method, the energy source is located outside the chamber, the use of ultrahigh vacuum (UHV) can be made to deposit ultrathin films with high purity and varying microstructures. In comparison with the more conventional vapor deposition techniques such as sputtering and evaporation, PLD provides additional parameters, i.e., laser energy, repetition rate, and angle of laser incidence, which should, in principle, afford greater flexibility to the process. Though these advantages have been recognized, literature on elemental metallic ultrathin films deposited by PLD is relatively scarce. [**51-55]**

There are no studies on initial stages of growth of metallic films by PLD on different substrates as a function of the ablation parameters and other process variables such as substrate–target distance, substrate temperature, and substrate material. These investigations assume importance since the number of devices based on complex oxides such as ferroelectrics, superconductors, and colossal magnetoresistance materials are on the increase. It is, therefore, inevitable that PLD will have to be considered as the processing tool for devices involving complex materials. This, in turn, would imply that the other components of the multilayer device structures, such as the metal electrodes, would also have to be deposited by PLD. As the thickness of the layers decrease to submicron and nanometer ranges, the role of interfaces and process parameters in the microstructural evolution and physical properties of these ultrathin metallic films has to be understood in detail.

The motivation, therefore, was to investigate the early stages of microstructural evolution of high vacuum pulsed laser deposited Ni and Ag thin films as a function of laser ablation parameters like incident energy and repetition rate and process variables such as substrate temperature, substrate type, and substrate– target distance. Dynamic force microscopy, which is the intermittent contact form of atomic force microscopy, has been used as the probe for studying the microstructure. A detailed correlation between the process variables and microstructure is presented.

[B] **Results and discussion**

(a) Nickel ultrathin films

(i) Effect of thickness

The effect of duration of deposition at constant laser energy of 92 mJ on Ni films was first investigated, and the results are shown in the form of topographical AFM images in DFM mode in Figure. 3.12(a)–3.12(c). Since the films were thin, corresponding phase contrast images (Figure 3.12(d)-(f)) resolved the morphological features better than the topographical images. It is evident from Fig. 3.12(a) that particles cluster at a shorter duration (20 min), and therefore the thickness is not as great (6 nm). This evolved into a film with continuous features with nanopores at greater thickness of 12 nm [Figs. 3.12(b) and 3.12(c)].

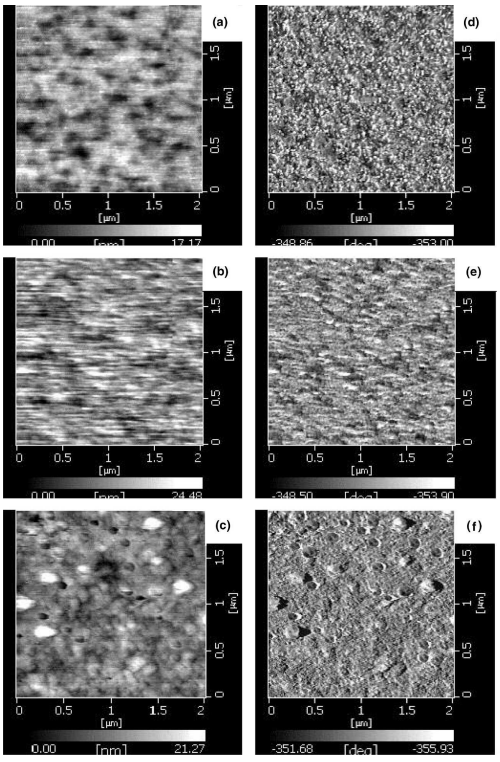

Figure 3.12 (a–c) Topographical images for nickel films deposited at incident laser energy of 92 mJ at RT at 8 Hz repetition rate 6, 8, and 10 nm, respectively.

(ii) **Effect of substrate temperature**

The effect of substrate temperature on 6-nm nickel films, varied from ambient temperature to 573K, on the microstructures is shown in Figs. 3.13(a)–(f). The

topography is shown in Figs. 3.13(a)–(c) while the corresponding phase contrast images are presented in Figs. 3.13(d)–3.13(f). At 373K, the films continue to exhibit the nanocluster behavior as observed for the ambient temperature deposited films [Fig. 3.12(a)]. The phase contrast images also reveal the presence of thin grain wall boundaries with increasing temperature due to the densification of the films. Clearly, surface coverage is a thermally activated process due to the greater adatom mobility at higher substrate temperatures.

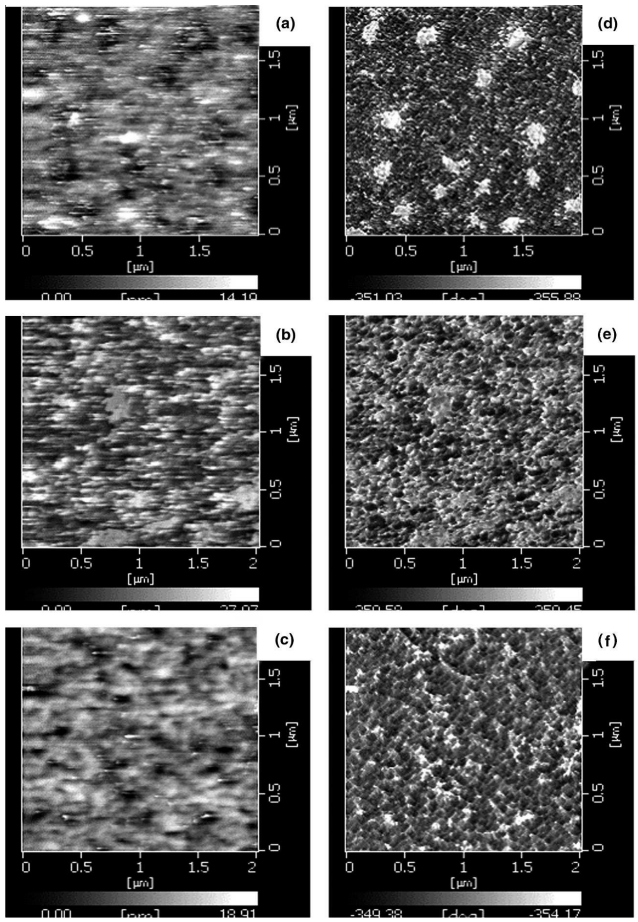

Figure- 3.13. (a–c) Topographical images for nickel films laser ablated at 92 mJ at 8 Hz repetition rate at 373, 473, and 573K, respectively; (d–f) corresponding phase contrast images.

(iii) **Effect of laser energy**

The effect of incident laser energy on the microstructural evolution is shown in Figs. 3.14 (a)–(f). The topography is shown in Figs. 3.14(a)–3(c), and the corresponding phase contrast images are presented in Figs.3.14 (d)–(f). The laser repetition rate was kept constant at 8 Hz, and the substrate was BSG in all cases. These images provide

an interesting insight into the microstructure of the films. Higher incident energy, contrary to expectation, did not result in greater densification of the films at ambient temperature. At 168 mJ, the films exhibited a significantly larger amount of clustering, and therefore island like morphology, than the films deposited at incident laser energy of 92 mJ. This can be attributed to the fact that higher laser energy results in higher rates of ablation at the target, and hence the rate of resputtering at the substrate is higher than the rate of deposition.

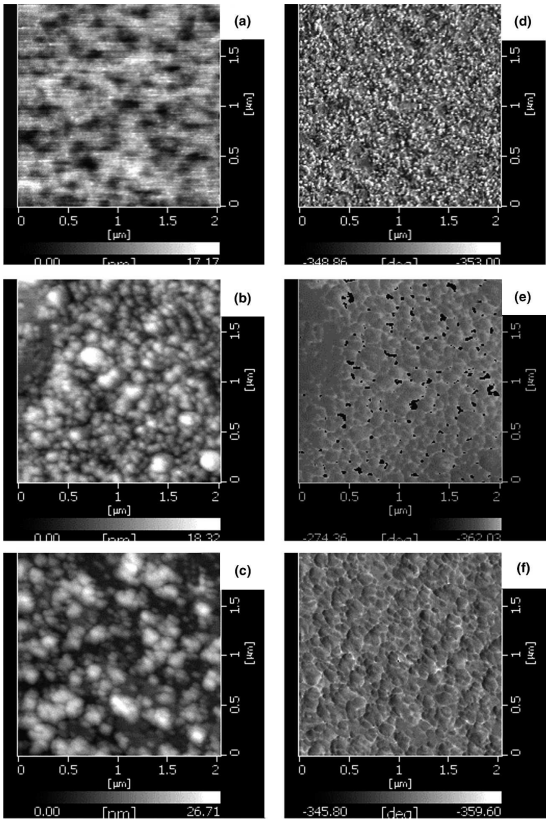

Figure 3.14 (a–c) Topographical images for nickel films laser ablated at RT at 8 Hz repetition rate at 92, 124, and 168 mJ, respectively; (d–f) corresponding phase contrast images.

(iv) Effect of substrate material

The effect of substrates on the growth is represented in Figs. 3.15 (a)–(d) for films deposited on BSG, fused silica, MgO (100), and Si (311) substrates, respectively. It is observed from these topographical images that the wettability of Ni onto different substrates is different, and these results in different kinds of microstructures. All the films were deposited at incident energy of 124 mJ, 8 Hz rep rate, and ambient

temperature. On BSG substrates, the coverage of the film is greater than 50%, whereas on the other three substrates, the coverage was on the order of 10%–20%. On fused silica substrates, the particle shapes were not clear, whereas on MgO and Si, they are spherical. It should be noted that on BSG substrates, the particle shapes are non-spherical.

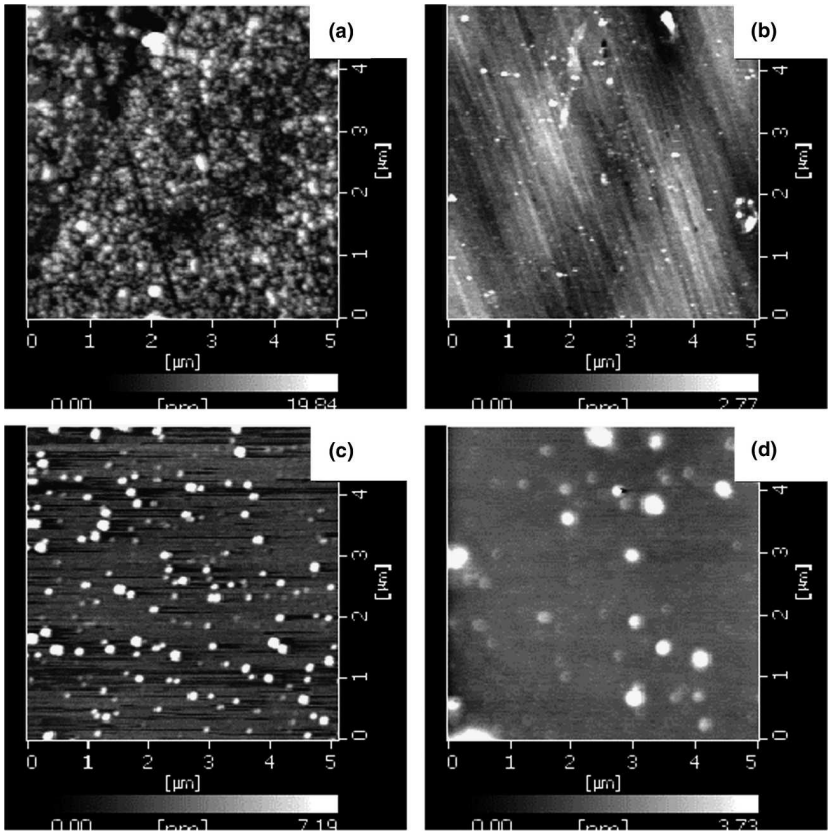

Figure- 3.15 Topographical images for nickel films laser ablated at 124 mJ at 8 Hz repetition rate at RT onto (a) glass, (b) quartz, (c) MgO, and (d) silicon.

(b) <u>Silver ultrathin films</u>

(i) Effect of thickness

To study the effect of thickness on the microstructural evolution for silver thin films, coating was done for 5 min, 20 min, and 1 h on glass substrates at laser energy of 130 mJ, repetition rate of 5 Hz, and ambient temperature deposition conditions. At higher deposition time, film is more clustered (oblate clusters) and larger features are visible. On the other hand, at smaller thickness, relatively smaller and spherical nanoparticles are visible [Figs. 3.16(a)–(f)].

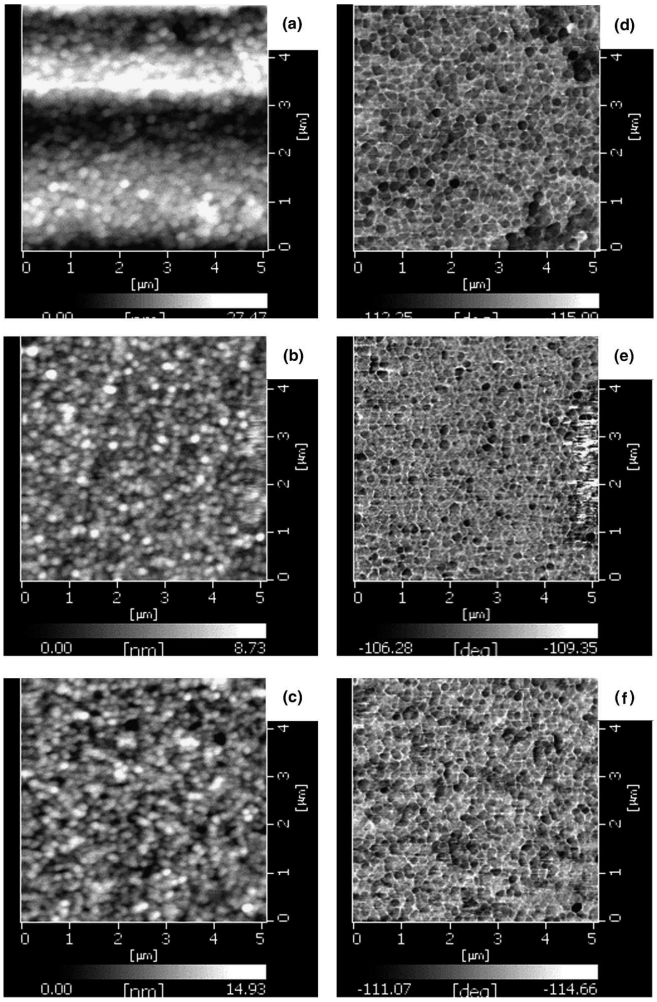

Figure 3.16. (a–c) Topographical images for silver films laser ablated at 130 mJ at 5 Hz repetition rate at RT to thickness of 6, 8, and 10 nm, respectively; (d–f) corresponding phase contrast images.

(ii) Effect of substrate temperature

The effect of substrate temperature on the silver film growth is shown in Figs. 3.17(a)–(f) for films deposited on BSG substrates at 130 mJ laser energy and 5 Hz repetition rate as substrate temperature was varied from RT to 573K. It is observed that as substrate temperature is increased, the packing density of the films increases while retaining the columnar microstructure. The columnar microstructure is evident in topographical images. The phase contrast images [Figs. 3.17(d)–(f)] clearly indicate that densification of the films is accompanied by decrease in grain boundary wall thickness with a degree of clustering. Instead of nanoparticles that grow at

ambient temperature, at higher substrate temperature deposition, large clusters (of average size 500 nm) are formed.

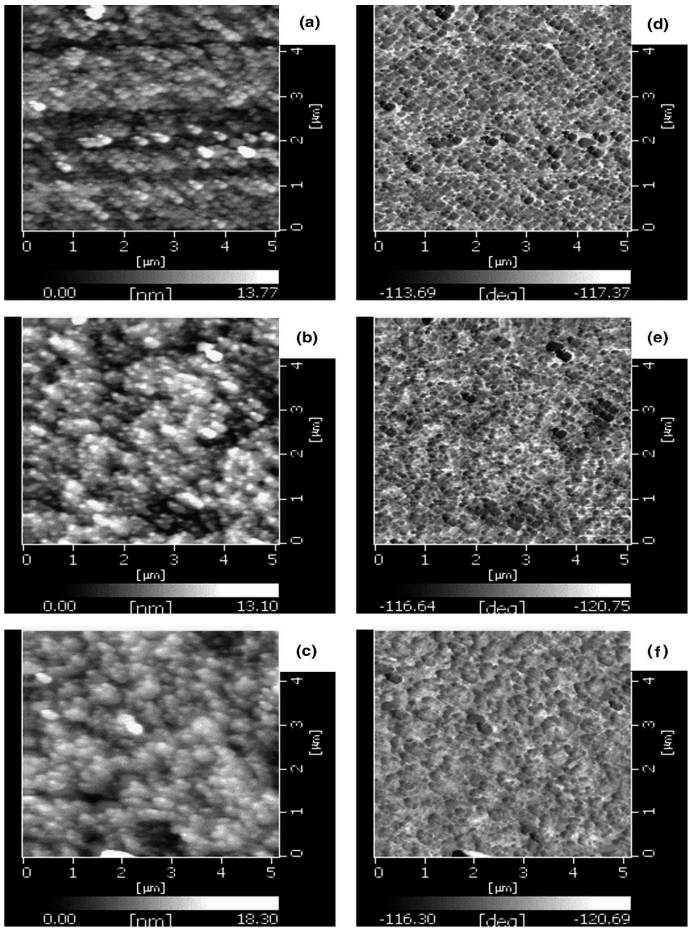

Figure 3.17 (a–c) Topographical images for silver films deposited at 130 mJ and 5 Hz repetition rate at 373, 473, and 573K, respectively; (d–f) corresponding phase contrast images.

(iv) Effect of laser energy

The increase in laser energy variation causes drastic change in microstructure as is evident from Figs. 3.18(a)–(f) for films deposited at RT on BSG substrates. The laser energy was varied from 130 to 500 mJ. It was observed that at 130 mJ laser energy, nanoparticulate films with spherically symmetric nanoparticles were formed, but at higher laser energy, nanoclustering starts and large clusters form. At 500 mJ laser energy, packing density of silver material has been found to be much larger than that for the films deposited at lower laser energy. The phase contrast images in Figs. 3.18(d)–(f) clearly show that porosity decreases, and there is increased clustering of particles as laser energy is increased.

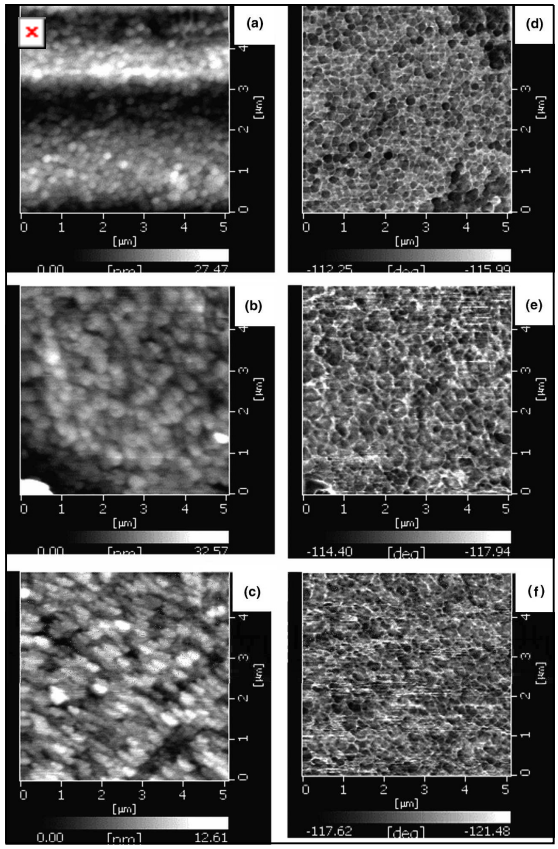

Figure 3.18. (a–c) Topographical images for silver films deposited at 5 Hz repetition rate, at RT substrate temperature and for 130, 350, and 500 mJ respectively; (d–f) corresponding phase contrast images.

(iv) Effect of substrate material

To observe the effect of substrates, films were deposited at laser energy of 132 mJ, 5 Hz repetition rate and ambient temperature onto different substrates, namely BSG, fused silica, silicon, and MgO, and the images are shown in Figs. 3.19 (a)–(d). On MgO and silicon substrates, as in the case of nickel, nanoparticulate thin film growth is visible. Small nanoparticles with large separation (500 nm) are observed on MgO, while coverage was still lower for the case of deposition on silicon and fused silica substrates, but nanoparticle size was almost the same as that on MgO substrate. On BSG substrates, growth was almost continuous with nanoparticles (80–200 nm) making a relatively dense structure. It is evident that the differences in wettability of the metal to the substrate surfaces cause the variation in microstructures. Interestingly,

there is a large difference in wettability of silver onto fused silica and BSG, although both are SiO2-based substrates.

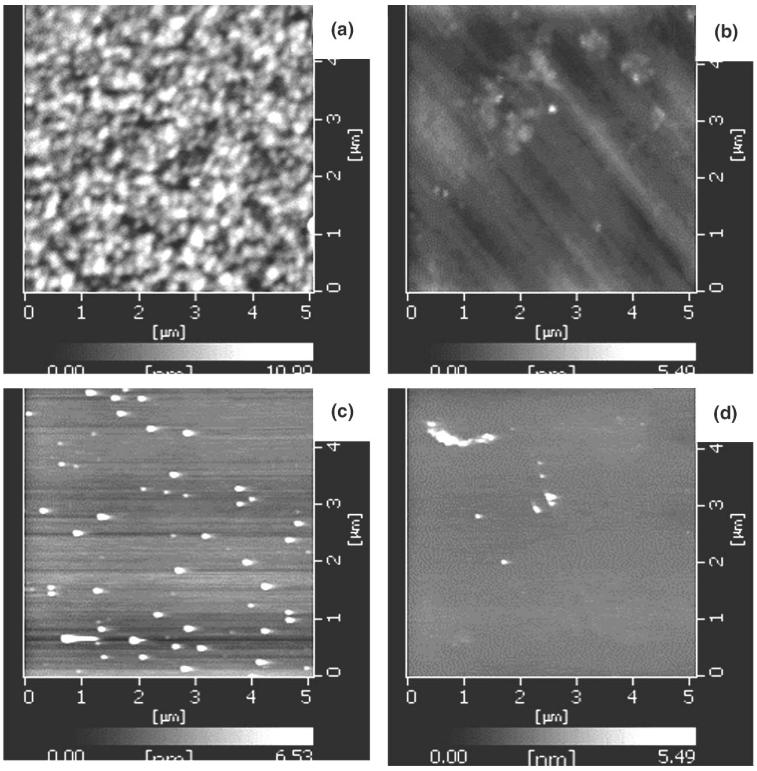

Figure 3.19. Topographical images for silver films laser ablated at 5 Hz repetition rate, RT and 130 mJ onto (a) glass, (b) quartz, (c) MgO, and (d) silicon substrates.

(c) Discussion

The effect of substrate temperature and laser energy on the grain size distribution for nickel films is shown in Figs.3.20 (a). The distribution broadens and shifts to larger values as both the laser energy and the substrate temperature increase. The effect of increase of laser energy from 92 to 168 mJ is more pronounced than that due to substrate temperature increase from RT to 573 K, as is apparent from the larger broadening of the distribution. Figure 3.20 (b) shows the histograms for effect of substrates on the grain size distribution in nickel. It is evident that grain size on silicon and MgO substrate peaks at a higher value than it does on BSG substrates. The values of average grain size for films grown on silicon, MgO, and BSG substrates are approximately 175, 125, and 75 nm, respectively.

The trends for z_{av} (particle height), grain diameter (d), standard deviation, skewness, and aspect ratio versus laser energy and substrate temperature. have been plotted for

nickel films in Figs. 3.21(a) and (b), respectively. With the increase in laser energy from 92 to 168 mJ, grain diameter increases from around 40 to 200 nm. Higher laser energy gives rise to higher roughness as is evident from the larger *z*av values. At increased laser energy, the standard deviation increases, i.e., broader distribution, as is evident from the histograms for grain size distribution. The skewness reduces and aspect ratio increases and then saturates as a function of increasing laser energy. Substrate temperature also exhibits similar trends for Z_{av}, grain diameter (d), standard deviation, skewness, and aspect ratio, but the effect of substrate temperature is less pronounced than that due to laser energy. Grain size increases from 40 to 100 nm with increase in substrate temperature from 300 to 573 K, while it increases from 40 to 200 nm for laser energy from 92 to 168 mJ. Both laser energy and substrate temperature give rise to flatter particles.

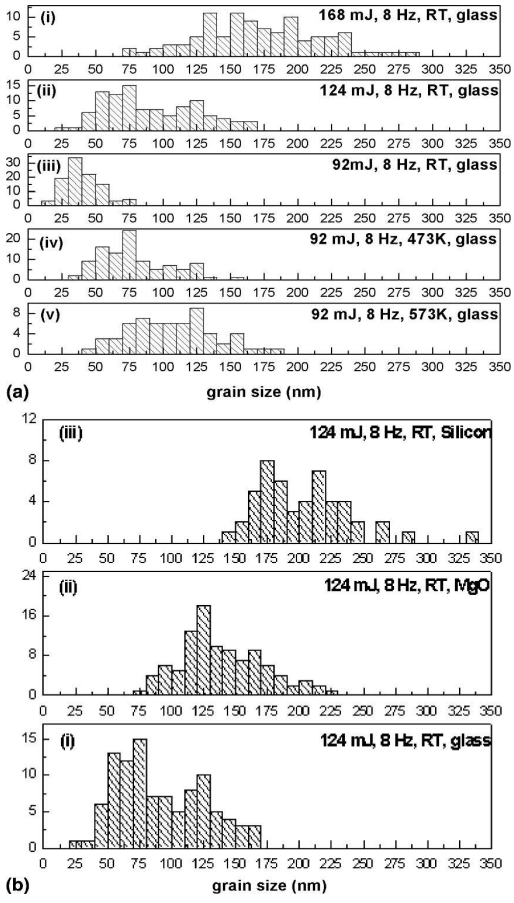

Figure 3.20 (a) Histograms representing the grain size distribution for nickel films for (i) 168 mJ, (ii) 124 mJ, and (iii) 92 mJ laser energy and RT deposition on glass substrate at 8 Hz, and (iv) 473 K and (v) 573 K substrate temperature. (b) Histograms representing the grain size distribution for nickel films deposited on (i) glass, (ii) quartz, and (iii) MgO at 124 mJ laser energy, 8 Hz rep-rate at RT.

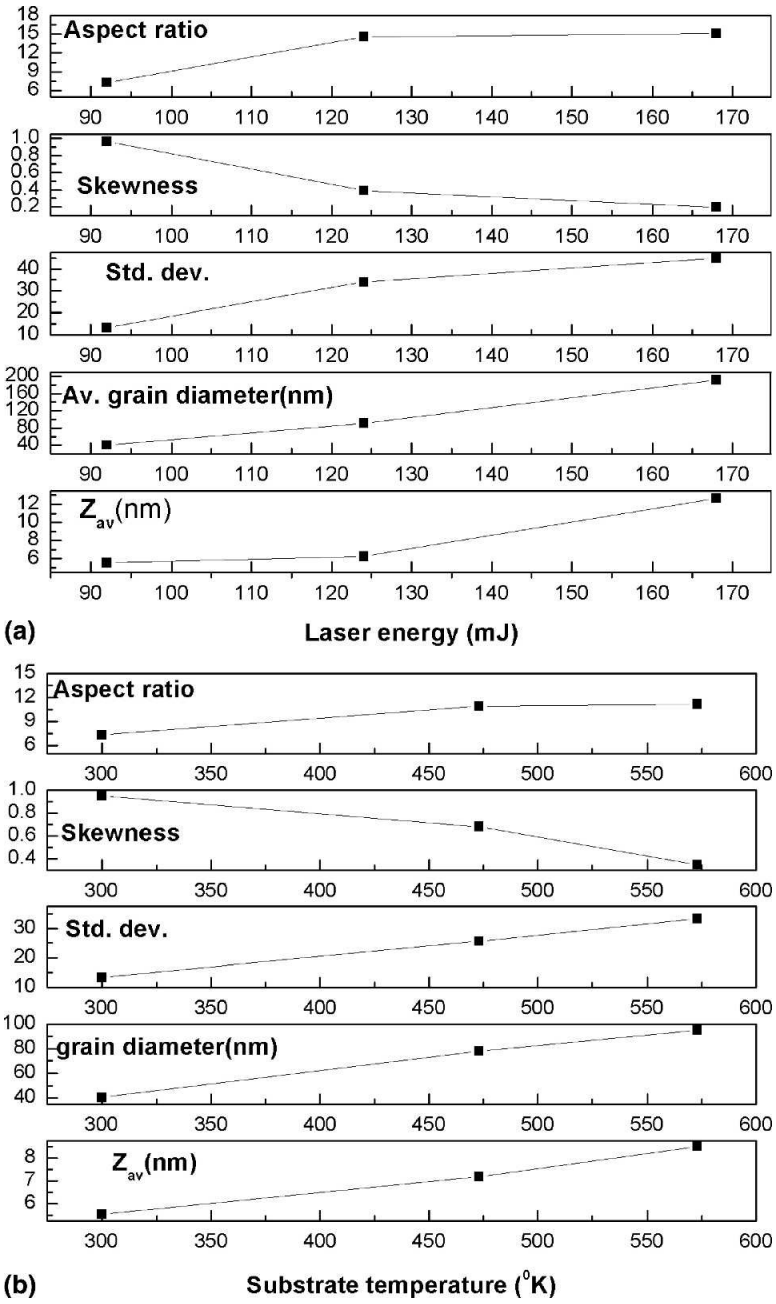

Figure 3.21 Trend of Z_{av}, grain diameter (d), standard deviation in grain diameter, skewness from Gaussian distribution, and aspect ratio for nickel films with the variation of (a) laser energy and (b) substrate temperature.

For silver thin films, with the increase in laser energy and substrate temperature, the distribution shifts to larger values and also broadens. The peak values of the grain size distribution are 100, 350, and 425 nm for 130, 300, and 500 mJ, respectively. As the substrate temperature increases from RT to 573 K, the mean grain size increases from 100 to only 150 nm. Clearly, the effect of incident laser energy and the consequent impingement rate of vapor molecules on the substrate have a more pronounced effect than the substrate temperature on grain growth. The effect of substrates and that of the substrate– target distance is as shown in Figs. 3.22(a) and (b). Interestingly, on MgO, the particle size distribution is narrow, peaking at approximately 125 nm, whereas it peaks at 80 nm on BSG, also displaying a larger distribution.

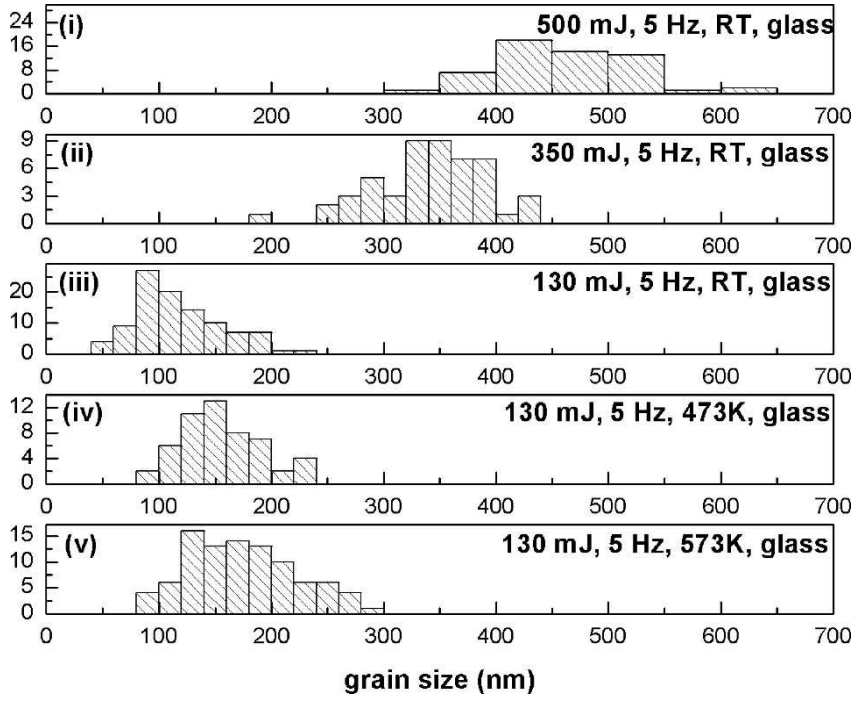

Figure- 3.22 Histograms representing the grain size distribution for silver films for (i) 500 mJ, (ii) 350 mJ, and (iii) 130 mJ laser energy and RT on glass substrate at 5 Hz, and (iv) 473 K and (v) 573 K substrate temperature at 130 mJ.

The effect of substrates and that of the substrate– target distance is as shown in Figures 3.23 (a) and (b). Interestingly, on MgO, the particle size distribution is narrow, peaking at approximately 125 nm, whereas it peaks at 80 nm on BSG, also displaying a broader distribution.

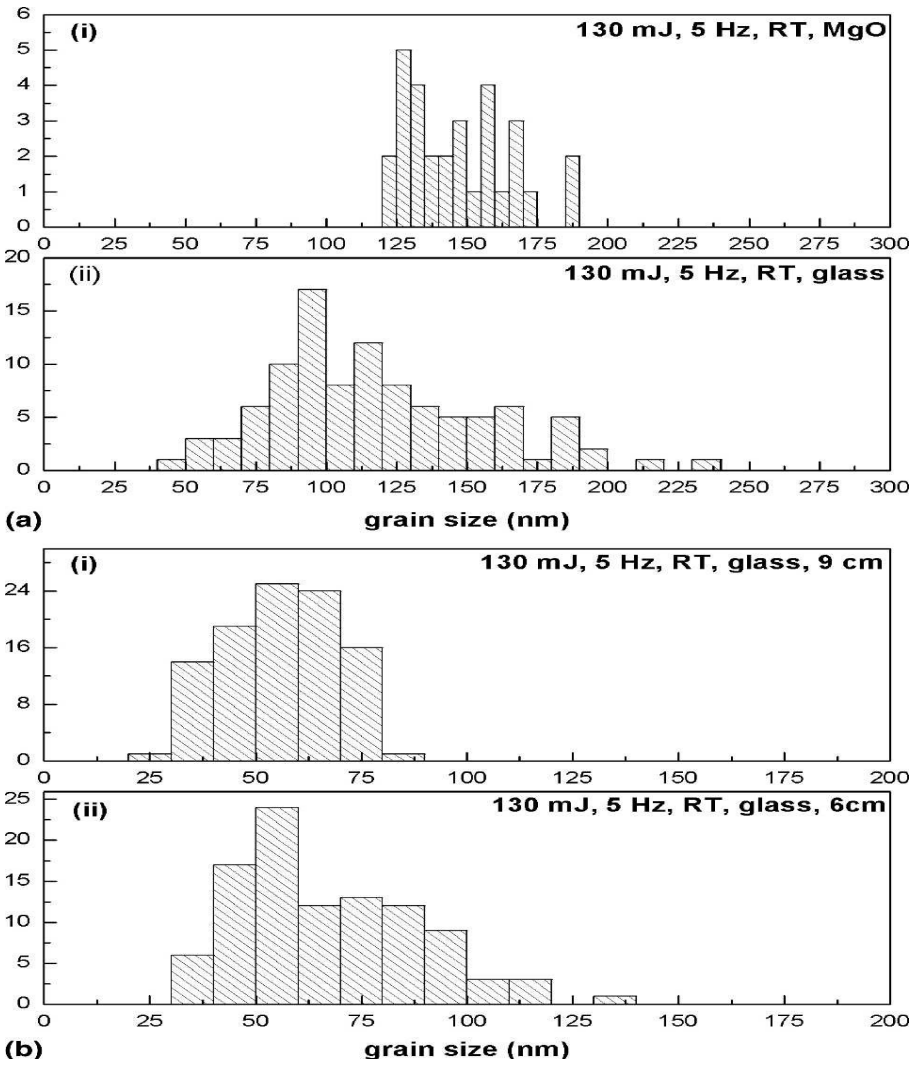

Figure 3.23 (a) Histograms representing the distribution of grain sizes for silver films deposited on (i) MgO and (ii) glass for 124 mJ laser energy and 8 Hz rep-rate at RT. (b) Histograms representing the distribution of grain size for silver thin films at a substrate-target distance of (i) 9 cm and (ii) 6 cm.

The variation of Z_{av}, grain diameter (d), standard deviation, skewness, and aspect ratio with laser energy, substrate temperature, and substrate-target distance are shown in Figs. 3.24(a), (b), and (c), respectively. It is observed that grain size increases from 120 to 310 nm when laser energy is increased from 130 to 500 mJ. Higher laser energy gives rise to increased aspect ratio, and then it saturates. Substrate temperature has a similar effect on the grain size, i.e., increase in grain size with substrate temperature, whereas it has the opposite effect on the aspect ratio of the grains.

Smaller substrate–target distance gives rise to higher average grain size, standard deviation, and aspect ratio.

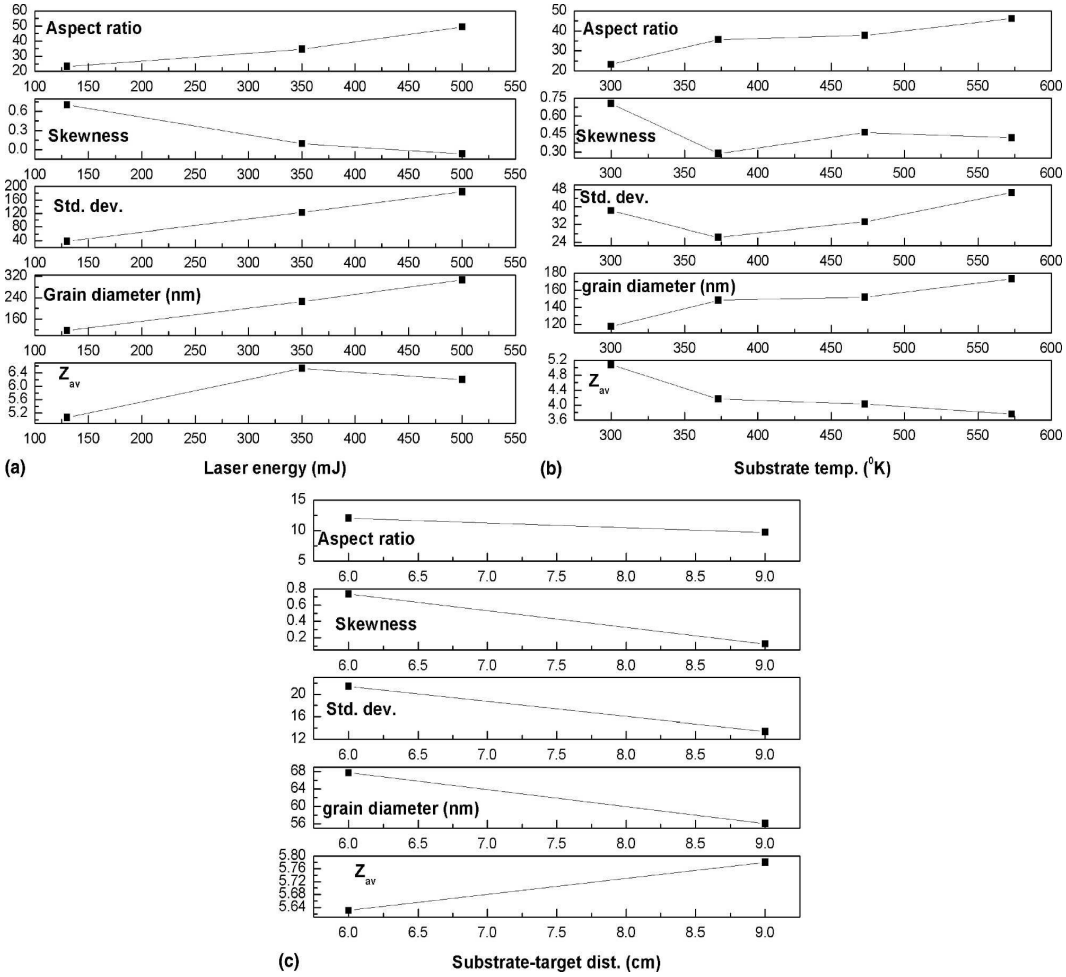

Figure 3.24 Trend of Z_{av}, grain diameter (*d*), standard deviation in grain diameter, skewness from Gaussian distribution, and aspect ratio for ultrathin silver films with the variation of (a) laser energy, (b) substrate temperature, and (c) substrate–target distance. (The connecting lines are only a guide to the eye)

Nickel films deposited on single-crystal substrates of silicon and MgO exhibit lower roughness, larger grain diameter, and flatter nickel nanoparticles, as indicated by the increased aspect ratio [Fig. 3.25(a)]. In the case of silver films, however, it is evident from Fig. 3.25(b) that grain size is larger and nanoparticles are flatter (increased aspect ratio) on single crystal substrate than on the BSG substrates.

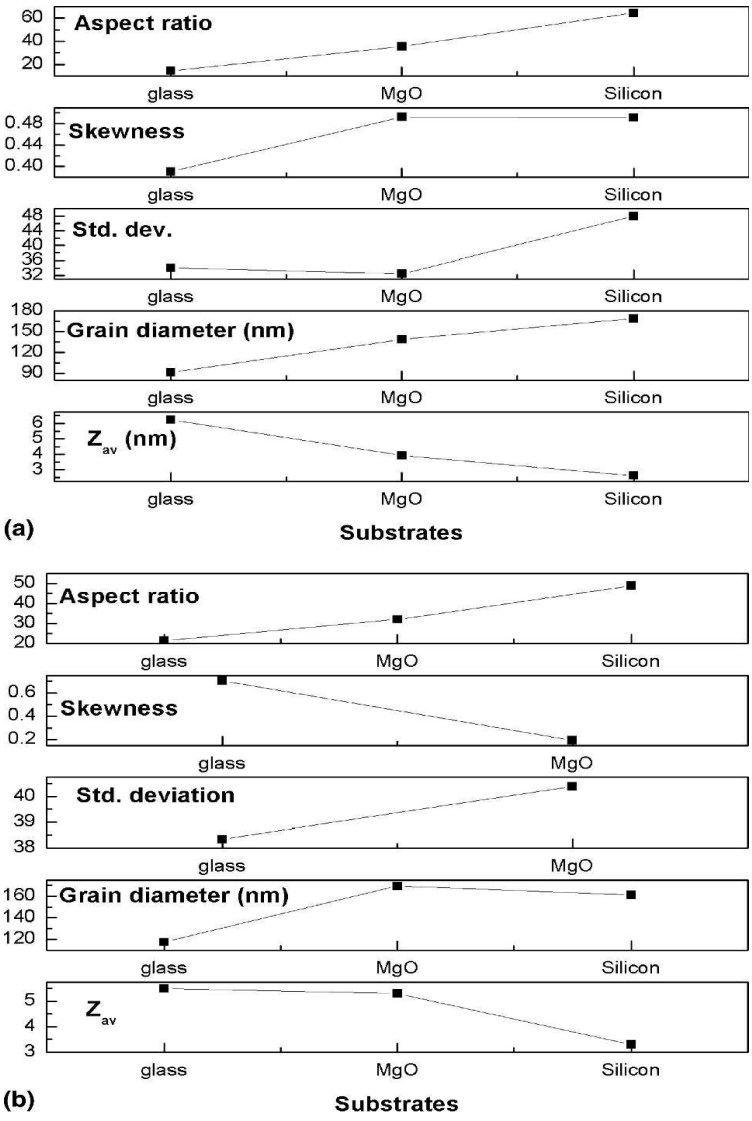

Figure- 3.25 Trend of Z_{av}, grain diameter (d), standard deviation in grain diameter, skewness from Gaussian distribution, and aspect ratio for the variation of substrate for the thin films of (a) nickel and (b) silver. (The connecting lines are only a guide to the eye)

The results shown above can be analyzed from three perspectives. These are based on the processes that occur at the metal surface on impact of laser radiation, during transport of vapor from target-to substrates, and at the impact of vapor on the substrate surface. The fast and strong heating of the target surface by the intense laser beam (typically up to temperatures of more than 5000 K within a few nanoseconds, corresponding to a heating rate of about 10^{12} K/s) ensures fast ablation of materials from the target surface. When the ablation rate is sufficiently high (which normally is

the case at laser fluences well above the ablation threshold), a so-called Knudsen layer is formed and high temperature plasma [**56]** on further heating, which then adiabatically expands in a direction perpendicular to the target surface. Therefore, during PLD, the material transfer between target and substrate occurs in a material package where the separation of the species is small. To obtain sufficiently high ablation rates (on the order of 0.01 nm per pulse) for the deposition of metallic systems in high vacuum, high laser fluences of more than 5 J/cm^2 are necessary. [**57-58**]

Under these conditions, the film deposition occurs under the influence of energetic particles. At a laser fluence of 8 J/cm^2, the velocities of the plasma plume expansion correspond to average kinetic energies [**59-60]** of the ablated ions of more than 100 eV. The mean energy of the atoms is much lower, the order of 5–10 eV. Acceleration of the ions in the strongly increasing space charge field incurred by the more mobile electrons, collectively moving away from the ions, [**61]** is assumed to be responsible for the higher energies of the ablated ions. In our experiments on nickel and silver thin films, the laser energy was varied from 92 to 500 mJ. For 100 mJ laser energy incident, in our case, and a laser spot size of 2 mm diameter, the areal energy density is 3.6 J/cm^2, while for 500 mJ laser energy; the areal energy density is 18 J/cm^2.

Most of the experiments carried out in the present study were between 92 mJ for nickel and 130 mJ for silver, corresponding to laser areal energy density (laser fluence) of 3–4 J/cm^2, which is just above the ablation threshold. Such a laser fluence can give rise to an average kinetic energy of the deposited particles of approximately 100 eV. In most materials, ultraviolet radiation is absorbed by only the outermost layers of the target to a depth of about 100 nm. The energy coupling to the metal target is much higher for short-wavelength ultraviolet lasers. The extremely short laser pulses each lasting less than 50 ns cause the temperature of the surface to rise rapidly to thousands of degrees Celsius, but the bottom of the target remains virtually unheated. To obtain high quality thin layers, one must avoid particle formation. Two main causes of particle formation during laser evaporation are the breakaway of surface defects under thermal shock and splashing of liquid material due to superheating of subsurface layers. The last phenomenon appears for fast heating rates as in our case of 30 ns FWHM KrF laser. Thus, the processes during transport of

vapor by means of a plume, as well as those that cause the plume to form, are dependent on the incident laser energy and fluence.

After transport the substrates and conditions on the substrate surface play an important role in determining the microstructural evolution of the films. It is pertinent at this point to recall the process of condensation of vapor into thin films on substrates.**[62]** Initially small nuclei, depending on the effective surface energy available, form on the substrate. These satisfy the condition of nucleation (supersaturation ratio >1), which in turn is dependent on the substrate material itself. Once a few nuclei form, they work as nucleation centers. Coalescence between nuclei occurs, and this finally gives rise to the growth of continuous layers. Nanoparticulate formation in particular is not only due to the lower melting point of the target materials, but can also be attributed to the metal–substrate interactions. Energetics decides the contact angle of the condensate onto the substrate, residual strain, and size and shape of the nanoparticles deposited. The radius of the particle is given as

$$r^* = (-2\sigma_{v\text{-}c})/\Delta G_V \quad \text{----------(1)}$$

$$\Delta G^* = (4\pi\, \sigma_{v\text{-}c}{}^3)(2 + \cos\theta)\,(1 - \cos\theta) / 3\Delta G_V{}^3 \text{.-------(2)}$$

If the surface free energy of the nucleus is anisotropic in shape, its shape will be a circular disc of height h, in that case;

$$\Delta G^* = (-\pi h\ \ \sigma_{v\text{-}c}{}^3) / (\Delta G_V + \Sigma\, \sigma / h) \text{----------(3)}$$

Where

$$\Sigma\, \sigma = \sigma_{c\text{-}v} + \sigma_{s\text{-}c} + \sigma_{s\text{-}v}\text{.----------(4)}$$

σ terms are specific free energy contributions from the surface, interface, and substrate, respectively._G_v is the free energy (ergs/cm^3) of condensation of the film material in the bulk under the condition of supersaturation

$$\Delta G_V = (kT / V)\,[\ln (R / R_e\,(b))] \text{---------- (5)}$$

Substrate temperature is another dominant parameter that determines the microstructural growth of ultrathin films. Thermal accommodation coefficient is given by

$$\alpha_T = (E_V - E_r) / (E_V - E) = (T_V - T_r) / (T_V - T) \text{----------(6)}$$

where E_V, E_r, and E are energy of the incident vapor, the material before reaching equilibrium, and the material after reaching equilibrium. Since thermal energy can be expressed in terms of temperature as kT, the thermal accommodation coefficient can be expressed in terms of corresponding temperatures. Higher substrate temperature ensures higher mobility of adatoms on the substrate surface. With heating of the substrate, densification occurs, and the grain wall boundary width is thinned.

At RT deposition conditions, because sufficient energy is not available for mobility of adatoms on the substrate surface, the size is not enhanced much due to coalescence. In our studies, it has been observed that increase in laser energy causes a greater enhancement in the grain size than the increase in substrate temperature over the same order of magnitude. This would indicate that particulate formation is aided during transport when incident laser energy is substantially higher than the ablation threshold and that the condensation takes place by means of a rapid quenching process, which retains the large size. The effect of substrate temperature is to cause disintegration of these vapor-generated clusters and increase adatom mobility, leading to higher densification. The role of the substrates is even more interesting since the contact angle and wettability of the surfaces studied are widely different. The condensation process occurs due to an energy minimization process on impact of vapor at the substrate. Therefore, the initial shapes of the grains are determined both by strain and interfacial energy minimization routes. A significant feature of the present study is to demonstrate that the aspect ratios of grains are significantly higher on single-crystal substrates than on amorphous BSG substrates. The grains are flatter and exhibit elongated oblate shapes on MgO and Si. On amorphous substrates, in contrast, the particles are more spherical in nature. As expected, the transport of clusters has a limited mean free path, and the size of the particles decreases drastically with increase in target substrate distance. These effects can be caused by two factors, one is that at higher distance, only slow particles can reach the substrates since particles having

higher velocity will collide with each other and possibly disintegrate in the path between the target and the substrate. On the other hand, if distance is sufficiently large, massive particles should collapse before lighter particles due to weight. This is evident from the fact that at shorter target–substrate distance, there is a larger distribution in size of the particles on the substrate.

References

1. N Gupta, A. Verma, S C. Kashyap and D.C. Dube, J. Mag. Mag. Mater 308**,**137 (2007)
2. C.T. Hsieh, J.Q. Liu and J.T. Lue, Appl. Surf. Sci. 252, 1899 (2005)
3. K. Zhang, F. Rotter, M. Uhrmacher, C. Ronning, J. Krauser and H. Hofsäss, New J. Phys. 9, 29 (2007)
4. E. Girgis, S. P. Pogossian, M L Benkhedar J Nanosci Nanotechnol. 6, 1135 (2006)
5. E. E. Shalyguina, M.A. Mukasheva, N.M. Abrosimova, L. Kozlovskii, E. Tamanis and A.N. Shalygin J. Mag. and Magn. Mater. 300, e367 (2006)
6. K. Sedláčková, P. Lobotka, I. Vávra and G. Radnóczi, Carbon 43, 2192 (2005)
7. S. Amoruso, G. Ausanio, C. de Lisio, V. Iannotti, M. Vitiello, X. Wang and L. Lanotte, Appl..Surf. Sci. 247, 71 (2005)
8. S.W. Chang, J. H. Liu and J. T. Lue. Meas. Sci. Technol. 14, 583 (2003)
9. S. Guan and B. J. Nelson., J..Mag. Mag. Mater. 292, 49 (2005)
10. D. Ravinder, K. Vijay Kumar and A. V. Ramana Reddy, Materials Letters 57, 4162 (2003)
11. D. Flynn and M. Desmulliez J. Phys.: Conf. Ser. 34, 112 (2006)
12. P. Klapetek, I. Ohlídal and J. Buršík Meas. Sci. Technol. 18, 528 (2007)
13. V. Yu. Novikov Acta Materialia 47, 4507 (1999)
14. AG. Dirks and H. J. Leamy, Thin Solid Films 47, 219 (1977)
15. S.C. Seel, C.V. Thompson, S.J. Hearne and J.A. Floro, J. Appl. Phys 88, 7079 (2000)
16. R. Messier, A.P. Giri and R.A. Roy, J. Vac. Sci. Technol., A 2, 500 (1984)
17. D.W. Snyder, S. Mahajan, E.I. Ko and P.J. Sides, Appl. Phys. Lett. 58, 848 (1991)
18. J. Hong, S.W. Gary, J. Wayne Jones and N.R. Moody, J. Appl. Phys. 81, 6754 (1997)
19. J Yang, Y Huang and K Xu Surface and Coatings Technology 201, 5574 (2007)
20. J. Swerts, K. Temst, N. Vandamme, C. Van Haesendonck and Y. Bruynseraede, J. .Magn. Magn. Mat. 240, 380 (2002)

21. H. Shimizu, T. Hayashi, T. Nishinaga and M. Tanaka, Appl.Phys. Lett. 74, 398 (1999)
22. D. Aurongzeb, K. B.Ram and L. Menon, Appl. Phys. Lett. 87, 172509 (2005)
23. Y. P. Zhao, R. M. Gamache, G. C. Wang, T. M. Lu, G. Palasantzas and J. Th. M.De Hosson, Jour. Appl. Phys. 89, 1325 (2001)
24. Y. H. Wang, D. K. Sood and M. K. Ghantasala, Proceedings of SPIE 394, 4936 (2002)
25. L. Castaldi, M. R. J. Gibbs and H. A. Davies, Jour. Appl. Phys. 96, 5063 (2004)
26. N. D. Ha, M.-H. Phan and C.-Oh Kim, Jour. Appl. Phys. 99, 08F105-1 (2006)
27. L. K. E. B. Serrona, A. Sugimura, N. Adachi, T. Okuda, H. Ohsato, I. Sakamoto, A. Nakanishi, M. Motokawa, D. H. Ping and K. Hono, Appl. Phys. Lett. 82, 1751 (2003)
28. S. A. Haque, A. Matsuo, Y. Seino, Y. Yamamoto, S. Yamada, H. Hori, Physica B 305, 121 (2001)
29. R. A. Lukaszew, Zhengdong Zhang, V. Stoica and R. Clarke Appl. Surf. Sci. 219, 74 (2003)
30. J. B. Yi, Y. Z. Zhou, J. Ding, G. M. Chow, Z. L. Dong, T. White, Xing Yu Gao, A. T. S. Wee, X. J. Yu, Jour. Magn. Magn. Mat. 284, 303 (2004)
31. K. Y. Chan, T. Y. Tou, B. S. Teo, Microelectronics Jour. 37, 930 (2006)
32. Yu Ya Gafner, S. L. Gafner, and P. Entel Phys. Sol. Stat. 46,1327 (2004)
33. K. Fujikawa, S Suzuki, Y. Koike, W. Chen and K Asakura, Surf. Sci. 2006.
34. K. Barmak, J. Kim, C. S. Kim, W. E. Archibald, G. S. Rohrer, A. D. Rollet, D.Kinderlehrer, S. Ta'asan, H. Zhang, D. J. Srolovitz, Sripta Materialia 54, 1059 (2006)
35. G. Bertotti, "Hysteresis in magnetism", Academic press, ISBN 0-12-093270-9, pp. 375
36. J G Kim, K H Han, Seok Ho Song, A Reilly, Thin Solid Films 440, 54 (2003)
37. H. Kachkachi, M. Nogues, E. Tronc, D. A. Garanin, J. Mag. Mag. Mat. 221, 158 (2000)
38. W. H. Zhang, C. Q. Sun, S. Li, Sol. Stat. Comm. 130, 603 (2004)
39. X. Battle and A. Labarta, J. Phys. D, Appl. Phys. 35, R15 (2002)
40. R. C. Ohandley, "Modern Magnetic Materials", Wiley Interscience, New York, pp. 306 (2000)

41. B. D. Cullity, “Introduction to Magnetic Materials”, Addison-Wesley, MA, pp. 387 (1972)
42. G. P. Zheng, D. Gross and M. Li, J. Appl. Phys. 93, 7652 (2003)
43. G. Herger, Jour. Magn. Magn. Mat. 112, 258 (1992)
44. K. Ha, M. Ciria, R.C O’Handley, P. W. Stephens and S. Pagola, Phy. Rev. B, 19, 13780 (1999)
45. C. V. Thompson, J. Mater. Res.14, 3164 (1999)
46. D.P. Norton: in Pulsed Laser Deposition of Thin Film Applications Led Growth of Functional Materials, edited by R. Eason (Wiley-Interscience, Hoboken, NJ, 2007), Chap. 1, p. 3.
47. J. Shena, Z. Gai, and J. Kirschner, Surf. Sci. Rep. 52, 163 (2004).
48. T. J. Jackson and S.B. Palmer, J. Phys. D: Appl. Phys. 27, 1581 (1994).
49. K.C. Magdalena, R. Chmielowski, A. Kopia, J. Kusinski, S. Villain, C. Leroux, and J-R. Gavarri, Thin Solid Films 458, 98 (2004).
50. T. Venkatesan and S.M. Green, The Industrial Physicist 2, 22 (1996).
51. J.M. Warrender and M.J. Aziz, Appl. Phys. A 79, 713 (2004).
52. S.J. Henley, J.D. Carey, and S.R.P. Silva, Phys. Rev. B: Condens. Matter 72, 195408 (2005).
53. T. Donnelly, B. Doggett, and J.G. Lunney, Appl. Surf. Sci. 252, 4445 (2006).
54. D. Jang and D. Kim, Appl. Phys. A 79, 1985 (2004).
55. S.K. So, H.H. Fong, C.F. Yeung, and N.H. Cheunga, Appl. Phys. Lett. 77, 1099 (2000).
56. C.R. Phipps, T.P. Turner, R.F. Harrison, G.W. York, W.S. Osborne, G.K. Anderson, X.F. Corlis, L.C. Haynes, H.S. Steele, K.C. Spicochi, and T.R. King, J. Appl. Phys.
64, 1083 (1988).
57. H.U. Krebs and O. Bremert, Appl. Phys. Lett. 62, 2341 (1993).
58. H.U. Krebs, J. Non-Equilibrium Proc. 10, 3 (1997).
59. S. Fahler and H.U. Krebs, Appl. Surf. Sci. 96, 61 (1996).
60. J. Lunney, Appl. Surf. Sci. 86, 79 (1995).
61. W. Demtraoder and W. Jantz, Plasma Phys. 12, 691 (1970).
62. C.A. Neugebauer: in chapter “Condensation, nucleation and growth of thin Films”, in book titled “Handbook of Thin Film Technology”, edited by L. I. Maissel and R. Glang (McGraw Hill, New York), Chap. 8, p. 8.3 (1970)

Section 3.2

Template assisted technique for the fabrication of nanowires

Abstract:

Template-assisted fabrication of nanowires in thin films of nickel, gold, indium and silicon is demonstrated. Thin films have been deposited on to Borosilicate Glass (BSG) and Si substrates by evaporation and Pulsed Laser Deposition (PLD), In and Si have been evaporated onto BSG substrates while gold was deposited by DC sputtering on to BSG substrates. The 10–200 nm thickness films were grown in to trenches scribed on to substrates. Nickel, Gold, Indium and silicon nanowires of diameter 50–400 nm have been found to form as a result of the template-assisted growth. The growth of the nanowires in all the cases follows a pattern, as a function of thickness, that starts with self-organisation of nanoparticles then continuous nanowire and finally at higher thickness a combination of nanoparticles and continuous nanowires. Since formation of the nanowires is dependent on the shadowing phenomenon at the sidewalls of the trench, it was found that at large trench widths (50 μm) no nanowires could be formed. Length of the nanowires is completely dependent on the length of the trench whereas the diameter of the nanowires is dependent on the thickness of the thin film. Ferromagnetic Resonance (FMR) measurements on the Ni nanowires show magnetic anisotropy while the magnetotransport measurements reveal 3–4% of Magnetoresistance (MR). For Indium nanowires, shift in the surface plasmon peak have been observed as compared to that of the continuous thin films. In the case of Gold, apart from peak shifts; additional plasmon resonance peaks have also been observed. This technique is shown to be a simple, yet effective way of fabricating nanowires with good control over dimensions of the nanowires as well as achieving novel properties.

3.2.1 Introduction

Nanowires are nanostructures that have attracted recent attention due to their possible widespread applications. Challenges ahead in the way to integration of nanowire systems are to manipulate the placement of nanowire and organise them in the circuit. Template assisted growth of nanowires is a technique with which nanowires can be grown at a pre-determined position and in desired directions. Usually for template assisted synthesis of nanowires, nanoporous alumina templates [1-3] which works on shadowing phenomenon are used. Some nanowire materials show a preference for formation along exposed 'steps' in the atomic structure of the substrate [4-5]. Directed assembly of nanowires of various materials making use of atomic cluster deposition into v-trenches has been reported earlier [6-9]. As far as applications are concerned, gold nanowires have been material of interest in its surface plasmonic devices[10-12], photonic transport and the study of non-diffraction-limited light transport [13-14] behaviour.

In the current work, a simple and economic technique for the fabrication of nickel, gold, indium and silicon nanowires employing v-trenches as template for nanowire growth is demonstrated. It is shown that the growth per se is independent of processing technique but that it occurs through a self-shadowing route during the growth process. To demonstrate this Ni nanowires have been grown by evaporation and PLD, indium and silicon by evaporation and the gold nanowires by the DC sputtering route. The grown nanowires have been characterized by scanning electron microscopy and atomic force microscopy in the dynamic force mode. Ferromagnetic Resonance (FMR) spectra were taken to investigate magnetic anisotropy and the magnetotransport was investigated from Magnetoresistance (MR) measurements on Ni and the optical properties of the gold and indium nanowires were studied using UV-VIS-NIR spectropohotometer.

3.2.2 **Results and discussion**

(a) **V-trench template**

The trenches were scribed on BSG, quartz and single crystal Si substrates using a commercial diamond scriber. It was observed that using the diamond scriber trenches of 3–50 μm width and depth of 0.1–0.5 μm can be scribed on a glass substrate depending on the force used. On the other substrates it was however found that trench depth was much greater. The formation of the nanowires is based on the phenomenon of self-shadowing at the edges of the trench causing selective deposition within the trench over a width that is a small fraction of the trench. Hence it was found that on substrates such as quartz and Si there was greater shadowing and therefore film deposition could not be observed. Experiments to overcome this problem are being carried out currently. An additional reason for selecting BSG substrates is that it is a hard substrate and therefore straight trenches can be patterned onto this without affecting parts of the substrate in between the trenches. Figure 3.26(b) shows the actual profile of a scribed trench with dimensions before and after coating. It can be observed that the h_1 and h_2 are in the range of 200–560 nm while the depth is 240–300 nm and the width is ~4 μm. The change in height before and after coating as well as the height of the sidewalls of the trench is clear from this figure. The profile clearly shows that the effect of the trench creation by scribing is to cause the formation of a valley like structure with a hillock on either side of the width of the trench. The height of the sidewalls could be from 60 to 500 nm using this technique and therefore the diameter of th

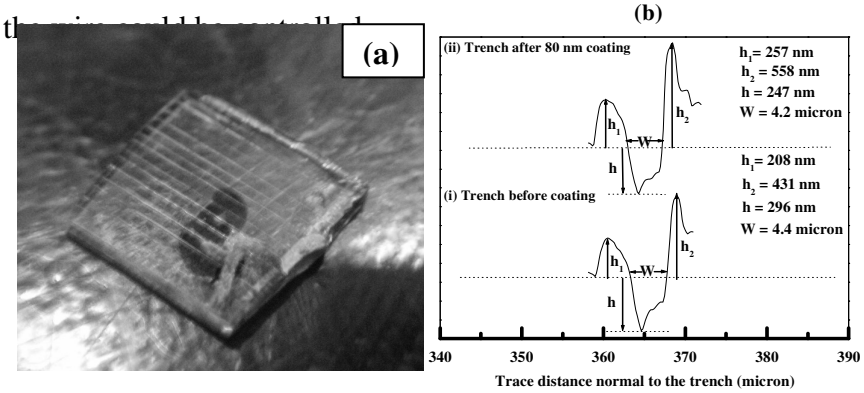

Figure-3.26 (a) Photograph of scribed trench on BSG glass substrate (1" x 1"), (b) Surface line profile of the scribed trench before and after the coating.

It is expected that the sidewalls will cause shadowing of the condensate attempting to deposit within the width of the trench and therefore the effective width of the deposits within the trenches will be much less than the width of the trench. First evidence for this is in the form of the surface profiles of the trenches after the films are deposited. It is seen from Figure 3.26(b)(ii) that the height of the sidewalls has increased and that the roughness has also changed. Furthermore the surface profile of the trench itself shows a decrease in depth of the trench indicating that the film has deposited even inside the trench and this is of the order of 50 nm.

(b) Nickel

(i) Mictrostructure

In the growth of condensates in to the trenches, the diameter and the depth of the trench are the two parameters that control the dimensions of the material grown inside it. Hence, these can in principle be used as size-selective filters for controlling dimensions of the resulting nanowires. The width, *W*, determines the angle from the normal for the entry of the vapour inside the trench and the depth, *h*, defines the final width, *D*, over which the material will deposit. Hence, trench patterned growth in principle can be used to grow single metallic nanowires if *D* and *h* are selected in the proper range to suit the desired diameter of nanowire to be grown. As shown in Figure 3.27 (a), untemplated 50nm Ni thin film shows island type of growth. For higher trench width (20μ) which is much larger than that required to yield single nanowires and therefore, several zig-zag nanowires are expected to form. It was observed that the larger trench width smears out the formation of the nanowire (Figure 3.27 (b)). Smaller the trench width, stronger is the shadowing effect and higher is the probability of achieving isolated nanowires (as shown in Figure 3.27(c)). The other two parameters that determine the width of the nanowires are the height of the sidewalls and the actual depth/width ratio of the trench. Growth within the trenches can be considered similar to oblique incidence deposition. Oblique incidence, in general, enhances the velocity components of the adatoms migrating on the surface and thus yields high mobility effects. With the increase in the incidence angle of vapour, agglomeration will be enhanced. Substrate temperature also plays an important role. Columnar growth is more prominent at higher angles only at lower substrate temperature, but at higher substrate temperature, growth is non-columnar

and dense. Reduction in flatness of the film growth inside a trench can be attributed to such oblique incidence induced growth. However, organization into a long chain of nanoparticles or nanowire is possibly due to the length of the trench. Higher sidewalls will cause more shadowing and therefore reduce the diameter of the wires. Similarly, when the trench depth is much larger than the width, the deposit is contained in regions close to the top of the trench. Roughly it has been found that diameter of the trench should be one order different than the nanowire structure to be achieved.

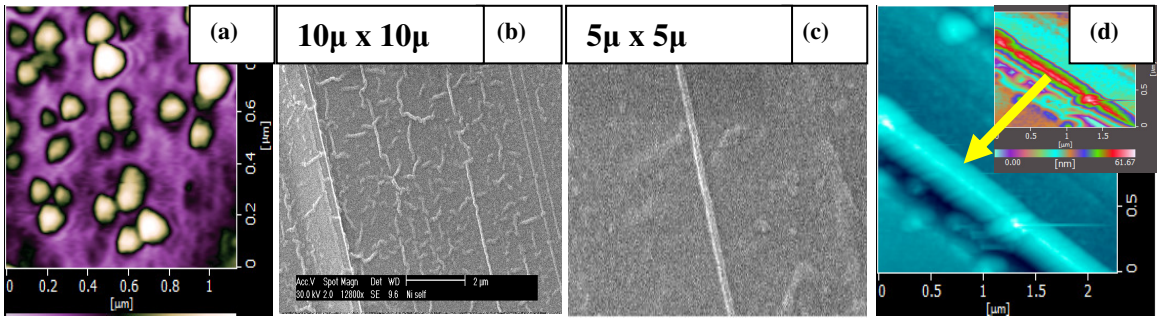

Figure 3.27 (a) AFM image of the untemplated Ni thin film (b) SEM image for multiple and zig-zag nanowires formation at higher trench width (20 µ), (c) SEM micrograph of nickel nanowire for 10 µ trench width, (d) AFM image of Ni nanowire showing SK type of growth.

Uniformity of the diameter of nanowires is another issue that has been investigated. The uniformity of the nanowires is clear from the SEM images shown in Figure 3.27(c) and the DFM image in Figure 3.27(d) for Ni wires grown on BSG substrates. It can be observed that the next layer has started forming onto the thicker nickel nanowire already formed, which then acts as the template for the next layer and so on (Figure 3.27(d)). The widths of the wires in this case are 250 nm for the 150 nm thick coating and 120 nm for the 80 nm coating. It is thus observed that with reducing thickness there is a decrease in the diameter of the nanowires. On Si substrates it was found that the wires are much larger in diameter than those deposited on BSG substrates.

A closer examination of the SEM micrographs also revealed that the films, at lower thickness, self-assembled in the form of connected nanoparticles that became continuous at thicknesses greater than 100 nm. There is, thus, a critical thickness above which the nickel nanowires are continuous. It is seen that in general there are

regions of discontinuities in the wires caused by strains along the plane of the nanowires. These can be overcome by appropriately optimising the deposition conditions. To ensure that there is trench-to-trench isolation of the nanowires a sacrificial layer of Maleic acid was deposited. In the case where the Maleic acid is not used there is evidence for film formation on the outside of the trenches. This was confirmed by making resistivity measurements inside and outside the trenches.

The effect of processing technique on the formation of the nanowires has been studied by depositing thin films of Ni in to the trenches by the PLD technique. The untemplated PLD Ni ultrathin 10nm film exhibits island type (Figure 3.28(a)) microstructure. As energy of the laser pulse is increased, for the same duration of deposition, nanowires form at lower energy (Figure 3.28 (b)) and a combination of nanowire and film growth inside the trench (Figure 3.28(c)). It is evident from Figure 3.28(c) that nanoparticles are assembling in the direction of the nanowire already formed. The nanowire diameters are 100 nm in the nanowire case which increases to 140 nm in the mixed case. It should be noted that in the rest of the discussion, sample containing nanowires are referred to as nanowire samples. Thus the differences in properties between a pristine thin film and a thin film with nanowires have been investigated.

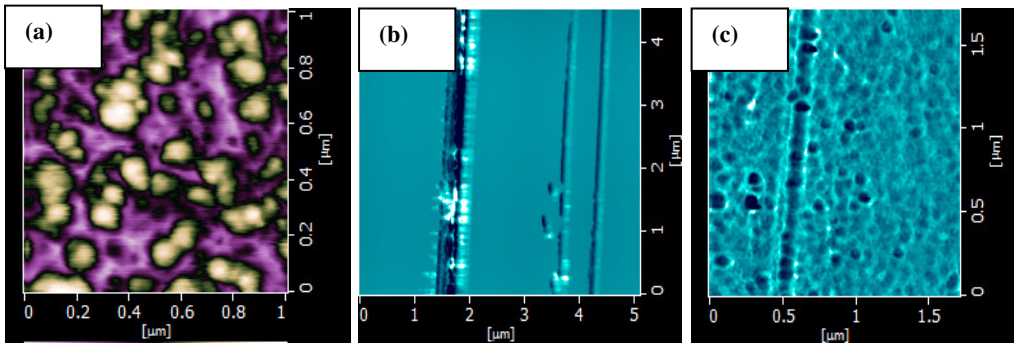

Figure 3.28 AFM images of (a) untemplated PLD 10nm Ni unltrathin film, nanowires grown by the PLD technique at laser energy density of (b) 0.1 and (c) 0.18 J/cm^2.

(ii) Long range crystalline order

X-ray diffraction studies were carried out on the nanowire Ni films of the thickness of 80nm. It was observed that similar to the continuous film nanowire sample too showed a reflection that could be attributed to the (111) plane (Figure 3.29). It has

been found that nanowires do crystallize better than the usual thin film for the same thicknesses.

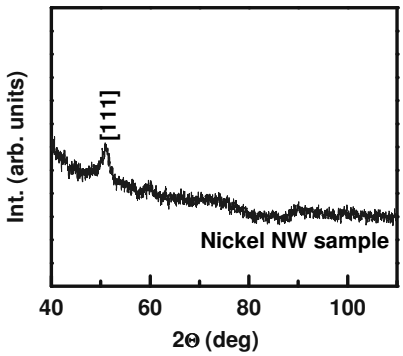

Figure 3.29 X-ray diffraction pattern for thermally evaporated 80 nm nickel thin film

(iii) Magnetic behaviour

Magnetic transport study was done using a MR setup. MR (%) for the nickel nanowire sample (Figure 3.30 (a)) and that for the thin nickel films (Figure 3. 30 (b)) of coating thickness 80 nm was done at room temperature and up to 0.3 T magnetic field. MR was measured for the voltage lead separation of 4 mm. MR of 3–4% (Figure 3. 30 (a)) was observed for the nanowires that compares favourably with values reported in literature. As the diameter of the nanowire decreases, the effective easy axis direction goes from along the wire axis to the normal to it. Therefore, it is expected that for nanowires the MR for field parallel to the current case should be comparatively high and that for the field normal case should be negligible. Further, for very thin nanowire (approximately 30 nm), where the easy axis is near to the normal to the nanowire axis, it is expected that MR for parallel case should be negligibly small and that for the normal case should be enhanced. In the current case, MR for the parallel case is relatively higher (3–4%) than those reported for 30–40 nm nanowires because the nanowire diameter is larger (120 nm) in our case and the easy axis is not exactly completely parallel or normal to the nanowire axis. For the nanowire sample achieved by reducing the film thickness to 40 nm, and where very thin nanowires had formed, the MR for the field parallel to the nanowire axis case showed large noise and the resistance signal did not respond to the magnetic field, giving rise to almost zero MR. Therefore, it seems that with the reduction of the diameter of nanowires, longitudinal MR (field parallel to current applied) also decreases.

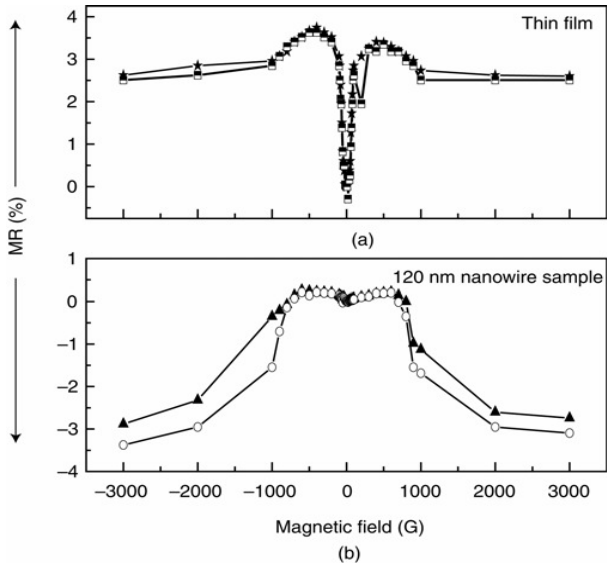

Figure 3**.** 30. The variation in (MR %) as a function of the applied magnetic field at RT for (a) thin film of the same thickness coated by the evaporation technique and (b) 120 nm diameter nanowire.

The direction of easy axis can be determined from FMR measurements as shown in Figure 3.31. It is observed that the resonance field for both nanowire axis in field plane and that for nanowire axis normal to the field plane are almost equal (~336 G) but the intensity is marginally different for the nanowire parallel to the magnetic field case than that for the normal case. It signifies that the easy axis is just off the nanowire axis, but still far from being exactly normal to nanowire axis. Comparing the MR curves for the nanowire sample and that for the continuous thin film of same thickness, we infer that switching field is smaller in case of thin film as compared to that for the nanowire sample. Secondly, after the traversal of field from the highest value (in our case 3 kG) to the lowest value (–3 kG) the MR curve exhibits hysteresis in case of the nanowire sample but is absent in the case of the thin film. It seems that several components are present and are contributing to the total effective MR measured. Ordinary magetoresistance and anisotropic MR are the primary source of contribution. Moreover electrical point contacts too have possibly contributed to the effective magetoresistances. It can be seen from Figure 3.31 that the resonance field values vary depending on whether the sample is rotated in-plane with respect to the applied magnetic field or out-of-plane with respect to the applied field. A similar study done on continuous thin films, in the absence of nanowires does not show any anisotropy due to in-plane rotation and hence it can be concluded that the nanowires

induce in-plane anisotropy in addition to the out-ofplane anisotropy. The continuous films do not show any magnetic anisotropy because there is no microstructural anisotropy. However, normal to the axis of the growth of nanowires the magnetic moments will be confined resulting in magnetic anisotropy. This clearly indicates anisotropy in magnetic behaviour that can be exploited for applications.

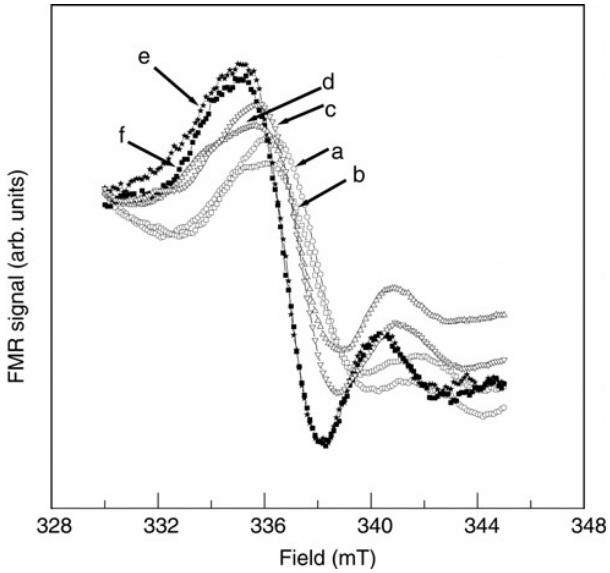

Figure 3.31 FMR spectroscopic picture for nickel nanowire and thin film on BSG substrates by evaporation technique for (a) continuous thin film parallel to field, (b) continuous thin film normal to field, (c) nanowire sample vertical and normal to the field (film plane in the direction of the field), (d) nanowires vertical and normal to the field (film plane normal to field), (e) nanowires horizontal and parallel to the field (film plane in the direction of the field) and (f) nanowires horizontal and normal to the field (film plane normal of the field)

(c) Gold

(i) Microstructure

Gold nanowires were fabricated by depositing thin films on to BSG substrates by DC sputtering. The as deposited non templated thin film shows island like morphology as shown in Figure 3.32(a). Gold nanowires were then fabricated on to trenches that were 10 microns wide. It was observed that at 25 nm thickness the nanowires were just forming, while at 40 nm the nanowires are fully formed (Figure 3.32(b)) whereas at 150 nm thickness the nanowires are smeared out. The diameter of the wires is 150 nm for the 40 nm film and 300 nm for the thickest film. Similar to the behaviour

observed for nickel nanowires, gold nanowire growth follows the pattern of first, organisation in the form of nanoparticles to continuous nanowire then a mixed structure of nanowire and particles. Figure 3.32(c) shows the AFM image for the gold nanowires, which clearly indicate that, both nanowires as well as self-organised nanoparticles form in the process. It appears that the gold nanowires are much uniform than the nickel nanowires, which can be attributed to the better wettability of gold to BSG than nickel.

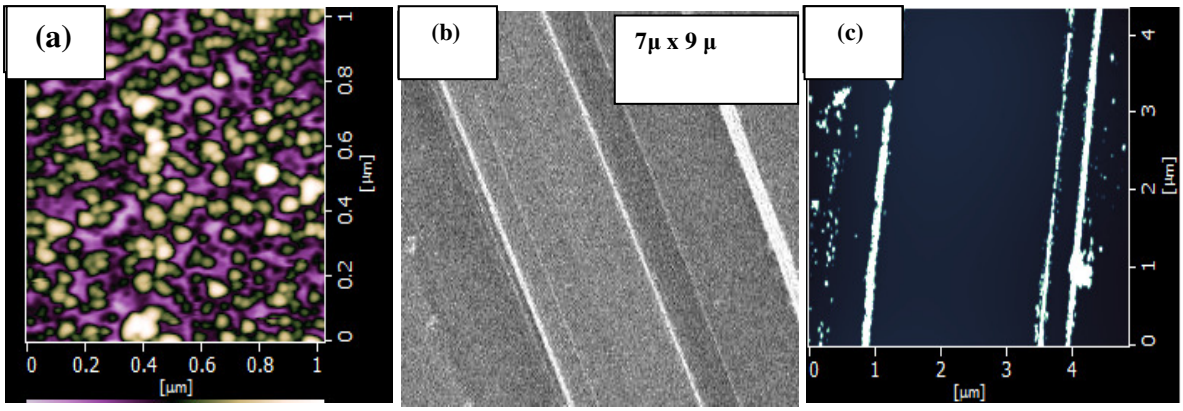

Figure 3.32 (a) AFM image in DFM mode for untemplated growth of 40nm thin DC sputtered gold thin film, (b) SEM image of the 40 nm thick nanowire film and (c) AFM image of the 40 nm thick nanowire film showing the nanoparticle nature of the nanowires.

(ii) Long range crystalline order

DC sputtered gold nanowire sample exhibited polycrystalline nature as shown in Figure 3.33. Five peaks corresponding to the planes [111], [200], [220], [311] and [222] have been observed.

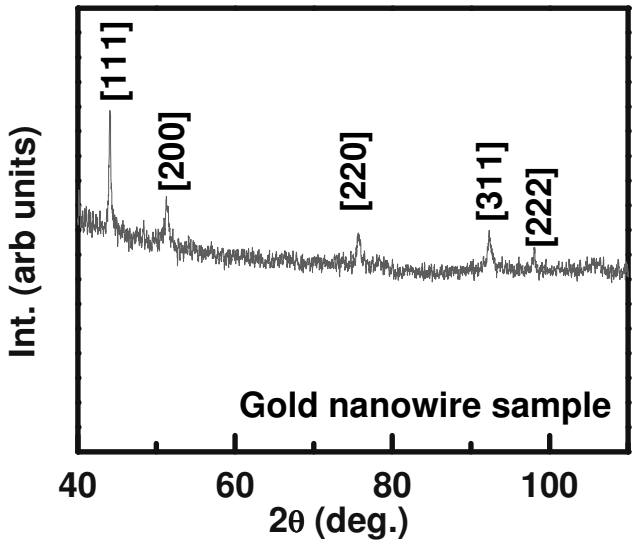

Figure-3.33 X-ray diffraction pattern showing polycrystalline nature of DC sputtered gold nanowire sample.

(iii) Specular reflectance

The gold nanowires were characterised for optical reflectance in the range of 190–2500 nm by UV-VIS-NIR spectrophotometer. Typical spectra are shown in Figure 3.34(a) and (b). The specular reflectance spectrum of a 40 nm thick film, in Figure 3.34(a), shows one absorption peak at 480 nm. However, the corresponding nanowire sample shows a number of additional peaks at 215, 310 and 570 nm and only a weak absorption at 480 nm. When the thickness of the film is increased to 80 nm (Figure 3.34(b)), the absorption at 480 nm remains invariant but the corresponding nanowire sample exhibits absorption peaks at 300, 420 and 620 nm.

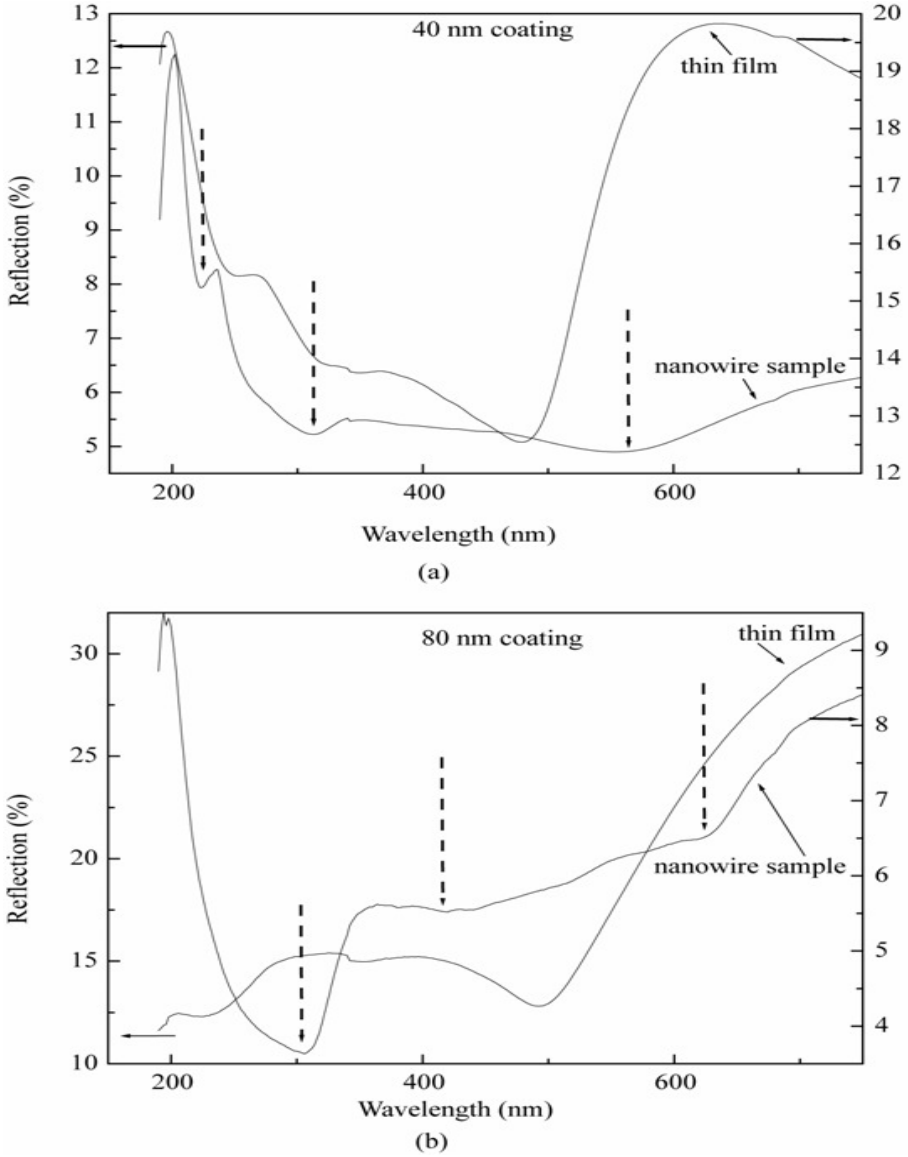

Figure 3.34 Specular reflectance spectra for gold thin films for (a) 40 nm gold coating, nanowire sample and thin film of same thickness and (b) 80 nm gold coating, nanowire sample and thin film of same thickness.

Thus, the absorption peaks are independent of thickness in the continuous film but exhibit a shift with thickness in the case of the nanowire samples. The origin of the absorption peaks in both the nanowires and the continuous thin films can be attributed to the presence of localised plasmons. The main surface plasmon resonance band centred around 480 nm is due to the transition between the $5d^{10}$ level and unoccupied

conduction bands in Au nanoparticled systems [15]. Additional resonances can be excited due to interplasmon coupling effects as a consequence interparticle coupling. This is the reason for the additional surface plasmon resonance peaks in the nanowire systems in our case. In addition, this result confirms that the extra modes are present in the reflection spectra mainly due to the formation of nanowires. Such tunable modes due to nanowires can therefore be further exploited for applications.

(d) Indium

(i) Microstructure

As the coating thickness increases, thermally evaporated untemplated indium thin films show that particle size increases and surface roughness too increases as shown in Figure 3.35 (a) to (c). Due to restricted vapour supply at minimal thickness, 10 nm, inside trench gives nanowire growth with some zig-zag pattern (Figure 3.35). Nanowire diameter increases by increasing the thickness of the coating.

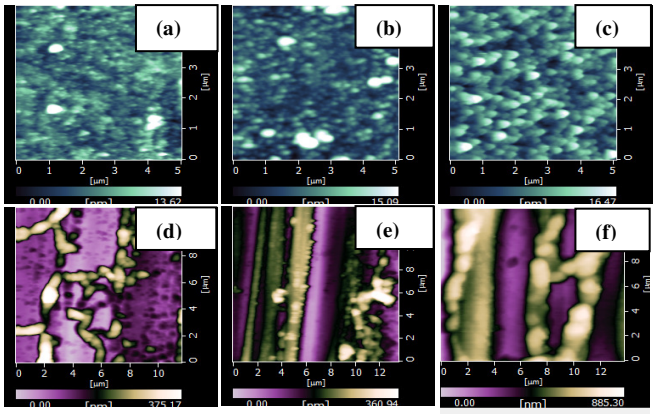

Figure-3.35 AFM image of nanostructured Indium thin films for (a) 10nm as deposited thin films, (b) 15nm as deposited thin film, (c) 60nm as deposited thin film, (d) growth inside the template for 10nm thin film, (e) growth inside the template for 15nm thin film and (f) growth inside the template for 60nm thin film.

(ii) Specular reflectance

Specular reflection spectra of thermally evaporated templated and untemplated indium thin films are as shown in Figure 3.36. It was observed that for lower thickness of coating, shift in surface plasmonic peak is more pronounced.

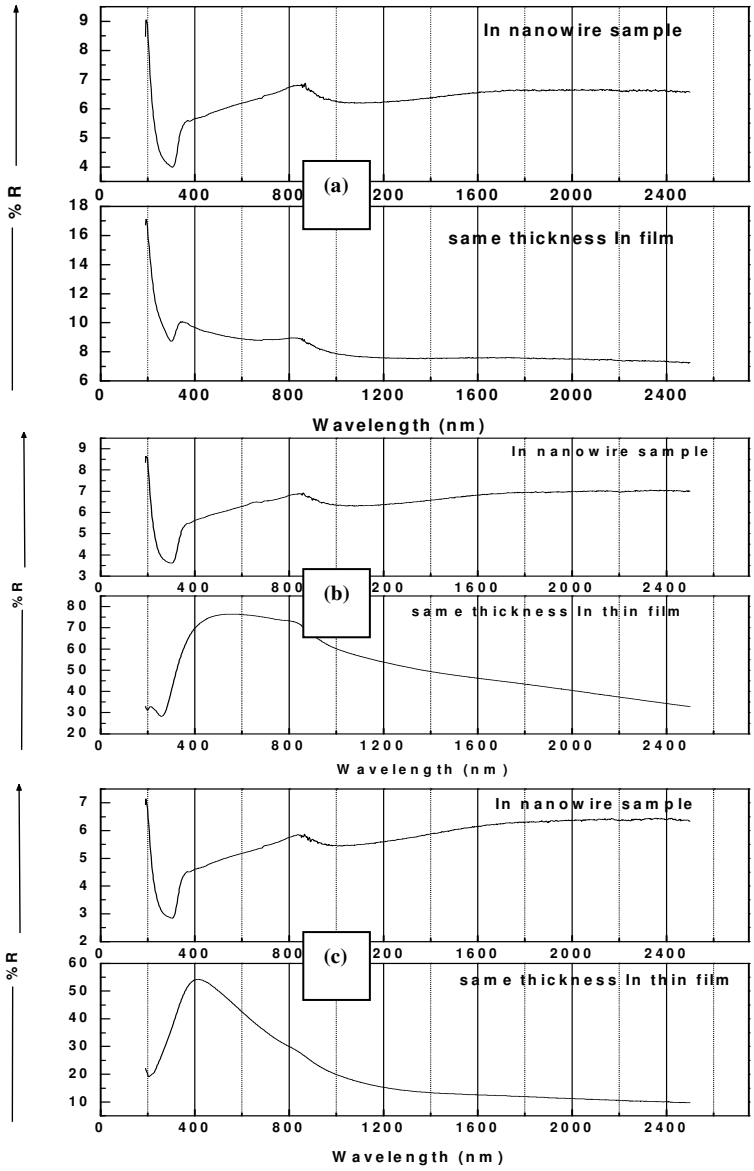

Figure-3.36 Optical reflection spectra for nanowire sample and corresponding untemplated thin film for (a) 60nm coating, (b) 15nm coating, (c) 10nm coating.

(e) Silicon

Microstructure

For silicon thin film deposited inside the trench template; it was observed that the growth follows similar pattern as is the case with other materials. At 30nm coating

organized nanoparticles form and at higher thickness of 60 nm coating, nanowires form (Figure 3.37)

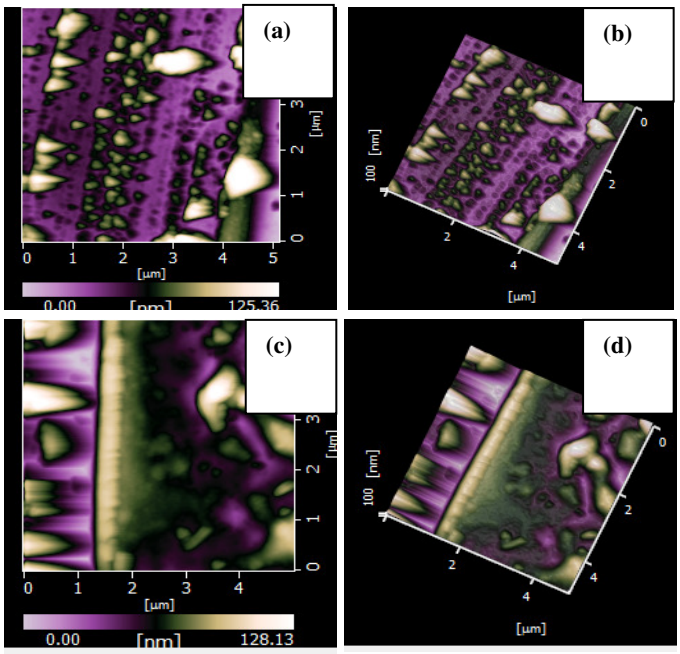

Figure 3.37 AFM images in DFM mode for templated growth of silicon (a) and (b) 30nm coating, (c) and (d) 60 nm coating.

References

1. M. R.Black, Y. M.Liu, S. B.Cronin, O. Rabin, M. S. Dresselhaus, Phys. Rev. B, 65,195417 (2002).

2. Y. Lei, L. D. Zhang, Jour. Mater. Res., 16, 1138 (2001).

3. K. Nielsch, R. B. Wehrspohn, J. Barthel, J. Kirschner, U. Gösele, S. F. Fischer, H. Kronmüller, Appl. Phys. Lett., 79, 1360 (2001)

4. O. Gurlu, O. A. O. Adam, Appl. Phys. Lett., 83, 4610 (2003)

5. J. L. Li, X. J. Liang, J. F. Jia, X. Liu, J. Z. Wong, E. G. Wang, Q. K. Xue, Appl. Phys. Lett., 79, 2826 (2001)

6. J. G. Partridge, S. A. Brown, A. D. F. Dunbar, M. Kaufmann, S. Schott, M. Schulze, R. Reichel, C. Seigert, R. J. Blaikie, Nanotechnology, 15, 1382 (2004)

7. J. G. Partridge, S. A.Brown, C. Seigert, R. Neilsen, A. D. F. Dunbar, R. J. Blaikie, Microelectr. Engg., 73, 583 (2004)

8. J. G. Partridge, S. Schott, A. D. F. Dunbar, M. Schulze, S. A. Brown, A. Wurl, R. J. Blaikie, IEEE Trans. Nanotechnol., 3, 61 (2004)

9. J. Schmelzer Jr., S. A. Brown, A. Wurl, M. Hyslop, R. J. Blaikie, Phys. Rev. Lett., 88, 226802 (2002)

10. K. M. Byun, S. J. Kim, D. Kim, Opt. Exp., 13, 3737 (2005)

11. S. Karim, M. E. T. Molares, A. G. Balogh, W. Ensinger, T. W. Cornelius, R. Neumann, Poster presentation, TNT, Grenoble France. (2006)

12. Q. Xu, J. Bao, F. Capasso, G. M. Whitesides, Angewandte Chemie, 118, 3713 (2006)

13. J. R. Krenn, B. Lamprecht, H. Ditlbacher, G. Schider, M. Salerno, A. Leitner, F. R. Aussenegg, Europhys. Lett., 60, 663 (2002)

14. J. R. Krenn, J. Felid, J. Aubard, G. Levi, J. R.Krenn, A. Hohenau, G. Schider, A. Leitner, F. R. Aussenegg, , Appl. Phys. Lett., 82, 3095 (2003)

15. Y. Yang, S. Matsubara, M. Nogami, J. Shi, W. Huang, Nanotechnology, 17, 2821 (2006).

Electric field induced nanostructuring

Abstract

Electric-field-induced nanostructuring effects for thin films and surfaces, such as organization into an array of nanoparticles, formation of nanowires and transition from amorphous to nanocrystalline states, are demonstrated. It is further shown that the nanostructures can be manipulated by simply changing the direction of the applied field. Control parameters include separation of field probes (2–5mm), duration (20–60 s) and direction of the field applied, and thickness (10–100nm). High fields cause field-induced emission in the films. It is observed that while the microstructural reconstruction of the surfaces can be manipulated, the amorphous–crystalline transition is irreversible. Indium thin films show substantial shift in surface plasmonic peak position under the influence of the applied field. Grain growth, crystallization and organization have distinct energy barriers. Electric field treatment has also been employed to nanostructure single crystal silicon surfaces. As the field intensity is increased, first nanopores form with some small nanoparticles spread nearby, then large clusters of nanoparticles form and just above the spark threshold, formation of trench like structure is observed. Field nanostructuring of single crystal silicon surfaces makes them absorbing and nanocrystalline.

3.3.1 Silicon wafer

[A] Introduction

Quantum confinement effect plays an important role in optical absorption and luminescence in nano-scale particles and structures of semiconductors [1]. Silicon nanocrystals are widely considered a material with great potential for a wide spectrum of applications and novel devices such as single electron transistors [2], vertical transistors [3], and floating gate memory devices [4-7] as photoluminescent material [8], light emitting devices (LEDs) [9], quantum dot lasers [8], chemical sensors, and molecular electronics [10]. A wide spectrum of synthesis methods is known to produce silicon nanocrystals. Liquid phase processes [11-14] are widely established for the production of silicon quantum dots. Unfortunately, none of the liquid phase approaches which are known to yield narrow size distribution; has so far resulted in the highly desirable high-yield production of silicon nanocrystals. Gas-phase processes do have high processing rates, but they all suffer from rapid particle agglomeration due to the fact that particles are usually electrically neutral. Semiconductor nanostructures are conventionally fabricated by dry fabrication methods e.g. electric spark processing [1], gas evaporation [15], rf magnetron co-sputtering [16, 17], cluster-beam evaporation [18] etc. Agglomeration of nanoparticles is a severe problem, since it usually annihilates the desired nanoparticle properties. Therefore, new approaches of semiconductor nanocrystal formation have to evolve. Here, we report on very economic novel approach for semiconductor nanoparticle formation by the application of DC electric field in the range as low as 0.1-1.5 kV/cm. We demonstrate the surface phenomena using dynamic force microscopy and optical microscopy of the nanostructured surfaces. Effect of field treatment has been studied for long range crystalline order, specular reflection and photoluminescence spectra for the nanostructured surfaces.

[B] Results and discussion

As values of the DC electric field treatment were increased progressively onto samples of cleaned [400] silicon surfaces, just above the critical fields, plasma was seen to form in the vicinity of the surface and along the line of field. These experiments were carried out on wafers placed on paper sheet and it was found to be completely burnt on application of field. This confirms the high temperature

developed as a result of application of electric field. Threshold field values for breakdown (where visible spark occurred) were 0.66 kV/cm for silicon.

(i) Microstructure

Optical microscopic images shown in Figure 3.38(a) indicate the formation of 20 μm wide linear trench. At the location of the electrode pin however, there is an evidence of explosion (Figure 3.38(b)). Material is visibly sprinkled around the electrode pin and the diameter of the area where visible effects can be seen in the image is approximately 300 μm, out of which the central part of diameter 150 μm gives clear evidence of local melting.

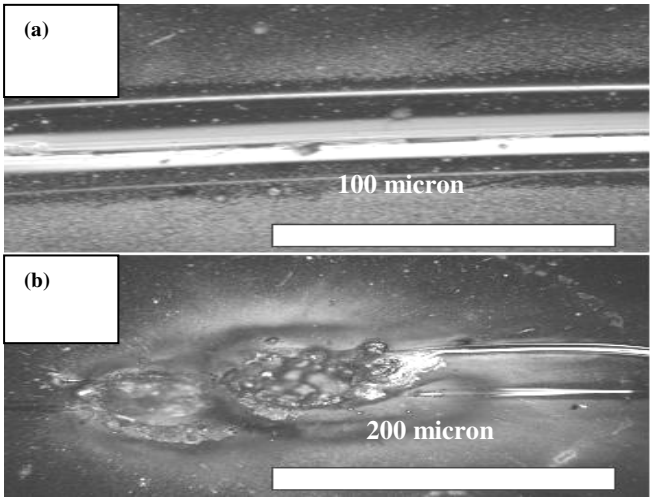

Figure -3.38 Optical microscopic images for trench formation when electric field of magnitude 1.33 kV/cm is applied onto wafer surface for (a) trench formed in between two electrode pins, (b) explosion site where exactly, one of the electrode pin was situate

Application of electric field in the range of 0.1-1.5 kV/cm on the silicon [400] surface (Fig-3.39(a)) showed variety of nanostructures including nanoparticles (Fig-3.39(b)), 30-100nm diameter nanopores (Fig-3.39(d)), and clustered nanograins (Fig-3.39(e) and (f)).

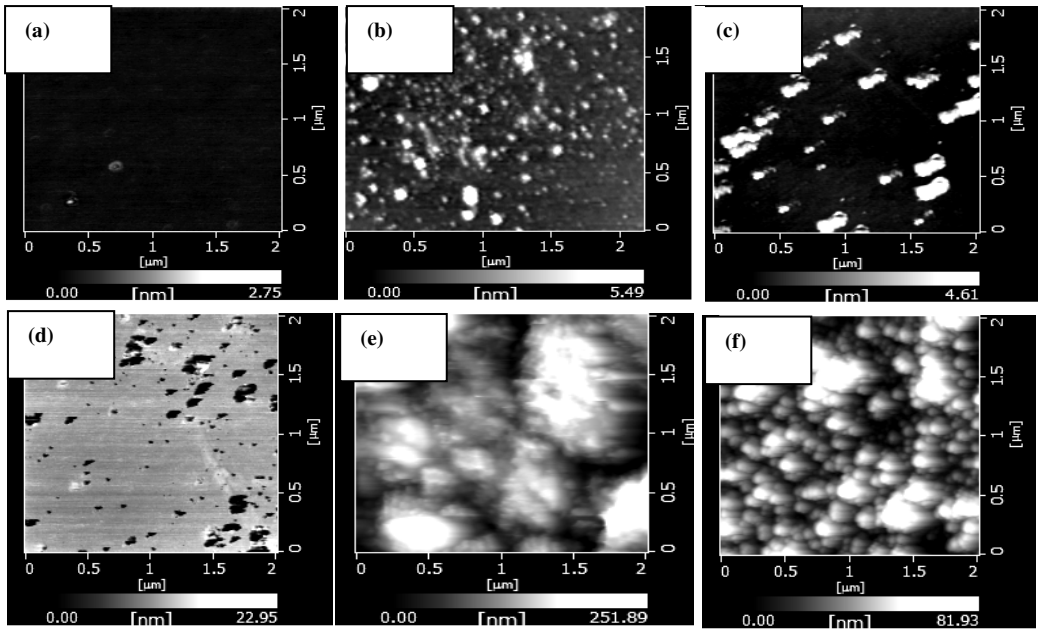

Figure-3.39 Electric field nanostructured surface of silicon wafer at the field values (a) 0V, (b) 0.16 kV/cm, (c) 0.33 kV/cm, (d) 0.50 kV/cm, (e) 0.66 kV/cm, (f) 1.33 kV/cm

To understand the grain growth better, grain size distribution (Figure-3.40) were plotted for the different field values. There is a clear grain growth as field is increased from 0.16 kV/cm to 1.33 kV/cm. Average grain size for silicon increases from 67nm at 0.16 kV/cm to 170nm at 1.33 kV/cm.

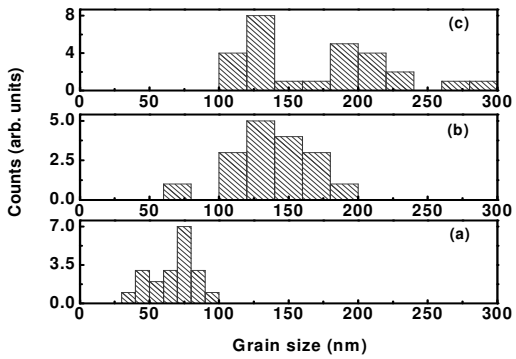

Figure-3.40 Nanoparticle size distribution for field nanostructured silicon surface (a) 0.16 kV/cm, (b) 0.33 kV/cm, (c) 1.33 kV/cm.

(ii) Long range crystalline order

As the field increases, the [400] oriented silicon surface turns nanocrystalline in a systematic manner (Figure-3.41). Nanocrystallization of the silicon surface in general can be attributed to the rapid heating and cooling as a consequence of the applied field leading to the melting of the surface and therefore quenching into the nanocrystalline state. This means that the effect of field is to reconstruct the silicon single crystal into silicon nanocrystal embedded in an amorphous SiO_2 matrix.

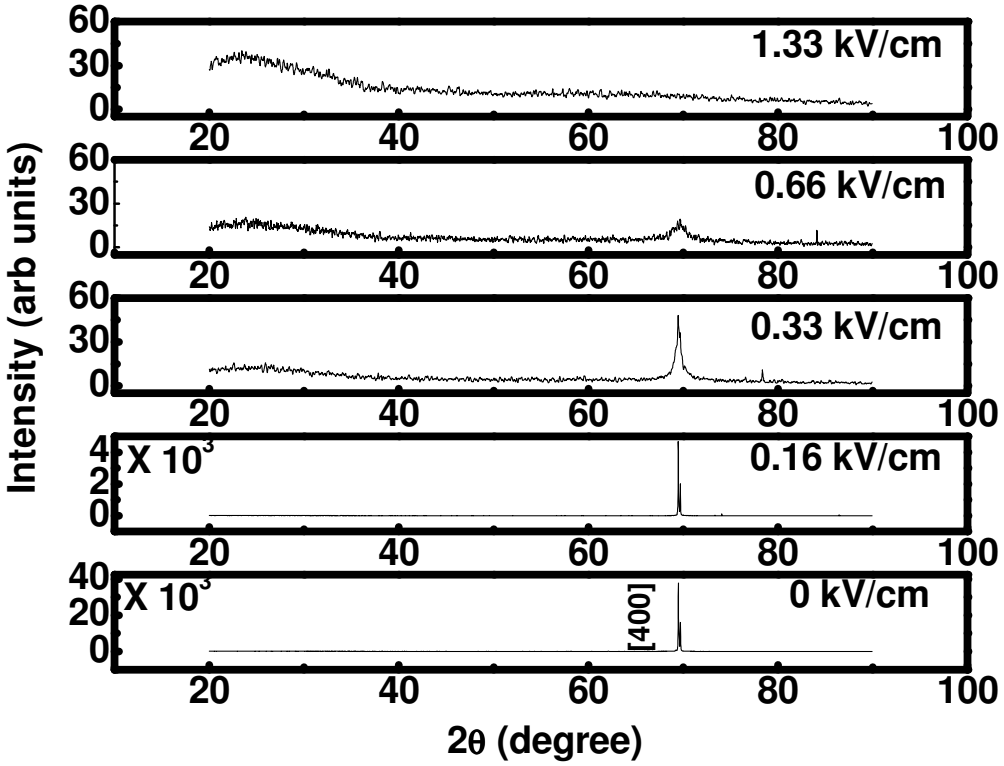

Fig-3.41 X-ray diffraction pattern for (a) untreated silicon, (b) 0.33 kV/cm, (c) 0.66 kV/cm, (d) 1.33 kV/cm.

(iii) Specular reflectance

Specular reflectance reduces systematically with the increase of the field for the treatment of wafers upto maximum 15-20% (Fig-3.42).

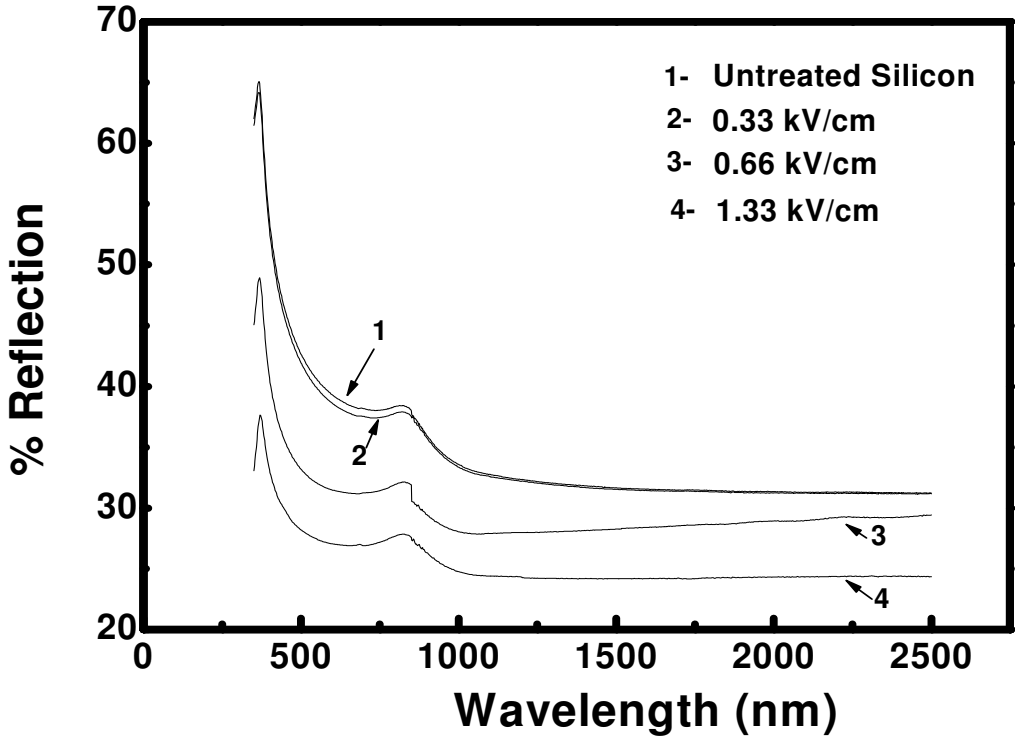

Figure 3.42 Specular reflection spectra for field nanostructured silicon surfaces.

(iv) Photoluminiscence

Photoluminescence spectra shows peak at approximately at 487nm (green), which demonstrates very large bandgap of silicon nanocrystal formed in the process (Fig-3.43). Inset image shows reflection mode optical confocal microscopic image for the field nanostrcutured surface at the site chosen for PL spectra.

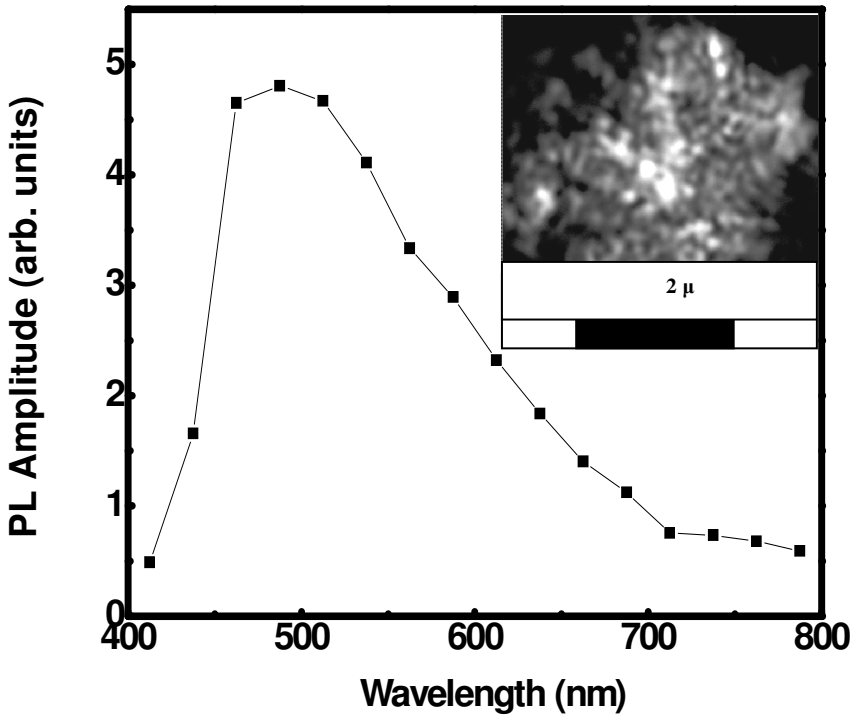

Figure-3.43 Photoluminescence spectra for field nanostructured silicon surface at 0.66 kV/cm. Inset picture is the reflection mode image.

3.3.2 Discussion: Silicon wafer

The spark threshold of field for silicon has been found to be very small value in our experiments most possibly due to doped n-type nature of silicon wafer used. Dopant sites are the defect sites which give a channel of conduction and which in turn reduces the critical breakdown field. Here, Joule heating of material is responsible for the grain growth. With the increase of field value grain size increases but its increase becomes milder at higher field values and in principle, grain size growth should peak at the supersaturation limit. Beyond the supersaturation limit, grain size should decrease again. Nanostructuring of the surface starts far below the spark threshold values. When field value is progressively increased, the local temperature is increased tremendously, which gives rise to extremely high strain gradient radially with respect to the field line. The melting threshold is far below the spark threshold and on increasing the field further, the surface ruptures causes cracks to occur and porous

structures to form. The material then comes out of the pores. At very high field, solid material vaporizes and channel forms in the direction of field. Due to the back pressure of air, it condenses back on the wafer in the form of nanoparticles. Defect sites obstruct the charge flow and get charged at the interface which gives extra heating locally and brings local melting and nanostructuring effects below spark threshold. All these defect sites are the most possible sites of pore formation. Nanopore positions are expected to follow the defect profile in the material.

Material specific properties like melting point, electric conductivity, thermal conductivity, density of material, crystalline texture and doping percentage etc. determine the breakdown voltage and are responsible for the nanostructuring extent. The size of nanoparticles achieved in our experiments are in the range 30-200nm. This is the nanoparticle size where size effects can be exploited for optical, electronic and optoelectronic applications.

3.3.3 Thin films

[A] Introduction

Physical vapor deposition (PVD) processes, when used to deposit thin films at ambient temperature, produce thin films that lack long-range order and have to be heated during or after deposition to achieve long-range order. There have been reports in the past [19-23] that a field can be applied during PVD to obtain crystalline films. There has also been reference to enhanced crystallization by subjecting the films to an electric field during post-deposition heating [24-29]. In contrast, we demonstrate in our work that the films, under the influence of the field, crystallize without an external thermal input with crystallite sizes in the nanometer range. Furthermore, there is morphological reconstruction that leads to the formation of nanoparticle arrays, nanowires and nanopillars. This, we believe, it will have an enormous impact on nonlithographic approaches to nanostructuring thin films. Nanostructuring can be achieved by an optimal combination of probe separation, field strength, direction and duration. The current method can also be used to obtain nanostructures in the direction normal to that of the growth, which is extremely useful for microelectronics applications This effect is demonstrated in Ni, In, Au and Si thin films (<100 nm)

deposited by PVD (Ni, In and Si by evaporation and Au by sputtering), subjected to a post deposition DC electric field in the range of 1–3.3 kV/cm, on their structure and nanostructure. Further, physical property like surface plasmonic behaviour was also looked into. Control parameters for such an experiment are also presented.

[B] Results and discussion

(a) Nickel thin films

(i) Microstructure

In the study, all the films deposited were in the thickness range of 10–100 nm and therefore were expected to have an island-like microstructure, typical of thin evaporated films. Some signs of grain size change are visible (Figure 3.44) for 15nm nickel thin film after the field application; however no organizational effect were observed for this thickness of nickel thin film.

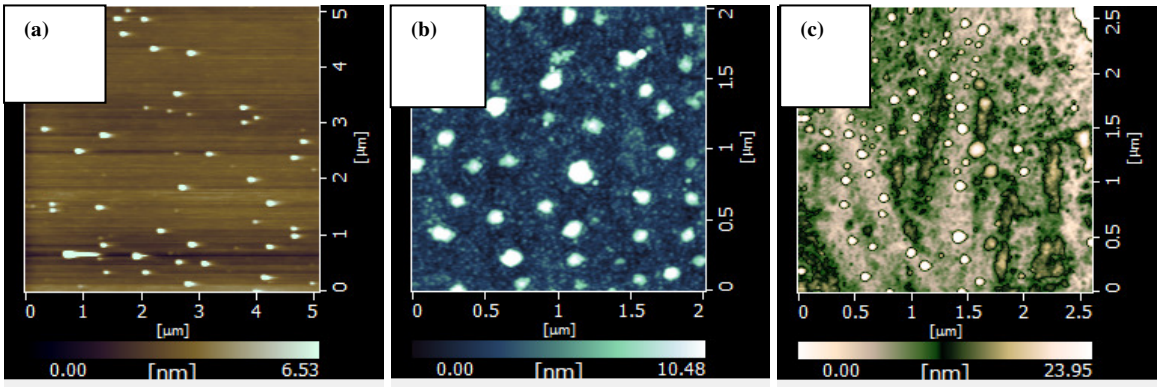

Figure- 3.44 Atomic force microscopic image for (a) 15nm nickel thin film, (b) after the application of 3.3 kV/cm, (c) after the application of 3.3 kV/cm and 3.3 kV/cm perpendicular to each other.

The morphology of the as-deposited 50 nm nickel thin film shown in Fig. 3.45(a) indicates the formation of nanoparticles with sizes in the range of 70–200 nm. The films were subjected to different electric fields sequentially between 1 and 3.3 kV/cm. It was observed that up to 2 kV/cm there were no substantial changes in microstructural features. However, at a field of 2.66 kV/cm, a remarkable change in microstructural features was visible [Fig. 3.45(b)]. The thin film surface had been reconstructed in the form of a self-organized array of nanoparticles along the direction of the applied electric field, with an average diameter that was higher than the average

diameter of the particles in the as-deposited state. To determine whether the organization could be manipulated by changing the direction of the DC electric field, a field of strength 3.3 kV/cm for 20 s was applied in the direction perpendicular to the already self-organized structure shown in Fig. 3.45(b). Indeed, the surface again reconstructed itself partially along the new direction of the applied field [Fig. 3.45(c)]. Field treatment clearly caused enhancement in the size of self-organized nanoparticles.

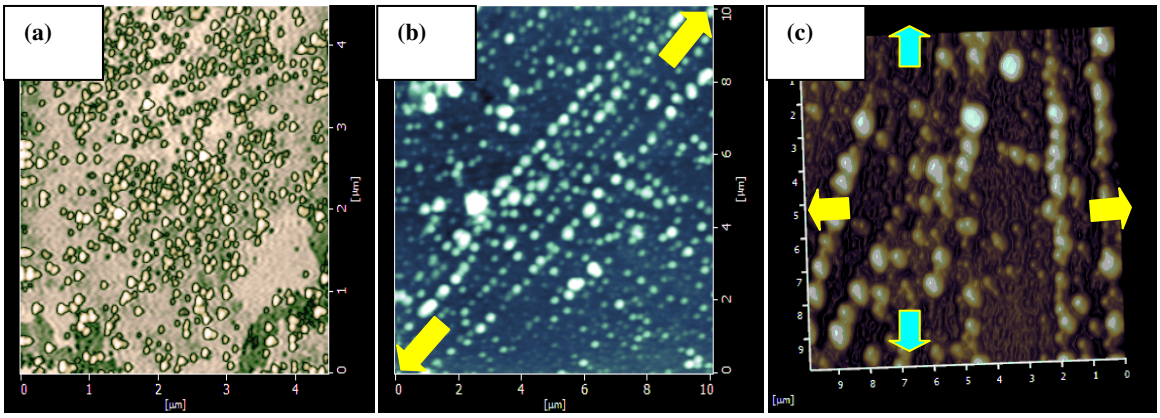

Figure- 3.45. Topographical images of the 50 nm nickel thin film (a) as-deposited, (b) after an applied field of 2.66 kV/cm for 20 s, and (c) after an applied field of 2.66 kV/cm for 20 s in the perpendicular direction (shown by yellow arrows).

The grain size distribution in the films before and after electric field treatment is shown in Figures.3.46(a)–(c). It is evident that while the as deposited films show a peak grain size of 160 nm [Fig. 3.46a)], they show a peak value of 350 nm at 2.66 kV/cm [Figure. 3.46(b)], which increased to 650 nm when subjected further to a field of 3.3 kV/cm [Figure 3.46(c)].

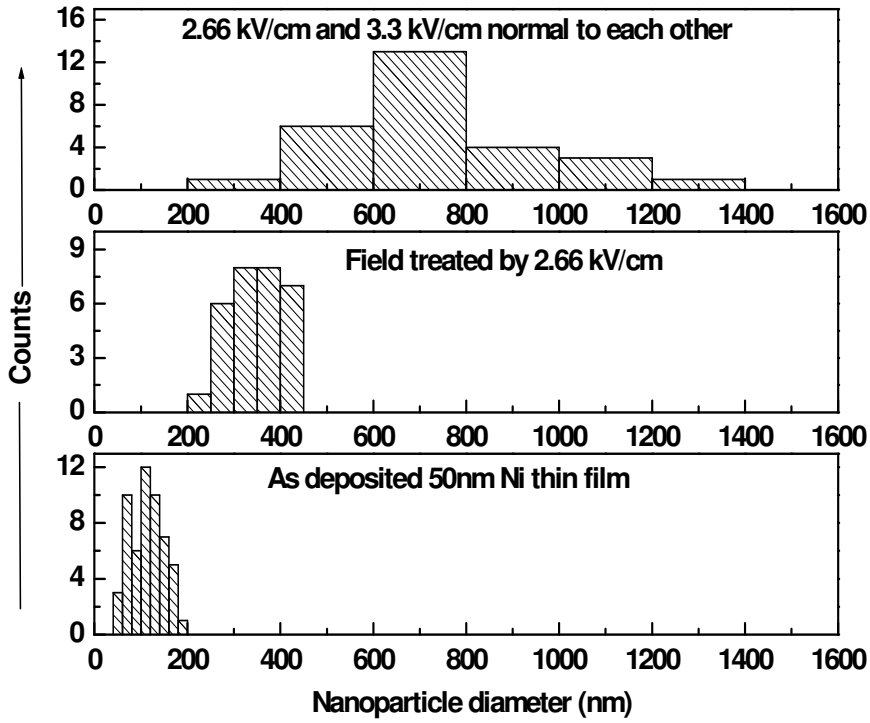

Figure- 3.46 Grain size distribution for the field nanostructured nickel thin films, (a) untreated 50nm nickel thin film, (b) treated by 2.66 kV/cm field for 20s, (c) treated by 2.66 kV/cm field for 20s after the first treatment in perpendicular direction.

Longer duration of application of field gives rise to the formation of nanowires with diameter in the range of 40–80 nm and a length of up to 15 microns (Figure 3.47(a)). Thermal stability of the nanoparticle array was checked by leaving the samples in an oven at 473 K for 30 minutes and it was observed that the organization actually disappears (Figure 3.47(b)). The possibility of the use of field application technique to grow vertical nanopillars was explored by fabricating nickel thin film sandwiched between two layers of silver coating onto the BSG substrate. A field of 0.66 kV/cm was sufficient to give rise the growth of vertical nanopillars (Figure 3.47(c)). From this figure the formation of vertical nanopillars is evident, clearly indicating that grain alignment is along the direction of the applied field.

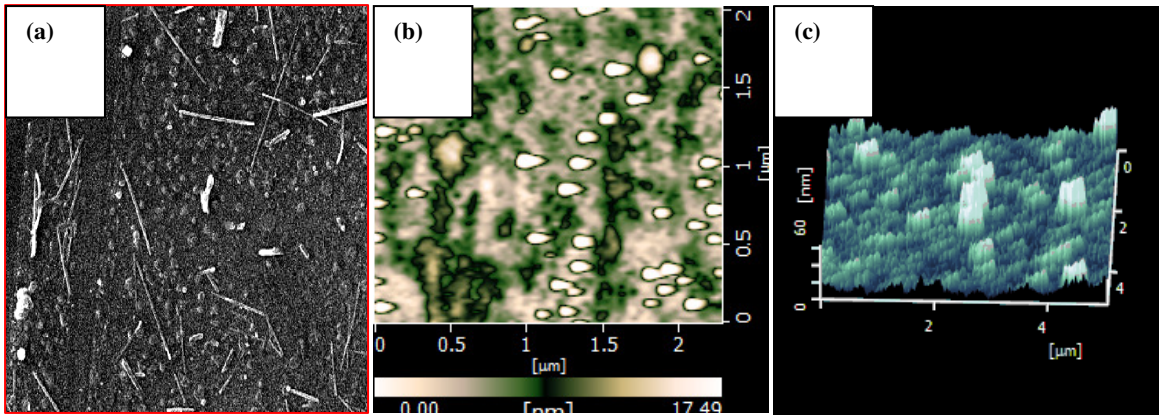

Figure 3.47 (a) SEM image of field nanostructured nickel thin film by 2.66 kV/cm for 1 minute, AFM image for (b) field nanostructured nickel film after the heating at 200 ^{0}C for 30 minutes, (c) vertical nanopillar growth achieved by the application of 0.66 kV/cm for 20s in the direction perpendicular to the film plane.

Nickel thin films on silicon and stainless steel substrate were also subjected to field nanostructuring. However; no organized growth was observed on these surfaces. (Figure 3.48)

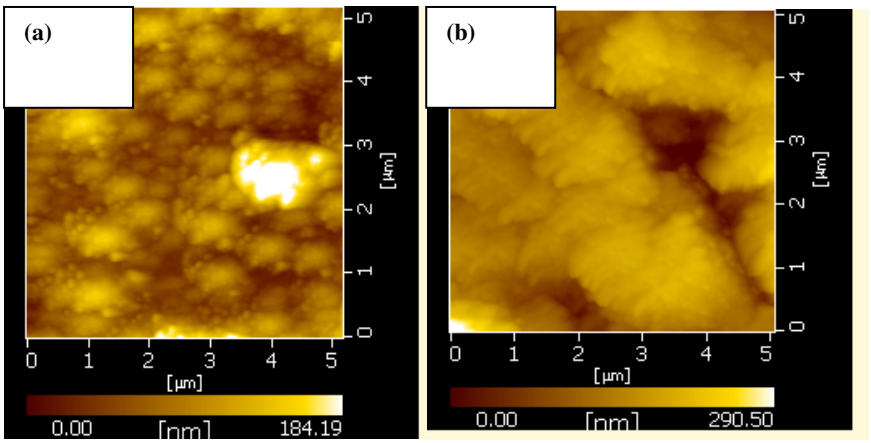

Fig. 3.48 AFM images for nanostructured nickel thin films after the application of 2.66 kV/cm coated on (a) silicon substrate, (b) stainless steel substrate.

The morphology of the 70 nm thin nickel film, shown in Fig. 3.49(a), revealed densely packed particles with a diameter in the range of 120–150 nm. In this case, the microstructural reconstruction due to the field started at a value as small as 1.3

kV/cm, against 2.66 kV/cm in the case of 50 nm film. Field treatment of 1.3 kV/cm for 20 s gave rise to self-organization of closely packed nanoparticles in the direction of the field and an enhanced average particle size of 150 180 nm [Fig. 3.49(b)]. Even in this case, the manipulation of already-organized particles was studied by applying a 2 kV/cm field in the direction perpendicular to the self-organized structure. It is evident from Fig. 3.49(c) that the organization of particles is destroyed and the surface is reconstructed in the form of large aggregates with an enhanced size (300-600 nm) in the direction of the final field. For extended durations of the applied field, i.e. >20s, the surface reconstruction of the thin film was followed by an electric breakdown.

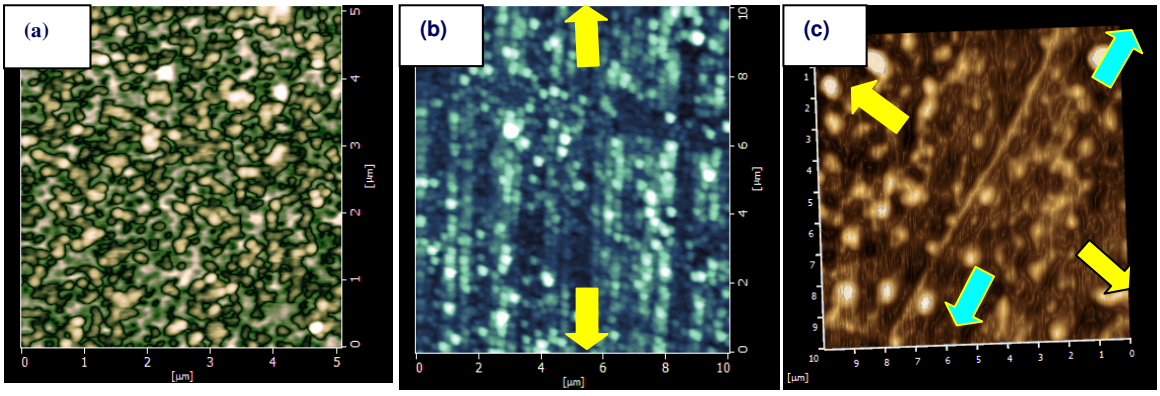

Fig. 3.49 Topographical images of the 70 nm nickel thin film (a) as-deposited, (b) after an applied field of 1.33 kV/cm for 20 s, and (c) followed by an applied field of 1.98 kV/cm for 20 s in the perpendicular direction (yellow arrows).

A further observation was that an electric breakdown (arc) occurred at 0.66 kV/cm only for 100 nm nickel thin film, causing delamination of the film, whereas for the thinnest film (15 nm) the effects were negligible even at the highest applied field, i.e. 3.3 kV/cm (this was the limit of the power supply). These factors, therefore, determined the time, thickness and field strength limits in the current study for Ni. 100nm nickel thin film was also nanostructured by field to study the effect of coating thickness on field nanostructuring in detail and it was found that at 0.5 kV/cm field, film reconstructs itself into well aligned nanowires in the field direction.(3.50)

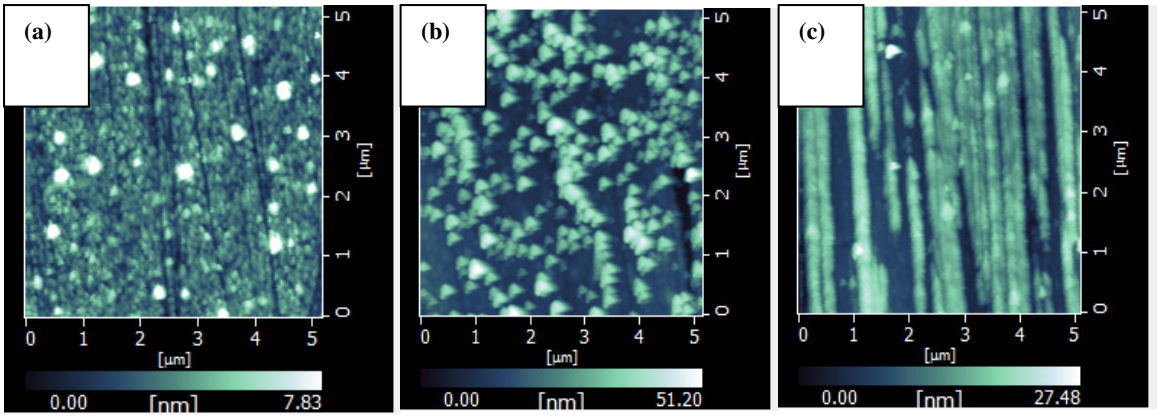

Figure- 3.50 AFM images in DFM mode for 100nm thin nickel film for (a) untreated thin film, (b) treated by 0.33 kV/cm and (c) treated by 0.5 kV/cm.

(ii) Long range crystalline order

A remarkable effect of the applied electric field was that on the crystallographic texture of the Ni films. X-ray diffraction patterns of the as-deposited 70nm nickel thin film indicate the absence of detectable long-range order [Fig. 3.51(a)]. However, the onset of nanocrystallinity is evident at a field of 1.32 kV/cm for 20 s [Fig. 3.51(b)] and the [111] peak becomes pronounced at a field of 2 kV/cm [Fig. 3.51(c)]. Crystallization at elevated temperatures in the presence of an applied field has been reported earlier. However, such an enormous effect on long range order has not been observed previously in the absence of external heating.

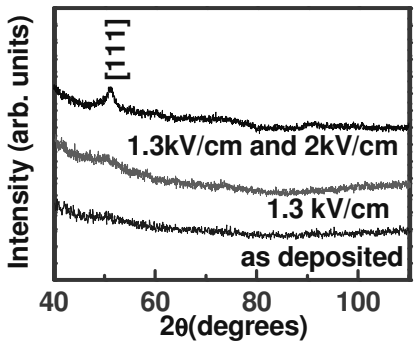

Figure 3.51 X-ray diffraction pattern for field nanostructured 70nm nickel thin films.

(b) Indium thin films

(i) Microstructure

To determine whether the observed effects were material-specific or more general in nature, indium films in the same range of thickness were subjected to the same field treatment. An electric breakdown for indium thin films occurred at 50 nm itself and at an applied field of 0.66 kV/cm. Therefore, the study was done at a lower thickness of 15nm for indium thin films, compared to the 50–70 nm range of thickness for Ni films. The morphology of the as-deposited 15-nm-thick indium films in Fig. 3.52(a) shows that the particle size is in the range of 60–120 nm. An electric field of 1.33 kV/cm for 20 s reconstructed the surface, leading to the formation of nanowires with a diameter in the range of 80–100 nm and a length of up to 5 μm [Fig. 3.52(b)]. To investigate the possible manipulation of nanowires, an electric field of 2 kV/cm was applied in the direction perpendicular to the previous field direction. It was observed that this change in direction resulted in randomization of the surface reconstruction and formation of nanowires with a larger length [Fig. 3.52(c)]. At a higher electric field of 2.66 kV/cm for 20 s, the length of nanowires extended up to 8–10microns, mainly along the direction of the applied electric field [Fig. 3.52(d)]. Thinner and longer nanowires formed when a field of 3.33 kV/cm for 20 s was applied in the direction perpendicular to the previous treatment direction with a field of 2.66 kV/cm for 20 s, [Fig. 3.52(e)]. To establish the effect of the area of electrode tip, on the nanostructuring, a field of 2.66 kV/cm was applied for 20 s on the 15nm In thin film with electrode tip diameter half of the earlier tip diameter. One observation can be made from the resulting nanostructure is that it gives more directional growth features in the field line (Figure 3.53).

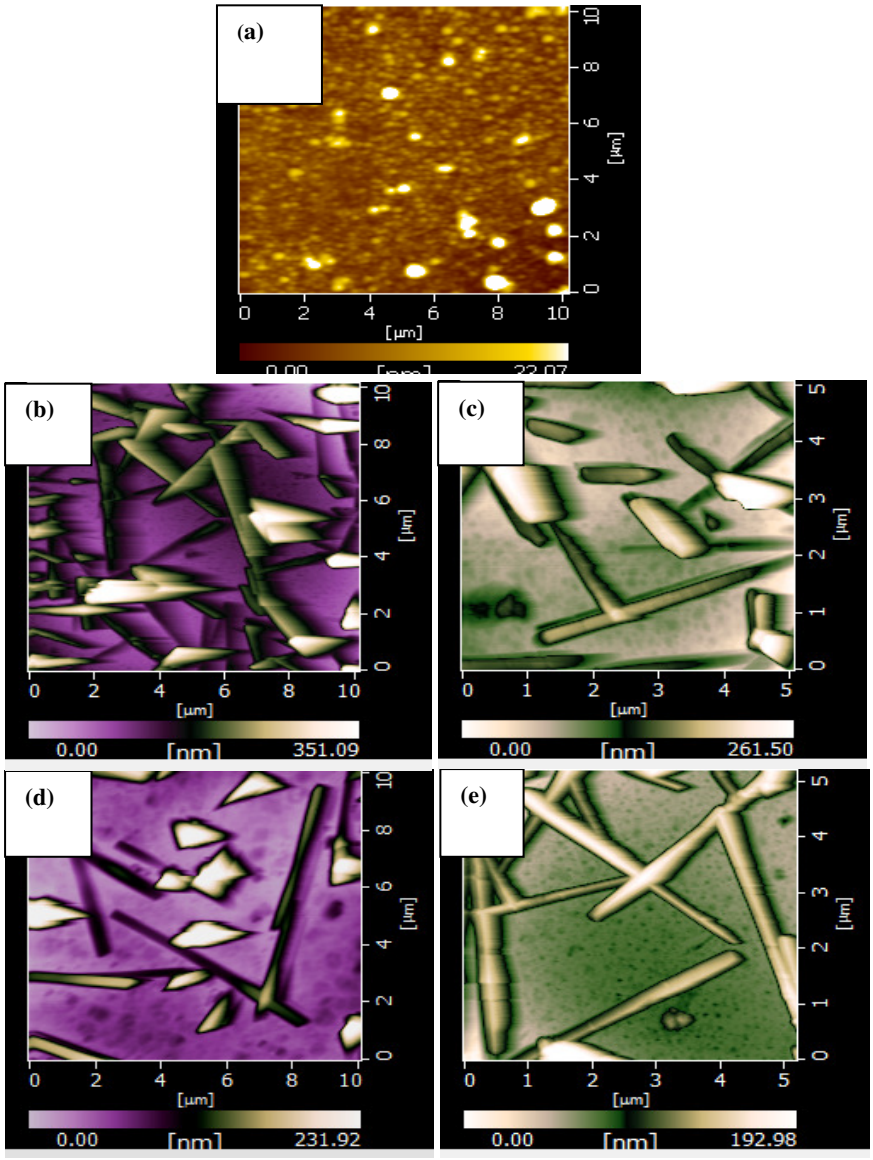

Figure- 3.52 Topographical images of the 15 nm indium thin film (a) as-deposited, (b) after an applied field of 1.33 kV/cm for 20 s, (c) followed by an applied field of 1.98 kV/cm in the perpendicular direction, (d) after an applied field of 2.66 kV/cm for 20 s, and (e) followed by an applied field of 3.3 kV/cm for 20 s in the perpendicular direction.

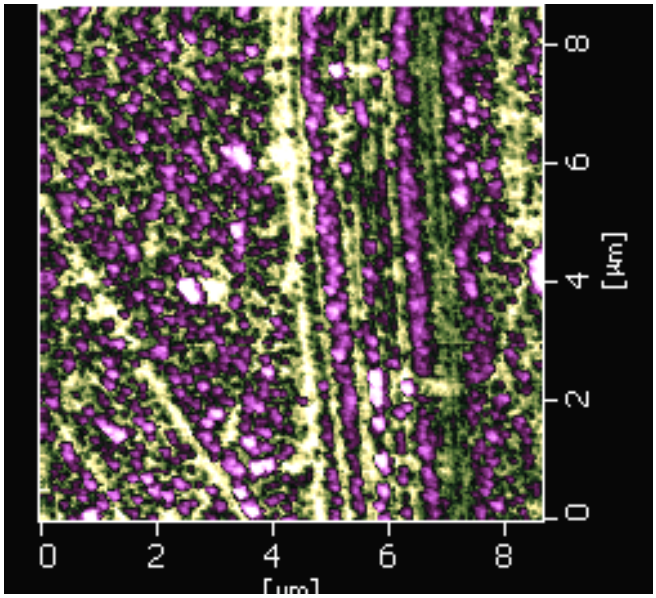

Figure- 3.53 AFM image for the resulting nanostructure onto the surface of 15nm In thin film when field of 2.66 kV/cm was applied for 20 s with smaller electrode tip area.

(ii) Long range crystalline order

The effect of the field on the crystalline behavior of In films is similar to that on the Ni films discussed earlier. The as-deposited 15 nm indium thin film was XRD-amorphous [Fig. 3.54(a)] but made a transition to the nanocrystalline state under the influence of the electric field treatment. At a field of1.33 kV/cm for 20 s, peaks due to the crystallization started evolving [Fig. 3.54(b)]. For 1.33 kV/cm and 3.33 kV/cm, applied for 20 s each and perpendicular to each other in succession, the evolution of three peaks [Fig. 3.54(c)] corresponding to the planes [112], [202] and [213] was observed. The crystallite size as calculated from the full width at half maximum (FWHM) gave a value of approximately 50 nm, which was larger than the 20 nm size observed for the Ni films.

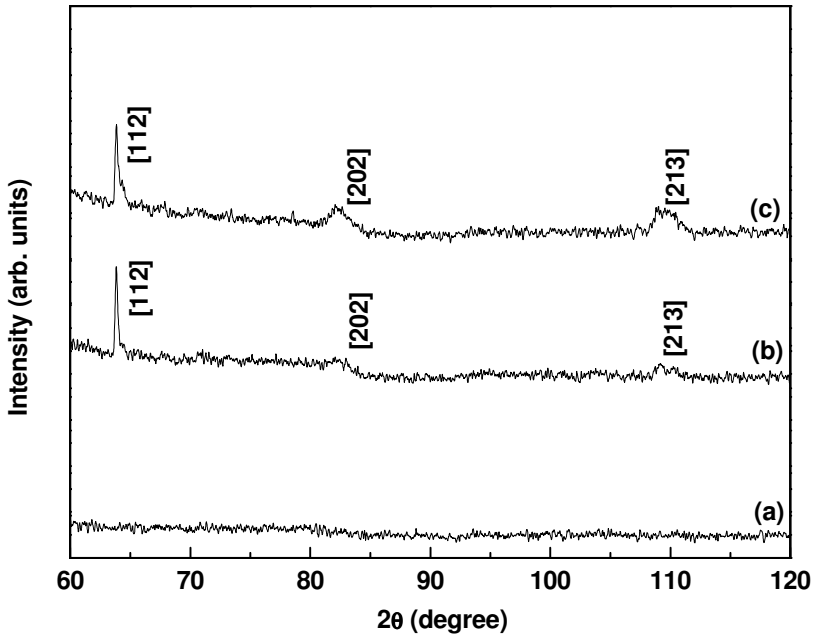

Figure 3.54. X-ray diffraction pattern for the 15nm indium thin film (a) as-deposited, (b) after an applied field of 2.66 kV/cm for 20 s, and (c) after an applied field of 3.3 kV/cm for 20 s in the perpendicular direction. [X-ray diffraction done instrument equipped with cobalt target]

To further investigate field induced nanostructuring, 10nm thick films were subjected to applied field. As is the case with nickel films, organization does not display itself below a certain thickness, and that thickness threshold is material dependent. Below that threshold only grain growth without organization is observed. Grain size was found to increase with the increase in field strength. Indium thin films that show broad particle size distribution (Figure 3.55(a)) for as deposited thin film, experience visible grain growth as the field value is increased. At the field strength 3.3 kV/cm (this was the limit of the instrument) huge grain growth is apparent. (100-300nm) (Figure 3.55(b)).

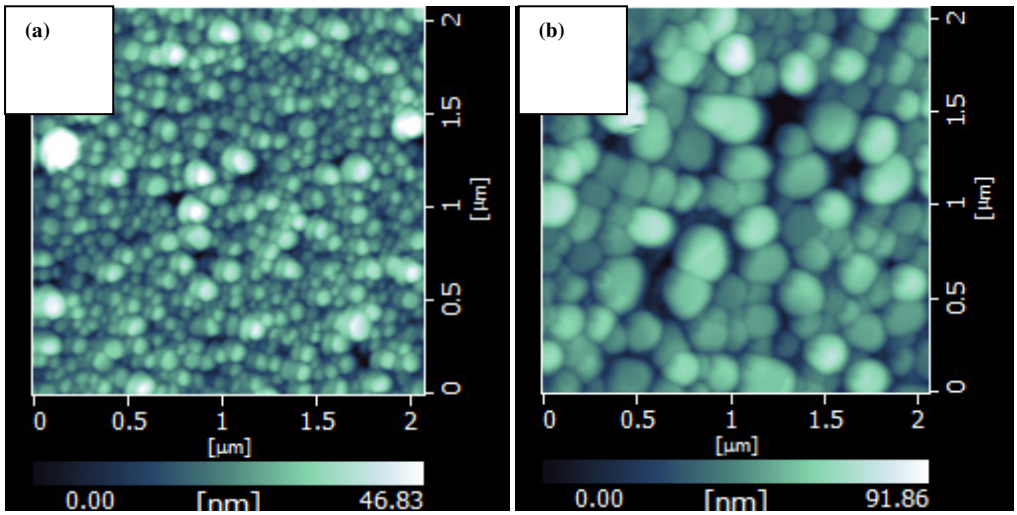

Figure-3.55 Atomic force microscopic image in DFM mode for (a) as deposited 10nm indium thin film, (b) after the application of 3.33 kV/cm.

The effect of field application is also evident in the evolution of long range crystalline order. The as deposited 10nm amorphous In thin film (Figure 3.56(a)) becomes nanocrystalline. (Figure 3.56(b)) on being subjected to an applied field of 3.3 kV/cm.

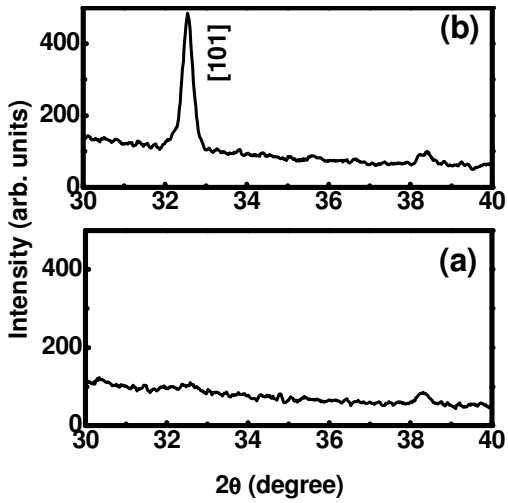

Figure-3.56 X-ray diffraction pattern for (a) untreated 15 nm indium thin film, (b) after the application of 3.3 kV/cm. [X-ray diffraction was done with another instrument equipped with Cu target.]

(iii) Specular reflectance

The effect of field application was also observed on the specular reflectance spectra. Surface plasmonic peak is observed to shift quite substantially.(Figure 3.57). As observed earlier, with the application of field both shape and size changed for the grains. Therefore there is a combination of these effects on surface plasmonic behaviour.

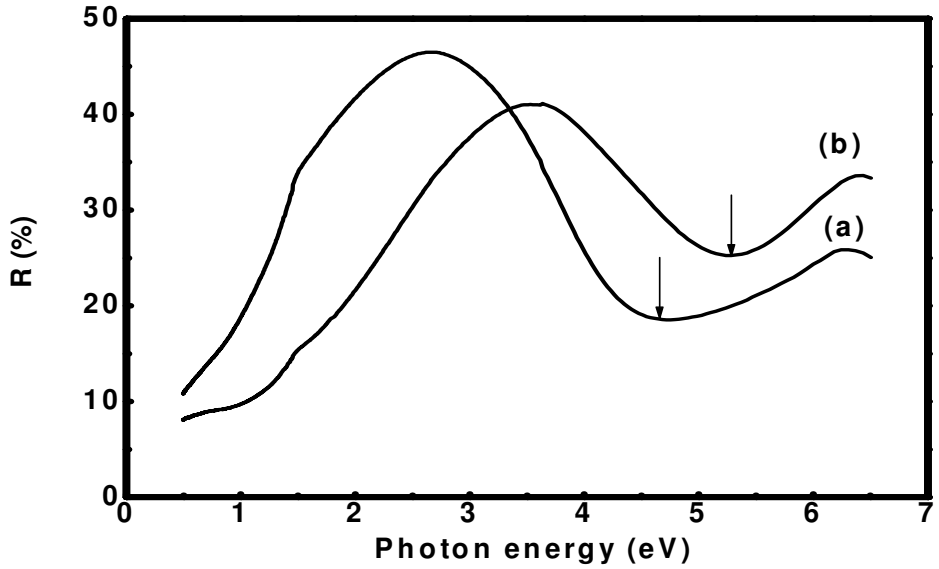

Figure-3.57 Specular reflection spectra for 10 nm indium thin film, (a) as deposited, (b) after the application of 3.3 kV/cm.

(c) Gold thin films

(i) Microstructure

In the case of DC sputtered 40nm gold thin films, when subjected to electric field treatment a process of densification of the films can be observed (in figure 3.58)). The as deposited films show well separated particles which at a field of 0.4 kV/cm exhibited a dense well ordered nanostructured morphology with an average diameter of 30-40 nm. At a higher field strength 0.66 kV/cm, the film delaminates and is accompanied by field induced emission in the form of arcing. Very fine and well

separated nanoparticles having broad distribution (20-80nm) is observed for as deposited 40nm gold thin films. The surface reconstructs into a variety of nanostructural features e.g. densification, monodisperse particle formation and again surface smoothening at the surface. Surface feature looks quite smoother for 0.66 kV/cm field treated film with some buried nanoparticles (100-160nm) and visible nanopores. For the gold case particle sizes do not change drastically in contrast to that for indium case.

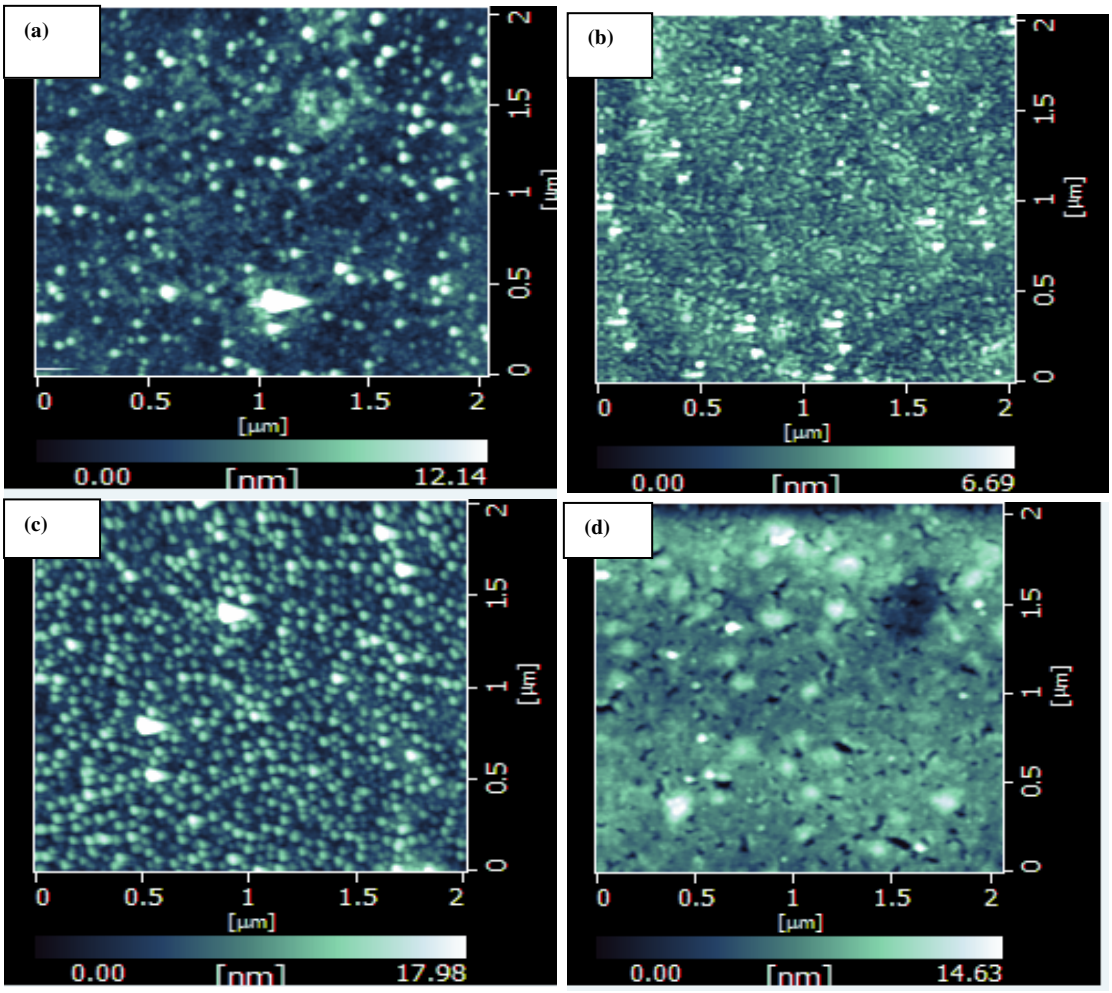

Figure-3.58 AFM image of nanostructured DC sputtered 40nm Au thin films for electric field nanostructuring (a) as deposited, and after subjecting the films to a field strength of (b) 0.4, (c) 0.5, (d) 0.66 kV/cm.

(ii) **Long range crystalline order**

With the application of DC electric field, long range crystalline order has also been observed to be enhanced for gold thin film. Gold crystallizes into approximately 35nm nanocrystal ([111] peak) at 0.66 kV/cm. (Figure 3.59)

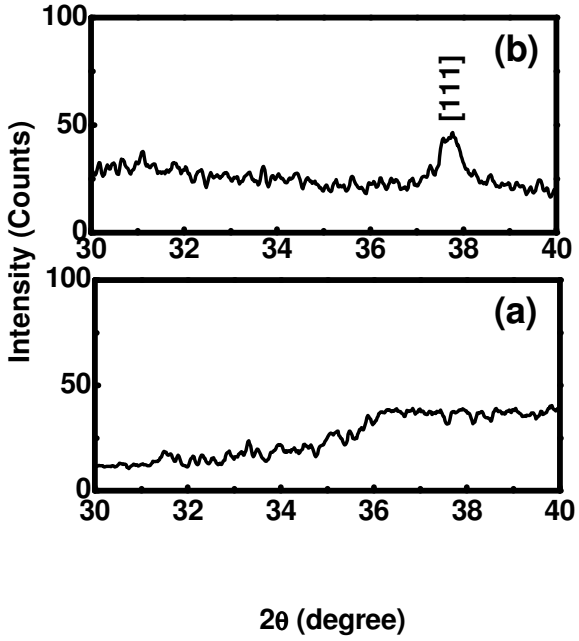

Figure-3.59 X-ray diffraction pattern for (a) untreated 40 nm gold thin film, (b) after the application of 0.66 kV/cm field.

(iii) Specular reflectance

As a consequence of grain growth and evolution of long range crystalline order, the surface plasmonic peak gets blue shifted, although the extent of shift for the gold case is marginal (just 0.05 eV at 0.66 kV/cm). Such a small shift in gold case is attributed to the minimal grain growth experienced by gold thin films. (Figure 3.60).

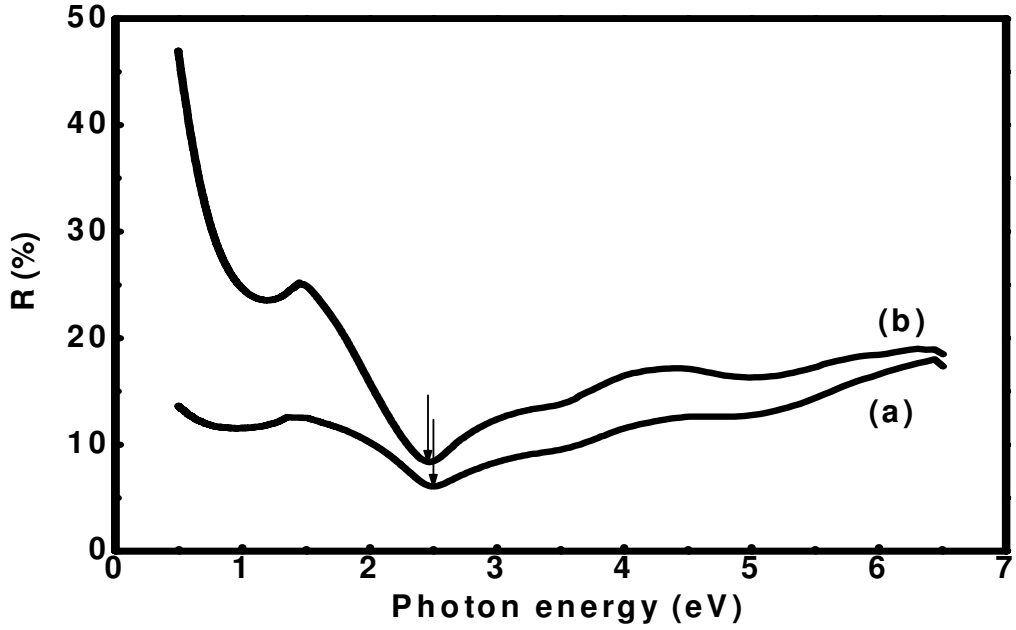

Figure-3.60 Specular reflectance spectra for 40 nm gold thin film,(a) as deposited, (b) after the application of 0.66 kV/cm field.

(d) Silicon thin films

(i) Microstructure

Silicon being a semiconductor, the effect of applied field on nanostructuring is expected to be different as compared to that for the metals. To explore this, 30nm silicon thin films deposited by thermal evaporation (figure 3.61) and ion beam sputtering (figure 3.62) were subjected to field upto 3.3 kV/cm for 20 seconds. In both the cases, grain growth is quite apparent however there is no organization even at extreme fields. Some evidence for crystallization in the form of very small peak corresponding to [400] plane appeared after the application of 3.33 kV/cm for 20 seconds. (Figure 3.63)

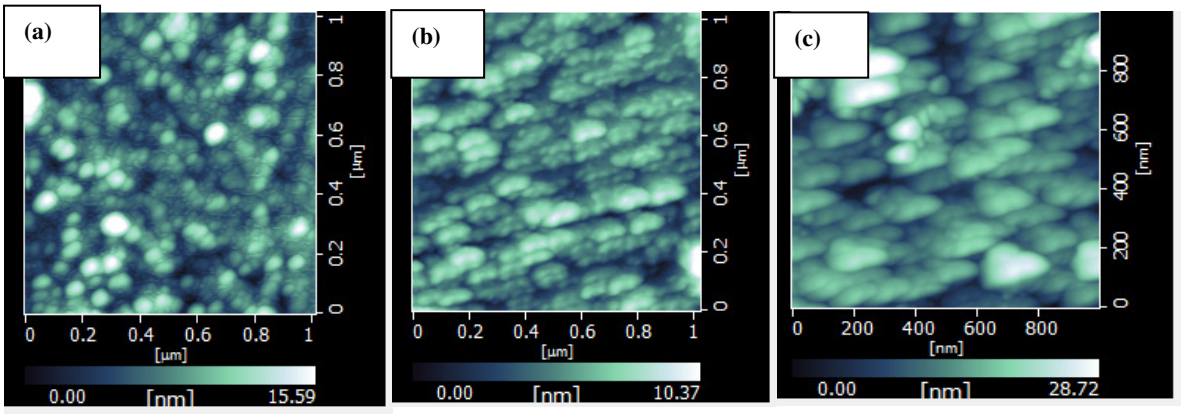

Figure 3.61 AFM images for field nanostructured thermally evaporated 30nm silicon thin films for (a) untreated thin film, and after the application of (b) 2.66 kV/cm and (c) 3.33 kV/cm.

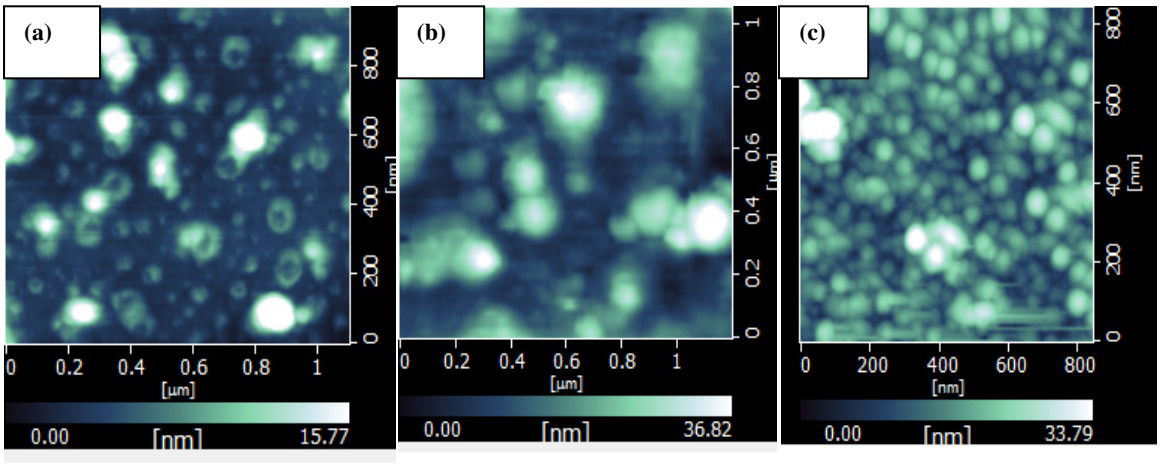

Figure 3.62 AFM images for field nanostructured ion beam sputtered 30nm silicon thin films for (a) untreated thin film, after the application of (b) 2.66 kV/cm and (c) 3.33 kV/cm.

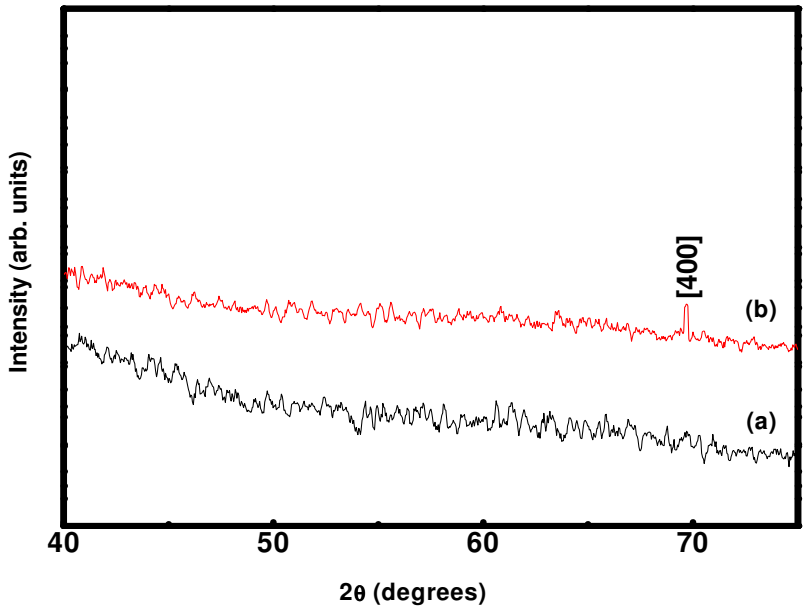

Figure 3.63 X-ray diffraction pattern for (a) as deposited 30nm thin film and (b) after the application of 3.3 kV/cm field.

3.3.4 Discussion: Thin films

It is evident from the observations presented earlier that there are three effects of the applied electric field on the films. These are (1) grain growth, (2) alignment of grains along the direction of the applied field and (3) crystallization of the films. Each of these has a threshold, energy above which the effects are evident. The process of grain growth has the lowest threshold, followed by that for the alignment of these grains, and the highest is the threshold for crystallization of the films.

We now examine the reasons for the existence of threshold field strength. In the presence of a DC electric field of magnitude less than 10 kV/cm, the energy transferred into the molecule is low compared to the bonding energy, but still contributes to the total internal energy of the system. It has been shown [30] that the introduction of an uncharged conductor into an electric field reduces the total energy of the system when it is attracted toward the field if it is located outside it. Similarly, a

conductor charged or uncharged cannot remain in equilibrium in the presence of an electric field. Consequently, if the conductor is bound, as in the present case of the film on a substrate, then it will undergo a change in shape and size, depending on the conditions at the surface and the duration of the application of the field. The magnitude of the electric field through the conducting thin film can therefore be employed to produce local nanostructural changes in the direction of the applied field and its proximity.

Accelerated crystallization has been reported when a DC field is applied in conjunction with heating. It has also been found to accelerate the dissolution of metallic nanoparticles buried inside glass substrates.[31] A very high dc electric field has been reported earlier to give rise to rapid crystallization of thin films.[32,33] Such an electric field can generate a very high temperature, due to Joule heating causing thermal migration of particles and their agglomeration. Grain growth is usually stimulated in the presence of an electric field. Without any external field, the grain growth of a polycrystal is driven by the curvature of the grain boundaries, as proposed by Hillert.[34]

Thus, atoms located at the surface, grain boundary and dislocations etc. exchange momentum with fast-moving electrons under a high electric field, causing the atoms to move in the same direction as the electrons. The as-deposited films are frozen in the amorphous phase due to low atomic mobility at ambient temperature. Application of the electric field and its resulting Joule heating provides the driving force and enhanced mobility for atoms to move and crystallize. It can therefore be speculated that if the electric field is small, it fails to generate enough thermal energy and driving force to overcome the diffusion energy barrier, causing the existence of an electric field threshold. Above the threshold, crystallization is accelerated. Thinner films require a higher field for surface reconstruction effects to be apparent, while for the thicker films such effects happen at a lower field. When the thin film is subjected to successive field treatments in different directions, the final direction of reconstructed organization is dictated by the final field treatment. The existence of a threshold electric field for grain growth as well as the crystallization processes observed in the current study, therefore, can be explained by thermodynamic considerations.

Furthermore, the field can increase or decrease the nucleation barrier, depending on the dielectric constants of the crystalline and mother phase of the material, which means that the field can inhibit or stimulate the nucleation rate. In addition, particle separation in the as-deposited film will decide the final nanostructures resulting from the field treatment. Thus, if the initial microstructure consists of closely packed grains, these will constitute paths of low resistance locally. For a large coverage density of nanoparticles, their separation has to be small enough for possible electron tunneling.[35] However, for lower coverage, the layer beneath the nanoparticulate surface provides the path of least resistance. If the surface beneath the line joining the voltage leads is continuous, current will flow along this linear path because it will provide the path of minimum resistance. In addition, small metallic nanoparticles have their own polarizability and effective dielectric function.[36] Therefore, with the application of the field, nanoparticles will be polarized electrically in the vicinity. Delamination of the films at high electric fields could be due to the large strain at the film interface resulting from the rapid migration of grains.

From the observations presented above, it can be inferred that the threshold electric field for grain growth to occur is 0.1–0.2 kV/cm, whereas that for crystallization is of the order of 1 kV/cm or greater. The alignment of grains and the formation of nanowires occur at intermediate field strengths. These field values compare reasonably well with earlier reports on electric-field-enhanced crystallization rates as well as grain growth.[24] It should be mentioned that all these studies were carried out in conditions where the electric field was applied at elevated temperatures. For example, Liu *et al.*[37] have reported accelerated crystallization and enhanced grain growth in amorphous-Fe based ribbons at a temperature of 600°C for 1 h in a field of strength of the order of 10^4 V/m. Similarly, Jang *et al.*[24] have reported accelerated crystallization and enhanced grain growth in amorphous Si films placed in an electric field of strength of 80V/cm at 500°C. In contrast, the experiments in the current study are performed in the absence of any external heating, but in the presence of fields of strength ranging from 10^2 to 10^3 V/cm.

Significantly, while the current study indicates the possibility of aligned nanostructures in addition to crystallization and grain growth, the earlier reports demonstrated only enhanced crystallization and grain growth. Nanostructuring by this

technique, therefore, affords several control parameters crucial for ***nanostructuring of films*** that can be controlled accurately, viz. bias voltage, electrode tip diameter, voltage leads separation (this which determines the field value), substrate material (this should be robust to heat treatment), film material (lower melting points lead to agglomeration of the material and require a lower field for organization) and film thickness (which controls the diameter and separation of nanoparticles).

References

1. G. Kartopu, S. C. Bayliss, R. E. Hummel, and Y. Ekinci, J. Appl. Phys. 95, 3466 (2004).

2. Y. Fu, M. Willander, A. Dutta, and S. Oda, Superlattices and Microstructures 28(3), 177 (2000).

3. K. Nishiguchi, and S. Oda, J. Appl. Phys. 88(7) 4186 (2000).

4. S. Banerjee, S. Huang, , T. Yamanaka, , and S. Oda, J. Vac. Sci. Technol. B 20 (3) 1135 (2002).

5. M. L. Ostraat, J. W. De Blauwe, M. L. Green, L. D. Bell, M. L. Brongersma, J. Casperson, , R. C. Flagan, and H. A. Atwater, Applied Physics Letters 79(3) 433 (2001).

6. S. Tiwari, F. Rana, H. Hanafi, A. Hartstein, E. F. Crabbé, and K. Chan, Appl. Phys. Lett. 68, 1377 (1996).

7. S. Tiwari, F. Rana, , K. Chan, L. Shi, , and H. Hanafi, Appl. Phys. Lett. 69 1232 (1996).

8. L. Canham, Nature 408, 411 (2000).

9. N.-M. Park, T.-S. Kim and S.-J. Park, Applied Physics Letters 78(17) 2575, (2001).

10. S. Oda, Mater. Sci. Eng. B 101 19 (2003).

11. K. A. Pettigrew, Q. Liu, P. P. Power, and S. M. Kauzlarich, Chemistry of Materials 15(21) 4005 (2003).

12. J. D. Holmes, K. J. Ziegler, C. Doty, L. E. Pell, K. P. Johnston and B. A. Korgel, J. Am. Chem. Soc. 123 3743 (2001).

13. M. Nayfeh, O. Akcakir, J. Therrien, Z. Yamani, N. Barry, W. Yu, and E. Gratton, Applied Physics Letters 75(26) 4112 (1999).

14. J. P. Wilcoxon, G. A. Samara and P. N. Provencio, Phys. Rev. B 60(4) 2704 (1999).

15. H. Morisaki, F. W. Ping, H. Ono, and K. Yazawa, J. Appl. Phys. 70, 1869 (1991).

16. S. Okamoto and Y. Kanemitsu, Phys. Rev. B 54, 16421 (1996).

17. S. Takeoka, M. Fujii, S. Hayashi, and K. Yamamoto, Phys. Rev. B 58, 7921 (1998).

18. S. Sato, S. Nozaki, H. Morisaki, and M. Iwase, Appl. Phys. Lett. 66, 3176 (1995).

19. J. G. Buijnsters, M. Camero and L. V´azquez, Phys. Rev. B 74, 155417 (2006).

20. Q. Li, L. D. Marks, Y. Lifshitz, S. T. Lee and I. Bello, Phys. Rev. B 65, 045415 (2002).
21. B. W. Karr, D. G. Cahill, I. Petrov and J. E. Greene, Phys. Rev. B 61, 16137 (2000).
22. K. Y. Lee, T. Ikuno, K. Tsuji, S. Ohkura, S. Honda, M. Katayama, K. Oura and T. Hirao, Jpn. J. Appl. Phys. 42, 713 (2003).
23. S. Kawakami, T. Kawashima and T. Sato, Appl. Phys. Lett. 74, 463 (1999).
24. J. Jang, J. Y. Oh, S. K. Kim, Y. J. Choi, S. Y. Yoon and C. O. Kim, Nature 395, 481 (1998).
25. K. O. Kim, A. Y. Kim, S. J. Park, K. C. Park and J. Jang, Thin Solid Films 451–452, 320 (2003).
26. O. Englander, D. Christiansen, J. Kim, L. Lin and S. J. S. Morris, Nano Lett. 5, 705 (2005).
27. M. Saka and R. Ueda, J. Mater. Res. 20, 2712 (2005).
28. M. Saka and R. Nakanishi, Mater. Lett. 60, 2129 (2006).
29. R. D. Fedorovich, A. G. Naumovets and P. M. Tomchuk, J. Phys.: Cond. Mat. 11, 9955 (1999).
30. S. Szpak, P. A. Mosier-Boss, C. Young and F. E. Gordan, J. Electrol. Chem. 580, 284 (2005).
31. A. Abdolvand, A. Podlipensky, G. Seiferl, H. Graener, O. Deparis and P. G. Kazansky, Opt. Exp. 13, 1266 (2005).
32. T. Sameshima, N. Andoh and H. Takahashi, J. Appl. Phys. 89, 5362 (2001).
33. W. E. Hong and J. S. Ro, Thin Solid Films 515, 5357 (2007).
34. M. Hillert, Acta Metall. 13, 227 (1965).
35. P. Lobotka, I. Vavra, F. Fendrych and O. Chayka, Phys. Stat. Sol. (a) 201, 1493 (2004).
36. C. Noguez, Opt. Mater. 27, 387 (2005).
37. W. Liu, J. Tang, B. Huang and Y. Du, J. Alloys Comp. 420, 171 (2006).

Excimer laser induced nanostructuring

Abstract

Excimer laser has been employed to nanostructure bulk silicon wafer and PVD coated thin films of Ni, In, au and Si in the thickness range 10-100 nm. The effect of KrF excimer laser energy density (below and above the ablation threshold), number of shots and angle of laser incidence on the morphological reconstruction, structure and specular reflectance of Si [311] surfaces is reported. At low laser fluence (0.1 to 0.3 J/cm^2) laser irradiation results in a variety of nanostructures, depending on laser energy density and number of shots, such as nanopores (40–60 nm dia) and nanoparticles (40–80 nm dia). At fluences greater than the laser ablation threshold (2 to 5 J/cm2) the formation of nanowires (200 nm dia, 6–8nm length), and closely spaced silicon nanograins (100–150 nm dia) is observed. Experiments to study the effect of laser irradiation in the proximity of a fixed shape such as a linear step edge in the form of a stainless steel blade and a cylindrical cross-section Cu wire were also carried out. In both cases, linearly organized nanoparticles (150–200 nm diameter) and nanowires (60–80 nm diameter) formed close to the edge. There is a systematic degradation of long-range order with the number of shots and laser energy density as evidenced from X-ray diffraction studies. At an energy density of 2 J/cm2, and 100 shots the [311] oriented silicon surface made a transition to a randomly oriented nanocrystalline state. When 40nm gold thin film surface was treated by excimer laser in unfocussed condition (at 90^0 incidence angle with the fluence of 0.02-0.04 J/cm^2), surface features were observed to change with respect to laser dressing parameters namely laser energy and number of shots. Grain growth is observed with number of shots at 0.02 J/cm^2 laser fluence mainly upto 20 shots where particle size is near to monodisperse. With the increase in laser fluence, surface became densely packed with some traces of nanopores. Higher laser fluence gives grain growth apart from nanopore formation on the surface. In 10nm indium thin film case, flat disc shaped grains for as deposited thin film were transformed to spherical grains at 0.02 J/cm^2 laser fluence for 10 shots and cubical grains at 0.05 J/cm^2 laser fluence for 10 shots. Silicon (30nm) and nickel (50nm) thin film shows grain size and shape change with laser energy and number of shots. Excimer laser treatment triggers long range crystalline order in thin films. At extreme laser fluence used in our experiment; XRD amorphous indium and gold thin films turned nanocrystalline with visible evolution of [101] indium peak and [111] gold peak with crystallite sizes 50nm and 10nm respectively. Amorphous silicon thin film shows the evolution of polynanocrystalline peaks. Surface plasmonic peak has been observed to shift for indium and peak sharpening is observed for gold case. For indium case however, new surface plasmonic peaks have been observed to appear due to changes in shape of grains.

3.4.1 Single crystal silicon surface

[A] Introduction

Laser induced modification of silicon surfaces has been reported extensively.[1–10] It has recently been shown that silicon surfaces become luminescent[11] in the visible range when they undergo size reduction to the nanometer dimensions. Creation of a thin layer on silicon surfaces using the intense conditions at the focus of a high-intensity excimer laser pulse can make silicon highly absorbing and an excellent choice for photovoltaic applications.[12] Further, desired band gap of silicon can be achieved in nanostructured form for application in antireflection coatings for micro lens application.[13] Anisotropic growth features cause a gradient in refractive index and can therefore be used for polarization sensitive Si based optical devices.[14] Nanostructured porous silicon can be used as a sensitive sensor to chemical species.[15] Si nanowires [16–18] as special forms of crystalline Si are expected to exhibit unusual quantum confinement effects as well as potentially useful applications. Recently, research is on for its application as a high performance Lithium battery anode [19] and in memory devices. [20]

There is, thus, continued interest both in developing new techniques to realize Si nanostructures in a controlled and reproducible manner as well as adapting the laser induced surface modification process to realize Si nano structures. Interactions between an intense laser pulse and a material surface trigger photo-induced surface processes which result in nanostructuring of the surfaces. Understanding the underlying mechanisms and processes of nanostructure formation is crucial for establishing control over their dimensions, spatial distribution, and uniformity. Control of laser parameters can, in principle; give rise to adequate control over various nanostructures formed and hence can be used for an appropriate application.

Many of the applications of Si are critically dependent on the crystallographic texture, whether it is single crystalline, polycrystalline or amorphous. The effect of excimer laser irradiation on the crystallinity of the Si surfaces is therefore an important parameter to be investigated. A review of literature reveals that detailed reports on nanocrystallization of Si crystal surfaces are limited; though laser induced

amorphization of Si is well-known. [21] In this part of the work, it is demonstrated that excimer laser irradiation provides a suite of parameters that can be employed to achieve a variety of nanostructures on Si single crystal surfaces and also cause a transition to nanocrystallinity. These are expected to have important technological implications especially since poly/nano crystalline Si is undergoing resurgence as a material for a variety of devices e.g., solar cells and flat panel display.

The current work presents a detailed systematic study on the effect of excimer laser irradiation on the morphology, structure and optical properties of Si [311] surfaces. The experimental set up has been designed to enable variation of angle of laser incidence from 10 to 90^0. Studies were carried to investigate the effects as a function of incident laser energy density, ranging from 0.1 J/cm^2 to 5 J/cm^2, as well as the number of laser shots (from 1 to 1000).The resulting surfaces were characterized using X-ray diffraction, atomic force microscopy and specular reflectance.

[B] <u>Results and discussion</u>

(i) Microstructure

The effect of energy density on the spatial spread of the morphological reconstruction showed that at energy densities greater than the ablation threshold (2 to 5 J/cm^2), the influence could be observed over a diameter of up to 3 mm. In contrast, at lower energy density the diameter of the laser "spike" was of the order of hundreds of microns. Optical microscopic images of the irradiated spot clearly demonstrate the "catastrophic" nature of microstructural reconstruction that occurred due to laser incidence. These are shown in Figures 3.64 (a) for an energy density of 5 J/cm^2 and in (d) for laser irradiation of 2 J/cm^2. In both cases the distance over which the effects are observed are >1 mm. At energies greater than the laser ablation threshold (2 to 5 J/cm^2) the formation of nanowires (200 nm dia, 6–8 μm length), and closely spaced silicon nanograins (100–150 nm dia) is observed (Figs.3.64 (b) and (c)). A detailed observation of the area within the spike reveals elliptical ripples (Fig.3.64(d)), while inside the ripples there is evidence of island-like fibrous structures (Figs.3.64(e) and (f)).

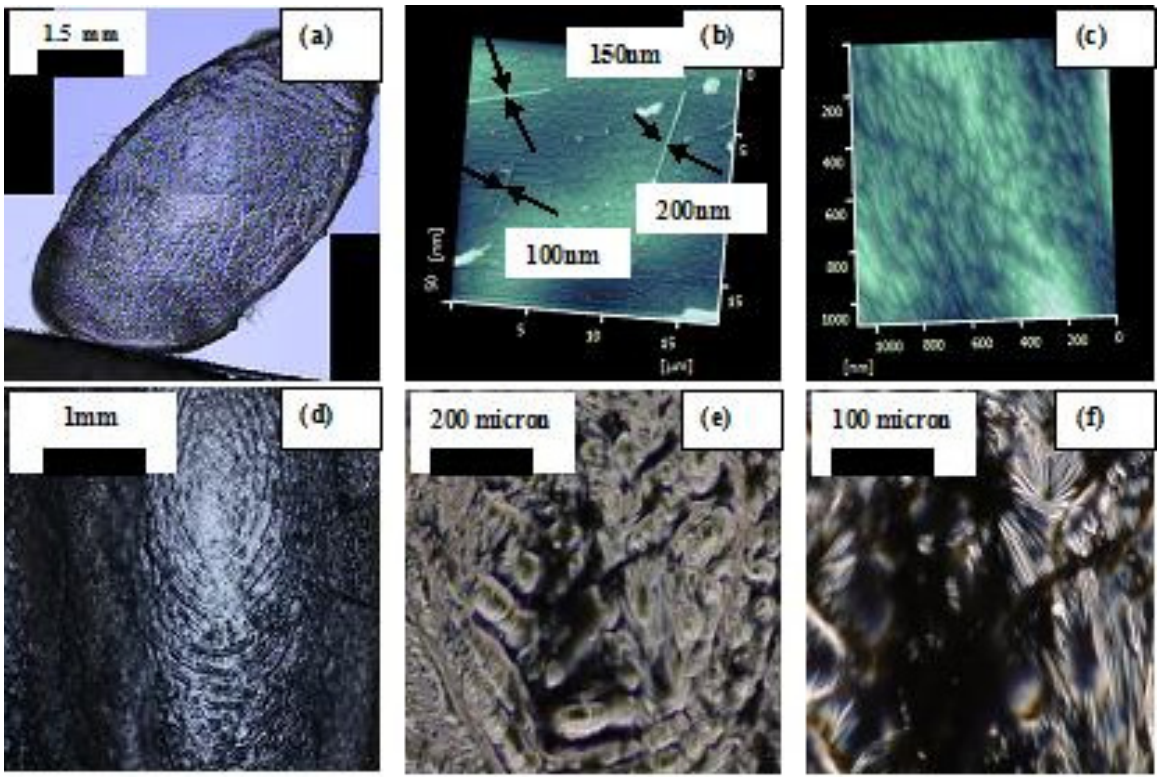

Figure-3.64 **(a)** Optical images for focussed laser irradiated site for 2 J/cm^2, (b) AFM image for 20 shots at 2 J/cm2, (c) AFM image for 100 shots at 2 J/cm2, (d) Optical image for 5 J/cm^2, micron ripples, (e) to (f) fibrous and hair bundle like microstructures, actually zoomed view of Fig 1(d).

The effect of angle of incidence on the morphological features at 5 J/cm^2 is shown in Figures 3.65(a) to (d). At low angles (10 and 20^0) there is evidence for melting causing the formation of island like structures organized linearly. At higher angles, however, these structures are more randomly distributed.

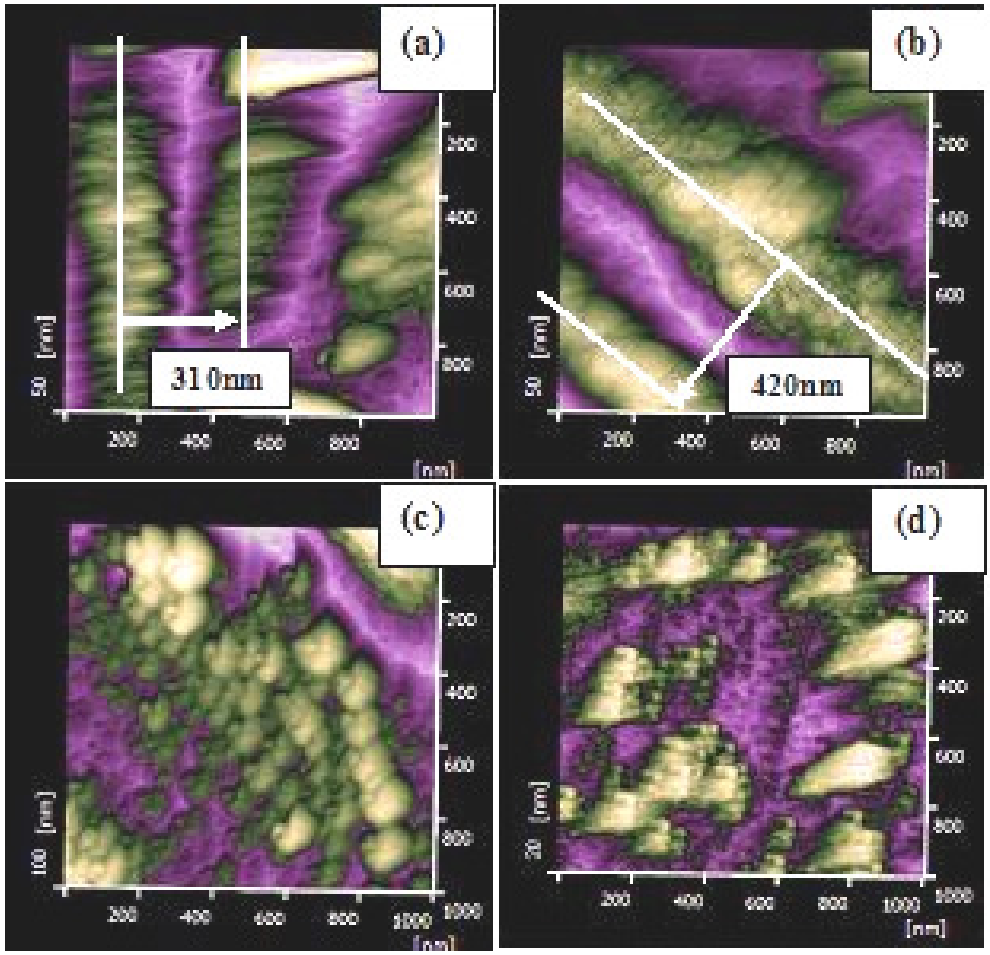

Figure 3.65 AFM image in DFM mode for 5 J/cm^2 for 8 shots at different incident angles, (a) 10^0, (b) 20^0, (c) 30^0, (d) 90^0.

The visible focal spot for the laser beam was elliptical in shape as shown in Figure 3.64(a). Ellipses were traced using the measured values of length of the semi-major and minor axes. The variation of the spot area plotted as a function of incident laser energy density and the number of shots shows that focal spot area usually increases both with number of shots and energy density (Figs.3.66(a) to (d)). It is observed that the change in spot area for 1 shot and 5 shots are drastically different for incident energies of 2 and 5 J/cm^2. Significantly, the effect is observed over diameters that are much larger than the actual diameter of the beam. The diameter of the spike saturated as the number of shots increases from 1 to 100 at a value of approximately 3 mm.

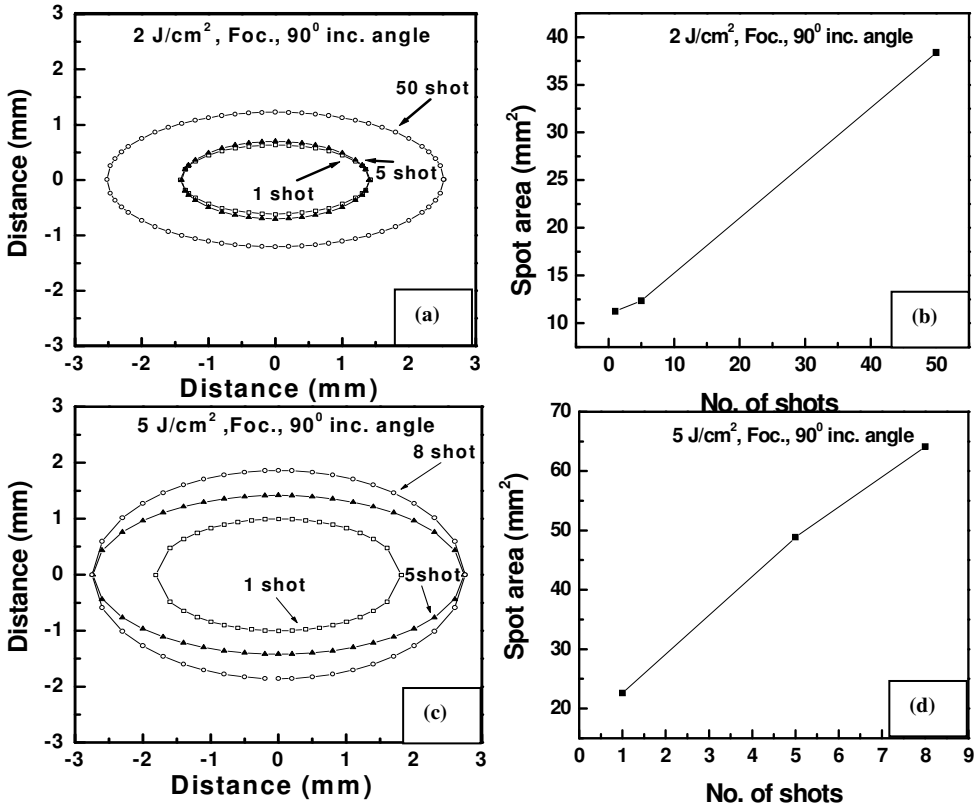

Figure-3.66 Dependence of spot area on number of shots (a) and (b) for 2 J/cm^2 at 90^0 angle of incidence and (c) and (d) for 5 J/cm^2 at 90^0 angle of incidence of the laser beam.

Further studies were therefore carried out at laser energy densities that were lower than the ablation threshold. The morphology of an unirradiated Si surface is shown in Figure 3.67(a).The effects of irradiation on the morphology are immediately evident as observed from Figure 3.67(b) that at an energy density of 0.1 J/cm^2 there is formation of nanopores (40–60 nm diameter) after 200 shots. On further increasing the number of shots to 1000, at the same energy density, cones are formed inside the nanopores (Figure 3.67(c)).These nanopores are initially very few in numbers and distributed on the surface, but new ones form and progressively cover the entire irradiated area. At the same time, the depth of the nanopores increases continuously with the number of laser pulses. Laser irradiation at higher energy density on silicon surface leads to the formation of silicon nanoparticles for 1000 shots at 0.2 J/cm^2 and

0.25 J/cm^2 (Figs.3.67(d) and (e)). Nanopores and nanoparticles formed by this method are quite isolated as can be observed from the line profiles in Figures 3.67(f) and (g).

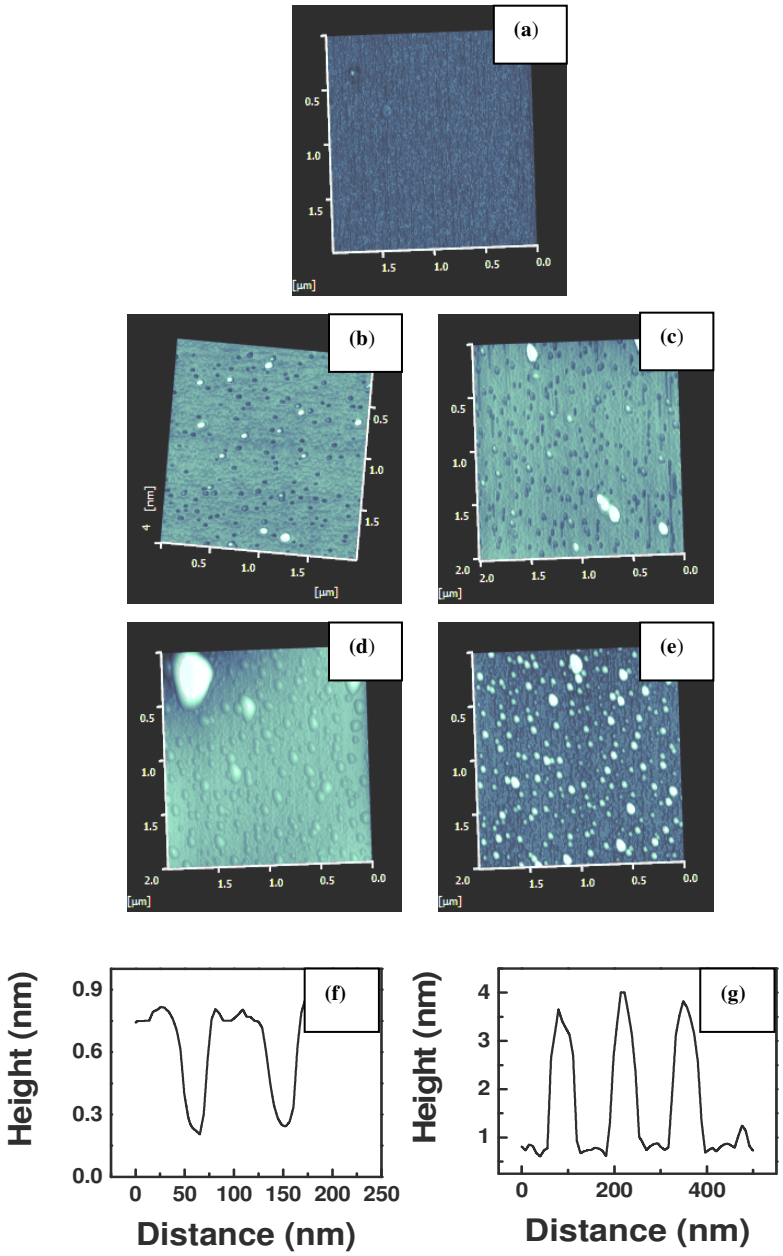

Figure-3.67 Atomic force microscopic images for unfocussed excimer laser irradiated samples (a) without irradiation, (b) 0.1 J/cm^2 for 200 shots, (c) 0.1 J/cm^2 for 1000 shots, (d) 0.2 J/cm^2 for 1000 shots, (e) 0.25 J/cm^2 for 1000 shots, Line profiles for (f) nanopores formation, (g) nanoparticles formation.

The various stages of silicon cone formation inside a typical nanopore for 1000 shots as a function of laser energy density is shown in Figures 3.68(a) to (d).

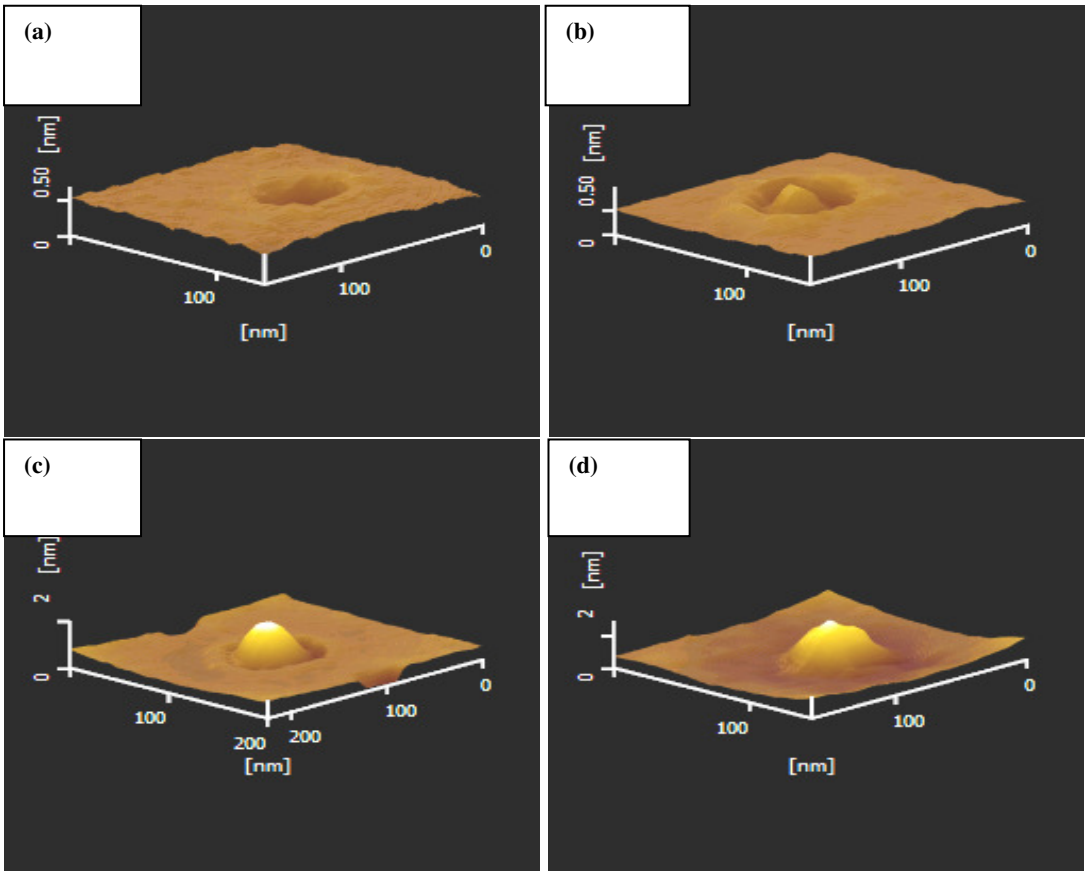

Figures 3.68 Silicon cone formation for 1000 shots at laser energy density of (a) 0.1 J/cm^2, (b) 0.15 J/cm^2, (c) 0.2 J/cm^2 and (d) 0.25 J/cm^2.

The roughness increased with the number of laser pulses and after 100 pulses the irradiated region showed an irregular distribution of uneven morphology, several hundreds of nm in diameter separated by 3–8 nm deep crevices. It is observed that particle size distribution broadens at higher laser energy density values and the size distribution of particles peaks at higher values at higher laser energy density (Fig.3.69 (a)).It is seen that the average particle size increases from 48 nm for 0.1 J/cm^2 to 95 nm for 0.25 J/cm^2 (Fig. 3.69(b)).

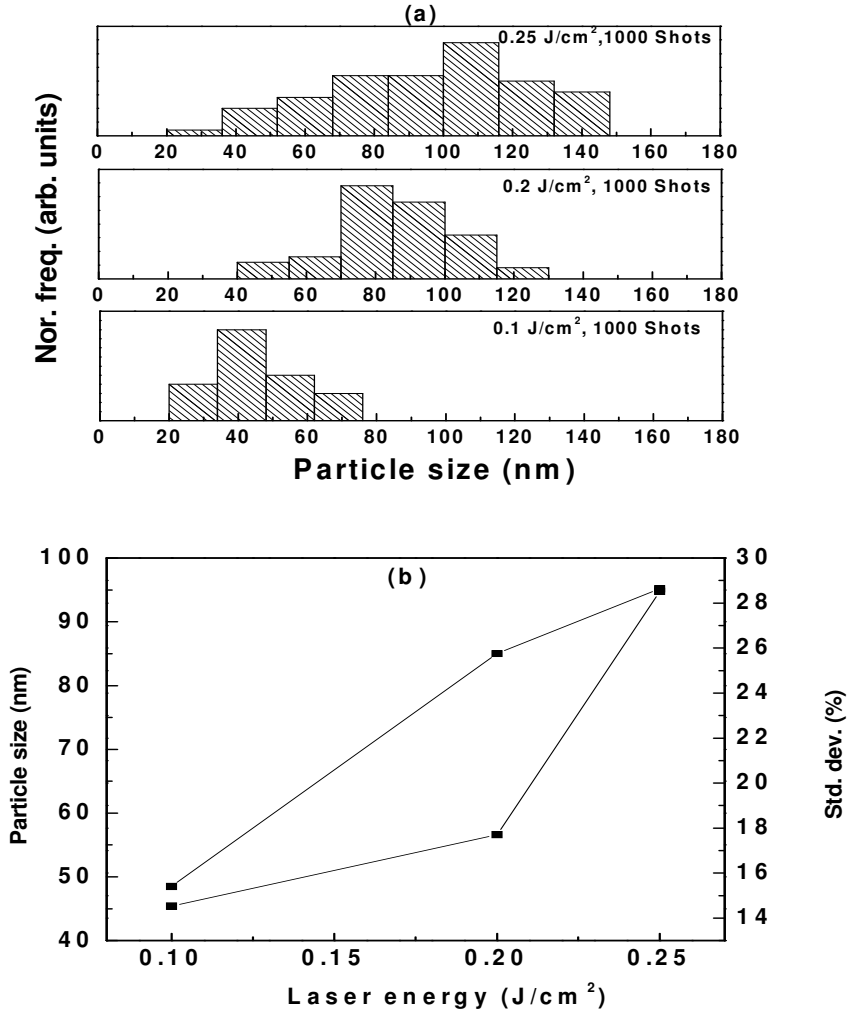

Figure-3.69 Particle size distribution for various laser irradiation energy at 90^0 angle of incidence for 1000 shots**.**

An interesting effect was observed when a "step-edge" was introduced in the path of the laser beam in the form of a blade or thin wire.The results of this experiment are shown in Figure 3.70. At 0.15 J/cm^2, in the absence of these edges, irradiation of a cleaned surface of silicon results in completely isolated nanoparticles (Fig.3.70 (a)). However, when a step-edge in the form of a blade is introduced, nanowire formation (40 nm diameter) is observed to the edge (Fig. 3.70(b)). In contrast when a 30 μm diameter copper wire is introduced, a linear array of nanoparticles is observed (Fig.3.70(c)).

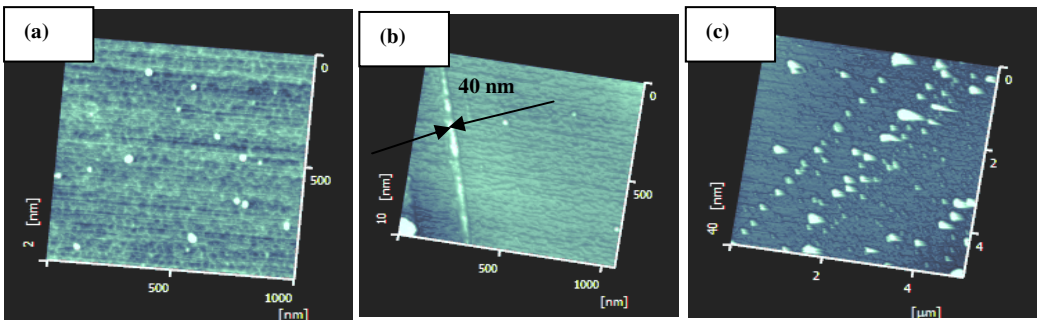

Figure-3.70 Atomic force microscopic images in DFM mode for effect of micron thick mask on the effect of irradiation just at the edge of the mask with unfocussed 0.15 J/cm^2 at 90^0 incidence angle for (a) unmasked irradiation, (b) 25micron thick blade edge mask, (c) 25 micron diameter copper wire mask.

Relaxation time is very crucial for nanostructure formation because the kind of nanostructure formed is determined by the cooling rate apart from other parameters. Therefore, to establish this fact, experimentation with the relaxation time between laser shots were carried out for 2 J/cm^2 for 8 shots, in one case all 8 shots were irradiated at one go and in another case 4 shots each were irradiated after a time gap of 2 hours and the results are quite suggesting (Figure 3.71) to the role of relaxation time as compared to the number of shots.

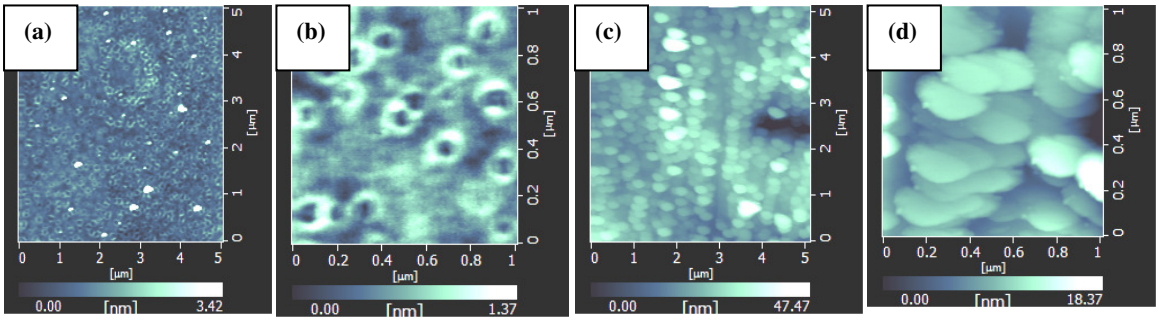

Figure-3.71 Atomic force microscopic image in DFM mode for excimer laser nanostructured silicon wafer surface for (a) and (b) 2 J/cm^2, 4 shots irradiated twice one after the other after few hours, (c) and (d) 2 J/cm^2, 8 shots at a time.

A comparison has been made for nanostructuring of silicon in air and deionized water as media for a laser fluence of 2 J/cm^2 and 100 shots. The schematic of the experimentation with water media is as shown in Figure 3.72 (a); where quartz tube was filled with de-ionized water and laser were incident normal to the silicon wafer surface hanging vertically down. Nanostructural features for water and air media are as shown in Figures 3.72 (b) and (c). As can be observed from the figures, silicon surfaces irradiated in air had denser morphology that may be due to more backscattered particulates and also lower velocity of propagation of capillary waves onto the surface in the water medium.

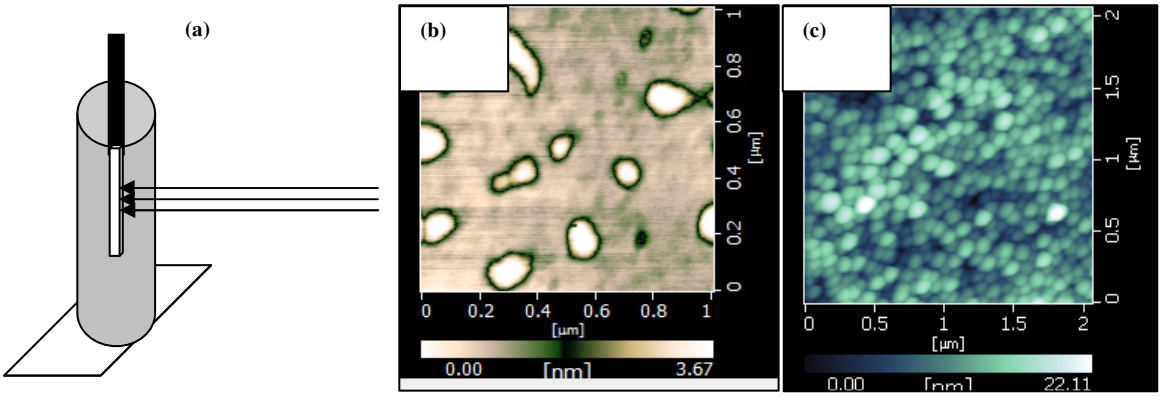

Figure 3.72 (a) Schematic of experimentation with water as medium for nanostructuring, and nanostructured surface of silicon wafer at 2 J/cm^2 and 100 shots for (b) water medium and (c) air medium.

To compare the effect of laser fluence, number of shots and reprate, a set of experiment was performed and the resulting nanostructures were studied closely. Nanostructuring by fluence 2 J/cm^2 was compared with that for 3 J/cm^2; both for 100 shots and 1 Hz as reprate. Higher fluence has resulted in anisotropic fibrous kind of structures (Figure 3.73(c)); while that for lower fluence is more symmetric and almost all grains are spherical. At higher number of shots (500 shots) at the same laser fluence 2 J/cm^2, spherical grains as well as some fragmented features were observed (Figure 3.73(b)). For higher reprate(10 Hz), the evidence of backscattering of re-sputtered particles from the nanoparticulate surface is evident(Figure 3.73(d)).

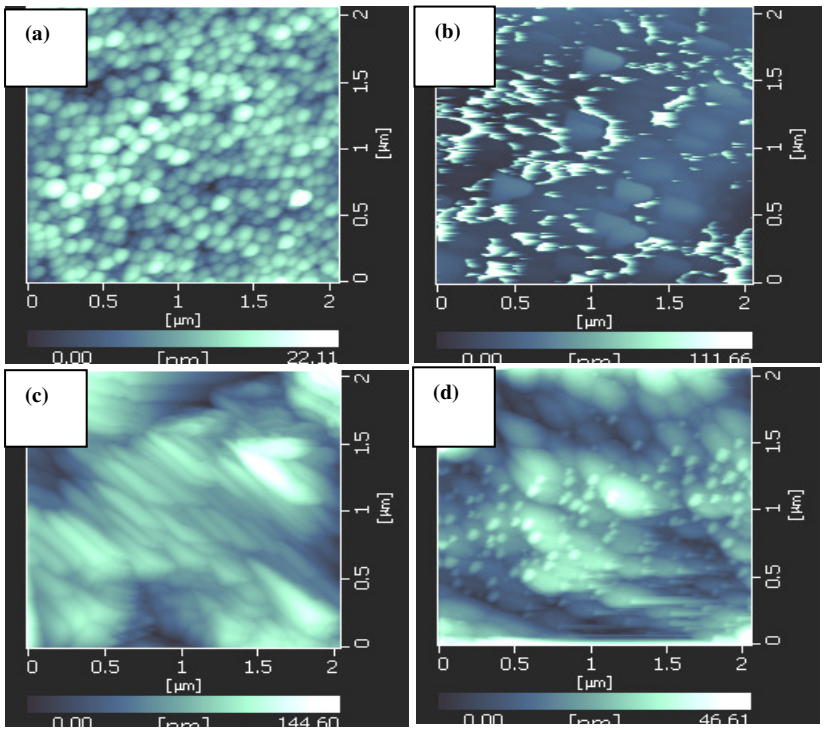

Figure 3.73 AFM images for (a) 2 J/cm^2, 100 shots, 1Hz. (b) 2 J/cm^2, 500 shots, 1Hz. (c) 3 J/cm^2, 100 shots, 1Hz. and for (d) 3 J/cm^2, 100 shots, 10 Hz.

(i) Long range crystalline order

The effects of laser irradiation on the structural properties have also been investigated. X-ray diffraction data show systematic nanocrystallization of the silicon surface with the variation of the number of shots (Fig.3.74(a)) for fixed energy density of 0.1 J/cm^2 and also varying laser energy density (Fig.3.74(b)) at a fixed number of 1000 shots. The surface that was originally oriented along the [311] plane becomes nanocrystalline and randomly oriented. This is evidenced by the broadening of the peak corresponding to the [311] plane, which finally disappears with the increase in the number of shots and the laser energy density. For example at a laser energy density of 2 J/cm^2 with increase in the number of shots, onset of the [311] peak broadening occurs at 20 shots indicating nanocrystallinity and at 100 shots this nanostructured silicon makes a transition to the polycrystalline state (Fig.3.74(c))

exhibiting peaks corresponding to the [111], [220], [311], [400], [331] and [422] planes. Interestingly, there is a drastic decrease in crystallite size, from 50 nm for the unirradiated surface to 3–5 nm for the irradiated surfaces.

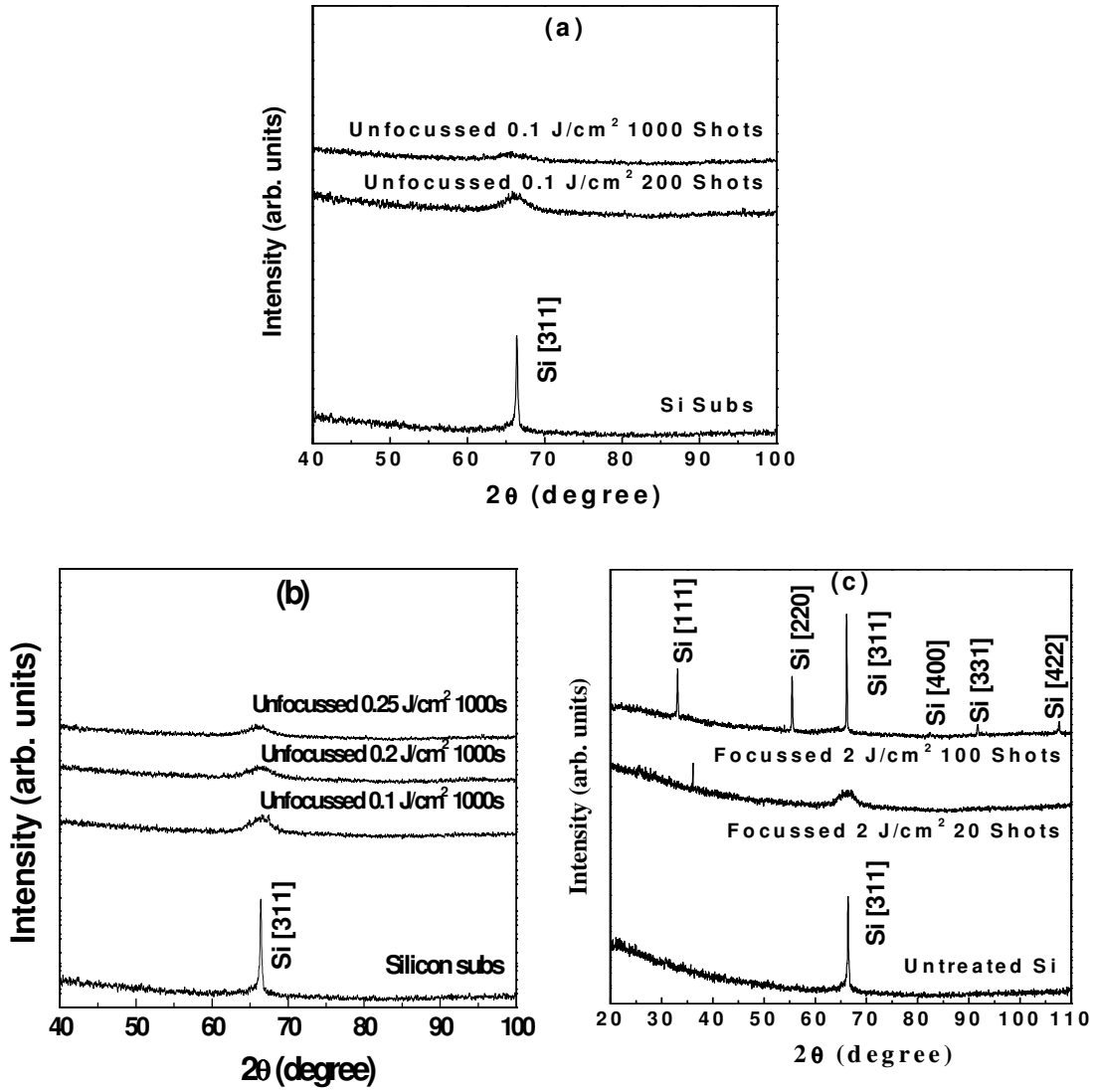

Figure-3.74 X-ray diffraction pattern for excimer laser irradiated silicon wafer for variation of (a) no. of shots for 0.1 J/cm^2 unfocussed laser, (b) unfocussed laser energy and (c) no. of shots for focussed laser, 2 J/cm^2.

(ii) **Specular reflectance**

Specular reflection spectra show the systematic broadening of reflection minima and decrease in percentage reflectance with variation of irradiation time (Fig.3.75(a)) and laser energy density (Fig.3.75(b)); correlating with the nanocrystallization of silicon surface caused by laser irradiation. At 100 shots for 2 J/cm^2, specular reflectance

values decrease from 70–90% to 7–8% over the entire measured range, indicating highly absorbing nature of nanostructured silicon surface (Fig.3.75(c)).

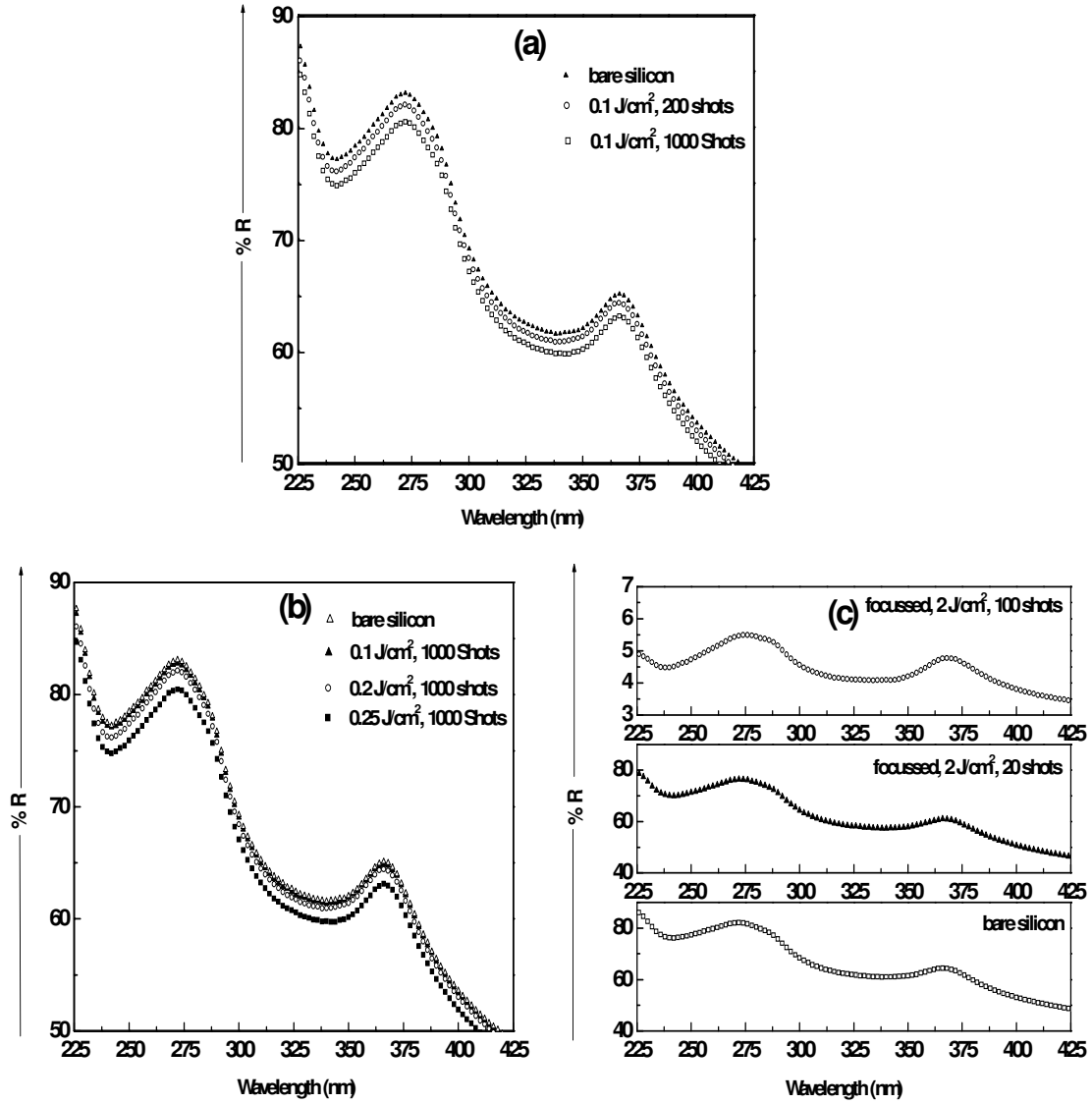

Figure-3.75 Specular reflection spectra for excimer laser irradiated silicon wafer for variation of (a) no. of shots for 0.1 J/cm^2 unfocussed laser, (b) unfocussed laser energy and (c) no. of shots for focussed laser, 2 J/cm^2.

(iii) Photoluminescence

Photoluminescence spectra for laser nanostructured silicon surfaces are shown in Figure 3.76. Untreated silicon surface shows no peak in PL spectra. Major effects

have been registered with variation in laser fluence values and reprate. At 3 J/cm^2, fluence there is a blue shift of PL peak, as compared to that for the surface nanostructured by 2 J/cm^2 fluence and with same number of shots (100 shots) and at same reprate(1 Hz). Apart from the blue shift, the peak becomes sharper too. However, when fluence was maintained at 3 J/cm^2 and reprate was increased to 10 Hz, the effect was to smear out the effect of higher laser fluence resulting in a broad PL peak again red shifted as compared to that for the silicon surface nanostructured by the same fluence but at reprate 1 Hz.

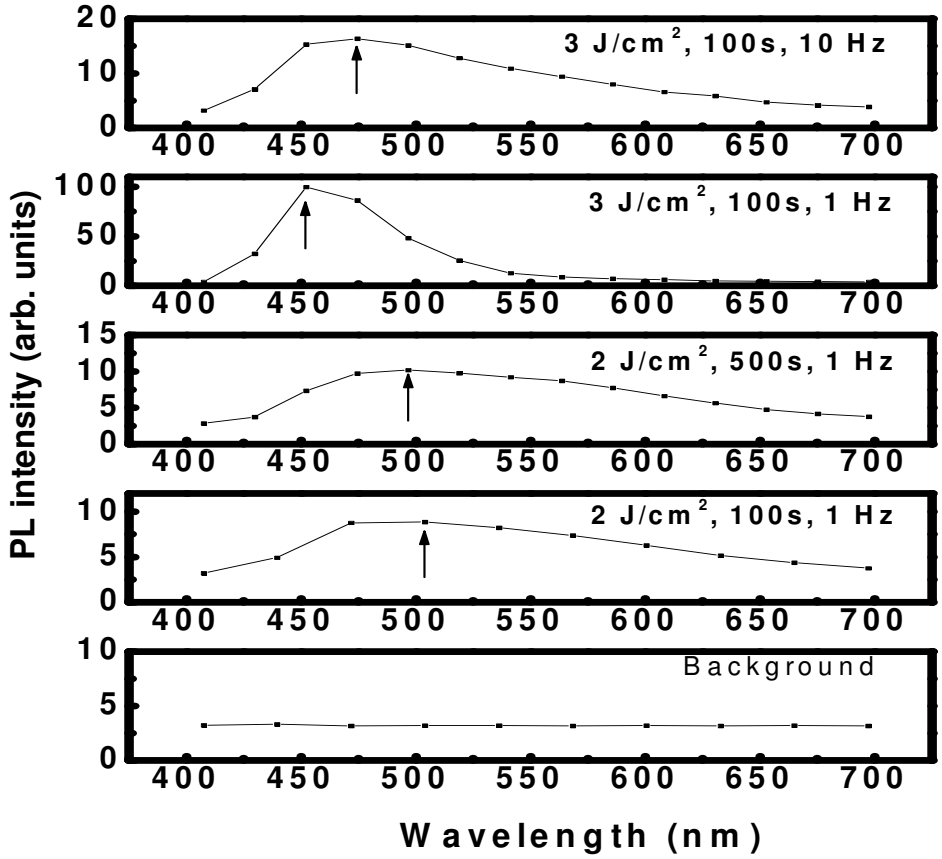

Figure 3.76 Photoluminescence spectra for various laser parameters.

3.4.2 Discussion: single crystal silicon surface

Sub-laser ablation threshold effects have been reported by many workers.[22-25] Costache et al.[22] have postulated that the various patterns formed on Si surfaces in the sub threshold regime under the influence of fs laser were a result of a self

organization from an instability induced by the ablation process. Skantzakis et al.[23] state that capillary waves that form at sub threshold fluences are the initial templates for the formation of micro spikes. Crawford et al.[24] have also reported modified Si surfaces similar to those observed in the present study at very low fluences of the fs laser. The most plausible reason for the morphological reconstruction at such low fluences is that the melting threshold is significantly lower than the ablation threshold for Si. Jeschk e et al.[25] have calculated values of 3.7 eV/atom corresponding to a value of 0.17 J/cm^2 for ablation and 2.6 eV/atom for melting. At the point of melting, the liquid-solid interface velocity is determined by the temperature gradient that builds up during the irradiation process, which in turn depends on laser parameters such as pulse width, fluence and the absorption length. The dynamics of melting depends more on the energy absorbed than the incident energy. Evidently, therefore, very high energies are not required to cause surface modification over the absorption lengths at a given wavelength of laser. At 248 nm, this length is of the order of 10 nm and significantly, all the features observed in the present study, below the ablation threshold, are of this order of magnitude or smaller.

The amorphization of Si surfaces under the influence of laser irradiation has been reported over the years.[26-30] It is now understood that if a layer of Si is melted and rapidly cooled and the cooling time is much shorter than the time for epitaxial regrowth, the Si surface will amorphize. The regrowth velocity has been determined as 18 m/s and the estimated depth of absorption is 10 nm at 4.7 eV. The amorphization process has also been found to be critically dependent on laser wavelength as well as pulse width. The regrowth velocity for a 10 ns pulse is of the order of 5 m/s as against the 18 m/s at 2.5 ns for a wavelength of 347 nm. It would thus appear that the regrowth velocity in our case (λ = 248 nm and 30 ns pulse width) would at best be of this latter order of magnitude. Hence, the rate of cooling is much faster than the rate for epitaxial regrowth. This leads to nanocrystallization of the Si surface. The AFM images suggest that depth of the features formed is of the order of 10 nm which compares favourably with the absorption length reported earlier. However, in the present case, the energy used is sub-ablation threshold energy and therefore amorphization may not have occurred and surfaces have remained nanocrystalline.

A laser beam incident on the silicon surface gives rise to various nanostructures [31-38] arising from the laser material interactions which include local heating at so called hot-spots, radiation pressure effect and the propagation of the heat wave in silicon medium emanating from the laser spot. Hot spots of laser create extremely high local temperature. In addition, any defect sites on the silicon surface give rise to higher local heating due to field enhancement at the interface of defect with the surrounding material. Local high temperature evaporates the material and digs out nanopores. Nanopore diameter is a function of laser energy. Cooling of the silicon material just after pore formation gives rise to nanocone formation inside the pore. Such nanostructures possibly form, since cooling starts from the circumference and end up at the centre, giving rise to different density. After laser induced melting, there is re-solidification of the silicon surface. Resolidification starts at the edge of the molten zone and proceeds towards its centre.In contrast to the usual behaviour of materials with melting, the density of liquid Si, *l* (*l*-Si) = 2 .52 g/cm3, is larger than the density of solid Si, *s* (c-Si) = 2 .32 g/cm3.Thus, the volume of silicon increases during solidification. Prokhoro v et al.[31] have postulated that the formation of conical shapes in laser irradiated Ge is due to asymmetry of the processes of melting and crystallization caused by density variations along the direction of the solid/liquid interface. This model can be used here since, as in the case of Ge, Si is denser in the liquid state. More recent studies indicate a close correlation between the presence of the lateral resolidification condition after the laser pulse and the presence of conical structures on a solidified Si surface.[32] Formation of cones in single pulse irradiated Si surfaces have also been reported and attributed to the anomalous behavior of the density of silicon near the melting point.[33] Pedraza et al.[34] have postulated that there is first the development of a small protrusion and then its evolution into a growing column or cone in the formation of columns and cones. The growth process, on the other hand, is initiated by the formation of a silicon-rich vapor, followed by the transport of this vapor to the tip of the column, and eventually the liquid-phase silicon-deposition reaction.

If external forces can be neglected, surface tension forces will tend to promote oscillations in the liquid, and the oscillations will not allow the surface relief to increase with the number of pulses. Depressions on the surface can be considered as

capillary waves. The dispersion equation for capillary waves in liquid, neglecting gravity waves can be given by [35]

$$\omega(\lambda) = [1/\rho]\,[\sigma k^3 \tan h\,(kh)]^{1/2} \quad \text{----------(1)}$$

where k is the wave vector, σ is the surface tension, ρ is the density and h is the fluid depth. The fraction of the cycles completed by the capillary wave during the time that silicon remains melted, t_{melt} is given by

$$F_{cycle} = t_{melt}\,\omega(\lambda) / 2\pi \text{ ----------(2)}$$

Melting time and melting depth can be estimated using data by Unamuno and Fogarassy.[36]

$$t_{melt}\,(ns) = -11.79\,E^2_{dl} + 134.18\,E_{dl} - 53.64 \text{ ---------- (3)}$$

and

$$h_{melt}\,(nm) = -33.57\,E^2_{dl} + 509.4\,E_{dl} - 273.3 \text{ ---------- (4)}$$

where E_{dl} is the laser fluence in J/cm^2.

For 2 J/cm^2 therefore, the estimated value of h_{melt} will be 600 nm and the estimated value for t_{melt} will be 150 ns. The above equations will have to be modified for our case of air in the vicinity. Extra back air pressure will always be present on the reconstructing silicon surface, thereby not allowing these capillary waves to move freely as they would have done in vacuum. This leads to the formation of ripples on the surface. The impeded capillary velocity for air background will in turn reduce the ripple height and ripple separation too. For the non-perturbed case at fluence of 2 J/cm^2, capillary wavelength should be 16 μm and 40 μm for 5 J/cm^2. Angle of incidence of laser can be used to give rise to different ripple separation length. So, the incidence angle can work as a tuning parameter to change the ripple separation. For oblique incidence cases, the following grating equation will govern the ripple formation.[37]

$$K^{s,a}{}_{PAR} = k^{i}{}_{PAR} \; -/+ q \text{---------- (5)}$$

Where, $K^{s,a}{}_{PAR}$ are the wavevectors for the Stokes (–) and anti-Stokes (+) diffracted beams. $k^{I}{}_{PAR}$ is the projection of the wave vector of the incident wave on the substrate surface and q is the wave vector of the surface periodic structure.

At energies greater than the ablation threshold, silicon remains melted for a period of tens of nanoseconds and hence the gradient of surface tension is responsible for the formation of nanoripples. The modulated energy deposition during irradiation produces a temperature gradient, which in turn gives rise to the gradient in surface tension. Surface tension gradient drives the molten silicon from the hotter to the colder regions. Such ripples form only at higher fluences, usually greater than 0.4 J/cm^2 which are capable of melting the silicon surface globally and create such global capillary waves. We have observed such ripples for 2–5 J/cm^2 fluence. However, at low energy density of the order of 0.1–0.25 J/cm^2, no such ripples formation is there. Nanoparticles form at fluences just higher than 0.15 J/cm2 for several hundred of laser shots in the presence of air back pressure. Nanoparticle formation was investigated and accounted for earlier in detail.[38] For the special case of Eq.(5), where

$$\mathbf{Mod\ (q) = [(mod\ \{K^{s,a}{}_{PAR}\})^2 - (2\pi / \lambda)^2\ Sin^2\ \theta_i\ ]^{1/2}} \text{---------- (6)}$$

and

$$\mathbf{mod\ [K^{s,a}{}_{PAR}] = 2\pi / \lambda} \text{ ----------(7)}$$

yields incidence angle dependence of line spacing

$$\mathbf{\Lambda = \lambda / Cos\ \theta_i} \text{ ---------- (8)}$$

In our experiment, the small angle laser beam assisted assembled line separation as seen in Figures 3.65 (a) and (b) for 10^0 and 20^0 were found to be 310 nm and 420 nm

respectively which is in rough agreement with the above theoretical treatment since laser wavelength in our case of KrF laser is 248 nm.

Photoluminiscence spectra shows laser parameter dependent PL peak shape and position. Photoluminiscence signal coming from a nanostructured semiconductor surface might have several contribution other than the PL itself, e.g. from total internal reflected waves which is surface roughness dependent. However in our experimental set-up filtering of such contributions are not possible. Furthermore, there are various competing factors available which contribute to observed PL signal that might be reason of broad peak observed in our case.

3.4.3 Thin films

[A] Introduction

Size and shape dependent properties of nanostructured thin are interesting for technological applications, since novel materials with tailor-made performance may be fabricated by exploiting the size-dependent characteristics. Examples are the special chemical properties of supported metal clusters already exploited in heterogeneous catalysis [39] and the magnetic and optical susceptibilities of metallic aggregates currently discussed for applications such as new data storage media [40], all-optical switching devices [41] and improved biophysical sensors [42]. Due to the strong interest in nanostructured surfaces a very important issue in this field is the development of methods to produce such samples. The ultimate goal is the fabrication of monodisperse structures with predetermined size, shape and arrangement.

Miniaturization of electronics has compelled electronic components to be in thin film form. Today's electronics chip industry's requirement is ambient temperature deposition of thin film so that other components on the chip do not get affected. However, to exploit its functionality, the thin film has to be crystalline. BSG as a substrate is a good choice because of its low cost as well as its possible optical applications, but due to the limitation of substrate temperature for films on BSG, it is rather difficult to grow crystalline films. To achieve crystalline films deposited in ambient condition on BSG substrate, high energy trigger has to be employed. Use of

excimer laser is premier [43-44] among post deposition techniques for surface nanostructuring since it gives rise to large area nanostructuring in a reproducible manner.

In this part of the thesis, the systematic study of the use of excimer laser as high energy density trigger for surface nanostructuring of indium, gold, silicon and nickel thin films is reported. The effect of laser nanostructuring on microstructure, structure and optical properties is also reported.

[B] Results and discussion

(a) Indium thin film

(i) Microstructure

Indium thin films of 10nm showed shape change with the increase of laser fluence, from circular disc shaped grains for as deposited thin film (Fig-3.77(a)) to spherical grains at 0.02 J/cm^2 just with 10 shot irradiation (Figure-3.77(b)) to cubical grains at 0.05 J/cm^2 with 10 shot (Figure-3.77(c)).

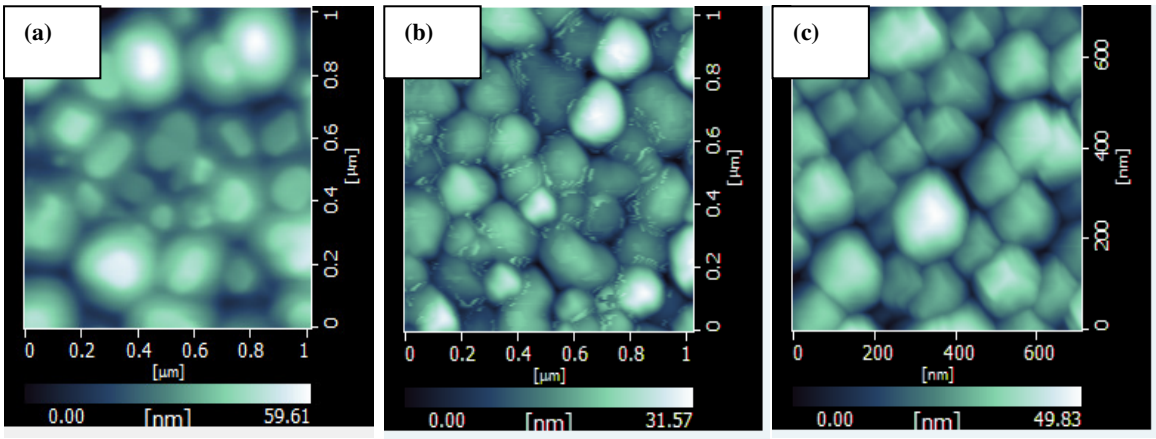

Figure-3.77 Laser nanostructured surfaces of 10nm In thin film (a) untreated, (b) 0.02 J/cm^2, 10 shots, (c) 0.05 J/cm^2, 10 shots.

(ii) Long range crystalline order

Long range crystalline order has been observed to increase with the application of excimer laser irradiation (laser annealing). XRD- amorphous 10nm indium thin film got transition to nanocrystalline with 35nm crystallite size for [101] peak (Figure-3.78)

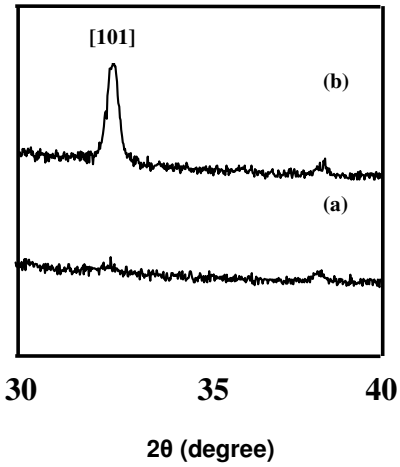

Figure 3.78 X-ray diffraction pattern for 10nm In thin film for (a) untreated and (b) laser nanostructured with 0.05 J/cm^2 with 10 shots irradiation

(iii) Specular reflectance

The effect of laser irradiation on the surface plasmonic peaks is shown in figure 3.79. It is seen that the as deposited In film exhibits a plasmon resonance at 4.76 eV. On being subjected to laser irradiation there is a red shift in the plasmon resonance, due to shape and size change and more interestingly there is a suppression of the plasmon resonance. The broadening of the plasmon resonance can be attributed to the large dispersion in particle sizes as well as the enhanced grain size as a result of laser irradiation.

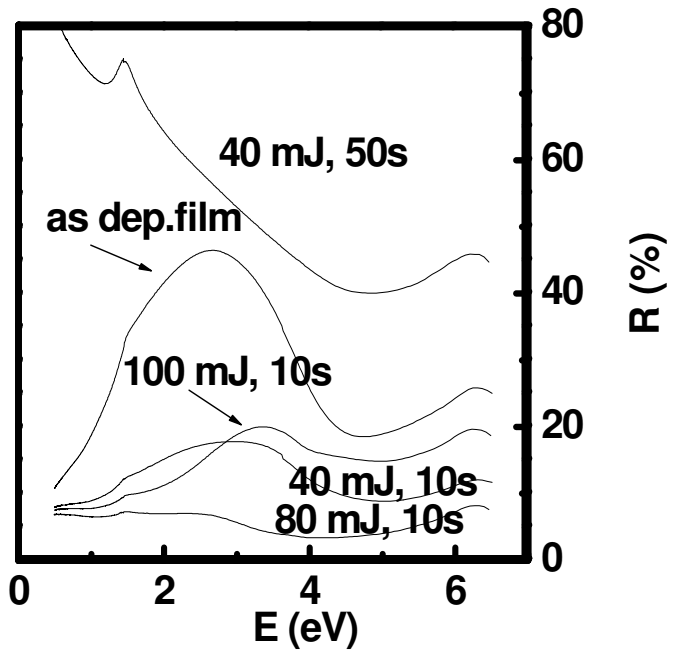

Figure 3.79 Specular reflection spectra for 10nm In thin film for laser nanostructuring.

(b) <u>Gold thin films</u>

(i) Microstructure

The effect of excimer laser pulse irradiation for laser fluence of 0.02 J/cm^2 on gold thin film surface morphology was observed for various number of shots upto 50 shots for fixed laser fluence of 0.02 J/cm^2 (Fig 3.80). It is observed that grain size saturates at a value of 80nm at around 20 numbers of shots for 0.02 J/cm^2.

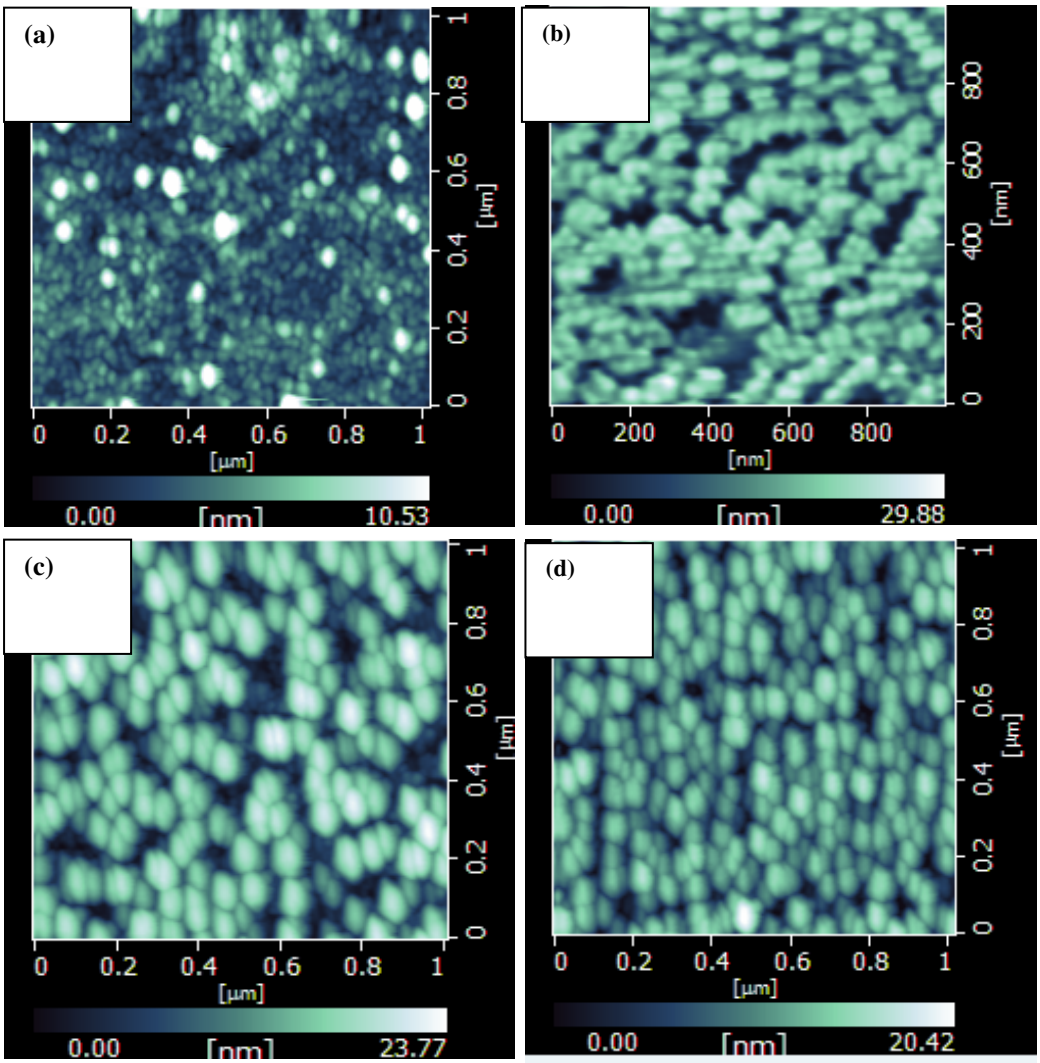

Figure 3.80 Laser nanostructured surfaces of (a) as deposited Au, (b) at 0.02 J/cm^2, 1 shots, (c) at 0.02 J/cm^2, 2 shots, (d) at 0.02 J/cm^2, 20 shots**.**

Further, the effect of excimer laser fluence was observed for the range of 0.02-0.04 J/cm^2 laser fluence. Surface features have observed to change drastically with laser fluence (Figure-3.81). However it is noted that nanopores and nanocracks have formed along with the nanoparticles on gold thin film surface at higher fluence values at 0.03 and 0.04 J/cm^2 respectively.

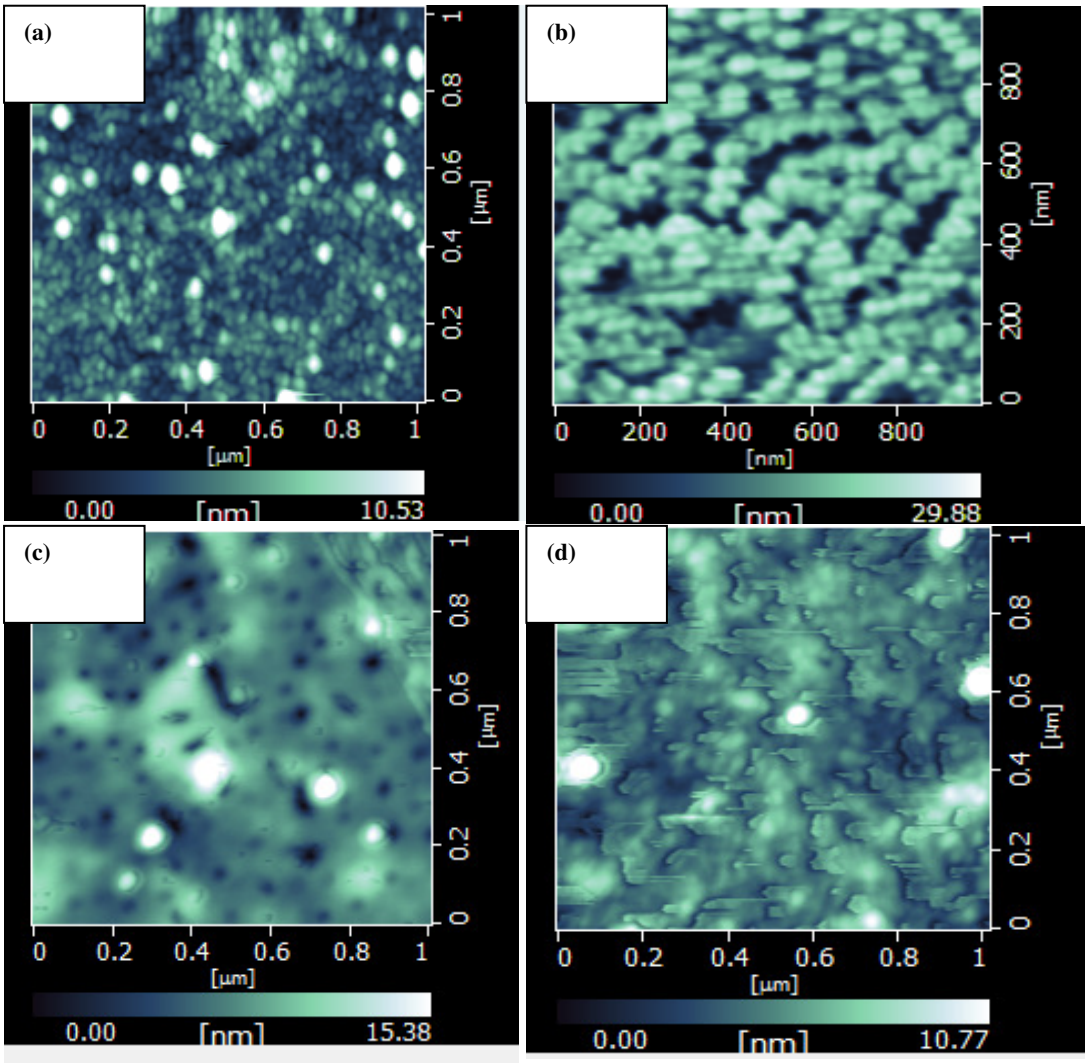

Figure-3.81 AFM images for 40nm gold thin films for (a) untreated, (b) 0.02 J/cm^2, 1 shot, (c) 0.03 J/cm^2, 1 shot and (d) 0.04 J/cm^2, 1 shot**.**

With the number of shots and laser fluence, grain size increase first (grain growth takes place) and then it reduces after the supersaturation limit. Grain size distribution changes at higher number of shots (Figure 3.82).

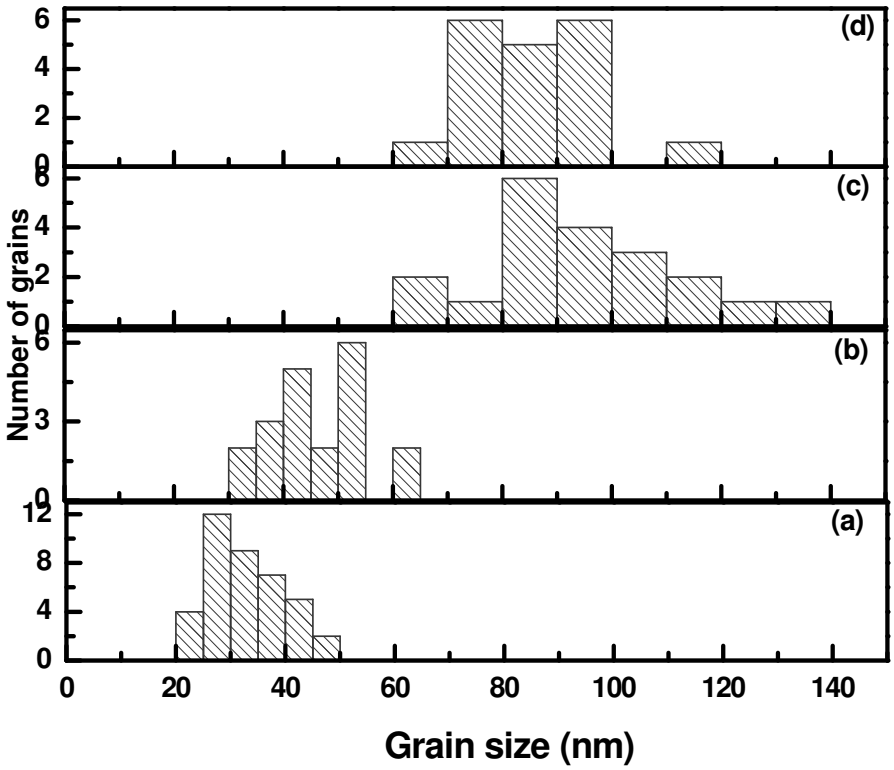

Figure- 3.82 Grain size distribution for 40nm Au thin films (a) untreated, (b) 0.02 J/cm^2, 1 shot, (c) 0.02 J/cm^2, 2 shots, (d) 0.02 J/cm^2, 20 shots.

(i) Long range crystalline order

40nm amorphous as deposited gold thin film got transition to nanocrystalline with 50nm as crystallite size for [111] peak at 0.04 J/cm^2, 1 shot. (Figure 3.83). One remarkable observation was that as a part of experimentation, XRD were taken for thin film treated by laser fluence of 0.02 J/cm^2 upto 40 shots but all nanostructured thin films showed no signature of long range crystalline order. Only higher laser fluence was capable to make amorphous thin film nanocrystalline. Rate of cooling is more important for crystallization dynamics that was probably achieved at higher laser fluence condition.

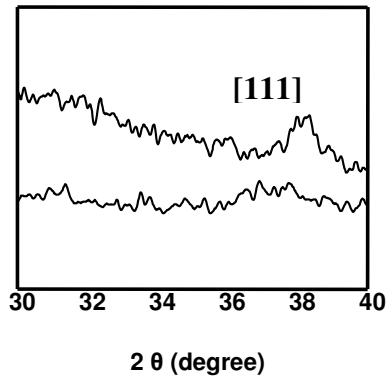

Figure 3.83 X-ray diffraction pattern for 40nm Au thin films for (a) untreated (b) treated by 0.04 J/cm^2, 1 shot.

(ii) Specular reflectance

For 40nm gold thin film case, surface plasmnic peak did not get shifted, rather peak sharpening is observed (Figure 3.84). This might be due to close to monodispersive nature of grain size after laser irradiation.

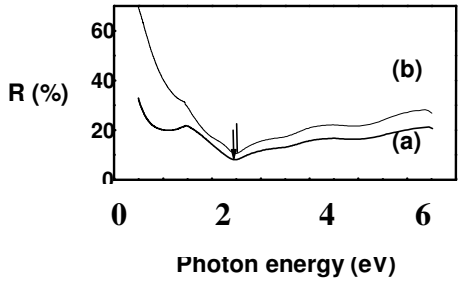

Figure 3.84 Specular reflection spectra for 40 nm gold thin film for (a) untreated, (b) treated by 0.02 J/cm^2 for 20 shots.

(c) <u>Silicon thin films</u>

(a) Microstructure

Si thin films being semiconducting in nature; had not shown much impressive effect with electric field nanostructuring, however little sign of grain growth was observed but long range crystalline order evolution was feeble. With excimer laser treatment

however, sufficient grain growth has been observed. Grain areas have changed 15-20 times (Figure 3.85) which is huge and is expected to affect long range crystalline order as well as other physical properties concerned.

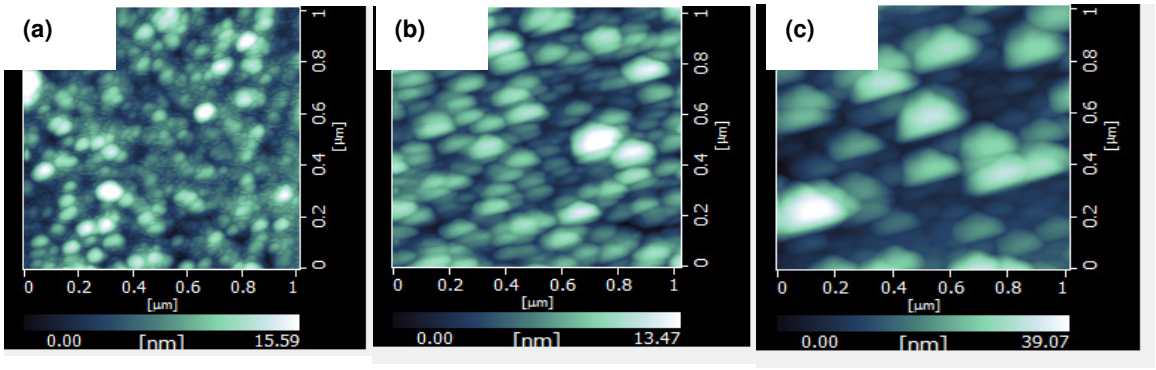

Figure 3.85 AFM images for 30nm thermally evaporated Si thin film (a) untreated, (b) 0.02 J/cm^2, 1 shot and (c) 0.04 J/cm^2, 1 shot.

(b) Long range crystalline order

Such a huge grain growth has really affected long range crystalline order and nanocrystalline peaks corresponding to [220], [311] and [400] planes have been observed (Figure 3.86) for the film treated by 0.04 J/cm^2 fluence and 1 shot.

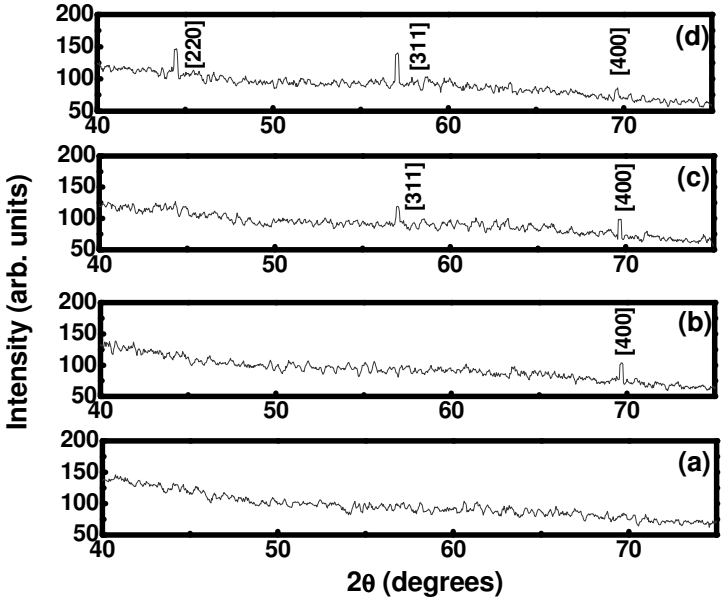

Figure 3.86 X-ray diffraction pattern for 30nm thermally evaporated Si thin film (a) untreated, (b) 0.02 J/cm^2, 1 shot, (c) 0.03 J/cm^2, 1 shot and (d) 0.04 J/cm^2, 1 shot.

(d) Nickel thin films

(i) Microstructure

Excimer laser treatment of nickel thin films has also been carried out and various nanostructures have resulted therein. For example, 50nm thermally evaporated nickel thin film which was nanoparticulate in nature has become quite smoother with laser irradiation treatment at the laser fluence of 0.04 J/cm^2 and single shot (Figure 3.87). The effect of the increase of thickness of nickel thin film on laser irradiation was quite apparent in the sense, 100nm thin film became nanoporous membrane kind of when it was treated by excimer laser at fluence as low as 0.02 J/cm^2 at 1 shot only(Figure 3.88). Similar effects were seen for gold also where it had become nanoporous(Figure 3.81(c)). Nanoporous and cracks might most possibly be appearing due to residual micro-strain in the sample. At 5 shots, it turned to an anisotropic kind of surface features, origin of which is under study.

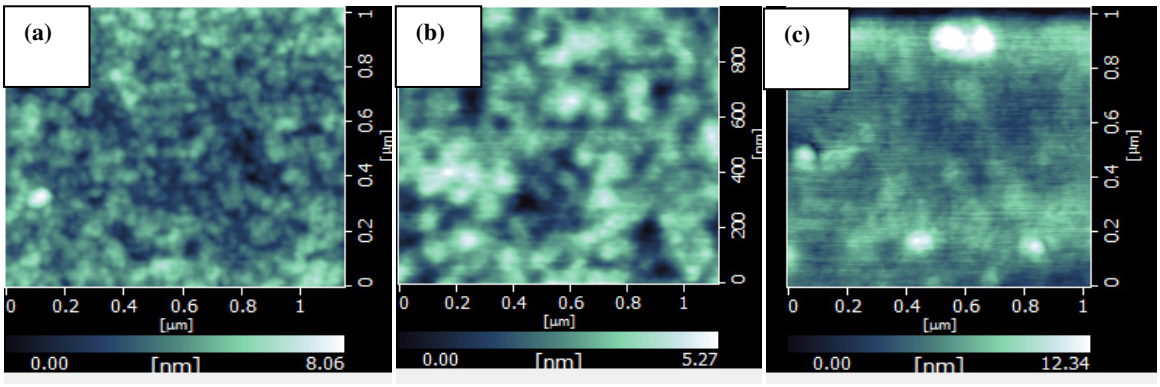

Figure 3.87 AFM image in DFM mode for thermally evaporated 50nm Ni thin films, (a) as deposited, (b) 0.02 J/cm^2, 5 shots, (c) 0.04 J/cm ^{2}, 5 shots

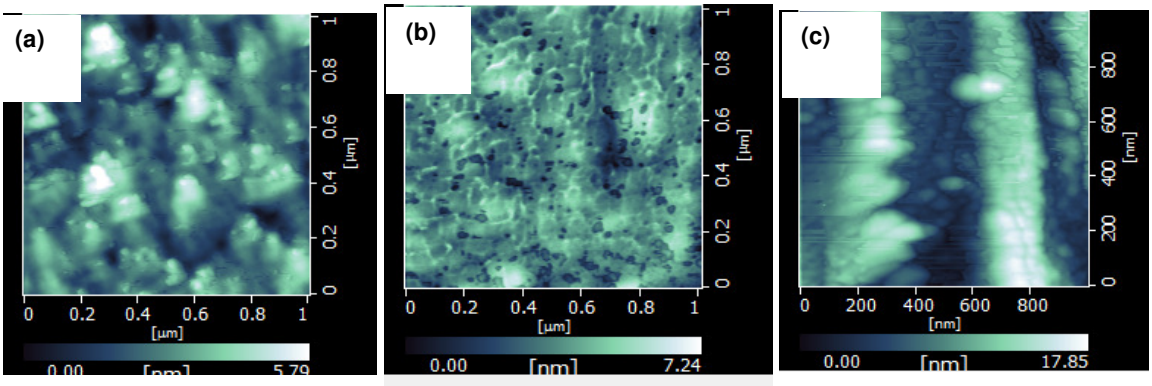

Figure 3.88 Atomic force microscopic images in DFM mode for excimer laser nanostructured 100nm nickel thin films for (a) as deposited thin film, (b) laser treated by 0.02 J/cm^2, 1 shot, (c) laser treated by 0.02 J/cm^2, 5 shot.

3.4.4 Discussion: Thin films

Because of the thermal resistance at the contact area, the temperature of the particle is by ΔT_{res} higher than that of the surface. ΔT_{res} is given by

$$\Delta Q_{out} / \Delta t = \pi r_s^2 \Delta T_{res} / R$$

Where r_s is the radius of the contact area and ΔQ_{out} is the energy transported into the substrate (Figure-3.89).

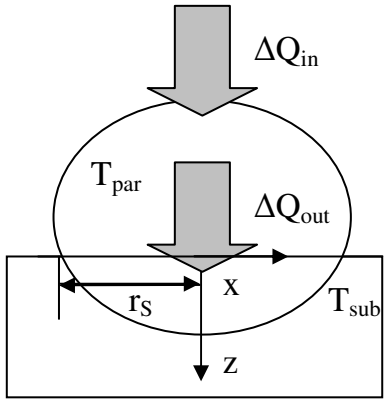

Figure 3.89 Schematic diagram for heat transfer through nanoparticle to the thin film.

Within the substrate, heat diffusion occurs in z-direction and also laterally. As a consequence, a certain particle is heated not only by the light that it absorbs but also through its neighbouring aggregates. In order to take this into account, the aggregates are assumed to be distributed on square lattice points with lattice constant D, which corresponds to the number density as determined from the experimental AFM images. Detailed calculations have shown that for dielectric substrates such as quartz with distances up to about 1000 nm contribute significantly to the temperature rise of a certain aggregate.

The complete temperature increase of a single cluster ΔT_{par} is the sum of all contributions $\mathbf{\Delta T_{sub}(t)}$, $\mathbf{\Delta T_{nei}}$ and $\mathbf{\Delta T_{res}}$. ΔT_{nei} is independent of ensemble size and shape and can, therefore, be regarded as a non-selective temperature offset. Only ΔT_{par} and ΔT_{res} are size and shape selective. The relative importance of the different contributions depends on the photon energy of the laser light used.

At this point, it should be noted that, in addition to evaporation, laser induced diffusion of atoms on the particle surface might contribute to the change of the shape [45, 46]. Diffusion also tends to equalize both axes, since the equilibrium shape of the aggregates is a truncated sphere with an axial ratio close to unity [47-49]. Decisive for the high size selectivity obtained in the experiments and the computations are the peaks in the temperature rise and the desorption rate, which come from resonant plasmon excitation in particles of certain geometry. The selectivity is further enhanced because of the exponential dependence of the evaporation rate on temperature. This allows control of the width of the manipulated size interval by variation of the laser fluence. There is a non-selective temperature offset due to heating of the particles introduced by their neighbours. This naturally determines the upper limit of the laser fluence suitable for size manipulation. If the fluence is too high, the contribution induced by neighbour-heating alone is able to stimulate evaporation of atoms resulting in the loss of selectivity.

The presence of tiny holes in an opaque metal film, with sizes smaller than the wavelength of incident light, leads to a wide variety of unexpected optical properties such as strongly enhanced transmission of light through the holes and wavelength filtering. These intriguing effects are now known to be due to the interaction of the light with electronic resonances in the surface of the metal film, and they can be controlled by adjusting the size and geometry of the holes. This knowledge is opening up exciting new opportunities in applications ranging from subwavelength optics and optoelectronics to chemical sensing and biophysics. In our experiment, we have been able to achieve nanoporous gold and nickel thin film by laser nanostructuring. Further, achieving monodisperse metallic nanoparticulate thin films are in itself very useful for a particular application which exploits size effect. Further we have achieved success to change the shape of nanoparticle of indium up to some extent which can be extremely useful for further research. Laser crystallization has been demonstrated in thin films and surface plasmonic peak has been showed to shift with laser nanostructuring parameters.

References

1. C. P .Grigoropoulos, A. Chimmalgi, D. J. Hwang, Nano-Structuring Using Pulsed Laser Radiation, Laser ablation and its applications, edited by Claude Phipps, Springer, Berlin, pp.473. (2007)

2. J. H. Y oo, S. H. Jeong, X. L. Mao, R. Greif, R. E. Russo, Appl. Phys. Lett. 76, 783 (2000).

3. L. Mariucci, A. Pecora, R. Carluccio, G. F ortunato, Thin Solid Films 383, 39 (2001).

4. V. Cracium, N. Bassim, R. K. Singh, D. Cracium, J. Hermann, C. Boulmer - Leborgne, Appl. Surf. Sci. 186, 288 (2002).

5. D. Klinger , E. L. owska, D. Zymierska, Mater. Sci. Semicond. Process. 9, 323 (2006).

6. A. J. Pedraza, J. D. F owlkes, S. Jesse, C. Mao, D. H. Lo wndes, Appl. Surf. Sci. 168, 251 (2000).

7. C. H. Crouch, J. E. Carey, J. M. Warrander, M. J. Aziz, E. Mazur , F. Y. Genin, Appl. Phys. Lett. 84, 1850 (2004).

8. T. Schwarz-Selinger, D. G. Cahill, S. -C. Chen, S.-J. Moon, C. P. Grigoropoulos, Phys. Rev. B 64, 155323 (2001).

9. R. L. Harzic, H. Schuck, D. Sauer , T.Anhut, I.Riemann, K.König, Opt. Exp. 13, 6651 (2005).

10. F. Sanchez, J. L. Morenza, V. Trtik, Appl. Phys. Lett. 75, 3302 (1999).

11. D. Riabinina, C. Durand, F. Rosei, M. Chaker, Phys. Stat. Solidi A 204, 1623 (2007).

12. G. Conibear , M. Green, R. Corkish, Y. Cho, E. C. Cho, C. W. Jang, T. Fangsuwannarak, E. Pink, Y. Huang, T. Puzzer , T. Trupke, B. Richards, A. Shalav, and K. L. Lin, Thin Solid Films 511, 654 (2006).

13. T. D. James, J. S. Milne, A .J. Keting, G. Parish, C. A. Musca, J. M. Dell, and L. Faraone, IEEE Transactions 431, 1-4244-453-3 (2006).

14. J. Diener, N. Kunzner, E. Gross, D. Kovalev, M. Fujii, Physica Status Solidi 202, 1432 (2005).

15. J. Ivan, C. Tomas, V. Vladimir, J. Jindrich, L. Miroslav, N. Daniel, N. Ivan, K. Vladimir, and D. Juraj, Chimica 10, 2533 (2005).

16. A. M. Morales C. M. Lieber, Science 279, 208 (1998).
17. T. Ono, H. Saitoh, M. Esashi, Appl. Phys. Lett. 70, 1852 (1997).
18. Y. F. Zhang, Y. H. Tang, N. Wang, D. P. Yu, C. S. Lee, I. Bello, S. T. Lee, Appl. Phys. Lett. 72, 1835 (1998).
19. C. K. Chan, H. Peng, G. Liu, K. McIl wrath, X. F . Zhang, R. A. Huggins, Y. Cui, Nat. Nanotechnol. 3, 31 (2008).
20. Q. Li, X. Zhu, H. Xiang, S. M. Koo, D. E. Ionnou, J. Kopanski, J. S. Suehlee, C. A. Richter , Nanotechnology 18, 235204 (2007).
21. Y. Izawa, Y. Izawa, Y. Setsuhara, M. Hashida, M. Fujita, R. Sasaki, H. Nagai, and M. Yoshida, Appl. Phys. Lett. 90, 044107 (2007).
22. F. Costache, S. Kouteva-Arguirova, J. Reif, Appl. Phys. A 79, 1429 (2004).
23. E. Skantzakis, V. Zorba, D. G. Papazoglou, I. Zergioti, C. Fotakis, Appl. Surf. Sci. 252, 4462 (2006).
24. T. H. R. Crawford, H. K. Haugen, Appl. Surf. Sci. 253, 4970 (2007).
25. H. O. Jeschke, M. E. Garcia, M. Lenzner , J. Bonse, J. Kruger , and W. Kautek, Appl. Surf. Sci. 197, 839 (2002).
26. J. Jia, M. Li, and C. V .Thompson, Appl. Phys. Lett. 84, 3205 (2004).
27. M. O. Thompson, J. W. Mayer , A. G. Cullis, H. C. Webber, N. G. Chew, J. M. Poate, D. C. Jacobson, Phys. Rev. Lett. 50, 896 (1983).
28. R. Tsu, R. T. Hodgson, T. Y. T an, J. E. Baglin, Phys. Rev. Lett. 42, 1356 (1979).
29. J. A. Yater, M. O. Thompson, Phys. Rev. Lett. 63, 2088 (1989).
30. P. Baeri, Physica Scripta T29, 183 (1989).
31. A. M. Prokhorov, I. A. Avrutsky, P. V. Bazakutsa, V. A. Sychugov, and A. V. Tischenko, Laser induced surface gratings, Nonlinear Surface Electromagnetic Phenomena, in the series Modern Problems in Condensed Matter Physics, edited by H. E. Ponath and G. I. Stegeman, North Holland, Elsevier Science Publishers, B.V ., Amsterdam, The Netherlands (1991), Vol.29, p.552.
32. J. Eizenkop, I. Avrutsky, D.G.Georgiev, and V. Chaudchary , J. Appl. Phys. 103, 094311 (2008).
33. G. Wysocki, R. Denk, K. Piglmayer , N. Arnold, and D. Bauerle, Appl. Phys. Lett. 82, 692 (2003).
34. A. J. Pedraza, J. D. Fowlkes, D. H. Lowndes, Appl. Phys. Lett. 74, 2322 (1999).
35. G. D. Crapper , Introduction to Water Waves, Ellis Horwood Ltd., John Wiley & Sons, New York (1984).

36. S. D. Unamuno, E. Fogarassy, Appl. Surf. Sci. 36, 1 (1989).
37. Y. Guan, A. J. Pedraza, Mat. Res. Soc. Symp. Proc. 818, M11.47.1 (2004).
38. A. B. Brailovsky, S. V .Gaponov, V. I. Luchin, Appl. Phys. A 61, 81 (1995).
39. C.R. Henry, Surf. Sci. Rep. 31, 231 (1998)
40. D.D. Awschalom, S. von Molnar, In Nanotechnology, ed. by G. Timp (Springer, New York 1999)
41. R.F. Haglund Jr., D.H. Osborne, R.H. Magruder, III, C.W. White, R.A. Zuhr, D.E. Hole, P.D. Townsend, F. Gonella, P. Mazzoldi: In Science and Technology of Atomically Engineered Materials, ed. By P. Jena, S.N. Khanna, B.K. Rao (World Scientific, Singapore 1996) p. 411
42. T. Schalkammer: Chem. Mon. 129, 1067 (1998)
43. F. Stietz, Appl. Phys. A 72, 381–394 (2001)
44. S.J. Henley, J.D. Carey, S.R.P. Silva, Applied Surface Science 253, 8080, (2007).
45. T. Wenzel, J. Bosbach, A. Goldmann, F. Stietz, F. Träger, Appl. Phys. B 69, 513 (1999)
46. H. Kurita, A. Takami, S. Koda, Appl. Phys. Lett. 72, 789 (1998)
47. C.R. Henry, Surf. Sci. Rep. 31, 231 (1998)
48. R. Kern, In Morphology of Crystals, ed. by I. Sunagawa (Terra Scientific Publishing 1987)
49. D.W. Pahsley, M.J. Stowell, M.H. Jacobs, T.J. Law, Philos. Mag. 10, 127 (1964).

Chapter-4

Summary and scope for future work

4.1 Summary:

Non-lithographic techniques have been employed to nanostructure thin films and bulk wafer surfaces. To realize nanostructuring *in-situ*, thin film growth at early stages and template assisted guided growth of nanowires and organized nanodots has been studied. To realize nanostructuring *ex-situ,* external high energy density stimuli e.g. excimer laser and DC electric field have been employed. Nanostructured surfaces include thin films of nickel, indium, silver, gold and silicon and single crystal bulk silicon surface. A variety of nanostructures have been demonstrated to form. Origins of formation have been treated under the basic thermodynamic platform. Few physical properties which are surface sensitive have been studied to establish the tuneability of properties with the variation of preparation parameters.

Preparation parameters viz. thickness of the film, substrate materials, substrate temperature, laser fluence have been varied to control the thin film growth in case of ***in-situ*** growth of nanostructures via early stage of thin film growth. For ***in-situ*** template assisted technique of nanostructuring, coating thickness, trench diameter, trench depth and substrates were varied. For ***ex-situ*** laser induced nanostructuring technique, apart from coating thickness and coating material, laser parameters e.g. laser fluence, reprate, number of shots and angle of incidence were varied. For ***ex-situ*** electric field induced nanostructuring technique, apart from coating thickness and coating material, field parameters e.g field value, electrode pin diameter, electrode distance and duration of field application were varied.

4.2. Controlled early stage of thin film growth

(a) Resistive thermal evaporation

Resistive thermal evaporation has been used for the growth of nickel thin film (500nm > t > 50nm). Control parameters include, thickness, substrate material and substrate temperature. Atomic force microscope has been extensively used to monitor microstructure. Long range crystalline order and magnetic behaviour have also been studied. It is shown that grain area as well as the grain boundary width stagnates beyond a certain value, with increase in substrate temperature. Phase contrast microscopy has been used to illustrate this effect. The magnetic properties such as

coercive field and saturation magnetization are shown to be critically dependent on the thickness as well as substrate temperature. Thin film growth depends profoundly on the thickness at early stages of growth. Substrates affect the microstructural growth features of thin films as well as the subsequent magnetic behaviour. Some interesting features like the formation of self-organization of nickel nanoparticles has been observed which is believed to be strain mediated. With the reduction of thickness of nickel thin films, both long range crystalline order as well as coercive field reduces and again for already reduced thickness case; long range crystalline order as well as coercive field increase with the increase of substrate temperature. This means that structurally and magnetically crystalline nickel makes a transition to nanocrystalline form with lowering thickness and it regains its crystallanity at higher substrate temperature. Trends with the variation of preparation parameters viz. thickness, substrate temperature and substrate material have been summarized in table 4.1.

(b) Pulsed laser deposition technique (PLD)

The early stages (< 10nm) of microstructural evolution of metallic thin films of nickel and silver grown by Pulsed laser deposition (PLD) in a high vacuum environment are governed by the laser–target surface interactions, the nature of transported vapor molecules, and eventually the vapor–substrate surface interactions. It is evident that there is a complex interplay between these processes that provides a rich variety of parameters to be used for the growth of ultrathin metal films by PLD. Laser energy density is a key parameter and has relatively more prominent effect than other parameters like substrate temperature in determining the extent of clustering.

Preparation parameter	Range of Variation	Average grain size	Nanostructural feature on surface	Average crystallite size	Coercive field (H_c)
Thickness	500nm-50nm (Ambient temperature, BSG substrate)	Reduces with reduction in thickness	As thickness is reduced features changes from large islands having common boundaries to isolated nanodots	Reduces with reduction in thickness	As thickness is reduced, H_c increases first then it decreases.
Substrate temperature	RT-593K (50nm thick, BSG substrate)	Increases with the increase of substrate temperature.	As substrate temperature is increased, isolated dots become huge flat interconnected grains	Increases with the increase of substrate temperature.	As substrate temperature is increased, H_c increases first then it decreases.
Substrate material	BSG, Si, MgO (RT dep., 50nm)	Minimum on BSG and larger on Si and MgO	BSG shows isolated grains, self-organization on Si and vertical growth on MgO.	Minimum on BSG and larger on Si and MgO	Not much difference

Table 4.1 Summary of thin film growth by resistive thermal evaporation.

Different substrates, depending on the crystallinity, surface smoothness and relative wettability have given rise to different shapes and sizes to resulting grains. Deposition on MgO substrate in particular has resulted in isolated nanodots of nickel and silver. Grain size distributions are strongly dependent on various preparation parameters. Both nickel and silver material have similar trends for grain size, extent of clustering and grain size distribution as the preparation parameters were varied and the trends have been summarized in the following table 4.2.

Preparation parameters	Range of Variation	Average grain size	Extent of clustering	FWHM of grain size distribution
Thickness	6-10nm (RT dep. on BSG)	Increases with increase in thickness	Increases with increase in thickness	Reduces with increase in thickness
Substrate temperature(T_S)	RT-573K (6nm thick, on BSG)	Increases with increase in T_S.	Increases with increase in T_S.	Increases with increase in T_S.
Substrate material	BSG, Si, MgO (6nm at RT)	Grain size is minimum on BSG and maximum on Si	Isolated dots on MgO and isolated islands on Si, on BSG however closely spaced fine grains	Small on MgO and Si and relatively large on BSG
Laser energy (L.E)	100 to 500mJ	Increases with increase in **L.E.**	Increases with increase in **L.E.**	Increases with increase in **L.E.**
Substrate-target distance (d_{ST})	6 to 10cm	Reduces with increase in d_{ST}.	Reduces with increase in d_{ST}.	Reduces with increase in d_{ST}.

Table 4.2 Summary of thin film deposition by pulsed laser deposition technique

4.3. Template assisted nanostructuring

To achieve nanowire formation via in-situ technique, v-trench templated substrates have been utilized. Shadowing of vapour has resulted in the formation of nanowires inside the trench. Apart from substrate surface smoothness, condensing vapour material, substrate temperature, rate of cooling of condensate determine the resulting curvature of the frozen structure. Ni, In, Au and silicon deposition onto trench templated substrates have yielded nanowires of uniform diameter. It is clear from the results presented that the nanowires formed by the template assisted approach in the current work can be directed along any direction, depending on the direction of the trenches. Hence, in contrast to other approaches, no further manipulation is required to functionalize these nanowires. The microstructural evolution follows a Stranski-Krastanov type of growth. These clearly indicate formation of islands on top of already formed continuous nanowires, which is typical of Stranski-Krastanov type

growth. It also shows that the wettability of the nanoparticles is a function of the width of trenches and hence the angle of incidence of vapours molecules in to the trench. Therefore, there is a window of trench depth / trench width (d / W ratio) where for a given metal of a particular thickness, nanowires will form. In all the cases it was found that the wettability is also a function of the deposition time since nanowire formation followed the sequence; nanoparticle chain to nanowire to continuous film as a function of thickness. The above mentioned facts have been summarized in table 4.3.

Electric field induced nanostructuring

(a) Single crystal silicon surface

A novel and efficient approach to synthesize silicon nanocrystals has been demonstrated by using moderate DC electric field near spark threshold. Nanoparticle size is found to be field dependent. Field nanostrcutured silicon wafers have shown transition from single crystalline to nanocrystalline behaviour. Field nanostructured silicon surface is observed to be highly absorbing and photo luminescent (green). This approach of nanoparticle synthesis has the potential for further research and developments for variety of applications.

(b) Thin films

A post-deposition electric field treatment of metallic thin films of nickel and indium has been demonstrated to result in unique and controllable nanostructures in the form of nanowires and self-organization of nanoparticles. It has been shown that a DC field can also be used to manipulate these nanostructures for surface reconstruction.

Preparation Parameters	Range of Variation	Nanostructural features	Nanowire diameter	Physical properties
Coating thickness	**10-100nm**	As coating thickness is increased, unorganized nanoparticles become organized first and then at higher thickness, nanowires are formed.	Increases with increase in coating thickness.	
Trench diameter	**5-50µm**	There is a window of trench width where nanowire forms, above and below nanoparticulate or clustered features were observed.		
Coating material	**Ni, In, Au and Si**	All materials have yielded Nanowire formation has been observed for all materials and have shown similar trend of feature growth with coating thickness	Nanowire diameter is coating material dependent. Nickel, gold and silicon have given uniform diameter nanowires, however Indium did not	Ni NWs show magnetically anisotropic nature and approximately 4 % of MR value. Shift in plasmon peak with reduction in coating thickness is observed for In NWs. Gold NWs show additional surface plasmonic peak apart from shift in existing ones.

Table 4.3 Summary of template assisted technique for the growth of nanowires

Significantly, the electric-field-generated heat has been found to trigger evolution of long-range crystalline order in the films. Shape and size change of grains have yielded shift in surface plasmonic peaks. Further it was found that grain growth can be

manipulated by the field direction. An additional finding was that crystallization of thin films is irreversible. There are three different energy barriers for grain growth, crystallization and organization. Field induced crystallization without any external thermal input; in itself is an interesting effect for its various possible applications in tuning physical properties including surface plasmonic and magnetic behaviour.

Results of the resulting nanostructures via DC electric field induced nanostructuring technique have been summarized in table 4.4. Experimental variables have been mentioned and corresponding results for single crystal silicon surface and various thin films have been mentioned.

4.5 Excimer laser induced nanostructuring

(a) Single crystal silicon surface

The morphological reconstruction and nanocrystallization of Si [311] surfaces under the influence of excimer laser is demonstrated. It is shown that the process provides several control parameters such as incident laser energy density, repetition rates, angle of incidence of the laser beam and number of shots. A variety of nanostructures including nanowires and nanoparticle arrays have been observed. It is also demonstrated that the Si surface undergoes a transition to the nanocrystalline state from the single crystal state under the influence of the laser beam. This could have important implications for different Si based technologies. It is demonstrated that such nanocrystalline silicon becomes photo luminescent.

(b) Thin films

KrF excimer laser has been employed as high energy density trigger to give rise to grain growth for as deposited thin films of Indium, gold, silicon and nickel. Excimer laser has triggered long range crystalline order in these films. Laser treatment has yielded near to monodisperse gold nanoparticles and shape change has been witnessed for indium nanoparticles. Nickel thin film has exhibited change in surface feature and silicon thin films have shown huge response in terms of grain size enhancement of an

order of magnitude. Surface plasmonic peak has been shifted for indium after the laser treatment. Irrespective of materials, long range crystalline order has been found to be enhanced.

Experimental results for various experimental conditions for single crystal silicon surface and various thin film materials have been summarized in table 4.5.

Experimental parameters	Range of variation	Results	
Field value	**0.15-3.3 kV/cm**	There are three different threshold fields for grain growth, organization and crystallization of films. As field is progressively increased, first grain growth takes place, then it organizes and then crystallization takes place.	
Distance between the electrodes	**2-10 mm**	At larger distance no substantial effects were observed and at smaller distance sparks were observed which delaminates the film from the substrate and therefore there is a window of distance for this technique.	
Area of electrode	**0.03-12 mm^2**	At larger area, directions of the formed nanowire / organization is quite random, while on the other hand it organizes in the field line better for shorter area of electrode.	
Thin film thickness	**10-100nm**	A minimum thickness is required to observe the effect of electric field. Further increasing the field, affects the grain size but no organization is observed until a critical thickness gives rise to necessary conduction beneath the top layer of thin film. For very large thickness, there are problems due to its minimized spark threshold.	
Materials	**Thin films**	**Ni**	Nanowire formation, field assisted growth of organized nanodots as well as grain growth. Crystallization of amorphous films has also been observed.
		In	Nanowire formation, field assisted growth of organized nanodots as well as grain growth. Crystallization of amorphous films has also been observed. There are shifts in surface plasmonic peaks.
		Au	No nanowire formation, no directional organization, only grain growth takes place. At higher field, densification and nanopore formation has been observed though. Crystallization of amorphous films has also been observed. There are shifts in surface plasmonic peaks and also percentage of reflection changes.
		Si	No nanowire formation, no directional organization, only grain growth takes place. Some signature of crystallization of amorphous films has also been observed.
	Bulk	**Si**	Single crystal silicon surface becomes nanocrystalline and at higher field it shows close to amorphous nature. Specular reflection reduces and the surface becomes photo luminescent when silicon surface is treated with electric field.

Table 4.4 Summary of electric field induced nanostructuring

Experimental parameter	Range of variation		Results
Laser fluence	(a) For thin films, 0.01-0.05 J/cm^2		(a) With the progressive increase of laser fluence for thin films, amorphous surfaces becomes nanocrystalline and surface plasmonic peak is shifted.
	(b) For bulk silicon 0.1-5J/cm^2		(b)Single crystalline bulk silicon wafer becomes nanocrystalline, absorbing and photoluminiscent
Number of laser shots	(a) For thin films 1-50 shots		(a) With the progressive increase of number of laser shots thin films become more crystalline, and surface plasmonic peak gets shifted.
	(b) For silicon wafer 1-1000 shots		(b) Bulk silicon becomes nanocrystalline, more absorbing and photoluminescent.
Angle of incidence	0-90^0 for silicon wafer		Formation of anisotropic features including nanowires at small angles and isotropic island like growth at higher angles.
Gap time between the laser shots	From 1 second to 2 hours for 2 J/cm^2 laser fluence onto silicon wafer		Resulting surface features are altogether different
Material	**Thin films**	**In**	Irrespective of material of thin films, grain growth and long range crystalline order evolution have been observed. Apart from this surface plasmonic peak shift and absorption percentage increase has been observed.
		Au	
		Si	
		Ni	
	Bulk	**Si**	It becomes nanocrystalline, absorbing and photo luminescent

Table 4.5 Summary of excimer laser induced nanostructuring

4.6 Future scope:

This thesis demonstrates a variety of non-lithographic techniques for achieving nanostructures and nanostructured surfaces in general and nanowires in particular

which are promising for numerous technological applications. The current work is expected to have long term impact on future of non-lithographic techniques. Various interests evolve from the multidisciplinary nature of this thesis. However, a few selected directions are as follows:

A. Study on electroluminescence / field emission from the nanostructured surface.
B. Study on the crystallization, magnetic behavioral change ***in-situ.***
C. Study on template assisted growth for oxides and nitrides.
D. Study on the application of DC field / excimer laser to crystallize/nanostructure other materials.
E. Study on application of nanostructured semiconducting surface for various chemical sensors.
F. Study on nanowire magnetic tunnel junction, for achieving maximum MR (%) and minimum RA product.